Dissertation
submitted to the
Combined Faculties for the Natural Sciences and for Mathematics
of the Ruperto-Carola University of Heidelberg, Germany
for the degree of
Doctor of Natural Sciences

Put forward by

Diplom-Physikerin Nora Hünemohr

Born in: Wiesbaden, Germany

Oral examination: December 10th, 2014

Dual energy CT as an alternative for ion radiotherapy treatment planning

Referees:	Prof. Dr. Oliver Jäkel
	Prof. Dr. Wolfgang Schlegel

Erklärung

Ich erkläre hiermit, dass ich die vorgelegte Dissertation selbst verfasst und mich dabei keiner anderen, als der von mir ausdrücklich bezeichneten Quellen und Hilfen bedient habe.

Heidelberg, den 29.09.2014

Nora Hünemohr

Dual energy CT als Alternative für die Strahlentherapieplanung mit Ionen

Im Rahmen dieser Arbeit wurden die Unsicherheiten der Reichweitenkalibration (als das Verhältnis der Stoßbremsvermögen, SPR) von CT-Daten untersucht und das Zwei-Spektren-CT (dual energy CT, DECT) als mögliche Verbesserung für die Strahlentherapieplanung mit Ionen umfassend charakterisiert.
CT-Messungen von Gewebesurrogaten, welche die Basis für die sogenannte stoichiometrische Kalibration - den Goldstandard - darstellen, wurden unter einer Reihe variabler, klinischer Bedingungen durchgeführt. Die Ergebnisse zeigen, dass eine höhere Röhrenspannung und die Messung einer größeren Anzahl dichter Materialien zu einer verbesserten Kalibration führen.
Für einen Bilddatensatz eines Kopf-Hals-Patienten wurden SPR-Vorhersagen des DECT mit denen eines Standard-CTs verglichen. Bildbasiert wurde hierbei die Möglichkeit genutzt, die Elektronendichte und die effektive Ladungszahl getrennt darzustellen. SPR-Differenzen von 2 % in den Ventrikeln und 5-8 % im Felsenbein wurden festgestellt. Diese Unterschiede zeigen, dass ein absoluter Vergleich der DECT-basierten SPR-Vorhersagen mit einer Referenzmethode wie z.B. dem Schwerionen-CT wünschenswert ist. Messungen von Gewebesurrogaten zeigten eine gute Übereinstimmung ((0.6±0.3) %) der vom DECT vorhergesagten SPR mit gemessenen Referenzwerten, während das Bildrauschen um nur 0.2-0.4 Prozentpunkte erhöht war.
Für die Monte-Carlo-basierte Therapieplanung wird eine neuartige Methode vorgestellt, die beide DECT-Kontraste für die Verbesserung der Gewebezuordnung nutzt.
Es bleibt künftigen Untersuchungen überlassen, inwieweit die aufgezeigten Möglichkeiten des DECT auch in der klinischen Routine der Strahlentherapieplanung mit Ionen Anwendung finden.

Dual energy CT as an alternative for ion radiotherapy treatment planning

This thesis investigates uncertainties emerging from CT data to stopping power ratio (SPR) calibration and characterizes the potential of dual energy CT (DECT) as an alternative for treatment planning in ion radiotherapy.
The robustness of the stoichiometric calibration was tested for variations of the initial CT number measurements. Based on the results, it is suggested to use higher X-ray tube voltages and include more dense materials in the initial CT scan.
Complementarily, the separation of electron density and effective atomic number with DECT helps to resolve tissues with uncommon compositions: In a first patient (head and neck case), DECT-predicted SPR were found to differ by 2 % in the ventricles and by 5-8 % in the petrous part of the temporal bone compared to single energy CT (SECT) predictions. On the other hand, verification of DECT-based SPR prediction for tissue surrogates showed excellent agreement of (0.6±0.3) % with measurements, and noise levels of DECT-based SPR predictions were found to be elevated by only 0.2-0.4 pp compared to SECT. Both DECT contrasts were further exploited for Monte-Carlo-based dose planning and improved tissue decomposition.
A validation of DECT-predicted SPR in absolute terms with a reference method, such as heavy ion CT, would help to translate the presented potential benefits of DECT to its future clinical application in ion radiotherapy.

Contents

List of Abbreviations

BIC	Bayesian Information Criterion (page 107)
CT	Computed Tomography (page 1)
CTDI	Computed Tomography Dose Index (page 9)
DECT	Dual Energy CT (page 1)
DEI	Dual Energy Index (page 13)
DICOM	Digital Imaging and Communications in Medicine (page 7)
DIPP	DKFZ Image Processing Platform (page 34)
DLP	Dose Length Product (page 10)
DVH	Dose-Volume-Histogram (page 34)
FOV	Field Of View (page 11)
GSI	Gesellschaft für SchwerIonenforschung (page 33)
HIT	Heidelberg Ion-Beam Therapy Center (page 21)
HLUT	Hounsfield Look-Up Table (page 18)
MAR	Metal Artifact Reduction (page 110)
MC	Monte Carlo (page 2)
MITK	Medical Imaging Interaction ToolKit (page 34)
MRI	Magnetic Resonance Imaging (page 1)
MV CT	MegaVoltage CT (page 41)
PET	Positron Emission Tomography (page 1)
PFO	Posterior Fossa Optimization (page 101)
pp	percentage points (page 67)

SECT	Single Energy CT (page 21)
Sn	tin filter (page 21)
SPR	Stopping Power Ratio (page 1)
TOPAS	Tool for PArticle Simulation (page 34)
TPS	Treatment Planning System (page 7)
TRiP	TReatment planning for Particles (page 33)
Virtuos	VIRTUal Radiotherapy Simulator (page 33)
VOI	Volume Of Interest (page 22)
WEPL	Water-Equivalent Path Length (page 3)
WET	Water-Equivalent Thickness (page 19)

1 Introduction

In proton and ion radiotherapy, remarkably precise physical dose delivery with steep gradients can be achieved by taking advantage of the dose profile associated with the spread-out Bragg peak. While these advanced therapy modalities promise to spare healthy tissue better than conventional photon radiotherapy, they require an even more precise and accurate treatment planning. A good understanding of the uncertainties involved and the development of new approaches for their reduction is essential for the improved exploitation of the dose gradients. For this purpose, patient imaging plays an important role along the entire particle therapy treatment course.

Novel anatomical and functional contrasts that may provide additional, valuable information for the physical and biological dose planning are currently under research. Target delineation based on magnetic resonance images (MRI) as well as dose painting and treatment verification with positron emission tomography (PET) images are prominent examples. Furthermore, research projects aim to investigate image guidance for fast plan adaptation to inter- and intrafractional motions. Several of these imaging modalities are currently involved in the diagnostic clinical routine, but it remains to be seen which of these - besides the standard computed tomography (CT) - will find their way into radiotherapy treatment planning. The integration of novel imaging modalities and the replacement of old ones faces modality specific challenges and requires a precise linkage and comparison to other existing techniques, as well as novel quality assurance tests which take much research effort and time.

At the current clinical stage, CT images therefore still represent the gold standard for therapy planning, despite one of the main intrinsic uncertainties of physical dose delivery emerges from the CT data conversion to tissue-to-water stopping power ratio (SPR) for ions. The calibration has to link two different regimes: photons for imaging and ions for therapy. Tissues can exhibit similar photon attenuation but different SPR for ions and vice versa. Related range uncertainties due to the conversion hamper the full exploration of the steep dose gradients of ion beams. Target safety margins accounting for these uncertainties are as large as in the order of 3.5 % of the range + 1 mm in depth (Paganetti [2012]) and beams stopping right in front of organs at risk are usually avoided in the treatment planning. These concessions of range (and therewith dose) uncertainties come at a cost for additional side effects and therefore treatment efficacy.

This thesis quantifies uncertainties emerging from the CT to ion range conversion and investigates dual energy CT (DECT) as an alternative imaging modality that is ready to use in the clinical treatment planning routine.

To do so, the first part (Sec. 4.1) focuses on the stoichiometric CT calibration (Schneider et al. [2000]) that represents the current standard in particle therapy. The generation of a stoichiometric calibration in the clinical routine is a demanding and non-trivial task affected by several uncertainties. The underlying simplified parametrization of the photon attenuation varies with CT protocols and measurement setups. A detailed characterization of these uncertainties and recommendations for improvement are important for the clinical routine. Chapter Sec. 4.1.1 identifies and discusses therefore different factors that influence the optimization of the parametrization and systematically investigates the corresponding look-up tables.

Complementarily, the second part (Sec. 4.2) focuses on DECT which has been used in the diagnostic clinical routine since its commercial launch in 2006. DECT enables to scan the tissue at two different spectral energies. Ion radiotherapy may benefit in particular from the additional available tissue contrasts, namely the electron density relative to water $\hat{\rho}_e$ and the effective atomic number Z_{eff}. First, the accuracy of the $\hat{\rho}_e$ and Z_{eff} determination for defined materials was investigated. Subsequently, a novel conversion of $\hat{\rho}_e$ and Z_{eff} to SPR was established. Sec. 4.2.2 presents the first experimental validation of the approach suggested by Yang et al. [2010] with DECT images measured with a clinical dual source scanner for defined phantom materials.

The third part (Sec. 4.3) compares both of the two imaging modalities, SECT and DECT, for the case of a head and neck patient. Relative differences were evaluated in terms of SPR prediction for specific tissue types and image reconstructions. Additionally, a planning study with two carbon ion fields evaluated the relative differences in terms of range and dose coverage. Since imaging dose is expected to be increased with DECT, image noise levels of DECT and SECT were measured for homogeneous tissue surrogates while keeping the image dose constant for both modalities. The possibility to evaluated SECT-based $\hat{\rho}_e$ prediction for photon therapy is illustrated thereafter.

Nowadays, analytical dose algorithms dominate the treatment planning in ion therapy facilities. In the near future, dose calculation algorithms based on Monte Carlo (MC) simulations are expected to become an applicable tool in the clinical routine. The simulation of physical interactions of particles traversing the patient depends particularly on the precise physical characterization of the tissues. Here, DECT data has the potential to improve these material assignments. Therefore, the last part (Sec. 4.4) of this thesis exploits in a first study the novel DECT imaging contrasts for MC simulations. Range studies investigate which tissue compositions would benefit most from the additional information that DECT provides.

2 Background

2.1 CT imaging for treatment planning

CT images provide the spatial distribution of photon attenuation coefficients of the scanned object. Projections along a line s of a polychromatic photon beam of incident intensity $I_0(E)$ and energies E that is attenuated exponentially by the scanned object are detected under different angles in one axial plane in x and y. The transmitted photon intensity I can be reconstructed (Sec. 2.1.2) to a two dimensional map of the linear photon attenuation coefficient μ of the object (Kalender [2006]):

$$I = \int I_0(E) \cdot e^{-\int \mu(x,y,E) \mathrm{d}s} \mathrm{d}E. \tag{2.1}$$

In CT images, the measured μ_m of the medium is presented relatively to the linear attenuation coefficient of water μ_w as a CT number ξ defined by (Kalender [2006])

$$\text{'CT no':} \quad \xi = \frac{\mu_\mathrm{m} - \mu_\mathrm{w}}{\mu_\mathrm{w}} \cdot 1000\,\mathrm{HU}. \tag{2.2}$$

The CT number is measured in Hounsfield Units ([HU]), in honor of the CT inventor Godfrey Hounsfield (Hounsfield [1973], Kalender [2006]). By definition water has a CT number of 0 HU and represents one of the fix points for the CT scanner calibration at different photon spectra. The second calibration point is the CT number of air at -1000 HU.

CT images of the patient anatomy are the basis for treatment planning and dose computation in radiotherapy. In standard photon therapy, CT numbers are converted to mass density or electron density relative to water (Thomas [1999]). For ion therapy, CT numbers are used to predict the interaction with therapeutic ion beams in terms of the water-equivalent path length (WEPL, Sec. 2.3.4) for ions. Other imaging modalities (usually superimposed on the CT images after image registration) might be consulted by the therapists for therapy decisions, target definition and structure delineation. However, dose calculation is in the vast majority of cases based on CT images.

The next sections, therefore, repeat the main photon interaction processes with matter that are of importance for the understanding of the CT calibration and translation process mandatory in ion radiotherapy.

2.1.1 Interaction of photons with matter

The linear attenuation coefficient μ describes the probability of photon interaction with matter per unit path length Δx. From the initial number of N photons, ΔN photons undergo interaction and $N - \Delta N$ photons emerge the object unchanged and can be detected (Bushberg and Boone [2011]):

$$\mu = -\frac{\Delta N/N}{\Delta x}. \tag{2.3}$$

μ can be expressed by the number of atoms per unit volume of the absorber $n = \rho N_\mathrm{A}/A$ times the atomic cross section σ_a, with N_A denoting Avogadro's number, ρ the mass density and A atomic mass number of the object. σ_a can in turn be expressed by the number of electrons (atomic number Z) times the cross section per electron σ_e (measured in [cm^2/electron], McCullough [1975]):

$$\mu = n \cdot \sigma_\mathrm{a} = n \cdot Z\sigma_\mathrm{e}. \tag{2.4}$$

At diagnostic energies (X-ray tube voltage: 30-150 kV), photons interact with matter by

- Coherent "Rayleigh" scattering
- Incoherent "Compton" scattering
- Photoelectric absorption

Fig. 2.1 shows the individual photon mass attenuation coefficients μ/ρ for three human tissue compositions. The following subsections describe the three interaction effects in more detail.

Coherent scattering

When a photon is scattered coherently on an atom, no energy is converted and the scattered photon has the same wavelength as the incident photon (Johns [1983]). The probability for coherent ("elastic") Rayleigh scattering is increased for low-energy photons penetrating high Z materials (Podgorsak [2010]):

$$\sigma_\mathrm{e}^\mathrm{coh} \propto \frac{Z}{E^2}. \tag{2.5}$$

For diagnostic X-ray energies, the initial photon field is hardly changed as the scattered beam is forward peaked (Jackson and Hawkes [1981]). Coherent scattering is usually assumed to be negligible compared to the other two interaction effects at diagnostic photon energies. The only exception is mammography, where X-ray energies of 15-30 keV are employed (cf. also Fig. 2.1).

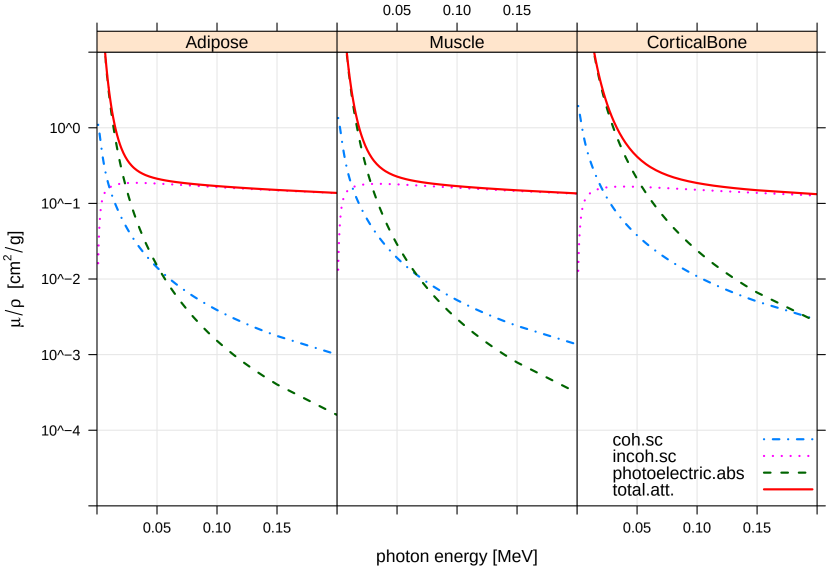

Figure 2.1: Mass attenuation coefficients (μ/ρ) for three reference human tissue compositions (ICRU [1989]) in the diagnostic photon energy regime. Data taken from Berger et al. [1998].

Incoherent Compton scattering

A photon is scattered inelastically on an atomic electron when part of its energy is transferred to the recoil electron. The interaction occurs most likely with outer valence electrons (Bushberg and Boone [2011]). The Klein-Nishina electronic cross section formulates the inelastic scattering for photons of incident energy $x = E/m_ec^2$ on *free* stationary electrons (Johns [1983])

$$\sigma_e^{KN}(E) = \frac{3}{4}\sigma_T\left(\left(\frac{1+x}{x^2}\right)\left(\frac{2(1+x)}{1+2x} - \frac{\ln(1+2x)}{x}\right) + \frac{\ln(1+2x)}{2x} - \frac{1+3x}{(1+2x)^2}\right). \quad (2.6)$$

σ_T denotes the Thomson cross section with the classical electron radius r_0, the electron rest mass m_e and the speed of light c (Johns [1983]):

$$\sigma_T = \frac{8\pi}{3}r_0^2 = \frac{8\pi}{3}\cdot\left(\frac{e^2}{m_ec^2}\right)^2 = 2.8\cdot 10^{-13}\text{cm}^2. \quad (2.7)$$

Since atomic electrons are always bound (with decreasing energy from the inner to the outer shells), effects of the atom specific binding energies have to be taken into account particularly at photon energies below 10 keV (Johns [1983], Williamson et al. [2006]). For photon energies exploited in radiotherapy (above a few MeV), binding energies can be neglected.

At a central hit of a photon of energy $h\nu_0$, the maximum energy is transferred to the recoil electron, which is ejected in forward direction while the scattered photon back scatters ($\theta = 180°$) with the energy $h\nu'$. The energy transferred depends on the photon scattering angle θ (Bushberg and Boone [2011]):

$$\frac{1}{h\nu'} - \frac{1}{h\nu_0} = \frac{1}{m_e c^2}(1 - \cos\theta). \tag{2.8}$$

The local energy released to the atomic electron increases with incident photon energy. At lower photon energies around 10-110 keV, photon beams transfer only a minor percentage (smaller than 2-20 %) of the beam energy to the tissues' electrons (Johns [1983]). At higher energies exploited for radiotherapy, the recoiled electrons receive the majority (about 80 %, statistical mean value) of the incident photon energy ($\equiv$ dose deposition due to ionization) and the scattered beam is more forward peaked (Johns [1983]).

Compton scattering is the dominant interaction process with tissue at diagnostic photon energies (Fig. 2.1). Compton scattering depends solely on the tissues' electron density (Eq. 2.4, Eq. 2.6) and the (poor) soft tissue contrast of CT is mainly determined by the small differences in tissues' electron densities (and related mass densities). Scattered photons degrade the image quality and the transmitted photon beam has to be collimated at the detector side.

Photoelectric absorption

The photoelectric effect describes the process when a photon is absorbed by an atomic electron and a photoelectron of energy $h\nu_0 - E_{\text{bind}}$ is ejected. The excited recoil atom emits characteristic photon radiation and/or ejects an Auger electron ("inner photoelectric effect") when the vacancy of the inner shell is filled by an outer electron (Evans and Noyau [1955]). Most likely, the photoelectric absorption occurs on tightly bound core electrons of the inner K or L shells having a binding energy E_{bind} just below the incident photon energy (Podgorsak [2010]). Photoelectric absorption increases strongly with the atomic number Z of the material which is responsible for the excellent CT contrast between soft tissue and bone. The electronic cross section of the photoelectric absorption in tissues falls rapidly with increasing energy and is proportional to (Johns [1983])

$$\sigma_e^{\text{photo}} \propto \frac{Z^n}{E^3} \text{ with } n \approx [3-4]. \tag{2.9}$$

2.1.2 CT protocol parameters

Today's scanners' hard- and software allow for a multiplicity of parameter settings that influence CT scans. In order to assure reproducible image transfer and evaluation, image data has to be provided in a standardized file format. In radiation therapy, CT protocols ensure a standardized scan setting for every patient and denote the basis for reproducible treatment planning based on CT images.

The majority of diagnostic medical images (including CT images) are provided in the Digital Imaging and Communications in Medicine (DICOM) format. Protocol and acquisition specific scan parameters are recorded next to the image data in the DICOM header. The treatment planning system (TPS) cross-checks parts of the DICOM tags in order to assure a correct and reproducible conversion of CT numbers to mass or electron density (photon therapy) or to the WEPL for ion therapy. The following sections describe protocol parameters important for this thesis.

X-ray tube voltage

In an X-ray tube, electrons emerging from the cathode are accelerated to the anode through an electric potential. Being deflected by the anode nuclei, the majority of the kinetic energy of the electron beam is converted to heat, while only a small fraction is emitted to Bremsstrahlung (≈1 %, Krieger [2009]). The electronic deflection depends on the distance to the atomic nuclei (Coulomb potential) and results in a polychromatic photon spectrum that decreases linearly with increasing photon energy. The maximum kinetic energy (measured in [keV]) that the electrons can release to the Bremsstrahlungs-photons is determined by the voltage applied between the cathode and anode (measured in [kV]).

The broad photon spectrum is further accentuated by the emission of characteristic photon radiation specific for the target material of the anode. An atomic electron of the inner shells is ejected after being hit by an accelerated electron ($E_{\text{kin}} > E_{\text{binding}}$). The free vacancy is filled with an electron of the outer shells by emitting X-rays. The energy of the characteristic radiation equals the differences of the binding energies of both levels (Bushberg and Boone [2011]). Tungsten, a typical anode material, has a characteristic line at 69.5 keV (Berger et al. [1998]).

X-ray filters and beam hardening

Low energy photons get attenuated most likely directly in the anode material and tube shielding. Additional aluminum slabs placed in the beam path remove remaining low energy photons that would not contribute to the image. The mean energy of a typical photon spectrum in air ranges from approximately 1/3 up to 1/2 of the maximum photon energy.

When the resulting polychromatic photon spectra penetrates the patient, photons of lower energies are more likely to get absorbed (Sec. 2.1.1). This increases the mean energy ("beam hardening") of the photon spectrum with penetrated path length. For a cylindrical homogeneous object positioned on the central scanner axis, measured photon attenuation would decreases towards the center. Beam hardening correction based on the assumption of water-like objects is applied by default in modern image reconstruction.

A quasi monoenergetic photon beam would be preferred for CT imaging, since no beam hardening can occur. However, X-ray tubes cannot produce such a high output necessary and exploiting high intensity synchrotron radiation is impracticable (Torikoshi et al. [2003]). Instead, the development of high power X-ray tubes allows the insert of additional filters that further narrow the resulting photon spectra as pursued in the the DECT scanners for the 140 kV spectrum (Sec. 3.1) .

X-ray tube current and acquisition pitch

Besides the applied tube voltage that determines the quality of the photon energy spectra, the applied tube current determines the quantity of photons produced and is measured in milliamperes [mA] (Bushberg and Boone [2011]). A higher electrical tube current improves the image quality as the photon statistics increase at the detector side but the dose deposited in the patient increases simultaneously. In order to obtain similar image quality at different tube voltages (similar photon statistics at the detector), it is necessary to increase tube currents for lower kV settings since (1) the photon output in the X-ray tube decreases with lower kV settings and (2) lower energy photons are more likely to get absorbed by the patient (Bushberg and Boone [2011]).

To include the scan time, tube currents have to be multiplied with the exposure time per rotation ("tube current time product", measured in [mAs]). If the pitch (table feed per gantry rotation divided by the beam collimation) is smaller than one, the X-ray tube "oversamples" the measurement volume. The tube current time product divided by the pitch is called the "effective mAs" or "exposure".

CT reconstruction

Raw-data sets of detected photon intensities have to be processed for image reconstruction. For the standard filtered backprojection, parallel projected X-ray intensities $p(\theta,l)$ recorded under different angles θ of one gantry rotation and with the distance l to the rotation center have to be filtered with a convolution kernel before being backprojected to the image plane (Bushberg and Boone [2011]). The convolution with a high-pass filter is necessary as the radial symmetry in CT imaging would provoke a "blurring" of the simple backprojected image (i.e. the density of geometrical X-ray beam paths increases towards the center, Bushberg and Boone [2011]). Since a convolution in the spatial domain is equivalent to a multiplication in the frequency domain, the raw data projections $p(\theta,l)$ are first Fourier-transformed and the multiplied with the convolution kernel k in the frequency domain. The subsequent inverse Fourier-transform yields the attenuation result $\mu(x,y)$ in the spatial domain (Bushberg and Boone [2011]):

$$\mu(x,y) = \mathrm{FT}_{\mathrm{2D}}^{-1}[\mathrm{FT}_{\mathrm{1D}}[p(\theta,l)]\cdot|k|]. \tag{2.10}$$

Eq. 2.10 represents also the central slice theorem saying that the 1D Fourier transformation of a projection of a 2D spatial distribution equals the 2D Fourier transformation of the projection in the frequency domain (Schlegel and Bille [2002]).

Convolution kernels have a significant influence on the image sharpness as well as the noise and are usually given in the frequency domain. High image frequencies are important for the edge definition and image details but are also associated to image texture and therewith image noise. Information on main image features is provided in low image frequencies.

Besides standard filtered backprojection, iterative reconstruction algorithms, already known from SPECT and PET, are available in the newest scanner generations. In the projection space, raw data of a pre-estimated, simple image is compared to the actual raw data measurement and iteratively improved until it approaches sufficiently the measured data. Furthermore, iterative reconstruction algorithms allow for metal artifact reduction in the raw data sinogram by removing projections through metals that do not contain any information. Missing data is then estimated by interpolating between neighboring projections (Meyer et al. [2010]). Iterative reconstructions improve the contrast-to-noise ratio significantly and are therefore beneficial for dose savings in CT image acquisitions. However, solving the large data set of linear equations for every image pixel is computing time and -memory consuming.

Nonlinear partial volume effect Due to the finite voxel size (more precisely the slice thickness), the nonlinear partial volume effect occurs when transmitted I_1 and I_2 through large lateral attenuation gradients in z are collected by one detector element. For the measured intensity I attenuated by two volumes of different attenuation μ_1 and μ_2, it applies with $I_0 = I_1 + I_2$:

$$I = I_1 e^{-\mu_1 \cdot z} + I_2 e^{-\mu_2 \cdot z} \neq I_0 e^{-(\mu_1 \cdot z + \mu_2 \cdot z)}. \tag{2.11}$$

As a consequence, CT numbers for pixels containing large attenuation gradients along the scanner axis such as bone/air or metal/tissue interfaces are underestimated (Kemerink et al. [1995]). A thinner slice thickness is most effective to reduce partial volume artifacts.

CT imaging dose report

CT scanning represents an invasive imaging modality and the awareness of secondary cancer risks emerging from ionizing radiation defines the tradeoff between image quality and image dose. In contrast to diagnostic images, CT protocols for treatment planning do not aim to provide excellent tissue contrast (i.e. no contrast agent is given) and image doses are usually elevated compared to diagnostic CT images.

The scanner output for the specific protocol settings under standard conditions is recorded and accessible in the DICOM image tag named Computed Tomography Dose Index (CTDI, measured in [mGy]). The CTDI is defined for various dose measurement settings. One standard index is the CTDI_{100} providing the approximate dose from a single rotation that would be deposited in a standardized PMMA phantom (head: radius= 16 cm; body: radius= 32 cm) in the center of a scan length of $z = 10\,\mathrm{cm}$ (McCollough et al. [2011], AAPM [2008]):

$$\mathrm{CTDI}_{100} = \frac{1}{l} \int_{-5\,\mathrm{cm}}^{+5\,\mathrm{cm}} D(z)\mathrm{d}z. \tag{2.12}$$

The detector collimation determines the beam collimation l which is the product of the number of detectors (specifically the number of data channels) times their collimation width (McNitt-Gray [2002]). A smaller detector collimation is less dose efficient but, at the same time, permits a reconstruction of thinner image slices. Nowadays, detectors elements can be spatially divided into non-uniform section widths in z direction.

The CTDI is not a measure for the actual dose to the patient but facilitates the comparison of dose values for different protocols. The dose length product (DLP) multiplies the actual scan length of the examined volume with the volumetric CTDI and gives a reference index for the specific dose of the scan.

CT image dose is directly proportional to the photon fluence which is represented by the X-ray tube output:

$$\text{dose} \propto \text{tube current}. \tag{2.13}$$

Besides the X-ray tube current, the X-ray tube potential has a significant impact on the dose. Photons of higher energies release much more energy to the local tissues environment when being scattered:

$$\text{dose} \propto (\text{tube voltage})^n, \text{ with } n = [2-3]. \tag{2.14}$$

For the same acquisition and reconstruction settings, quantum image noise depends on the inverse square root of the effective tube current

$$\text{noise} \propto \frac{1}{\sqrt{\text{tube current}}} \tag{2.15}$$

Noise can be reduced further by increasing the reconstructed voxel volume.

2.2 Dual energy CT imaging

The idea to scan an object with two different photon spectra was already formulated in the decade of the CT invention (Hounsfield [1973], Rutherford et al. [1976b], Alvarez and Macovski [1976]). Today, different technical realizations are commercially available or investigated in research projects. This section briefly summarizes the following four systems:

- Single source / dual energy
- Dual source / dual energy
- Fast kV-switching
- Energy discriminant detectors and dual layer detectors

Single source dual energy The oldest technical realization of DECT imaging is represented by the sequential scanning of the object with two different X-ray tube voltages. Tube currents can be adjusted according to the voltage which reduces the imaging dose. Single source dual energy is currently pursued in the SIEMENS Definition Edge scanner that is able to perform two consecutive scans with a length of 30 cm in less than 15 seconds ($\text{pitch}_1 = 0.6$, $\text{pitch}_2 = 1.6$). Although resulting images are registered and time delay is minimal, this technique is sensitive to motion between both image acquisitions.

Dual source dual energy The first dual source CT scanner was launched in 2006 (Flohr et al. [2006]). The dual source CT system is able to scan the patient simultaneously with two different photon spectra, nearly free of motion artifacts. X-ray tubes and detector arrays are mounted with an offset on the same gantry (90-95°, dependent on the scanner generation). Due to geometrical limitations, the detector system of the higher kV X-ray tube covers a smaller field of view (FOV) and the dual energy information is available only in the inner FOV (26-35 cm dependent on the scanner generation). Both applied tube currents can be individually adjusted according to the tube potential or projected scan volume ("dose modulation"). Filters can be inserted individually and the spectral overlap of both photon spectra is reduced to a minimum. In the newest, third dual source CT generation, the low kV "Vectron" X-ray tube can be operated at 70 kV and performs at very high tube currents while the second X-ray tube potential can be set to 150 kV with additional tin filtration. Post-processing applications (Sec. 2.2.1) in dual source scanners are usually applied in the image space since both raw data sets do not coincide in the spiral scan acquisition.

Fast kV-switching GENERAL ELECTRIC (GE) pursues the principle of single source scanner that alternates the X-ray tube potential rapidly between low and high kV during tube rotation (Zhang et al. [2011]). Tube potentials are changed in less than 0.5 ms (Goodsitt et al. [2011]) to minimize the rise and fall time. Similarly at the detector side, high temporal resolution and short afterglow times are mandatory. The full FOV is covered by both photon spectra. Additional scan time is given to the low tube potential to assure similar photon statistics. Spectral separation, however, is not as good as in dual source CT systems since independent filtration for both spectra is impossible. The main advantage of simultaneous acquisition is the spatial overlap of both acquired raw data sets: view-by-view photon beams of both spectra pass the same geometrical paths through the patient. In theory, beam hardening effects can be removed completely (Goodsitt et al. [2011]).

Energy discriminant detectors and dual layer detectors Standard CT detectors convert photon quanta into an electrical signal independent of the photon energy (except for the detector energy response). In contrast to these energy integrating detectors, photon counting detectors that resolve photon energies would be extremely beneficial for the extended tissue characterization and dose saving (Johnson et al. [2011]). In principle, even the information on characteristic k-edge determination specific for the electronic binding energies could be resolved (and much lower concentrations of contrast agent would be necessary). However, energy resolving demands an extremely high time resolution with fast decay and short afterglow times. Tube currents and tube rotations have to be lowered and longer scan times are expected. Currently, energy resolving detectors are research subjects facing high demands on the detector and electronic side, while the energy discrimination by one or more thresholds seems to be more feasible. The technical principle offers an excellent exploration of the polychromatic photon spectrum.

Layered detectors in which the first layer absorbs low energy photons and high energy photons are detected by the detector beneath are investigated by Philips (Johnson et al. [2011]). The method is tested in a prototype scanner.

2.2.1 Exploiting the spectral information

Dual energy CT scanning exploits the fact that photoelectric absorption is highly energy dependent (Fig. 2.1). Measuring $\mu(E_i)$ at two different effective photon energies E_i allows to extend the characterization of the object scanned. In contrast to SECT, where a single CT number is influenced by the electron density ρ_e and atomic number Z in combination, the DECT allows to separate both quantities.

Post-processing is possible either in the projection space or in the image space. Projection space based post-processing algorithms are intrinsically superior as they are free of beam hardening and other image artifacts but require the geometrical overlap of both projections (which applies for example for the GE rapid kV switching technique Johnson et al. [2011]). Image space post-processing algorithms achieve good results when precise beam hardening corrections are applied ahead.

In order to exploit the dual energy information and extract the information on the electron density relative to water $\hat{\rho}_\mathrm{e}$ and effective atomic number Z_eff, the first set of base functions separates the photon attenuation into a Compton and a photoelectric contribution (Sec. 2.1.1, Alvarez and Macovski [1976]):

$$\mu(E_i) = a_1 \cdot \rho_\mathrm{e} \cdot \sigma_\mathrm{e}^\mathrm{KN}(E_i) + a_2 \cdot \rho_\mathrm{e} \frac{Z^n}{E_i^3} \quad \text{with } n \approx 3. \tag{2.16}$$

a_1 and a_2 are constants and it is assumed that the energy dependence of the cross sections is the same for all elements (Brooks [1977]). Coherent scattering and corrections accounting for binding effects are supposed to be incorporated in the photoelectric term (Brooks [1977], Sec. 2.1.1).

Other DECT algorithms rely on the knowledge of the spectral photon distribution as presented for example in Bazalova et al. [2008] where the monoenergetic approach with synchrotron radiation from Torikoshi et al. [2003] was adapted. In this work, an image spaced $\hat{\rho}_e/Z_{\mathrm{eff}}$ algorithm that requires a single DECT measurement of a calibration material is presented in detail in Sec. 3.5.

The second set of base functions is the virtual decomposition of the object into two base materials with photon mass attenuation coefficients μ_1/ρ_1 and μ_2/ρ_2 with w_1 and w_2 denoting the concentrations of the two base materials that have to be determined (Goodsitt et al. [2011]):

$$\mu(E_i) = w_1 \frac{\mu_1(E_i)}{\rho_1} + w_2 \frac{\mu_2(E_i)}{\rho_2}. \tag{2.17}$$

Due to the physical attenuation processes described above, most algorithm decompose the DECT information into a low Z material responsible for the Compton attenuation (i.e. water) and a material that exhibits an elevated Photoelectric absorption such as iodine or liquid bone surrogates.

The wider the photon spectra are separated, the more meaningful is the additional information one can gain from DECT imaging (Zatz [1976], Rutherford et al. [1976a]). The DECT information is particularly sensitive to high Z elements in the tissues. This is exemplary reflected by the so called "dual energy index" (DEI) that is defined by the difference of both CT numbers divided by the sum of both CT numbers (Johnson et al. [2011]).

Based on the two possibilities to separate the DECT information, various different applications mainly related to diagnostic and therapy decisions are exploited in clinical routine and for research projects. Prominent examples are the quantification of iodine and calcium content, the chemical differentiation of kidney stones (uric acid versus calcified stones), the differentiation of inactive brain hemorrhage to fresh bleeding and the diagnosis of gout (Johnson et al. [2011], Seidensticker and Hofmann [2008]).

Three applications are particularly interesting for (ion) radiotherapy: metal artifact reduction, virtual non-enhanced images and the additional tissue information on $\hat{\rho}_e$ and Z_{eff}. Exploiting the $\hat{\rho}_e$ and Z_{eff} for ion therapy was already proposed by Chen et al. [1979] directly after Rutherford et al. [1976b] described the principle idea of DECT. However, Chen et al. [1979] formulated doubts concerning technical limitations of image misregistration (at that time) and the mandatory knowledge on the photon spectra. The invention of dual source CT scanners overcome these technical limitations and this thesis investigated how the information on $\hat{\rho}_e$ and Z_{eff} can be used for the ion range prediction. The image based calculation is described in detail in Sec. 3.5. Virtual non-enhanced images allow to scan the patient once with DECT and calculate a contrast-enhanced and non-enhanced image based on the principle of material decomposition into water and iodine and was assessed for standard photon therapy in Yamada et al. [2014]. This post processing method is of interest for ion therapy as contrast agent perfused tissues facilitate target delineation but impede ion range prediction (Wertz and Jäkel [2004]). Investigating this DECT method for treatment planning in ion therapy was, however, not the scope of this thesis. The principle of the metal artifact reduction is based on the reconstruction of a pseudo or virtual monoenergetic image via the material decomposition $\mu_i(E)$. The technique and its usefulness for ion radiotherapy planning is further discussed in Sec. 6.5.

2.3 Electronic energy loss of ions in matter

The energy loss of charged particles at therapeutic kinetic energies (app. 50 MeV/u-430 MeV/u) penetrating matter is overwhelmingly dominated by inelastic collision with target electrons. Locally dense ionization of the medium along the ion beam increases gradually towards the "Bragg peak" where the majority of primary ions that did not undergo fragmentation come to rest. The mean electronic energy loss along a path dx in a homogeneous medium is formulated in the Bethe theory and can be well approximated by the stopping power S without higher order corrections (Bethe [1930], Bloch [1933], Ziegler [1999]):

$$S = \left\langle \frac{\mathrm{d}E}{\mathrm{d}x} \right\rangle \approx S^{\mathrm{el}}_{\mathrm{coll}}(E) = -k \cdot \frac{z^2}{\beta^2} \cdot \rho_e \left(\ln\left(\frac{2m_{\mathrm{e}}c^2\beta^2}{I(1-\beta^2)} \right) - \beta^2 - \frac{C}{Z} - \frac{\delta}{2} \right) \tag{2.18}$$

with $k = 51\,\mathrm{MeV\,fm}^2$

β = projectile velocity divided by the speed of light

z = atomic number of the projectile

Z = atomic number of the medium

I = mean excitation energy of the medium

ρ_{e} = electron density per volume of the medium

The shell correction C/Z becomes important at projectile velocities comparable or smaller than the orbital electron velocities. Completely stripped ions then start to capture atomic electrons from the medium, reduce the mediums charge and therewith the stopping power (up to 6 % for 1-100 MeV protons, Ziegler et al. [2008]). The density correction term $\delta/2$ accounts for the dielectric polarization of the medium due to the ions' electromagnetic field (ICRU [1993]). The target polarization reduces the stopping power particularly for large projectile energies that are usually not employed for particle therapy (i.e. the density correction is 1 % for 500 MeV protons, ICRU [1993]).

The energy loss is independent of the projectile mass but depends on its charge and velocity. On the targets side, ρ_e and - to a smaller extend - the I-value of the medium influence the energy loss. Both target quantities are further characterized in the following sections.

2.3.1 Electron density

The electron density per unit volume of a compound composed of elements i is defined by (McCullough [1975])

$$\rho_\mathrm{e} = \rho N_\mathrm{A} \sum_i w_i \frac{Z_i}{A_i} \tag{2.19}$$

with N_A = Avogadro's number
ρ = mass density of the compound
Z_i = atomic number of element i
A_i = mass number of element i
w_i = mass weight of element i.

Z/A decreases slightly with higher atomic masses as the number of neutrons increases. With the exception of hydrogen, Z/A ratios can be regarded as relatively constant (0.47-0.50) for the main elements present in the human body (Tab. A.8). The electron density per unit mass is defined very similarly to Eq. 2.19 by $\rho_\mathrm{e}^\mathrm{mass} = N_\mathrm{A} \sum_i w_i \cdot Z_i/A_i$.

2.3.2 I-value

The mean excitation energy I defines the mean energy $< E_i - E_0 >$ that is required to excite an atomic electron from its initial ground state E_0 to any excited state E_i (Sakurai and Tuan [1993]). "The determination of the mean excitation energy is the principal non-trivial task in the evaluation of the Bethe stopping-power formula" (Seltzer and Berger [1982]) due to the complexity of the electronic configuration in atoms of more than one electron or even molecules.

Atomic electrons being bound to the nuclei are assumed to oscillate with a characteristic resonance frequency (descriptively illustrated in Bohr's classical model, Sigmund [2004], Fano [1964]). The electronic excitation spectrum of an atom or molecule is characterized by the spectrum of absorption energy levels with corresponding quantum mechanic resonance oscillator frequencies (hence energies) and weight factors named oscillator strengths (ICRU [2005]) that represent the probabilities for each possible excitation state (Sigmund [2006]). In contrast to the classical assumption that an ion releases continuously part of its energy to the surrounding electrons, quantum mechanically the energy release happens discretely. Both different views agree when analyzing the statistical mean (Jackson [2006]).

The mean energy transfer provoking an atomic excitation equals the weighted sum over the oscillator strengths f_i times the logarithm over the correspondent energies $E_i - E_0$ (Fano [1964], Sigmund [2004]):

$$\ln I = \sum_i f_i \ln(E_i - E_0) \qquad \text{with} \sum_i f_i = 1. \tag{2.20}$$

Eq. 2.20 includes energy transfers towards the continuum (hence ionization, Jackson [2006]), and the mean excitation energy equals approximately the mean ionization potential (Hsu [1979]). Both names are widely used interchangeable in ion therapy. The logarithmic dependency results from the integration of the energy transfer over the free-Coulomb scattering cross section (Sigmund [2006]).

Since electronic oscillator strengths are difficult to access, one relies on $semi-empirical$ approximations and direct measurements of the I-value (Sakurai and Tuan [1993]). Bloch's correlation of the I-value to the atomic number Z ($I = k \cdot Z$ with $k \simeq 10$, Bloch [1933]) is a good approximation for atoms of high Z. In the low Z region ($Z \leq 20$, Fig. 2.2) the correlation with Z is not as distinctive as for heavy atoms. Bloch's correlation was therefore modified by various authors for different intervals of Z. A comprehensive summary can be found in Hsu [1979]. He formulated a semi-empirical model that describes the I-value as follows "For adjacent elements in the same period only the lowest ionization potentials are different [...] due to the fact that they have the same core-electrons".

For compounds, I-values follow in a good approximation the empirical Bragg additivity rule that was originally formulated for the stopping power and can directly be translated for the I-value (Bragg and Kleeman [1905], ICRU [1984], ICRU [1993]):

$$\ln I = \frac{\sum_i w_i (Z_i/A_i) \ln I_i}{\sum_i (w_i Z_i/A_i)}. \tag{2.21}$$

In compounds, electronic binding energies are assumed to be elevated compared to free atoms and Seltzer and Berger [1982] adjusted elemental I-values for hydrogen, carbon, nitrogen, oxygen and chlorine according to molecular binding effects and phase from measured data. For all other atoms, elevating elemental I-values I_i by 13 % (Eq. 2.21) was found to match well with experimentally measured I-values of compounds (Seltzer and Berger [1982], ICRU [1993]). According to ICRU [1993], Bragg's additivity rule can induce stopping power errors up to 15 %.

Experimentally, I-values are accessible (with corresponding uncertainties) either in measurements of stopping power, relative stopping power, ion ranges as well as optical and photoelectric cross section measurements with X-rays (ICRU [1984], Mozumder [2002], ICRU [2005], Paul et al. [2009]). When measuring stopping power with the purpose to determine the I-value, density and shell corrections have to be accurately estimated prior to the measurement or one has to choose an initial particle energy of 300-700 MeV/u at which

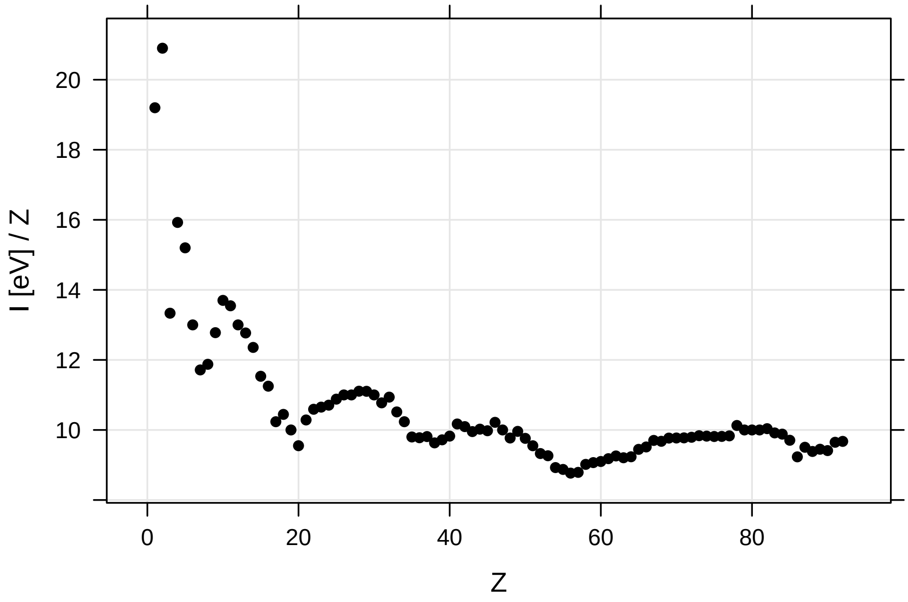

Figure 2.2: Mean excitation value I divided by the atomic number Z as a function of Z. Data taken from ICRU [1993]. Blochs relation of $I \approx 10\,\text{eV} \cdot Z$ applies particularly for high Z elements.

both correction terms are of minor importance (Fano [1964]). Absolute measurements of stopping power at standard conditions are rare but of high value. In contrast, stopping power measurements relative to a reference material (i.e. water) require the accurate knowledge on the I-value of the reference material that usually associated with high degree of uncertainty.

In literature, the I-value of water is discussed and published values range from 67.2 eV (ICRU [2005], Paul et al. [2007]), (75±3) eV (ICRU [1993], Sigmund et al. [2009]) to (80±2) eV (Bichsel and Hiraoka [1992]). Henkner [2009] found considerable range differences of 1.9 mm due to different I-values for water when simulating carbon ions of 270 MeV/u in water. Similar results were published in Andreo [2009].

2.3.3 Range

The mean path length of charged particles with initial energy E_0 in matter is defined in the continuous slowing down approximation by the integral of the inverse stopping power (Eq. 2.18, ICRU [2005]):

$$R = -\int_{E_0}^{0} \frac{\mathrm{d}E}{\mathrm{d}E/\mathrm{d}x}. \tag{2.22}$$

Although the mean rest kinetic energy is zero for the range definition, in reality energy loss varies stochastically which subsequently causes range straggling. The projected range distribution of charged particle beams penetrating inhomogeneous media is additionally broadened due to multiple Coulomb scattering on the target nuclei (Sawakuchi et al. [2008], Schneider et al. [1998], Urie et al. [1986], Schaffner et al. [1999]). For robust measurements of ion ranges, the position of the 80-90 % of the maximum energy loss at the distal edge of the Bragg peak is determined.

2.3.4 SPR or WEPL for treatment planning in particle therapy

The mean particle range in a medium "m" relative to the range in water "w" can be approximated by the ratio of stopping powers SPR[1] (without shell and density correction):

$$\mathrm{SPR}_{\mathrm{w}}^{\mathrm{m}} = \frac{\rho_{\mathrm{e,m}}}{\rho_{\mathrm{e,w}}} \cdot \frac{\ln(2m_{\mathrm{e}}c^2\beta^2) - \ln(1-\beta^2) - \beta^2 - \ln(I_{\mathrm{m}})}{\ln(2m_{\mathrm{e}}c^2\beta^2) - \ln(1-\beta^2) - \beta^2 - \ln(I_{\mathrm{w}})} = \hat{\rho}_{\mathrm{e}} \cdot f(I_{\mathrm{m}}, I_{\mathrm{w}}, \beta). \quad (2.23)$$

The SPR is linear in the electron density of the medium relative to water $\hat{\rho}_{\mathrm{e}}$:

$$\hat{\rho}_{\mathrm{e}} = \frac{\rho_{\mathrm{e,m}}}{\rho_{\mathrm{e,w}}} = \frac{\rho_{\mathrm{m}} \cdot \sum_i w_i \frac{Z_i}{A_i}}{1\,\mathrm{g/cm^3} \cdot (11.11 \cdot \frac{Z_{\mathrm{H}}}{A_{\mathrm{H}}} + 88.89 \cdot \frac{Z_{\mathrm{O}}}{A_{\mathrm{O}}})}. \quad (2.24)$$

$\hat{\rho}_{\mathrm{e}}$ of compounds which have the same mass density differ particularly when the hydrogen mass fraction is different. Factor f in Eq. 2.23 is greater than one for materials exhibiting a lower I-value than water ($I_{\mathrm{m}} < I_{\mathrm{w}}$). SPR variation with β is assumed to be negligible for particle energies above 10 MeV/u (Paganetti [2009]). Eq. 2.23 is often equated with the WEPL that can be measured with a water range telescope ("peakfinder") for homogeneous materials of known thickness described in Jäkel [2001]. In this thesis, WEPL and SPR are used interchangeable.

SPR is an important quantity for the analytical dose planning algorithm in particle therapy as it is based "on the assumption of water targets" (Krämer et al. [2000]). Pencil beam base data stored in the TPS is measured and interpolated in water. Consequently, CT images of the patient anatomy have to be translated by a Hounsfield look-up table (HLUT) to their water-equivalent stopping power images (Chen et al. [1979], Krämer et al. [2000], Jäkel [2001]). Ion energy assignments are subsequently determined with the SPR maps showing the projected proximity of the tumor target in its water equivalent depth. Therefore, the sum over all WEPL values times the pixel length (in beam direction) defines

---

[1] This definition should not be confused with "ratio of average stopping powers", a concept employed in dosimetry that integrates over all energies and the complete spectrum of primary and secondary particles, IAEA [2000].

the water-equivalent thickness (WET). Fig. 2.3 shows on the left hand side the CT number image and on the right hand side the corresponding WET (determined with the HLUT).

The HLUTs denote a key feature in the TPS that has to be implemented during commissioning and that needs to be adjusted when CT scanners or protocols are changed. Usually, protocol specific look-up tables are provided for head and body region separately. Different approaches to set up a HLUT have been presented in the literature (Chen et al. [1979], Schneider et al. [1996], Schneider et al. [2000], Kanematsu et al. [2003]). For this thesis, the stoichiometric calibration (Schneider et al. [2000]) was investigated in detail and compared to DECT based SPR prediction. The stoichiometric calibration method is described in more detail in Sec. 3.4.2.

Since SPR is independent of particle type, only one HLUT is necessary for proton and carbon ions. For light ions, e.g. protons, increased lateral scattering with the tissue mass density is taken into account by providing a further look-up table (Szymanowski and Oelfke [2003]) for different scattering behaviors.

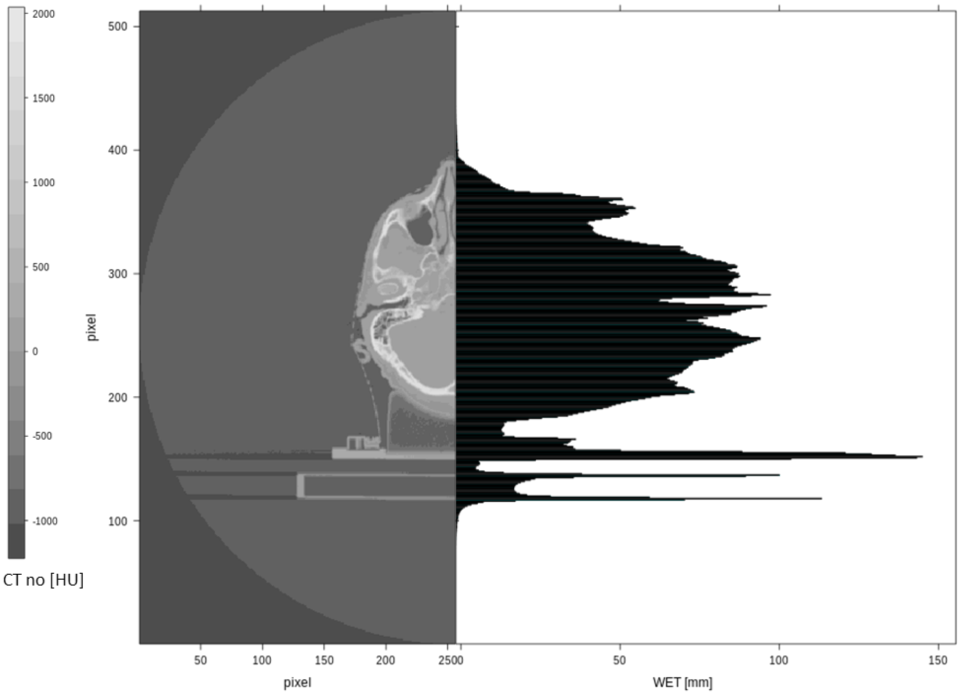

Figure 2.3: The left side shows the CT number map of a patients head (100 kV). The right side shows the corresponding WET image (translated with a HLUT) that an ion beam coming horizontally from the right would see.

3 Materials and Methods

3.1 Dual source dual energy CT scanner

The SIEMENS "Somatom Definition Flash" is the second generation of dual source CT scanners. Compared to the first generation ("Somatom Definition"), the Definition Flash scanner has a wider FOV of 33 cm covered by both X-ray tube-detector systems which are positioned on the gantry with a 95 ° offset to each other. The scanner provides X-ray tube potentials of 80 to 140 kV in steps of 20 kV. An optional 0.4 mm tin (Sn) filter at the high kV X-ray tube attenuates low energy photons ("additional photon shield") and narrows the spectrum. The reduction of the spectral overlap due to the additional tin filter is well observable in the large difference of the corresponding mean photon energies (approximately 40 keV, Johnson et al. [2011], Primak et al. [2010]).

Typical voltage pairs for DECT acquisitions are 100/140Sn kV and 80/140Sn kV. For this thesis, the scanner was also used in the single source mode for standard 120 kV image acquisitions (SECT). As for the DECT scanning protocols, DECT specific kernels (D30, D43) were exploited with a standard filtered back projection. The dual energy kernels reduce scattering noise which is mutually detected on the detector side while the D34 kernel provides an edge enhancement in combination with an advanced beam hardening correction. Images presented in Sec. 4.1.1 were additionally reconstructed with a H30 kernel for the DECT and SECT acquisitions. All images for this thesis had a slice thickness of 2 mm which is the standard thickness for radiotherapy planning. At the Heidelberg Ion-Beam Therapy Center (HIT) patients are scanned with 3 mm to facilitate contouring for the medical doctors.

Tube current ratios are usually adjusted by the scanner software in order to obtain the same image noise at both detectors (Sec. 2.1.2). This implies higher tube currents (Sec. 2.1.2) on the low energy X-ray tube. Tube current ratios of 1.3:1 and 2.5:1 for 100/140Sn kV and 80/140 kV tube potential combinations are typical for the scanner used.

Two protocols implemented in the DKFZ scanner database were used. The "Liver VNC" protocol was used for the DECT specific measurements (recommended by Dr. Bernhard Krauss, Siemens, personal communication). The second protocol is a dedicated protocol set up by the medical physicist staff of the department named "BPL KopfHalsDE" for the patient head and neck case (Sec. 4.3). Here, tube currents were not adjusted but kept fixed. Protocol details are summarized in Tab. A.1.

3.2 Investigated materials

Calibration procedures and quality assurance tests in radiotherapy require materials that mimic real tissue in terms of well-defined radiological properties, inhomogeneities, anthropomorphic shapes and other specific aspects. For this thesis, three different types of tissue substitutes have been investigated in order to characterize DECT imaging for ion therapy planning: Gammex tissue surrogates, polymers and two metal probes. All materials represent homogeneous materials in order to be able to evaluate CT contrasts in a predefined volume of interest (VOI). Materials were available in a cylindrical form with a radius of r = 1.4 cm (tissue surrogates, polymers, printing II and III), r = 0.75 cm for both metal probes and r=1 cm for the printing I material. Physical characteristics important for this thesis are summarized in Tab. 3.1 for the employed materials. Additionally, reference tissue compositions are published for specific calculation and simulation purposes (Schneider et al. [2000]). These tabulated tissue compositions are described in detail in the last paragraph of this section.

Table 3.1: Reference physical characteristics of employed phantom materials. For the Gammex tissue surrogates the $\hat{\rho}_e$, ρ and elemental mass weights (not batch specific) were provided by the manufacturer. For all other materials, ρ was measured and elemental mass weights were estimated. $\hat{\rho}_e$ (Eq. 2.19), I-value (Eq. 2.21) and Z_{eff} (exponent n =3.1, Eq. 3.18) were calculated from estimated compositions. WEPL of 1 cm slices of all materials were measured with carbon ions and the measurement method presented in Jäkel [2001]. WEPL of Gammex tissue surrogates were measured by Benjamin Ackermann (HIT). For the printing materials, metals and polymers the WEPL was measured with carbon ions of 200 MeV/u or 271 MeV/u at a mean intensity and a small beam focus (Tremmel [2012], Hünemohr et al. [2013], Hünemohr et al. [2014a]). Table partly reprinted from Hünemohr et al. [2014a].

Material	ρ	$\hat{\rho}_e$	WEPL	I [eV]	Z_{eff}	H	C	N	O	F	Mg	Al	Si	P	Cl	Ca	Ti
Lung	0.460	0.444	0.444	73.8	7.5	8.47	59.57	1.97	18.11	0	11.21	0	0.58	0	0.10	0	0
Adipose	0.942	0.925	0.943	66.6	6.2	9.06	72.30	2.25	16.27	0	0	0	0	0	0.10	0	0
Breast	0.988	0.965	0.983	68.2	6.8	8.59	70.11	2.33	17.90	0	0	0	0	0	0.10	0.95	0
True Water	1.000	1.000	1.000	75.0	7.4	11.19	0.00	0.00	88.81	0	0	0	0	0	0	0	0
Solid Water	1.018	0.989	1.001	70.4	7.5	8.00	67.30	2.39	19.87	0	0	0	0	0	0.10	2.31	0
Muscle	1.049	1.019	1.033	70.2	7.5	8.10	67.17	2.42	19.85	0	0	0	0	0	0.10	2.32	0
Brain	1.052	1.048	1.064	63.5	6.1	10.83	72.54	1.69	14.86	0	0	0	0	0	0.10	0	0
Liver	1.089	1.058	1.073	70.3	7.5	8.06	67.01	2.47	20.01	0	0	0	0	0	0.10	2.31	0
Inner Bone	1.147	1.099	1.099	80.1	10.1	6.67	55.64	1.96	23.52	0	0	0	0	3.23	0.10	8.86	0
B200	1.153	1.105	1.108	80.2	10.1	6.65	55.52	1.98	23.64	0	0	0	0	3.24	0.10	8.87	0
CB30	1.333	1.278	1.263	80.8	10.6	6.68	53.48	2.12	25.61	0	0	0	0	0	0.10	12.01	0
CB50	1.560	1.470	1.426	93.2	12.3	4.77	41.63	1.52	32.00	0	0	0	0	0	0.10	20.02	0
Cortical Bone	1.823	1.695	1.612	104.5	13.4	3.41	31.41	1.84	36.50	0	0	0	0	0	0	26.81	0
Tecapeek	1.305	1.230	1.241	74.7	6.3	4.76	76.19	0	19.05	0	0	0	0	0	0	0	0
Tecaform	1.410	1.353	1.354	77.5	7.0	6.67	40.00	0	53.33	0	0	0	0	0	0	0	0
Tecadur	1.463	1.364	1.315	81.1	6.8	3.61	57.83	0	38.55	0	0	0	0	0	0	0	0
PMMA	1.183	1.149	1.165	74.0	6.5	8.05	59.98	0	31.96	0	0	0	0	0	0	0	0
Teflon	2.151	1.860	1.782	99.1	8.4	0	24.02	0	0	75.98	0	0	0	0	0	0	0
PrintingI	1.198	NA	1.182	NA	NA	NA	NA	NA	NA	NA	NA	NA	NA	NA	NA	NA	NA
PrintingII	1.171	NA	1.160	NA	NA	NA	NA	NA	NA	NA	NA	NA	NA	NA	NA	NA	NA
PrintingIII	1.200	NA	1.179	NA	NA	NA	NA	NA	NA	NA	NA	NA	NA	NA	NA	NA	NA
Aluminum	2.699	2.343	2.140	166.0	13.0	0	0	0	0	0	0	100.00	0	0	0	0	0
Titanium	4.540	3.759	3.254	233.0	22.0	0	0	0	0	0	0	0	0	0	0	0	100.00

3.2.1 Tissue surrogates

A commercially available set of tissue surrogates for electron density calibration in conventional radiotherapy is manufactured by Gammex ("electron density CT phantom 467", Gammex [2011]). The set comprehends 13 cylinders of epoxy-based compounds. Materials are assigned to lung, adipose, muscle, breast, brain, liver and five different types of bone (soft to hard bone) as well as solid water.

The data sheet provides $\hat{\rho}_{\mathrm{e}}$ and ρ measured by the manufacturer. In addition, the manufacturer provides the approximate material composition (non batch specific, Tab. 3.1). The elemental mass fractions correlate to approximated mean values of the natural equivalences with the exception that the carbon and oxygen contents are interchanged (compare tissues listed in Schneider et al. [2000]).

3.2.2 Polymers and metals

Besides the tissue surrogates, PMMA, four different polymers (Tecapeek, Tecadur, Tecaform, Teflon) and two metals (aluminum, titanium) were investigated as a phantom material. PMMA, or "lucite", is a transparent polymer with $\rho \approx 1.19\,\mathrm{g/cm^3}$, available in slices of different thicknesses and volumetric bodies like cylinders and cubes. In radiotherapy, it is used to form solid bodies that simulate similar interactions with therapeutic beams and provoke similar X-ray beam hardening as patient tissue. The other four polymers were arbitrary polymers available in the DKFZ workshop and cover different elemental compositions. Tecapeek is a chemically stable material known to be used for stabilization cages of the spine. In clinical routine, high Z materials are added to enable visibility in X-ray projections for positioning checks of the tecapeek implants.

Aluminum is a low Z metal that barely allows the measurement of photon attenuation and the assessment of the DECT information. Titanium is typically used for implants that need to be very stable (e.g. hip prostheses and dental implants) but can cause severe metal artifacts due to photon starvation.

Additionally, three printing materials from a 3D printing machine were investigated. For radiotherapy needs, 3D printers can produce supportive devices of any shape like holders, screws and containers but also anthropomorphic phantoms like head shaped matrices (Gallas et al. [2014]) for multimodality end-to-end tests of the entire treatment course. Therefore, radiological properties and interaction properties with ions are important to know in order to estimate the tissue equivalence of the printing materials. For this thesis, three available printing materials showing different structure stability were investigated. The first ("printing I") was used for a multimodality phantom presented in Gallas et al. [2014], the other two materials ("printing II", "printing III") were exploited for a 3D printing machine recently installed in the medical physics department at DKFZ. Here, DECT-based characterization is appreciated for further possible decisions on which materials should be used for the manufacturing of radiological phantoms and organ shaped recipients.

3.2.3 Tabulated tissue compositions

Simulating radiation transport in tissues and calibration procedures in radiotherapy ask for specified elemental compositions and mass densities of human tissues. Body composition depends on various factors like age, sex, health status, nutrition and ethnic group. For this work, the same tissues as presented in Schneider et al. [2000] have been investigated. The tabulated tissues summarize compositions taken from Woodard and White [1986] and White et al. [1987]. These authors in turn had reassessed body compositions presented in ICRP [1975] as well as further published and unpublished data.

The earlier ICRP [1975] report intends to provide data of a defined "Reference Man". The comprehensive report of metric measurements of the body properties like mass, weight, length, volumes and body composition records data from several hundred publications. Where possible, variation ranges, mean and median values are documented. A good example can be found for "wet skeletal muscle" on page 110 of the report: for an adult person, the water content ranges for example from 68.9-80.3 % with a mean value of 79 %, the protein content is reported to be 12.9-20 % with a mean value of 17.2 %. Some of the data was available only for parts of the studied properties and Woodard and White [1986] reported inconsistencies also due to rounding processes, summations of different data sets and different experimental methods (such as using dried or wet tissue). The table in Schneider et al. [2000] documents these large variations by providing the mean composition for some tissues in addition to the composition of plus minus one standard deviation (e.g. "adipose 1", "adipose 2", "adipose 3").

Noteworthy, tissue compositions presented in ICRP [1975] were measured mainly in the middle of last century as for example presented by Forbes et al. [1953], Widdowson and Dickerson [1960] (comparison of body composition between a pig and a man), Sheldon and Ramage [1931] (measurement of trace elements) and Forbes et al. [1956]. These measurements are described as non-trivial tasks. Tissue groups and organs of dead bodies had to be carefully separated during dissection and dehydration of the specimens had to be avoided. As for the chemical analysis water, ether extract, crude proteins and ash are usually quantified as described in Forbes et al. [1953]. For water, the tissue probes are dried and the amount of moisture is measured. Elements of the dried probe are soluted in ether followed by a subsequent catalysis of nitrogen. The amount of protein determines the nitrogen content by a simple conversion factor. Calcium and phosphorus can be determined via the processing of ash with a muffle and a subsequent titration or calorimetry.

The 71 tissues presented in Schneider et al. [2000] are summarized in Tab. A.7 along with calculated tissue characteristic ($\hat{\rho}_\mathrm{e}$, Z_eff, SPR, I-value) important for this thesis. For this thesis, tabulated tissue compositions were mandatory to establish an $\ln I$-to-Z_eff relation for the DECT-based SPR calculation (Sec. 3.6.1) and for MC-based range simulations in tissues (Sec. 4.4.3).

3.3 Phantoms

Investigated materials (Sec. 3.2) were positioned in two different phantoms providing appropriate slots of $r = 1.4\,\mathrm{cm}$. For metals and the "printing I" material, an additional PMMA adapter was employed providing appropriate buildup material. Both phantoms are made from solid PMMA and have a diameter of 8 cm which approximates a typical photon beam hardening of a head. The first phantom ("PMMA tube") is the standard phantom for a typical head scan. It can be filled with eight Gammex rods that are positioned in a row on the central axis slot. In the second ("pizza") phantom, 9x2 inserts can be placed at different positions with respect to the central axis (two inserts in a row). In the "pizza" phantom CT numbers of all inserts can be evaluated at once in two image slices.

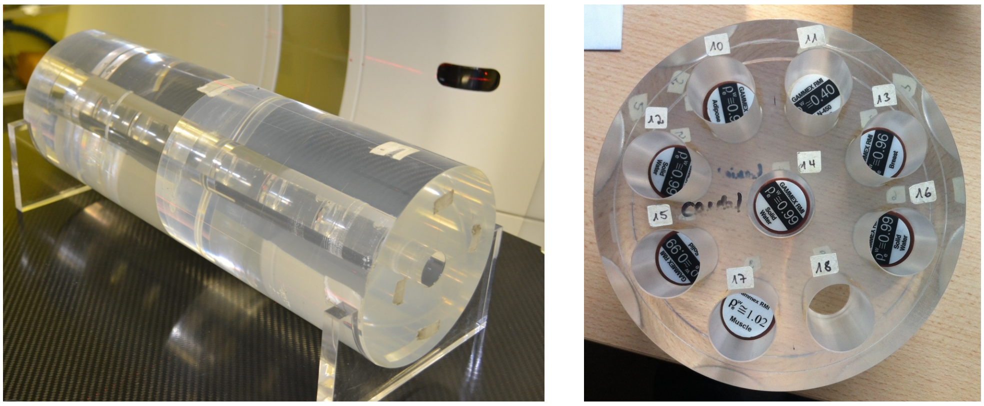
(a) (b)

Figure 3.1: (a) PMMA tube (b) "Pizza" phantom employed for the CT measurements. The PMMA tube ensures uniform beam hardening and avoids cross scattering and influence by the inserts' positions in the x-y plane. In the "pizza" phantom, cross talk of scattering and beam hardening from the surrounding inserts may influence the CT number measurement.

3.4 CT number to SPR conversion and material decomposition

As briefly described in Sec. 2.3.4, CT images of the patient have to be converted into SPR or WEPL maps with a calibration called HLUT for ion therapy. Different conversion methods are described in the literature (Chen et al. [1979], Schneider et al. [1996], Kanematsu et al. [2003]) and the two most relevant methods are described in the following sections.

3.4.1 Empirical calibration

At the beginning of CT-based treatment planning in particle therapy, the calibration was "empirically" generated: CT numbers of materials with known WEPL were measured with a specific CT protocol and then linearly correlated (Chen et al. [1979], Jäkel [2001]). The calibration consists in its most simplified version two linear segments that express the smallest residuals of CT number / SPR pairs for a set of measured materials. The lower line segment covers the CT number interval from -1024 HU to 0 HU with a steeper slope than the second line segment that starts at 0 HU and describes the correlation up to cortical bone. The separation into two different line segments results from the strong dependency of the photoelectric effect on the atomic number (Eq. 2.9), which is increased in bone tissues containing calcium and phosphorus. In addition, a large atomic number reduces the SPR for ions due to the elevated I-value (Sec. 2.3.4) and therewith additionally decreases the slope of the CT number to SPR for bone tissues. The accuracy of the empirical calibration relies heavily on the tissue equivalence of the measured materials since CT numbers are affected by $\hat{\rho}_\mathrm{e}$ and Z_eff (Sec. 2.1) and materials should be chosen carefully.

3.4.2 Stoichiometric calibration

To overcome the dependency on the tissue equivalence of the materials that impedes the empirical calibration, Schneider et al. [1996] and Schneider et al. [2000] presented a novel conversion method called "stoichiometric calibration". The method parametrizes the photon attenuation of a compound μ (composed of n elements with mass weights w_i) relative to water by (Jackson and Hawkes [1981], Schneider et al. [2000]):

$$\frac{\mu}{\mu_\mathrm{w}} = \frac{\rho}{\rho_\mathrm{w}} \frac{\sum_{i=1}^{n}(w_i/A_i)(Z_i + Z_i^{m_1}k_1 + Z_i^{m_2}k_2)}{(w_\mathrm{H}/A_\mathrm{H})(1+k_1+k_2)+(w_\mathrm{O}/A_\mathrm{O})(8+8^{m_1}k_1+8^{m_2}k_2)} \tag{3.1}$$

with $m_1 = 2.86$ and $m_2 = 4.62$. k_1 and k_2 parametrize the coherent scattering and photoelectric effect divided by the Klein-Nishina Compton electronic coefficient (Eq. 2.6, Schneider et al. [2000]):

$$k_1 = \frac{k_\mathrm{coh.sc.}}{\sigma_\mathrm{e}^\mathrm{KN}} \quad k_2 = \frac{k_\mathrm{photo}}{\sigma_\mathrm{e}^\mathrm{KN}}. \tag{3.2}$$

Corrections for the incoherent scattering due to the binding energies (Sec. 2.1.1) are assumed to be integrated in k_1 (Schneider et al. [2000]).

Measuring the CT numbers of arbitrary materials l of known elemental mass weight composition w_i ("stoichiometry") and a subsequent minimization of the CT number difference to the theoretical prediction from Eq. 3.1 (Schneider et al. [2000]) enables to optimize the values of k_1 and k_2:

$$\sum_{j=1}^{l}\left(\left(\frac{\mu}{\mu_{\mathrm{w}}}(k_1,k_2)\right)_l-\left(\frac{\mathrm{CT\ no}}{1000\,\mathrm{HU}}+1\right)_l\right)^2. \tag{3.3}$$

The determined spectra and protocol specific parameters k_1 and k_2 are utilized to predict CT numbers for tabulated tissue compositions (Sec. 3.2.3) according to Eq. 3.1. With the CT number/SPR pairs of these tabulated tissues, piece-wise linear calibration fits can be generated. The stoichiometric HLUT usually consists of several linear line segments. No standard procedure is specified in the literature on how to derive the linear fit segments (i.e. start and end point) in the scatterplot of the tissues.

In this thesis, protocol specific HLUTs were generated from both DECT CT number image stacks separately with measurements of the Gammex tissue surrogates according to the Schneider et al. [2000] method. Fig. 3.2 shows an exemplary HLUT generated for the 100 kV image acquisition.

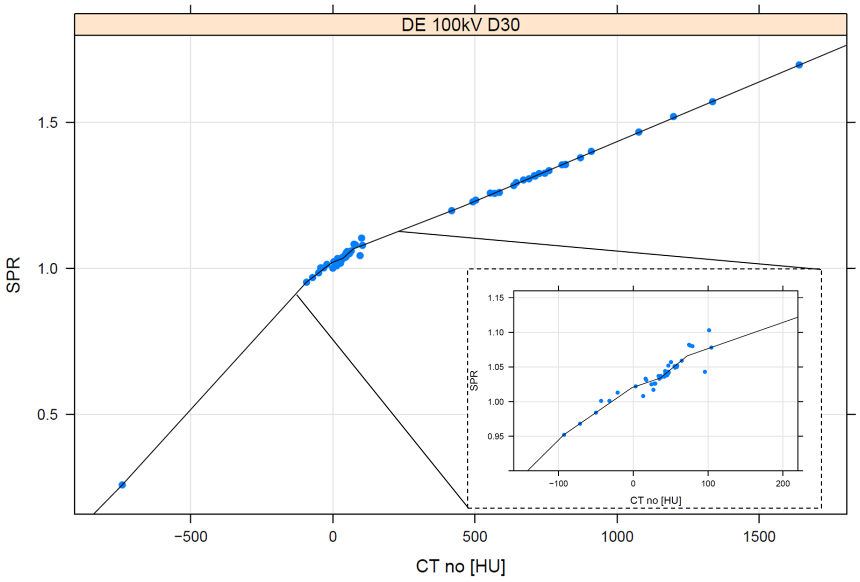

Figure 3.2: HLUT translating CT numbers to SPR or WEPL (100 kV, D30). The lower right corner shows a close-up of the piece-wise line segments in the soft tissue region.

3.4.3 Stoichiometric calibration for Monte Carlo

Complementarily to analytical dose planning algorithms requiring the CT number conversion to SPR, MC-based dose planning requires the assignment of ρ and elemental mass weights in every CT voxel. Both tissue parameters are needed to provide the nuclear cross sections and to precalculate the energy loss distribution to simulate radiation transport within the patient tissue. State of the art method to derive the tissue decomposition from the CT number was presented also in Schneider et al. [2000] and is reproduced in this section.

Predicted CT numbers for tabulated tissue compositions (derived from the stoichiometric calibration) are correlated by five different linear segments to ρ. For the majority of ρ intervals, only the two tissues at the interval edges were interpolated. One discontinuity of 0.04 g/cm^3 at 100 HU is observed and in the air-lung interval (ranging from -1024 HU to -98 HU) ρ was interpolated between air and adipose.

Elemental compositions are provided by a table with 24 CT number bins each with a fix composition. The bin width was chosen by Schneider et al. [2000] according to the expected difference from predicted CT numbers to actual measured CT numbers. This assumption results in a smaller bin widths for soft tissues (10, 15, 60, 40, 80 HU) and larger bin widths for bone tissues (100 HU). Nuclear cross sections can be easily predetermined for the 24 compositions and are then continuously adjusted with the CT number through the linear ρ fits. Assigning tissue composition further influences the I-value and stopping power determination. As for the elemental mass weight fractions w_i for each CT number bin, Schneider et al. [2000] assumed that bony tissues can be decomposed by two base materials, cortical bone (high CT number) and bone marrow (low CT number). The interpolation weights for bone tissues were derived from interpolation of both CT numbers that match the predicted CT numbers of the individual tissues. The composition for each bone CT number bin was derived by taking the mean of the interpolation function of this interval.

Soft tissue was assumed to be composed of three base materials (water, fat, protein, Sec. 3.2.3). The composition of soft tissue showed only a weak dependency on the CT number. Schneider et al. [2000] decided to interpolate elemental weights of four tissues (adipose/adrenal gland and small intestine wall/connective tissue) for two soft tissue regions ranging from -98 HU to 100 HU. The composition of each CT number sub-bins was derived by taking the mean composition of the bin interval.

It has to be stressed that this method is scanner specific due to the interpolation of protocol specific CT numbers to tabulated elemental mass weights. However, the majority of articles on MC-based dose planning or treatment verification utilize exactly the same tissue composition table and ρ fits presented in Schneider et al. [2000]. Significant CT number differences due to different employed scanners and protocols might hamper the correct assignment of tissue properties. To overcome this problem at least with regard to correct range prediction, the MC-based calculated SPR is adjusted in some publications according to the predicted SPR from the analytical TPS for each CT number by a multiplication factor for ρ (Parodi et al. [2007]).

3.5 Calculation of $\hat{\rho}_e$ and Z_{eff} from DECT images

DECT allows the image-based calculation of the electron density relative to water ($\hat{\rho}_e$) and the effective atomic number (Z_{eff}) in every CT voxel. Calculation of both parameters was provided in the framework of a scientific collaboration with Siemens by Dr. Bernhard Krauss. The MATLAB implemented algorithm is described in Hünemohr et al. [2014a] and reproduced in the following paragraphs.

According to Sec. 2.1.1 the linear photon attenuation μ of a tissue can be separated in good approximation into a photoelectric and Compton effect portion (Alvarez and Macovski [1976])

$$\mu(E) \approx a_1 \rho_e f(E) + a_2 \rho_e \frac{Z^n}{E^3} \qquad \text{with } n \approx 3. \tag{3.4}$$

a_1 and a_2 characterize the relative strength of both physical interaction effects that are assumed to be independent of Z (Alvarez and Macovski [1976]) and can be obtained from measurements or theoretical calculations (Hünemohr et al. [2014a]). $f(E)$ is directly related to the Klein-Nishina coefficient of the Compton scattering (Eq. 2.6). In contrast to the stoichiometric parametrization, not the relative strengths for the scattering and photoelectric absorption k_1 and k_2 have to be determined (Sec. 3.4.2), but the energy dependency of both effects is exploited to determine $\hat{\rho}_e$ and Z_{eff} by measuring the weighted average $\langle \mu(E) \rangle$ at two distinct photon spectra:

$$\langle \mu(E) \rangle_1 \approx a_1 \rho_e \langle f(E) \rangle_1 + a_2 \rho_e Z^n \left\langle \frac{1}{E^3} \right\rangle_1 \tag{3.5a}$$

$$\langle \mu(E) \rangle_2 \approx a_1 \rho_e \langle f(E) \rangle_2 + a_2 \rho_e Z^n \left\langle \frac{1}{E^3} \right\rangle_2 \tag{3.5b}$$

with

$$\langle \mu(E) \rangle = \frac{\int \mu(E) S(E) \mathrm{d}E}{\int S(E) \mathrm{d}E}. \tag{3.6}$$

$\langle \mu(E) \rangle$ is energy averaged due to the energy integrated X-ray detection of the photon spectra S(E).

Rearranging Eq. 3.5(b) and inserting $\rho_e Z^n$ in Eq. 3.5(a) leads to (Hünemohr et al. [2014a])

$$a_1 \rho_e = \frac{\langle \mu(E) \rangle_1 \cdot \langle \frac{1}{E^3} \rangle_2 - \langle \mu(E) \rangle_2 \cdot \langle \frac{1}{E^3} \rangle_1}{\langle f(E) \rangle_1 \cdot \langle \frac{1}{E^3} \rangle_2 - \langle f(E) \rangle_2 \cdot \langle \frac{1}{E^3} \rangle_1} = b_1 \langle \mu(E) \rangle_1 + b_2 \langle \mu(E) \rangle_2, \tag{3.7}$$

where the two constants b_1 and b_2 depend on the energy spectrum, but not on the materials' composition.

Applying the CT number definition (Eq. 2.2) on Eq. 3.7 results in

$$a_1\rho_\mathrm{e} = b_1\langle\mu_\mathrm{w}(E)\rangle_1 \cdot \left(\frac{x_1}{1000}+1\right) + b_2\langle\mu_\mathrm{w}(E)\rangle_2 \cdot \left(\frac{x_2}{1000}+1\right). \tag{3.8}$$

Dividing by $a_1\rho_\mathrm{e,w}$ leads to (Hünemohr et al. [2014a])

$$\frac{\rho_\mathrm{e}}{\rho_\mathrm{e,w}} = \frac{b_1\langle\mu_\mathrm{w}(E)\rangle_1}{a_1\rho_\mathrm{e,w}} \cdot \left(\frac{x_1}{1000}+1\right) + \frac{b_2\langle\mu_\mathrm{w}(E)\rangle_2}{a_1\rho_\mathrm{e,w}} \cdot \left(\frac{x_2}{1000}+1\right). \tag{3.9}$$

By introducing a new constant c_e

$$c_\mathrm{e} = \frac{b_1\langle\mu_\mathrm{w}(E)\rangle_1}{a_1\rho_\mathrm{e,w}}. \tag{3.10}$$

and exploiting that the CT number of water is per definition zero (Eq. 2.2), the electron density relative to water $\hat{\rho}_\mathrm{e}$ can be formulated as followed (Hünemohr et al. [2014a])

$$\hat{\rho}_\mathrm{e} = \frac{\rho_\mathrm{e}}{\rho_\mathrm{e,w}} = c_\mathrm{e} \cdot \left(\frac{x_1}{1000}+1\right) + (1-c_\mathrm{e}) \cdot \left(\frac{x_2}{1000}+1\right). \tag{3.11}$$

x_1 and x_2 denote the two CT numbers measured in Hounsfield Units with the DECT (Hünemohr et al. [2014a]). c_e is the unknown parameter that depends on the two employed effective spectra and can be derived from a dual energy scan of a single calibration material.

The effective atomic number can be derived in a similar way starting from the equation pairs Eq. 3.5

$$a_2\rho_\mathrm{e}Z^n = \frac{\langle f(E)\rangle_1 \cdot \langle\mu(E)\rangle_2 - \langle f(E)\rangle_2 \cdot \langle\mu(E)\rangle_1}{\langle f(E)\rangle_1 \cdot \langle\frac{1}{E^3}\rangle_2 - \langle f(E)\rangle_2 \cdot \langle\frac{1}{E^3}\rangle_1}. \tag{3.12}$$

Again, two constants c_1 and c_2 can be introduced that depend solely on the employed energy spectrum

$$a_2\rho_\mathrm{e}Z^n = c_1\langle\mu(E)\rangle_1 + c_2\langle\mu(E)\rangle_2. \tag{3.13}$$

Dividing by $a_2\rho_\mathrm{e}$ and inserting once more the definition of the CT number results in

$$Z^n = \left(\frac{\rho_\mathrm{e}}{\rho_\mathrm{e,w}}\right)^{-1}\left(\frac{c_1}{a_2\rho_\mathrm{e,w}}\langle\mu_\mathrm{w}(E)\rangle_1 \cdot \left(\frac{x_1}{1000\,\mathrm{HU}}+1\right) + \frac{c_2}{a_2\rho_\mathrm{e,w}}\langle\mu_\mathrm{w}(E)\rangle_2 \cdot \left(\frac{x_2}{1000\,\mathrm{HU}}+1\right)\right). \tag{3.14}$$

For the Z determination, the constant d_e can be introduced (Hünemohr et al. [2014a])

$$d_\mathrm{e} = \frac{c_1\langle\mu_\mathrm{w}(E)\rangle_1}{a_2\rho_\mathrm{e,w}}, \tag{3.15}$$

which ultimately shows how the effective atomic number can be determined from two CT number measurements x_1 and x_2 at different energies

$$Z_\mathrm{eff} = \left(\left(\frac{\rho_\mathrm{e}}{\rho_\mathrm{e,w}} \right)^{-1} \left(d_\mathrm{e} \left(\frac{x_1}{1000\,\mathrm{HU}} + 1 \right) + (Z^n_\mathrm{eff,w} - d_\mathrm{e}) \left(\frac{x_2}{1000\,\mathrm{HU}} + 1 \right) \right) \right)^{1/n}. \tag{3.16}$$

The effective atomic of a compound defines the "virtual" atomic number of a single element that would provoke the same photon attenuation as a compound of elements i for which holds true that

$$\rho_\mathrm{e} Z^n_\mathrm{eff} = \sum_i \rho_\mathrm{e,i} Z^n_i, \tag{3.17}$$

where $\rho_\mathrm{e,i}$ is the contribution of atom type i to the total electron density ρ_e (Hünemohr et al. [2014a]). This can be expressed through the number of electrons per unit volume $\rho \cdot N_\mathrm{A} w_i \frac{Z_i}{A_i}$ (cf. Eq. 2.19, Johns [1983], McCullough [1975])

$$Z_\mathrm{eff} = \left(\frac{\sum_i w_i \frac{Z_i}{A_i} Z^n_i}{\sum_i w_i \frac{Z_i}{A_i}} \right)^{1/n}, \tag{3.18}$$

where w_i denotes the elemental mass fraction by weight of element i to the compound. It should be stressed that Z_eff is defined by the electron density weights $w_i \frac{Z_i}{A_i}$ and not only by the mass weights w_i which differs particularly for hydrogen rich compounds.

Furthermore, it is important to notice that (average) atomic numbers of pure elements or compounds are quantities defined by the elemental mass weights of the compounds themselves whereas the Z_eff denotes a photon spectra dependent quantity characterizing radiological interaction of a compound with a specific photon spectra. Subsequently, the parameter n was optimized by X-ray absorption simulations to be n =3.1 for elements ranging from Z=[1-20] (Dr. Bernhard Krauss, Siemens, personal communication).

Eq. 3.4 does not apply for high Z materials exhibiting characteristic K-edge photoabsorption in the low photon energy range. Hence, Z_eff and $\hat{\rho}_\mathrm{e}$ cannot be calculated for these high Z materials.

For the image reconstruction, a single reference material for calibration was measured by Siemens and further image correction included a dedicated beam hardening correction dependent on the patient diameter (Hünemohr et al. [2014a]). Additionally, a low pass filter (2D boxcar, no further information accessible) to suppress noise was applied on both initial CT number images by Siemens (Hünemohr et al. [2014a]).

3.6 DECT-based SPR prediction

For a typical therapeutic particle energy of 200 MeV/u Eq. 2.23 simplifies to (Hünemohr et al. [2014a])

$$\mathrm{SPR}_{\mathrm{w}}^{\mathrm{m}} = \hat{\rho}_{\mathrm{e}} \cdot \frac{12.77 - \ln I_{\mathrm{m}}}{8.45}, \tag{3.19}$$

neglecting high order corrections and assuming an I-value of water of 75 eV (ICRU [1993]). The $\hat{\rho}_{\mathrm{e}}$ image can be used directly to predict the SPR, while the I-value of the medium remains to be determined from the Z_{eff} image.

3.6.1 Relating Z_{eff} to the I-value

Yang et al. [2010] suggested in a theoretical study to linearly correlate the logarithm of the I-value to Z_{eff}:

$$\ln I = a \cdot Z_{\mathrm{eff}} + b. \tag{3.20}$$

With both DECT images, the SPR can be calculated in an almost direct, and more physics related approach as compared to the SECT stoichiometric calibration which is based on the CT number that is influence by both, ρ_{e} and Z_{eff} (Sec. 3.4.2). This thesis presents the first experimental validation of the approach suggested by Yang et al. [2010] with DECT images measured with a clinical dual source scanner.

3.7 Image processing, treatment planning and visualization software

SIEMENS RT, the existing TPS software at HIT cannot handle and process two DECT DICOM image stacks ($\hat{\rho}_{\mathrm{e}}$ and Z_{eff}) for the conversion to SPR. Since the DECT-based SPR calculation does not require a look-up table, the SPR map calculated from the $\hat{\rho}_{\mathrm{e}}$ and Z_{eff} images were directly saved in combination with a "dummy" one-to-one HLUT calibration that is required by the TPS. The DICOM format can provide only integer numbers, therefore typical SPR values with three digits after the decimal point were scaled with a factor of 1000.

For this thesis, a customized protocol summarized in the appendix A was followed for the generation of SPR maps. The $\hat{\rho}_{\mathrm{e}}$ DICOM images show the $\hat{\rho}_{\mathrm{e}} \cdot 1000\text{-}1000$ while the Z_{eff} DICOM images show the $Z_{\mathrm{eff}} \cdot 10$.

3.7.1 R

R (R Development Core Team [2008]), originally developed for the bio-statistics community, is a free software environment to process, analyze and plot data. In this thesis, R (version 2.15.2) was used in combination with the comprehensive environment RStudio. Besides the statistical evaluation of irregular VOIs in CT images of a patient with MITK (Sec. 3.7.4), all analytical data processing, optimization and visualization was done with R. All CT images were available in the DICOM format which can be imported with the oro.dicom package in R (Whitcher et al. [2011]). Details on the image evaluation of mean values and standard deviations in VOIs are described extensively in Hünemohr et al. [2013]. SPR and I-value maps were calculated from the $\hat{\rho}_e$ and Z_{eff} images as matrices. For the treatment planning study of the head patient, SPR maps were exported to the VIRTUOS specific CT format ".ctx" in R. Here, a header file includes basic image information such as number of pixels, pixel size, slice thickness, data format and patient name. Due to the large amount of imaging data (the investigated patient head case comprehends three image stacks à 205 image slices à 512x512 pixels) a computer with 192 GB RAM had to be used for the SPR image calculation of the patient as a standard desktop PC reached its limits.

3.7.2 TRiP

The software code treatment planning for particles (TRiP) is a voxel-based dose planning tool originally developed at the Gesellschaft für Schwerionenforschung (GSI, Krämer et al. [2000]). TRIP is able to optimize physical and biological dose based on CT data, target volumes and organ at risk structures. For this thesis, only the physical dose optimization was employed as the focus was on the ion range determination. The dose calculation algorithm is designed for the active beam delivery raster scan method originally developed at GSI and employed at HIT (Haberer et al. [2004]). The treatment dose plan for a target defined in the CT voxel grid is optimized with available beam parameters (e.g. beam energy, beam intensity, raster points, spot size, spot distance, dose gradients etc.). In order to determine the particle energy that is necessary to reach a certain tumor slice located in depth, CT numbers of the tissue inhomogeneities are translated to WEPL with a HLUT (Sec. 2.3.4). TRIP interpolates in between the provided CT/WEPL calibration points of the HLUT.

3.7.3 Virtuos

The DKFZ in-house software Virtuos (Virtual Radiotherapy Simulator, Bendl et al. [1993]) provides the means for radiotherapy planning and is a graphical user interface to visualize the results of the dose calculation algorithms such as "voxelplan" for photons (DKFZ in-house TPS) or "TRIP" (for particle therapy, Sec. 3.7.2) for ion beams. VIRTUOS is able to load, register, save and visualize medical images as well as it enables target definition and dose evaluation of the treatment plans. The comprehensive tool box is described in the user handbook (Bendl [2011]). Besides the treatment planning and visualization mode, VIRTUOS also provides the means for rigid image registration with mutual information algorithms and a DICOM writer that allows to convert .ctx files to DICOM images.

Treatment planning study with TRiP and Virtuos

In the scope of this thesis, a SECT- and DECT-based treatment plan was compared for a head and neck patient. Both DECT images ($\hat{\rho}_e$ and Z_{eff}) were converted into a SPR .ctx images as described in the appendix. The SECT image was converted with a standard stoichiometric HLUT (Sec. 3.4.2) into a SPR .ctx image. The SPR .ctx images showed the SPR·1000 and consequently, the HLUT is a simple 1000:1 conversion for both SPR images.

The SECT- and DECT-based treatment plans were optimized with TRIP with the same standard optimization parameters. Resulting machine files (".rst.phys", providing for each energy slice the number of particles per spot) from the DECT-based plan were then forward irradiated on the SECT SPR images. The resulting dose map can be compared with VIRTUOS ("compare mode") to the SECT-based plan result that was originally optimized on the SECT-based SPR image. Difference maps of dose and dose-volume-histograms (DVH) can be evaluated as well.

3.7.4 MITK and DIPP

The Medical Imaging Interaction Toolkit (MITK) is an interactive software tool to visualize, analyze and process medical imaging data for various different purposes (Wolf et al. [2004]). The DKFZ Image Processing Platform (DIPP) is a modular application based on MITK (Wolf et al. [2005], Nolden et al. [2013]). The program enables to draw irregular VOIs with a region growing algorithm and allows evaluating statistical properties in the VOIs such as mean value, standard deviation and histograms. Evaluating statistical properties in different images that are not geometrically consistent (such as SECT vs. DECT images) but for the same defined VOI (saved in the ".nrrd" format) requires an image registration. DIPP provides different rigid registration algorithms customized for specific needs (Floca [2010]).

3.7.5 TOPAS Monte Carlo Simulation Tool

In 2012 Perl et al. [2012] presented a novel GEANT4-based MC platform named "Tool for Particle Simulation" (TOPAS) aiming to provide a reproducible and user friendly interface. The platform enables therewith a reliable and standardized scientific exchange of MC-based investigations (Perl et al. [2012]). TOPAS is based on input text files of simple structures that allows to easily use predefined setups and avoids inadequate settings of geometries, materials or wrong units due to over complex parameter structures (Perl et al. [2012]). TOPAS has a graphical output for visualization and is able to model passive and active scanning. It can model radiation transport based on CT grids and and provides standard scoring procedures (dose, fluence) all in 4D (Perl et al. [2012]). TOPAS is in principle able to transport different primary ion species, since it is the control interface of GEANT4. However, the TOPAS specified physics list relevant for clinical settings was benchmarked only for protons so far. TOPAS was used in this thesis for range simulations of carbon ions requiring a personalized version that enables heavy ion transport. The physics list in Pshenichnov et al. [2008] was used with default hadron therapy settings from Geant4 (the g4ionbinarycascade was changed to g4ion-QMD, Hünemohr et al. [2014c], personal communication David C. Hansen, Aarhus).

4 Experiments

This chapter describes the measurements and theoretical studies that investigate uncertainties in the existing standard CT calibration setup and characterizes DECT as an alternative image modality for ion radiotherapy planning. The chapter is divided into four main sections that structure also the following result and discussion chapters.

The first section (Sec. 4.1) investigates the robustness of the standard stoichiometric calibration. Measurement setups for the generation of the underlying CT number set were varied to investigate their influence on the parametrization and to quantify the uncertainties of the resulting calibrations.

Complementarily, the second section (Sec. 4.2) describes DECT measurements of tissue surrogates and phantom materials. A novel conversion of both DECT contrasts to SPR is described and evaluated for a range of materials.

The third section (Sec. 4.3) then compares both imaging modalities - single and dual energy CT - for a clinical head and neck patient case. Predicted SPRs for specific tissue regions and ion ranges of two carbon ion dose fields were evaluated relatively. The third section describes also, how DECT enables to assess a standard photon HLUT. Additionally, noise levels of predicted SPR based on both modalities were compared for two tissue surrogates measured at the same image dose level.

The last section (Sec. 4.4) presents a novel method to exploit DECT image contrasts for MC-based treatment planning in ion therapy. The presented method is compared to the conventional SECT-based method in a MC range study with tabulated tissue compositions.

4.1 Stoichiometric calibration robustness

Setting up a stoichiometric calibration consists of several tasks presented in Sec. 3.4.2. Each step of the process can influence the calibration result and demands the attention of the clinical medical physicist. The aim of this section is to study and quantify possible uncertainties via investigations of different experimental setups that could be varied in the clinical routine. The section focuses on the underlying basis for the stoichiometric calibration represented by the parametrization of the photon attenuation.

4.1.1 Parametrization of photon attenuation

Optimizing parameters k_1 (coherent / incoherent scattering) and k_2 (photoelectric absorption / incoherent scattering) that minimize Eq. 3.3 is major part in the generation of a stoichiometric calibration. The optimization depends on CT protocols, the set of measured materials, composition of the materials and the phantom setup (De Marzi et al. [2013], Yang et al. [2008]). Both resultant parameters influence significantly the subsequent theoretical CT number prediction for tabulated tissue compositions and therewith the calibration itself. For this thesis, it was decided to investigate these dependencies systematically with CT measurements under clinical conditions for the following variable settings:

A: X-ray tube voltages and kernels
  - 100 kV vs 120 kV vs 140Sn kV
  - D30 vs D34 vs H30

B: material selection, chosen set of tissue surrogates
  - without lung ("wo lung")
  - without cortical bone ("wo CB")
  - without brain ("wo brain")
  - without B200 and inner bone ("wo bone")

C: material composition of tissue surrogates
  - changed assumed elemental composition for hydrogen (-1 %) and calcium (+1 %) ("Ca up H down 1 %")

D: phantom geometry at 120 kV
  - central axis tube phantom (r=8 cm)
  - "pizza" phantom (r=8 cm)
  - cortical bone and adipose surrogate measured at different position in the "pizza" phantom ("CB Fat extra")

For the specified settings, k_1 and k_2 values (Eq. 3.3) were evaluated in combination with underlying corresponding residual CT number differences for the measured tissue surrogates. A detailed motivation for the variable settings is given below.

Resultant HLUTs show the sensitivity of the SPR prediction on the initial measurement settings. No standard operating procedure is known for the number and intervals of the look-up table line segments. In particular, generating line-segments appears non-trivial for the soft tissue region due to numerous CT number ambiguities. It was therefore decided to rather show corresponding look-up tables in the hard bone and adipose tissue section. Line segments for both tissue regions are easy to determine and enable to show the general systematic differences.

The CT protocol "RT 13 BPL KopfHalsDE" (Sec. 3.1, Tab. A.1(d),(e)) was used which is the same clinical protocol employed for the patient scan in Sec. 4.3. The scanner reported CTDI dose of 73 mGy was assured to be the same for the DECT (100 kV/140Sn kV) and SECT (120 kV) acquisitions. Eq. 3.3 was minimized with the default R multidimensional optimization function "optim()" based on the method presented by Nelder and Mead

[1965]. The approach is also suitable for non-linear optimization of multiple parameters as requested in de Kock and Schreuder [1996]. Initial values were set to $k_1 = 8.20 \cdot 10^{-4}$ and $k_2 = 3.39 \cdot 10^{-5}$. These values were derived from the MICROSOFT EXCEL optimization of Eq. 3.3 for the 120 kV spectrum and are similar to the values presented in Schneider et al. [2000], Landry et al. [2013b] and Vanderstraeten et al. [2007]. Exponents m_1 and m_2 in Eq. 3.3 were kept fixed for all voltages but their values are discussed in more detail in Sec. 6.1.

Detailed motivation for the variable measurement settings

Setting A: Different X-ray tube potentials were exploited as the absorption and scattering contribution to the total photon attenuation changes with photon energy (Sec. 2.1.1, Yang et al. [2008]). The convolution kernel influences the image quality by the tradeoff between image sharpness and noise.

Setting B: The impact of material selection was investigated due to the fact that radiotherapy facilities have different sets of tissue surrogates and exclude single inserts because of their suspect behavior in CT measurements. One prominent example is the Gammex brain surrogate that behaves suspicious in terms of CT numbers compared to the manufacturer provided composition data (Landry et al. [2011], Hünemohr [2011]). Lung and cortical bone were excluded since they are situated at the very ends of the CT number scale for tissues and may influence the parametrization significantly. Excluding lung is interesting also for another point: facilities sometimes observe unphysical behavior of the lung insert for head scans (Benjamin Ackermann, HIT Heidelberg, personal communication). In comparison to the body CT protocol, measured CT numbers can deviate significantly from predicted CT numbers for head protocols (up to 30-50 HU) derived with optimized k_1 and k_2 parameters. B200 and inner bone represent soft bones expressing CT numbers around 250 HU. Exclusion of both surrogates investigates the influence on the calibration for intermediate density bones that represent the majority of bones present in the human body.

Setting C: Assumed compositions of the measured surrogates may influence k_1 and k_2. Here, treatment facilities rely on the accuracy of the composition data provided by the manufacturer. Queries of the Gammex company resulted in the statement, that their material compositions show "approximate elemental compositions" (Bruce Longfield, Gammex, personal communication). Consequently it has to be assumed that actual compositions may deviate from provided data. Therefore - as a wors case scenario - the calcium and hydrogen amount was changed by 1 % for the surrogates that are composed of at least 2 % calcium (8 out of 13 inserts).

Setting D: Besides using the cylindrical PMMA tube phantom, the "pizza" phantom of the same diameter was investigated (Fig. 3.1). The influence of different beam hardening and crosstalk of the inserts on the optimization and CT calibration was characterized by two different fillings of the phantom (Fig. 4.1). In the first measurement, inserts were distributed according to the DKFZ medical physics protocol (Andrea Schwahofer, DKFZ, personal communication). In the second scenario, only the cortical bone and adipose surrogate were measured in the outer positions. CT numbers of both surrogates replaced the previously measured CT numbers of both surrogates (acquired with the complete filling of the phantom) and formed the third CT number set. This CT number set serves as a scenario of a different, random filling of the "pizza" phantom.

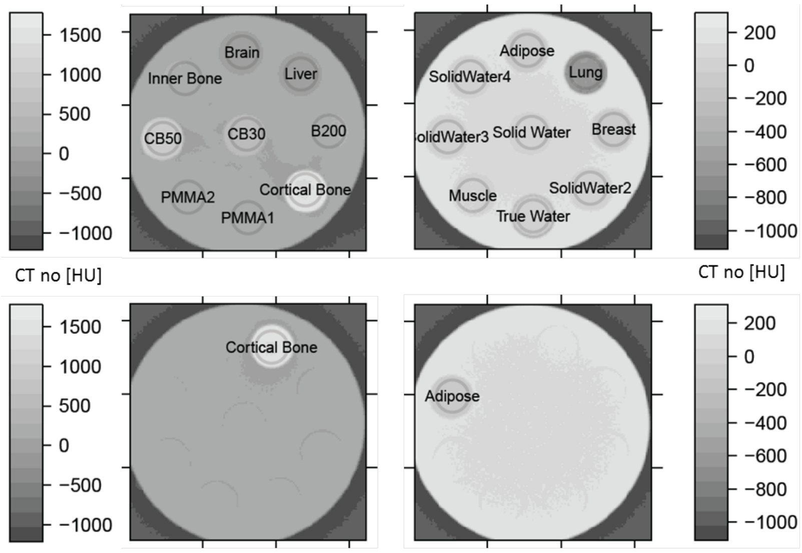

Figure 4.1: Rod positions in the "pizza" PMMA phantom for two different fillings. Both upper figures show the positions of all surrogates (front and back of the phantom). Only the inner solid water was used for the processing of the optimization and calibration. The two lower figures show the second filling of the phantom with cortical bone and adipose only. Empty holes were filled with PMMA rods.

4.1.2 Systematic influence HLUT polyline segments

As described in the previous section and Sec. 3.4.2, typical HLUTs consist of several line segments and no standard procedure exists on how to determine the line sections. CT numbers of homogeneous tissues are always affect by noise and register a certain spread in the CT number, usually assumed to be Gaussian distributed around a mean CT number. For tissues located right at the transition of two linear line segments, systematic errors in the translation to SPR may appear. To quantify this problem, six calibration points of a standard stoichiometric HLUT (120 kV, H30) at which the slopes of two adjacent line segments change were investigate (Fig. 4.2). At each point, a CT number distribution was statistically sampled with a standard deviation of 10 HU (Gaussian distribution, number of samples $n = 10000$). The SPR was derived with the HLUT in two different ways: the first one uses the normal HLUT and the translation slope changes (the HLUT "bends"). For the second way, the slope of the lower line segment was extrapolated and the slope does not change in the interval of the CT number distribution (the HLUT is "linear").

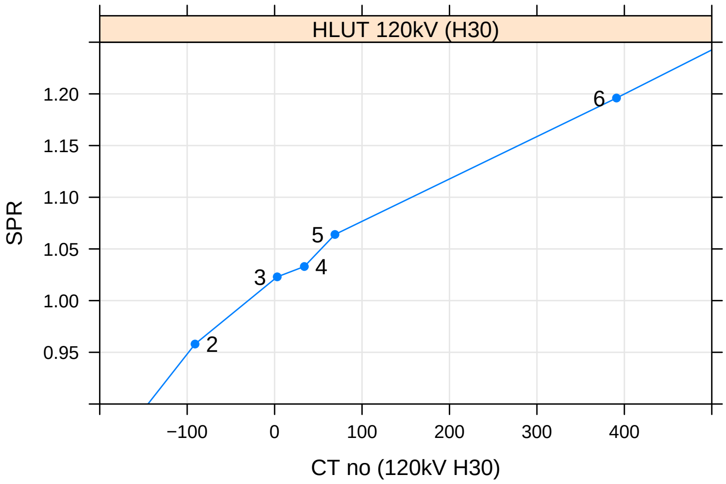

Figure 4.2: Calibration points of a standard HLUT (120 kV, H30, Sec. 4.1.1) for intermediate mass densities. The TPS interpolates in between the calibration points (blue line segments). The calibration point for lung tissue is not shown.

Additionally to the investigated 120 kV HLUT, it was systematically analyzed how the mean predicted SPR changes with the steepness of the slopes around the calibration point of water (0 HU/SPR=1.000). Changes in slopes were assumed to range from zero (a straight 1:1 line, observable in HLUTs for Mega-voltage CT, "MV CT") up to a decrease of the adjacent slope towards a 2:1 HLUT which is observed for standard kV settings (Newhauser et al. [2008]). The mean of each resulting SPR distribution can be related to the change in the slopes. Taking the mean of the SPR distribution is the correct value to analyze the systematic difference resulting from different slopes in the HLUT since the TPS usually adds up the SPR along the beam path to derive the WET.

4.2 DECT as an alternative image modality

As described in detail, DECT images provide new tissue contrasts ($\hat{\rho}_e$, Z_{eff}) that have the potential to improve the conversion of CT data to SPR. To do so, both contrasts have to be validated first in accuracy and precision for defined materials. In the following, these novel images were converted to SPR maps with a method different to the standard SECT stoichiometric calibration. This section and the corresponding result and discussion sections are based on the publications Hünemohr et al. [2014a] and Hünemohr et al. [2014b].

4.2.1 DECT-based measurement of $\hat{\rho}_\mathrm{e}$ and Z_eff

Tissue surrogates, polymers, metals and two printing materials (Sec. 3.2) were positioned in the PMMA tube on the central CT scanner axis to assure reproducible measurement settings for all materials. The DECT specific "Liver VNC" protocol was employed (Tab. A.1). Tube voltage pairs were set to 80/140Sn kV and 100/140Sn kV in order to quantify the influence of the lower voltage on the measurement accuracy of $\hat{\rho}_\mathrm{e}$ and Z_eff. Corresponding tube current ratios were chosen by the scanner software. The aluminum and titanium rods were measured with a single rotation at 650 mAs (Tremmel [2012]) to obtain an optimal image quality and test for DECT image information that can be achieved in metals. For both metals, the reconstruction comprehends a 16-bit Hounsfield Unit scale and a quantitative kernel similar to the D30 which includes a raw-data-based beam hardening correction (not yet commercially available, Tremmel [2012], Hünemohr et al. [2014a]).

The $\hat{\rho}_\mathrm{e}$ and Z_eff image stacks were calculated with the image-based algorithm described in Sec. 3.5. DECT contrasts and CT numbers could be analyzed for defined VOIs with R (Sec. 3.7.1) and could be compared to reference values listed in Tab. 3.1.

4.2.2 DECT-based SPR prediction

DECT-based SPR images were generated from the $\hat{\rho}_\mathrm{e}$ and Z_eff images according to (Eq. 3.19, Eq. 3.20):

$$\mathrm{SPR}_\mathrm{w}^\mathrm{m} = \hat{\rho}_\mathrm{e} \cdot \frac{12.77 - (a \cdot Z_\mathrm{eff} + b)}{8.45}. \tag{4.1}$$

Parameters a and b for the dependency of $\ln I$ on Z_eff had to be defined with the help of 71 tabulated tissues compositions taken from Schneider et al. [2000] (Sec. 3.2, Tab. A.7). For these 71 tissues, the I-value (Eq. 2.21) and Z_eff (Eq. 3.18) were calculated. This step is scanner specific (Z_eff exponent n =3.1) and therewith differs from the parametrization presented in Yang et al. [2010]. "Thyroid" was excluded due to its iodine amount which provokes a higher Z_eff compared to tissues in that range with usual compositions (Hünemohr et al. [2014a]).

Similar to the $\hat{\rho}_\mathrm{e}$ and Z_eff images, the I-value (calculated from the Z_eff image) and SPR images could be evaluated for the same defined VOI with R. DECT-based measurements of the I-values were compared to manufacturer data, while DECT-based predicted mean SPRs were compared to actual measurement of the materials' WEPL with carbon ions (Tab. 3.1).

4.3 Comparison of DECT- and SECT-based SPR prediction in a patient

In the course of this thesis, an image set of a head and neck patient (oropharyngeal cancer) scanned in dual energy mode with reasonable dose was accessible. The image set allowed a relative comparison of DECT- with SECT-predicted SPR for specific tissue regions and enabled to point out differences in range and dose in a schematic treatment planning study with carbon ions.

The patient was scanned at 100/140Sn kV with the CT treatment planning protocol "RT 13 BPL KopfHalsDE" (Tab. A.1(d)) as well as in the single energy mode at 120 kV with 215 mAs. This SECT scan included the administration of contrast agent and took place approximately three minutes after the DECT acquisition. The contrast agent affected images could be used for treatment planning in standard photon therapy (due to the broad depth dose curve of photons) but not for particle radiotherapy since contrast agent might hamper the SPR calculation in the perfused tissue significantly (Wertz and Jäkel [2004]). Additionally artifacts due to motion in between both acquisitions or image registration cannot be excluded. Therefore the 100 kV image of the DECT scan served as a surrogate for the SECT image. The 140Sn kV image differs much more from the standard 120 kV acquisition due to the additional tin filter (Sec. 3.1).

4.3.1 SPR images

The DECT-based SPR image was derived from the $\hat{\rho}_e$ and Z_{eff} image accoding to Eq. 4.1. For intermediate Z_{eff} values ([8.5,10] the ln$I$ was set to a constant value of 4.4.

The SECT-based SPR images were derived with protocol specific stoichiometric HLUTs (an example is shown in Fig. 3.2 for the 100 kV D30). The HLUTs were generated with the full set of Gammex tissue surrogates measured on the central axis of the PMMA tube phantom with the same DECT protocol as the patient was scanned.

Two axial image slices of the head patient were further analyzed: one slice of the ventricle region and one slice of the temporal bone region (Fig. 4.3). Systematic differences in SPR maps for (spatially coherent) tissue regions can be detected. Additionally, red horizontal lines in Fig. 4.3 indicate positions where profiles of SPR differences were analyzed. These SPR profiles show - besides the systematic SPR differences - the differences in reconstruction (e.g. sharpness at high attenuation gradients) and the impact of tube voltage settings for SECT-based SPR prediction. The two positions were chosen according to the SPR maps where largest systematic differences were observed in the ventricle and the petrous part of the temporal bone.

Additionally to the 100 kV image, the 140Sn kV image was also evaluated as a surrogate for the SECT image to analyze the influence of the harder spectrum on the SPR prediction. The differences of the two available DECT reconstruction kernels D30 and D34 were evaluated as well.

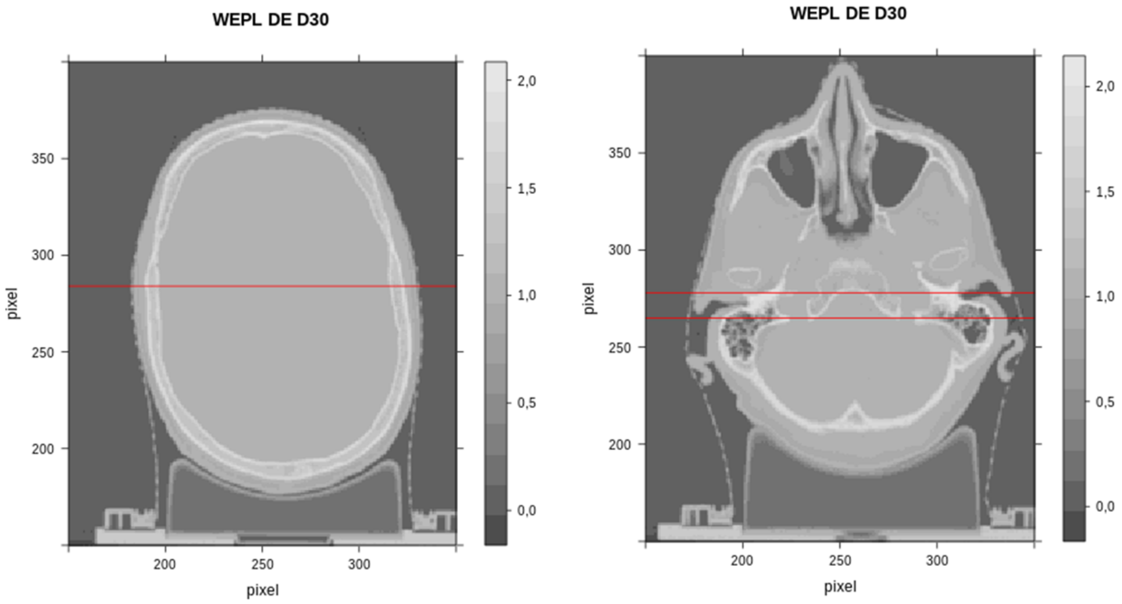

(a) (b)

Figure 4.3: Axial SPR images of a patient head and neck case in the ventricle region (a) and temporal bone region (b) showing the mastoid cavity and petrous part of the temporal bone. Red lines indicate the position where predicted SPR from DECT and SECT were additionally evaluated in line plots.

4.3.2 SECT- and DECT-based treatment plan comparison

Two basic treatment plans, one with a (hypothetical) target volume adjacent to the ventricle (Fig. 4.4a) and the other one with a target volume adjacent to the petrous part of the temporal bone (Fig. 4.4b) were investigated to study the impact on range difference and target coverage.

Pixels outside the patients contour were set to zero with the VIRTUOS "contour" tool in order to avoid any discrepancies emerging from different SPR assignments in low density pixels (a standard procedure in radiotherapy). Both SPR images, target contours and beam angles were intrinsically registered since the 100 kV image of the DECT acquisition served as a surrogate for the SECT. For each target volume, one carbon ion field of 2 Gy physical dose was applied (no biological optimization).

For the target positioned adjacent to the ventricles, the DECT- and the SECT- (140Sn kV) based plans were forward calculated on the SECT SPR map (100 kV, D30 kernel). Additionally, the SECT D34 (100 kV) plan was forward calculated on the D30 (100 kV) SECT SPR map to evaluate the influence of the reconstruction kernel.

For the target positioned next to the petrous part of the temporal bone, the DECT machine file (D30) was forward irradiated on the SECT SPR map (100 kV D30). Differences of

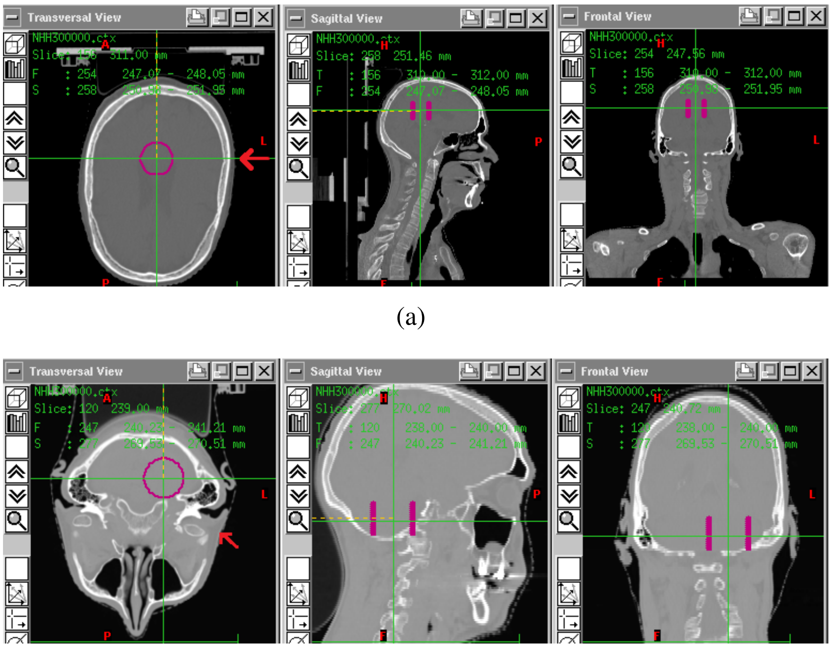

(a)

(b)

Figure 4.4: Two hypothetical treatment plans were created for the head patient. The 100 kV image served as a surrogate for the SECT. One target volume was positioned in the center of the brain next to the ventricle, the second target volume was positioned adjacent to the petrous part of the temporal bone and mastoid cavity.

dose distributions between SECT- and DECT-based treatment plans were evaluated with respect to range. The plan comparison followed the work-flow presented Sec. 3.7.3.

4.3.3 Tissue composition and photon HLUT verification

Measured $\hat{\rho}_e$ and Z_{eff} in the patient enable the comparison with reference values of tabulated tissues that represent the essential basis for the stoichiometric calibration (Sec. 3.4.2). Additionally, the $\hat{\rho}_e$ images could be exploited directly for photon therapy (Sec. 2.1).

In a first investigation, eight different tissue groups were contoured in the patient image set with DIPP (100 kV, Sec. 3.7.4, Fig. 4.5). Selected tissues cover a wide range of human tissues and were relatively easy to contour. Most of the contoured tissues were very homogeneous (except lung and the mastoid) and enabled the comparison with tabulated tissues. The 120 kV SECT was registered with the DIPP "multi-modal rigid default" algorithm to the DECT acquisition. The registered 120 kV image allowed the evaluation of statistical properties for the same VOIs originally defined in the DECT images. For the inhomogeneous tissues (lung, mastoid) the statistical evaluation might be not correct due to slightly different geometries.

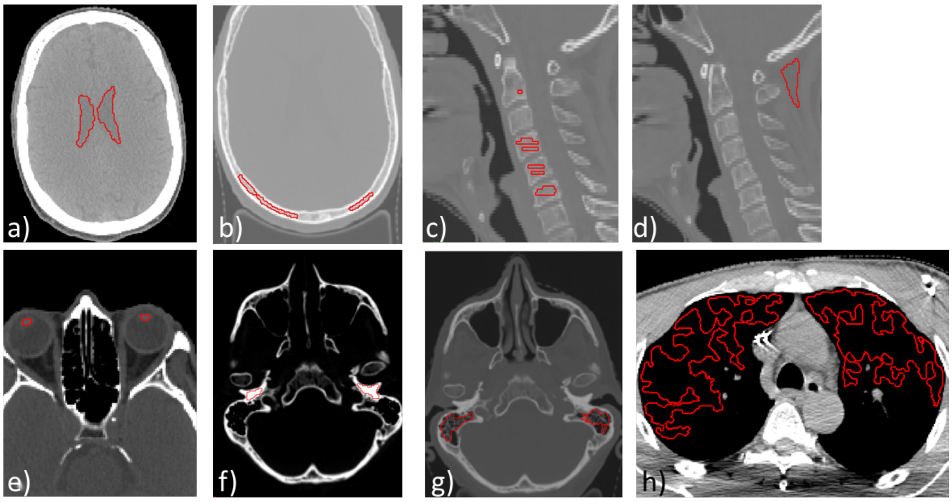

Figure 4.5: Tissue groups contoured in one head and neck patient scanned at DECT. a) ventricles, b) inner cortical bone, c) inner bone, d) adipose, e) eye lens, f) petrous part of the temporal bone ("cortical bone"), g) mastoid, f) lung. Contours were delineated in DIPP/MITK with a region growing tool.

Mean values and standard deviations of the CT numbers, $\hat{\rho}_e$ and Z_{eff} were evaluated for defined VOIs. Measured mean values can be compared to (predicted) values for tabulated tissue compositions from the stoichiometric photon HLUTs (Sec. 3.4.2). Predicted SPR from SECT and DECT could be calculated with the mean values (CT number for SECT and $\hat{\rho}_e/Z_{\mathrm{eff}}$ for DECT) of the contoured tissue regions.

4.3.4 Noise quantification of SPR prediction

Using DECT, the patient is scanned simultaneously with two different photon spectra. It is a matter of scientific discussion in the community whether the DECT noise and dose levels can be kept similar to the ones of the standard SECT (Schenzle et al. [2010], Yu et al. [2011]). For this thesis, noise levels in two tissue surrogates measured with SECT and DECT at the same CTDI dose index (73.5 mGy in a 16 cm phantom, Tab. A.1(d),(e)) were analyzed. Noise levels were evaluated in relative terms for the base data (CT numbers, $\hat{\rho}_e$ and Z_{eff}) but also in the resulting SPR maps predicted from SECT and DECT images.

4.4 Tissue decomposition for MC dose algorithms

This section presents a novel DECT-based approach of tissue decomposition for MC simulations in particle therapy to quantify the usefulness of the additional DECT contrasts.

The chapter and corresponding result and discussion sections are based on the publication Hünemohr et al. [2014c].

For the novel DECT approach one relies on standard tabulated tissues presented in Schneider et al. [2000] (Tab. A.7) as no comprehensive data set of tissue compositions along with DECT contrasts is available. For these 71 reference compositions, DECT contrasts ($\hat{\rho}_e$ and Z_{eff}, Eq. 2.24 and Eq. 3.18) were calculated. Only the six most important elements present in the human body were considered and high Z elements were excluded. The sum of the mass weights of these trace elements was smaller than 1.7 % for every tissue (Hünemohr et al. [2014c]). Including the high Z elements provokes a mean elevation of the reference Z_{eff} by $\approx$0.1 (excluding thyroid) and should be considered when applying the method for real dose calculations (Hünemohr et al. [2014c]). Reference mass weights of the remaining elements were normalized to give the sum of 100 % by dividing individual mass weights by the sum of all considered elemental mass weights (Hünemohr et al. [2014c]).

4.4.1 Deriving ρ from $\hat{\rho}_e$

The mass density ρ is related to $\hat{\rho}_e$ by the mean Z/A ratio of the compounds (Eq. 2.24) and can be derived by

$$\rho = a \cdot \hat{\rho}_e + b. \tag{4.2}$$

Fit parameters a and b were derived for tissues ranging from adipose to cortical bone (excluding lung). Lung is a mixture of soft tissue and air and its ρ depends on the respiratory phase. Consequently, the $\rho/\hat{\rho}_e$ pairs of air and muscle were interpolated and formed the second linear line segment ranging from air to adipose (Hünemohr et al. [2014c]).

4.4.2 Tissue composition

Predicting elemental composition from a single CT number is difficult as depicted in Fig. 4.6 and described in Sec. 3.4.3. "In order to take advantage of the available DECT information, elemental mass fractions w_i for each element i were derived as a function of $\hat{\rho}_e$, Z_{eff}, and an interaction of both for soft and bone tissue separately" (Hünemohr et al. [2014c]):

$$w_i = a_i \cdot \hat{\rho}_e + b_i \cdot Z_{\text{eff}} + c_i \cdot \hat{\rho}_e Z_{\text{eff}} + d_i. \tag{4.3}$$

The interaction term of both DECT contrasts reflects the fact, that elemental mass weights may behave differently dependent on $\hat{\rho}_e$ and Z_{eff} (e.g. carbon and oxygen weight in soft tissue Fig. 4.6, Hünemohr et al. [2014c]). Lung tissue represents again an exception: for all $\hat{\rho}_e$ smaller than the one of adipose tissue, the elemental composition was kept fix and is assigned to the reference lung tissue composition. This is necessary since the extrapolation of the linear elemental fits towards low $\hat{\rho}_\mathrm{e}$ would not represent lung tissue (Fig. 4.6, Hünemohr et al. [2014c]).

The presented DECT approach for tissue decomposition differs from the SECT approach summarized in Sec. 3.4.3. The SECT method discretizes the CT number scale and assignes for each HU interval a fix elemental composition but a continuous ρ that allows to scale the nuclear cross sections. Whereas the DECT approach also adjusts the compositions of nuclear cross sections continuously. A schematic comparison of both approaches is summarized in Fig. 4.7. DECT- and SECT-based predicted SPR, I-value, ρ and elemental mass weights w_i can be compared to reference data. With DECT, the SPR can be predicted in two different ways: using the $\hat{\rho}_\mathrm{e}$ directly and the composition only for the I-value prediction ("DECT with $\hat{\rho}_\mathrm{e}$") or by determining first the ρ and elemental mass weights and then calculate the $\hat{\rho}_\mathrm{e}$ and the I-value.

4.4.3 Range study

The impact of predicted tissue decomposition on MC based range calculation was tested for 12 tissues. Ranges of monoenergetic protons and carbon ions were simulated with the MC tool TOPAS (Sec. 3.7.5). I-values of predicted tissue compositions (Sec. 4.4.2) were defined specifically in the input text files according to Bragg's additivity rule and stick with the multiplication factor of 1.13 (Eq. 2.21).

Three different energies for protons (117, 183, 222 MeV, $2{\cdot}10^6$ primary particles) and one energy for carbon ions (10^5 primary particles of 350 MeV/u, equivalent to the range of the 183 MeV protons) were chosen (Hünemohr et al. [2014c]).

The tissue selection covers different CT number bins and includes compositions that would benefit most from DECT according to the previous comparison of SPR prediction (Hünemohr et al. [2014c]). Fig. 4.6 showed that the carbon and oxygen mass weight varies the most in soft tissues. To study the influence of both mass weight fractions on the ion range, an artificial material ("HCO", 10 % hydrogen, 30 % carbon and 60 % oxygen) was introduced. The carbon and oxygen mass weights were varied by ±10 % so that three "HCO" materials could be investigated (ρ and I-value were kept fixed).

For each selected tissue particle ranges were simulated in three compositions: (a) predicted from the SECT CT number (Schneider et al. [2000]), (b) predicted with the novel DECT based approach from $\hat{\rho}_\mathrm{e}$ and Z_eff and (c) in the ground truth reference composition (originally tabulated in Schneider et al. [2000]).

The dose to medium was scored in 0.1 mm z-steps along the beam axis which implies a lateral integration of absorbed dose in the axial slices (Hünemohr et al. [2014c]). Particle ranges were evaluated at 90 % of the distal edge of the Bragg peaks and differences were compared to the ranges in the reference compositions.

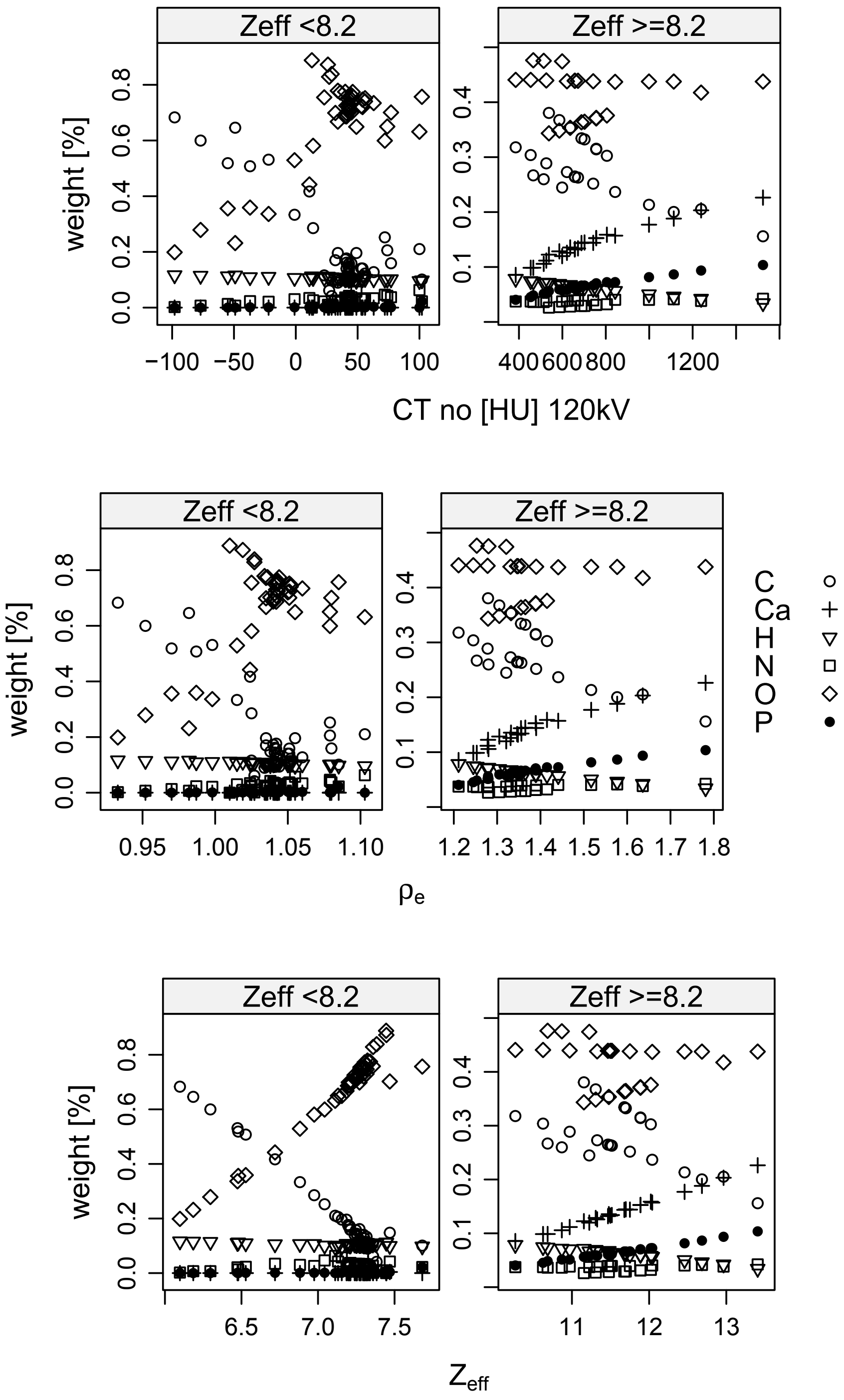

Figure 4.6: Elemental mass weights dependent on CT number (120 kV, Schneider et al. [2000]), $\hat{\rho}_e$ and Z_{eff} depicted for 70 tabulated soft (Z_{eff}<8.2) and bone tissues (Z_{eff}≥8.2) taken from Schneider et al. [2000] (Tab. A.7). Only the six major elements present in the human body were considered, lung tissue is not shown. CT number ambiguities are better differentiable using the the additional information of Z_{eff} in combination with $\hat{\rho}_e$. Reprinted from Hünemohr et al. [2014c].

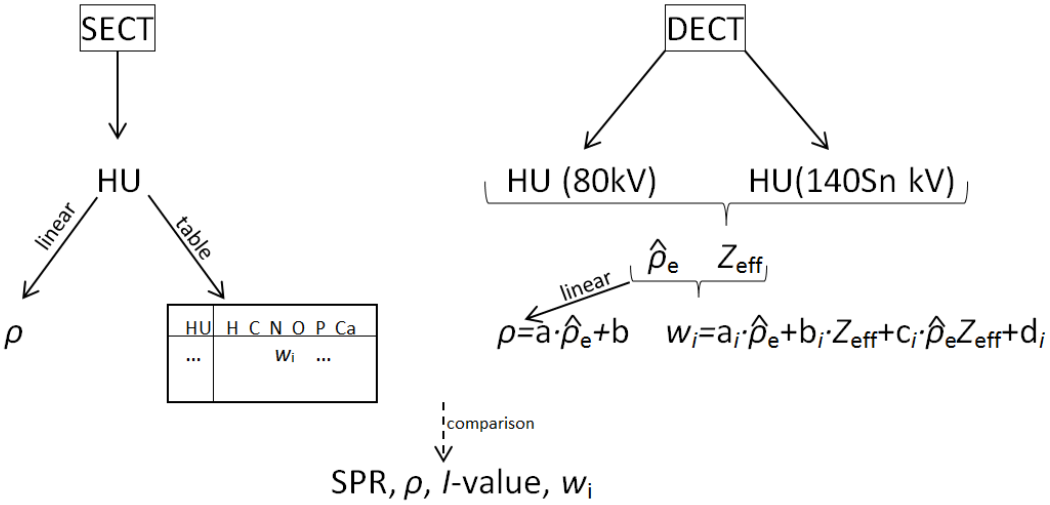

Figure 4.7: Conversion schemes of SECT and DECT image data for MC-based dose calculation. The standard SECT approach is summarized in Sec. 3.4.3. Figure adapted from Hünemohr et al. [2014c].

5 Results

5.1 Stoichiometric calibration robustness

The robustness of the stoichiometric calibration was investigated with variable settings of the basis CT measurements. Resultant k_1 and k_2 parameters are summarized and correspondent residual differences in CT numbers are depicted. The next section describes the differences in the resultant calibration curves. As the HLUTs are composed of poly-line segments, systematic differences in predicted SPR for tissues located right at the calibration points are analyzed.

5.1.1 Parametrization of photon attenuation

k_1 and k_2 optimized values

Setting A: The general decrease of photon attenuation μ with mean X-ray energy can be well observed through decreasing k_1 (from 100 kV to 140Sn kV) and k_2 (from 100 kV or 120 kV to 140Sn kV) values in Fig. 5.1. k_1 and k_2 change their relative contribution with photon energy (k_1 coherent scattering, k_2 photoelectric absorption relative to incoherent scattering, cf. Fig. 2.1). Negative k_1 parameters are observed for some acquisitions with the D30 kernel at 100 kV and 120 kV while half of the 140Sn kV acquisitions result in negative k_1 values.

Setting B: With increasing photon energy, intra-acquisition variances for the different material selection get smaller. k_1 is much more sensitive ($k_1 = (1.09 \pm 0.41)10^{-3}$ at 120 kV) to changes in the material set (Fig. 5.1). k_2 remains relatively robust against the investigated variations ($k_2 = (3.33 \pm 0.15)10^{-5}$ at 120 kV). k_1 and k_2 are both increased as compared to the standard ("normal") CT number acquisition when excluding the cortical bone surrogate. Neglecting the brain surrogate provokes a negative k_1 value for the D30 (100 kV) and D30/D34 (140Sn kV) acquisition.

Setting C: Changing the assumed insert composition (hydrogen and calcium) influences the k_1 and k_2 values significantly and provokes the largest difference to the image acquisition with the "reference" material composition (Fig. 5.1). Here, changing the compositions increases the k_1 value (for 100 kV and 120 kV) while k_2 decreases.

Setting D: The phantom geometry influences k_1 significantly while k_2 remains again relatively stable (Fig. 5.2).

Tab. A.2 summarized measured CT numbers and optimized k_1 and k_2 values are listed in Tab. A.3.

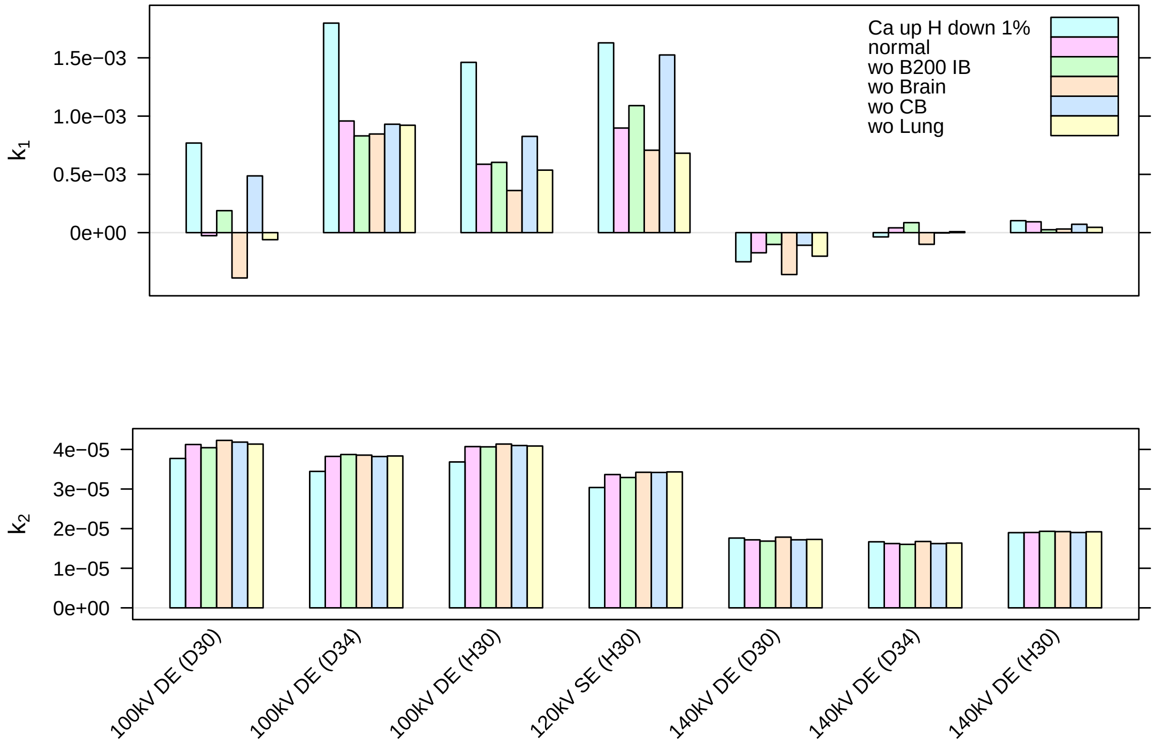

Figure 5.1: Optimized k_1 and k_2 values (Eq. 3.3) for specific surrogate selection and composition dependent on tube voltage and convolution kernel. SECT at 120 kV cannot be reconstructed with dual energy kernels. 100 kV and 140Sn kV were measured in the dual source dual energy mode.

Residual CT number differences

The residuals between predicted and measured CT numbers over a large set of tissue surrogates can help to identify systematic discrepancies emerging from the simplified parametrization of the photon attenuation.

A: Notably, CT number differences are smaller for higher X-ray tube potentials (Fig. 5.3, Fig. 5.4). For the 100 kV and 120 kV acquisition a systematic trend of negative residuals towards low $\hat{\rho}_e$ and a positive trend towards high $\hat{\rho}_e$ can be observed (with the exception of cortical bone at very high $\hat{\rho}_e$ and the D34 kernel reconstruction). No systematic trends in CT number residuals are observable for the 140Sn kV acquisition. The reconstruction kernel D30 results in higher residuals in predicted CT numbers than the H30 kernel, while the D34 achieves the smalles CT number residuals.

B & C: Changing the material composition or excluding the lung surrogate does not influence the residual CT number difference much (Fig. 5.4). An exclusion of the cortical bone surrogate is advantageous and decreases the residuals further. When the cortical bone surrogate is excluded a similar negative CT number residual for the next lower bone

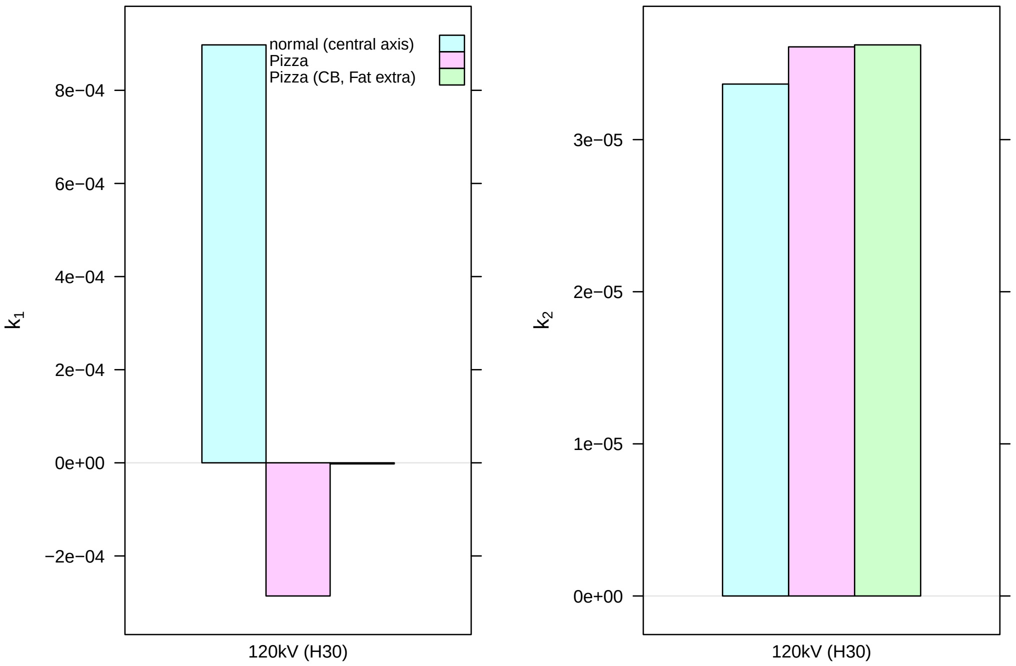

Figure 5.2: Optimized k_1 and k_2 values (Eq. 3.3) for the 120 kV SECT image acquisition dependent on the phantom used. Tissue surrogates were measured on the central axis in a PMMA tube phantom and in the "pizza" phantom filled in two different ways.

surrogate can be observed (CB50%, Fig. 5.4). For all variable material sets CT number residuals are the smallest with the 140Sn kV acquisition.

D: Fig. 5.5 shows the CT number residuals for different phantom settings. Measuring the tissue surrogates on the central axis provokes the highest CT number residuals which apply especially to the lung surrogate. Measuring on different positions in the "pizza" phantom results in smaller differences. Measured μ/μ_{H2O} differ by 1.5-2 % between the PMMA and "pizza" phantom while for lung tissue a much larger difference in the employed configuration was observed (Fig. A.1).

Three materials stand out: lung, brain and cortical bone. While all bony surrogates follow the trend of an increasing positive CT number difference towards higher $\hat{\rho}_e$, cortical bone registers a negative difference for the 100 kV and 120 kV acquisition (except for the D34 reconstruction). Lung tissue has a particular negative CT number difference at the 120 kV acquisition (reconstructed with the head kernel H30). An unusual high negative CT number residual is observed also for the brain surrogate. The same trends for these surrogates repeat for different material sets employed (Fig. 5.4).

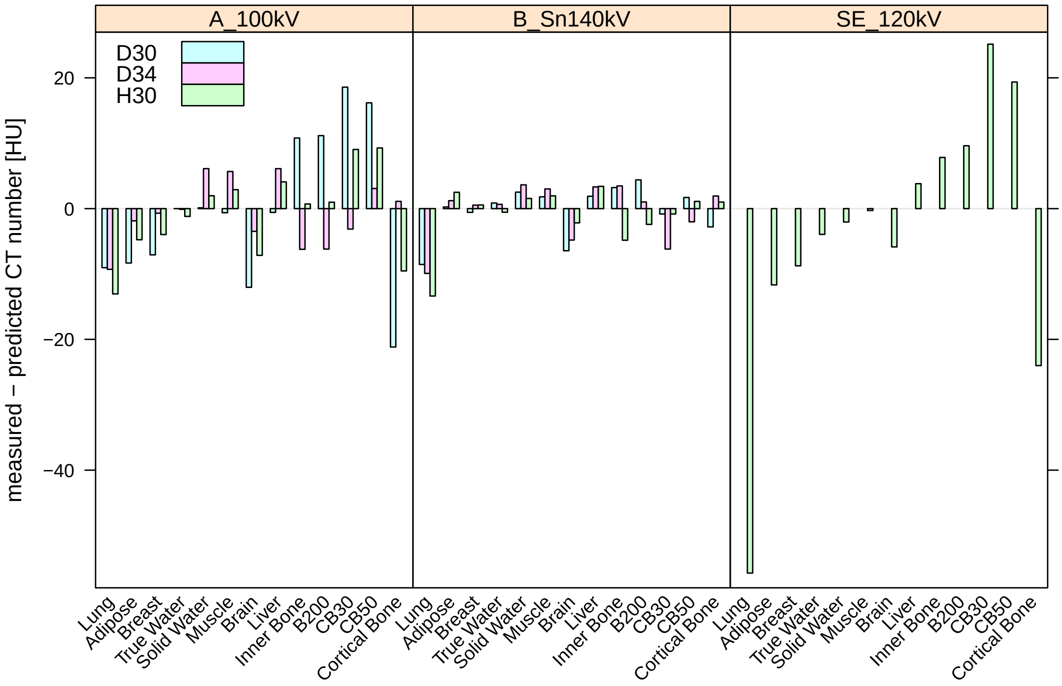

Figure 5.3: Differences between measured and predicted CT numbers of tissue surrogates dependent on tube voltage and reconstruction kernel. Predicted CT numbers were generated from optimized k_1 and k_2 parameters (Eq. 3.3).

Resultant look-up tables for variable CT measurement settings

A, B and C: Similar to the results shown in the previous paragraphs the corresponding HLUTs at 140Sn kV register the lowest variability with different material sets and measurement setups (Fig. 5.6). In contrast, HLUT for the 100 kV and 120 kV acquisitions are much more affected by these variations (Fig. 5.7, Fig. 5.8, Fig. 5.9). HLUTs vary the most for image reconstructions with the D30 and H30 kernels while the D34 kernel results in relatively consistent line segments for all variations at 100 kV (Fig. 5.7). Excluding the cortical bone surrogate provokes the largest separation of the resultant HLUT from the HLUT derived with the entire set of tissue surrogates.

SPR residuals emerging from different HLUT dependent on the measurement setting are as followed: For bone tissue, the SPR differs by up to 1.5 % at 120 kV, 0.5 % at 100 kV and 0.1 % at 140Sn kV (H30 kernel) compared to the standard setting (Fig. 5.8). For adipose tissue, SPR residuals are smaller than 0.6 % for all three voltages (H30, Fig. 5.9).

Image reconstruction with different kernels influence also the sensitivity of HLUT on different measurement settings: At 100 kV SPR residuals of up to 1.2 % (D30), 0.5 % (H30) and 0.4 % (D34) compared to the standard setting were observed (Fig. 5.7). At

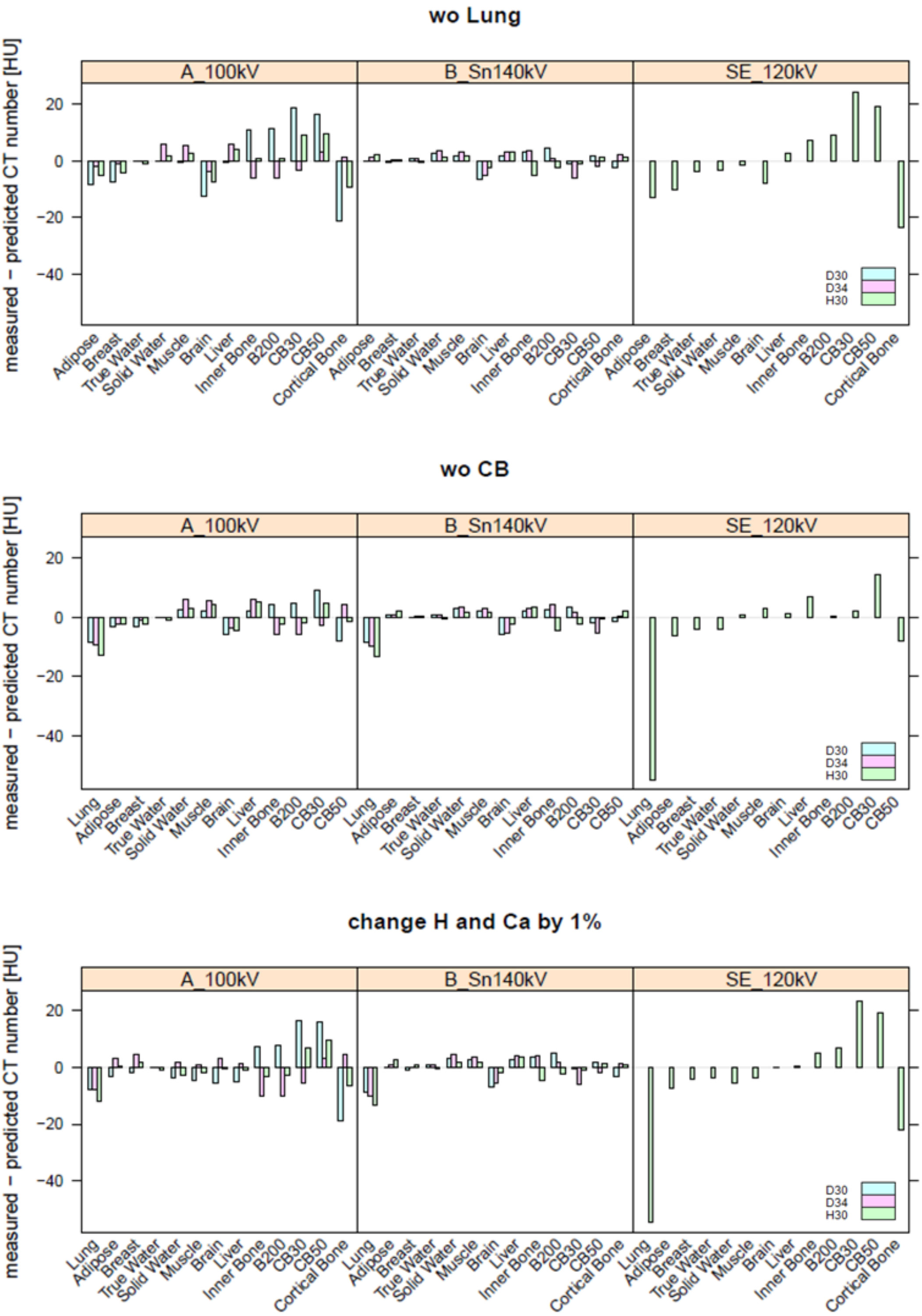

Figure 5.4: Differences of measured to predicted CT numbers of tissue surrogates dependent on tissue surrogate selection and composition. Predicted CT numbers were derived with optimal k_1 and k_2 values that minimized Eq. 3.3 for the specified settings.

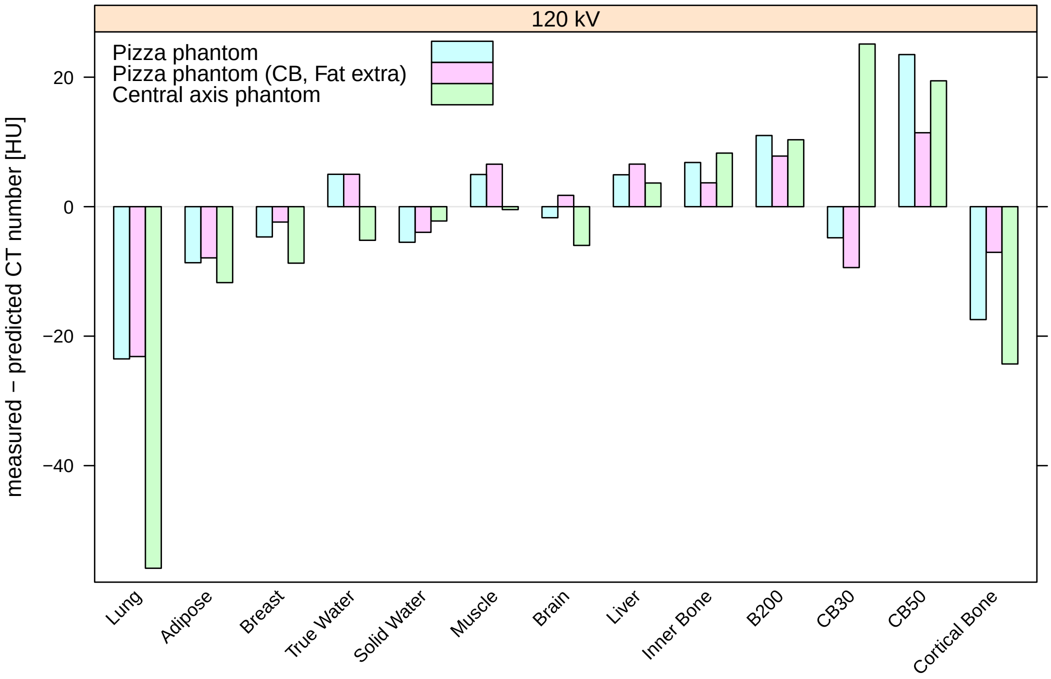

Figure 5.5: Differences between measured and predicted CT numbers of tissue surrogates dependent on different phantoms and phantom fillings. Predicted CT numbers were derived with optimal k_1 and k_2 values that minimized Eq. 3.3.

140Sn kV SPR predictions from different HLUT agree within 0.3 % for all three kernels and different measurement settings (Fig. 5.6).

D: Fig. 5.10 and Fig. 5.11 show the corresponding HLUTs for the three different phantom settings at 120 kV. The employed "pizza" phantom provokes a difference of predicted SPR in the resultant HLUT of up to 0.9 % (soft and bone region) compared to the HLUT derived with the surrogate measurement on the central axis PMMA tube phantom.

To summarize, SPR prediction for a single CT number (at 120 kV, H30) is estimated to vary in a simple additive scenario up to 0.9 % (phantom) + 1.5 % (material set)= 2.4 % when not assuming compensation or disproportional effects. This scenario (instead of the quadratic summation) implies that the effects of variations in the material set may aggravate in different phantom settings. For the 140Sn kV acquisition, variations due to material set are much smaller (0.4 %).

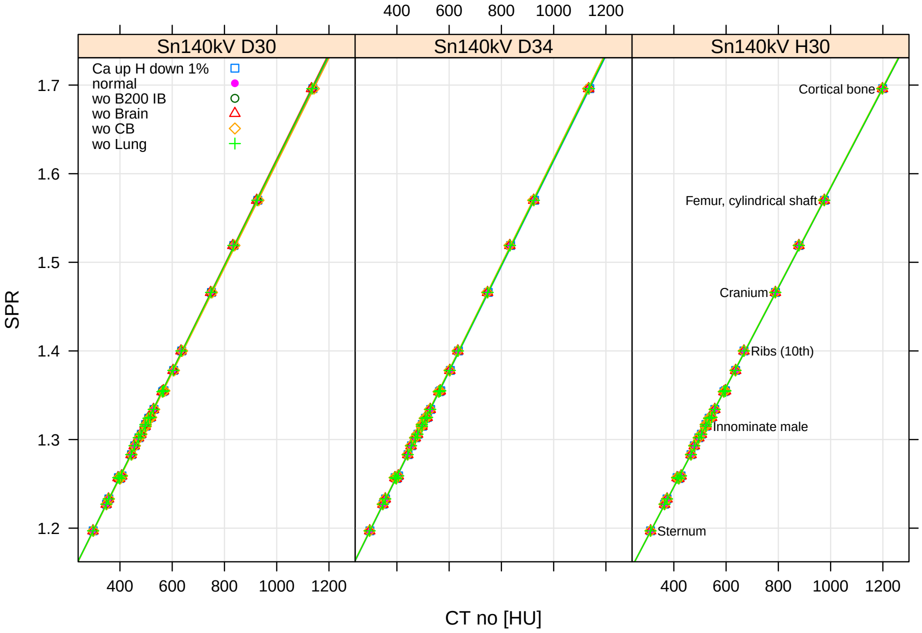

(a)

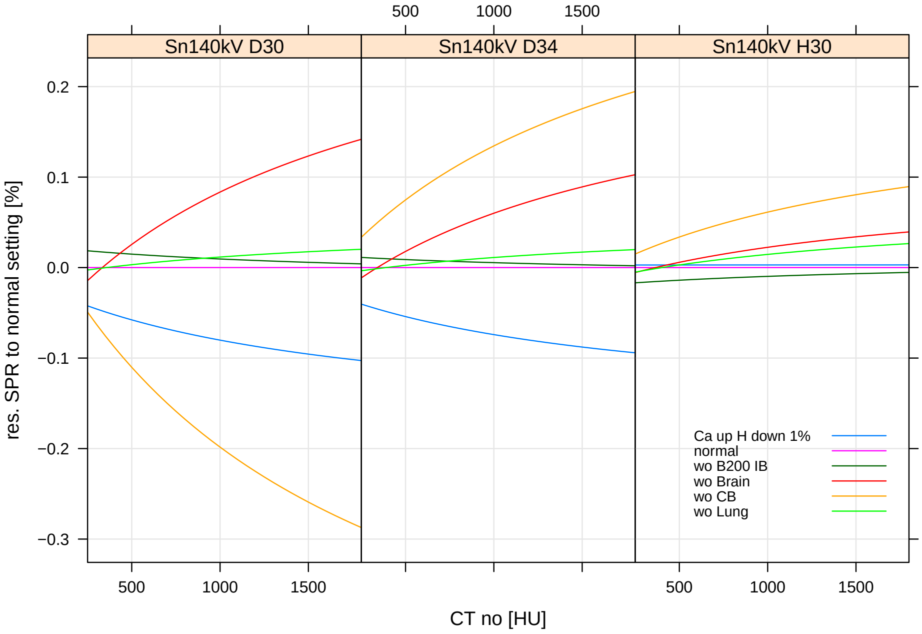

(b)

Figure 5.6: (a) SECT HLUT at 140Sn kV for variable measurement settings and reconstruction kernels in the bone region. (b) shows SPR residuals resulting from the different HLUTs compared to the HLUT generated with the normal measurement setting.

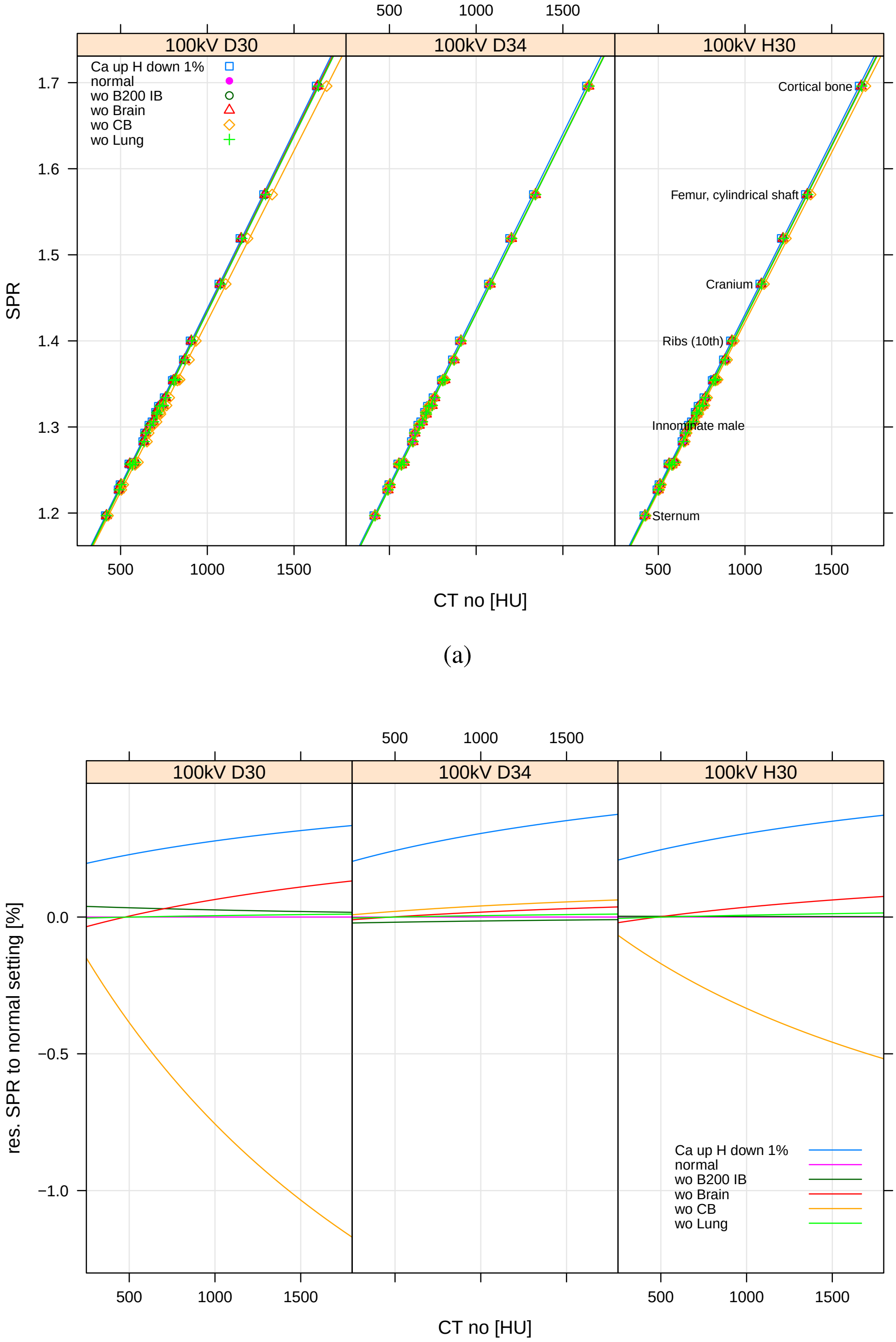

(a)

(b)

Figure 5.7: (a) SECT HLUT at 100 kV for different measurement settings and reconstruction kernels in the bone region. (b) shows SPR residuals resulting from the different HLUTs compared to the HLUT generated with the normal measurement setting.

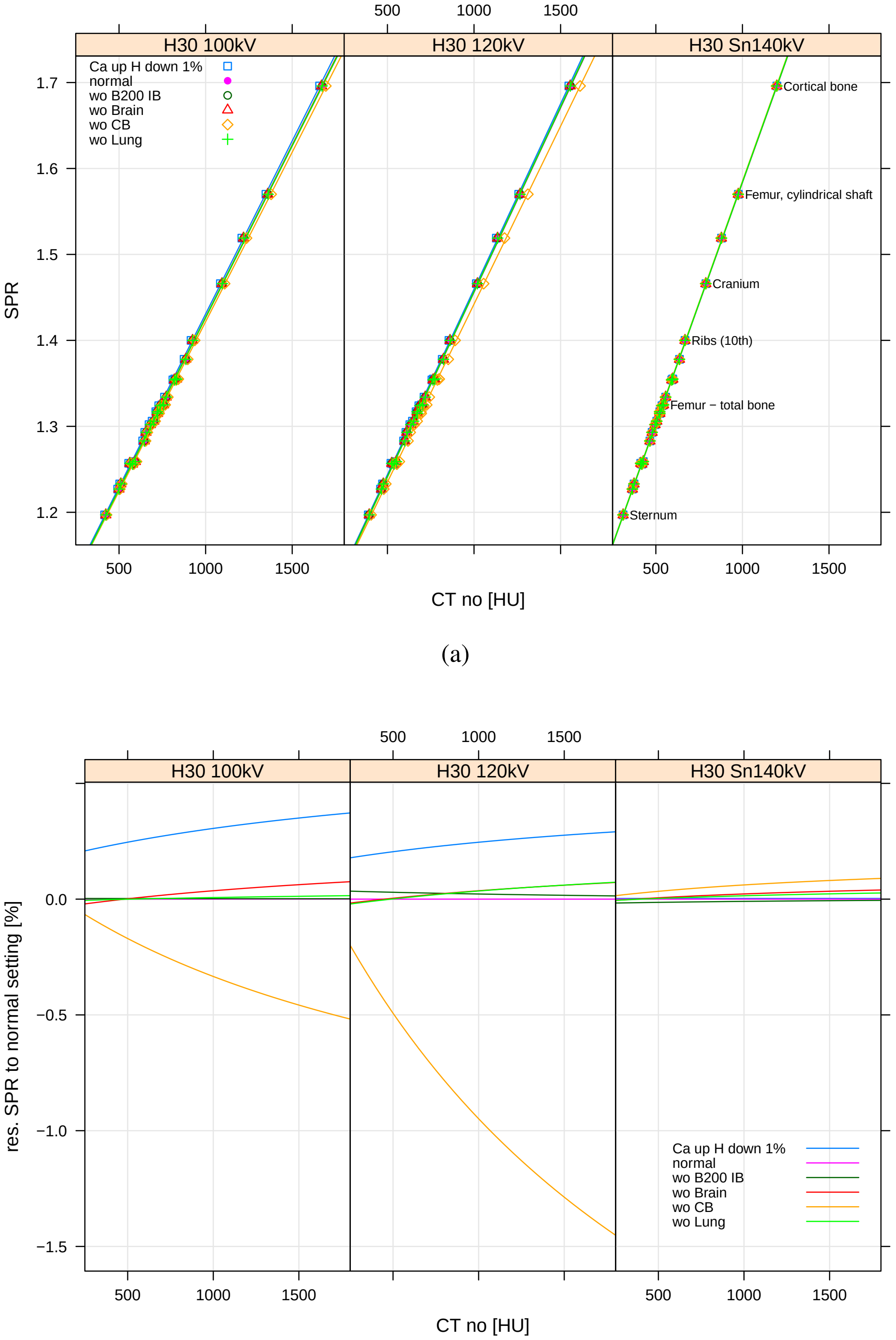

(a)

(b)

Figure 5.8: SECT HLUT with a H30 kernel for variable measurement settings and tube voltages in the bone region (a). (b) shows SPR residuals resulting from the different HLUTs compared to the HLUT generated with the normal measurement setting.

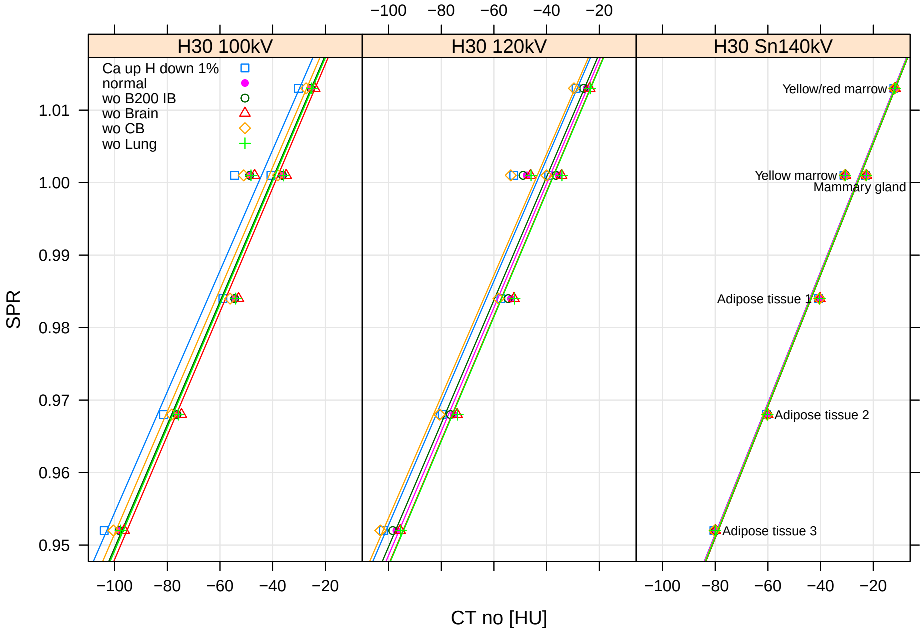

(a)

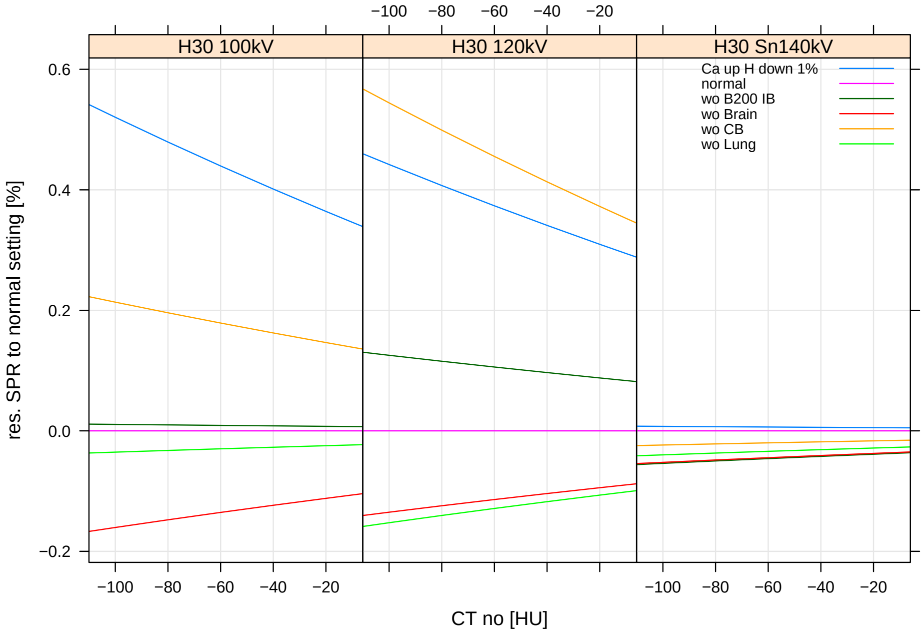

(b)

Figure 5.9: (a) SECT HLUT with a H30 kernel for variable measurement settings and tube voltages in the soft tissue region. (b) shows SPR residuals resulting from the different HLUTs compared to the HLUT generated with the normal measurement setting.

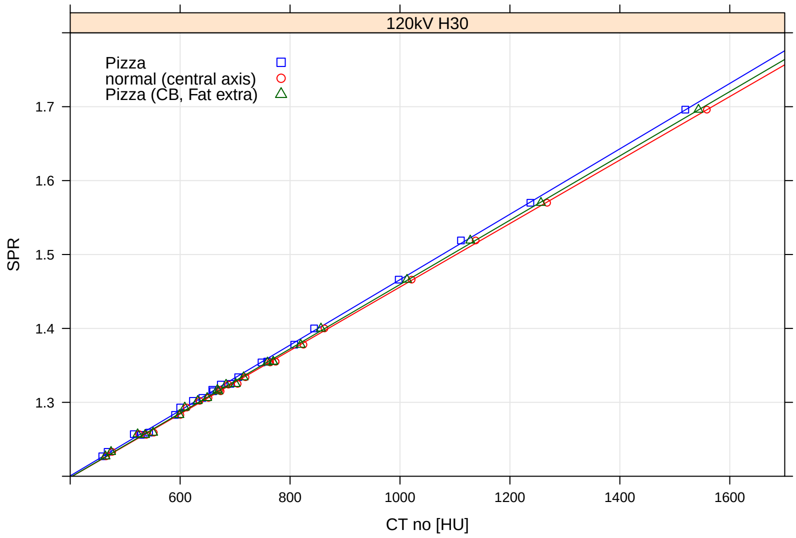

Figure 5.10: SECT 120 kV HLUT (H30) for the bone region derived from tissue surrogate measurements in three different phantom settings of the same radius (Sec. 3.3). SPR residuals can add up to 0.9 % (i.e. at 1400 HU) compared to the HLUT derived with measurement at the central axis.

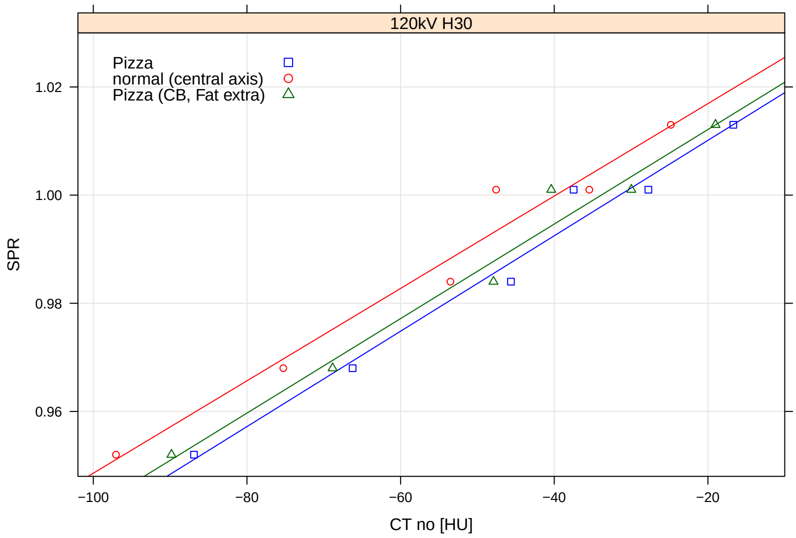

Figure 5.11: SECT 120 kV HLUT (H30) for the soft tissue region derived from tissue surrogate measurements in three different PMMA phantoms of the same radius described (Sec. 3.3). SPR residuals can add up to 0.9 % (i.e. at -80 HU) compared to the HLUT derived with measurement at the central axis.

5.1.2 Systematic influence HLUT polyline segments

The asymmetric distribution of predicted SPR due to different slopes of two adjacent line segments of the HLUT is depicted in Fig. 5.12. Tab. 5.1 summarizes the differences of mean SPR values derived from the two different HLUTs. A maximum systematic error in the SPR prediction of up to 0.22 % for tissues located at a calibration point can be observed.

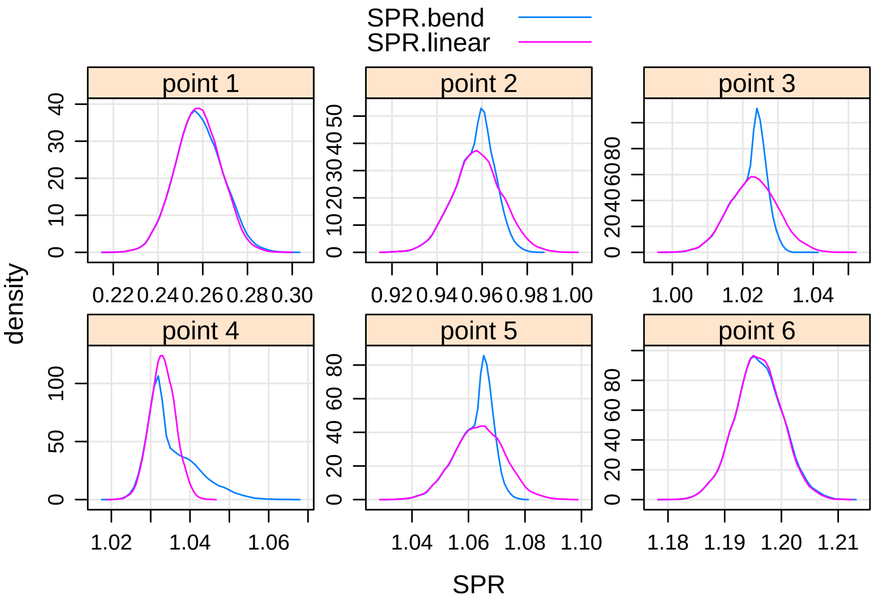

Figure 5.12: Density plot of the predicted SPR for CT distributions simulated around the calibration points of a standard HLUT. SPR were calculated with either one single line segment ("linear") or with two adjacent line segments of different slopes ("bend").

The systematic analysis of different slopes around the - virtual - calibration point of water is shown in Fig. 5.13. Due to the lower HLUT slope for bone tissues, the SPR of water is systematically underestimated by up to 0.27 %. The more the two adjacent slopes deviate, which applies for lower kV settings, the higher is the systematic error of the SPR prediction.

5.2 DECT as an alternative image modality

The first section analyzes the accuracy and precision of $\hat{\rho}_e$ and Z_{eff} measured in investigated materials. The second section evaluates the accuracy and precision of the DECT-based predicted SPR for these materials.

Table 5.1: SPR difference due to different slopes of the linear line segments at six calibration points (Fig. 4.2, Fig. 5.12). CT number distributions sampled around the calibration points were translated either with a single linear line segment or with two adjacent line segments of different slopes. .

calibration point	mean SPR	difference SPR prediction [%]
1	0.258	0.13
2	0.958	0.16
3	1.023	0.14
4	1.033	0.22
5	1.064	0.18
6	1.196	0.01

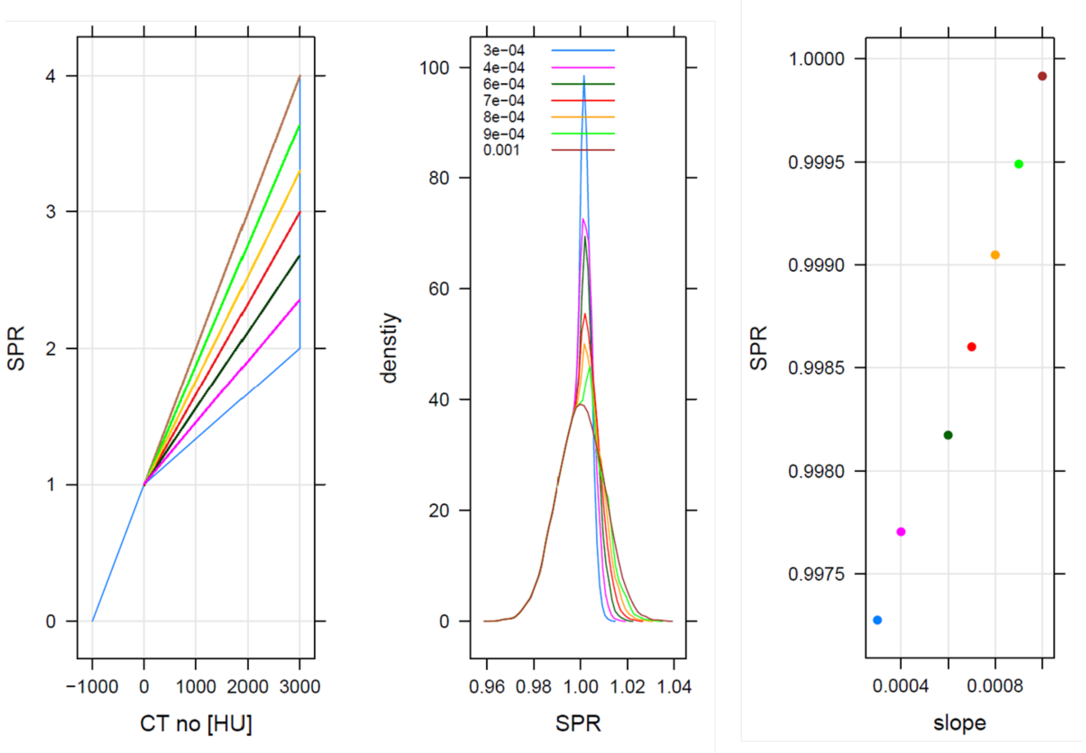

Figure 5.13: Systematic difference of SPR prediction due to different HLUT slopes. The left figure depicts the HLUT of different investigated slopes in the bone segment. Usually, the lower the slope the lower is the employed kV setting. The figure in the middle depicts resulting SPR distributions at the calibration point of water (0 HU/SPR=1). The more the slopes change the more asymmetric is the SPR distribution. The right figure depicts the mean SPR values as a function of the calibration slope in the bone region.

5.2.1 DECT-based measurement of $\hat{\rho}_e$ and Z_{eff}

Materials can have the same $\hat{\rho}_e$ but different Z_{eff} and vice versa as depicted in Fig. 5.14. Measured DECT contrasts are listed in Tab. A.4 for all investigated materials. Since the Gammex tissue surrogates are the only materials with defined properties provided by the manufacturer, the following paragraphs summarizes the results for these surrogates only.

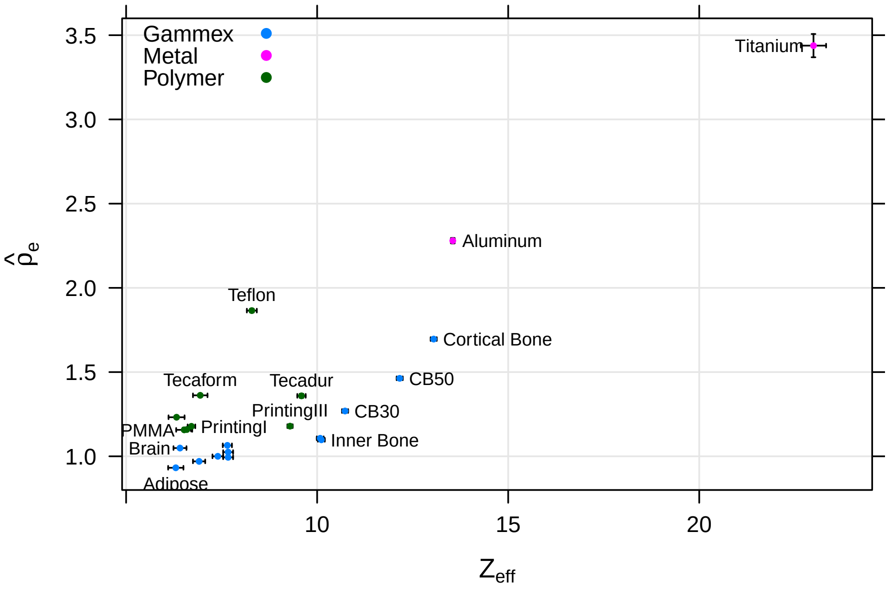

Figure 5.14: DECT-based measurements of $\hat{\rho}_e$ and Z_{eff} for all investigated materials scanned at 80/140Sn kV with corresponding standard deviations (1σ). Lung is not shown as Z_{eff} could not be determined by the algorithm (Sec. 3.5).

For the tissue surrogates, measured $\hat{\rho}_e$ was found to agree with reference values within (0.4 ± 0.3)% for both employed voltage pairs (mean difference ± one standard deviation). Residuals of $\hat{\rho}_e$ remain below 1 % for all surrogates (Fig. 5.15).

Residual differences of measured Z_{eff} compared to the manufacturer data were found to be higher: (1.7 ± 1.4)% at 80/140Sn kV and (2.0 ± 1.5)% for the 100/140Sn kV acquisition. The brain surrogates registers an unusual high Z_{eff} residual of 5 % (Fig. 5.15). Z_{eff} could not be calculated for material of low $\hat{\rho}_e$ which applies for the lung tissue surrogate (cf. Eq. 3.16). Systematic tendencies of $\hat{\rho}_e$ and Z_{eff} residuals towards higher $\hat{\rho}_e$ could not be observed. Absolute and relative residuals of $\hat{\rho}_e$ and Z_{eff} are summarized for the investigated materials in Tab. A.5.

Standard deviations of 6-12 HU in the CT number translate to an absolute standard deviation in $\hat{\rho}_e$ of 0.004-0.009 for the homogeneous tissue surrogates. Z_{eff} was found to be much noisier: absolute standard deviations of 0.07-0.2 were measured. Relative standard deviations of the DECT contrasts are depicted in Fig. 5.16. Standard deviations of Z_{eff} decrease from 3 % to 0.5 % towards higher $\hat{\rho}_e$, while standard deviations of μ/μ_{H_2O} and $\hat{\rho}_e$

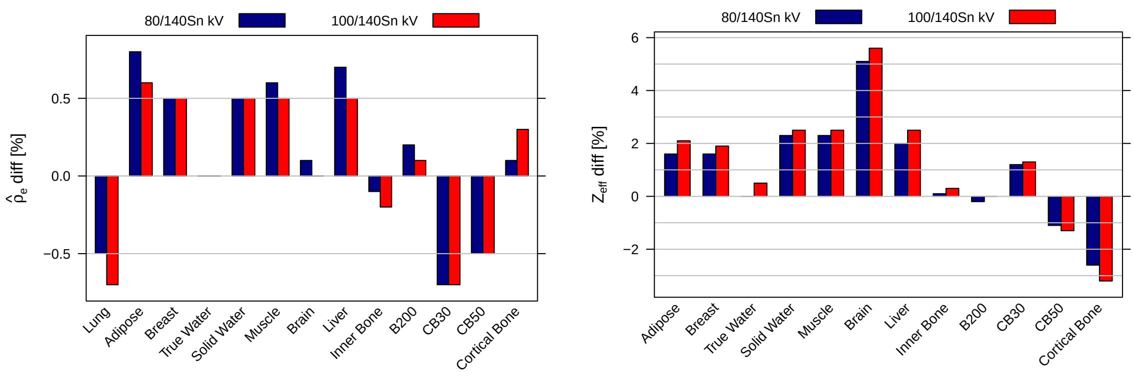

Figure 5.15: Residual differences of mean measured $\hat{\rho}_e$ (left) and Z_{eff} (right) for investigated homogeneous tissue surrogates compared to manufacturer data. Reference values of $\hat{\rho}_e$ were provided batch specific by the manufacturer while Z_{eff} had to be calculated from non-batch specific, approximate material composition. Figures adapted from Hünemohr et al. [2014a].

remain constant (Fig. 5.16). The lung surrogate is a porous, therewith an inhomogeneous material that registers a significant higher standard deviation in all contrasts.

5.2.2 DECT-based SPR prediction

Correlation of Z_{eff} to the I-value The logarithm of the I-value was linearly parametrized through Z_{eff} for soft ($Z_{\text{eff}} \leq 8.5$) and bone ($Z_{\text{eff}} > 8.5$) tissue by (Fig. 5.17)

$$\begin{aligned} a = 0.125,\ b = 3.379 \text{ for tissues with } Z_{\text{eff}} \leq 8.5 \\ a = 0.098,\ b = 3.376 \text{ for tissues with } Z_{\text{eff}} > 8.5. \end{aligned} \tag{5.1}$$

Elements of high atomic numbers (phosphorus Z=15, calcium Z=20) present in bones strongly influence the Z_{eff}. This rapid increase in Z_{eff} necessitates the separation of the bone fit from the soft tissue fit. The gap between both regions (Z_{eff}=[8.5-10]) does not involve any tissues as soft tissues do not contain a significant amount of high Z elements but only hydrogen, nitrogen, oxygen and carbon (Z=[1,6,7,8]).

I-value residuals of up to 6 eV (9 %) compared to the manufacturer reference data were observed (Fig. 5.18). Mean I-value differences can be summarized to $(3.9 \pm 3.0)\%$ for the 80/140Sn kV image acquisition of the surrogates. Absolute and relative I-values residuals are summarized in detail for all investigates materials in Tab. A.5.

DECT-based SPR prediction with Z_{eff} and $\hat{\rho}_e$ The SPR image was calculated with the $\hat{\rho}_e$ and I-value image according to Eq. 3.19 and Eq. 5.1. For pixels of low $\hat{\rho}_e$ (lung surrogate and air pixels), the Z_{eff} could not be calculated and the SPR was directly

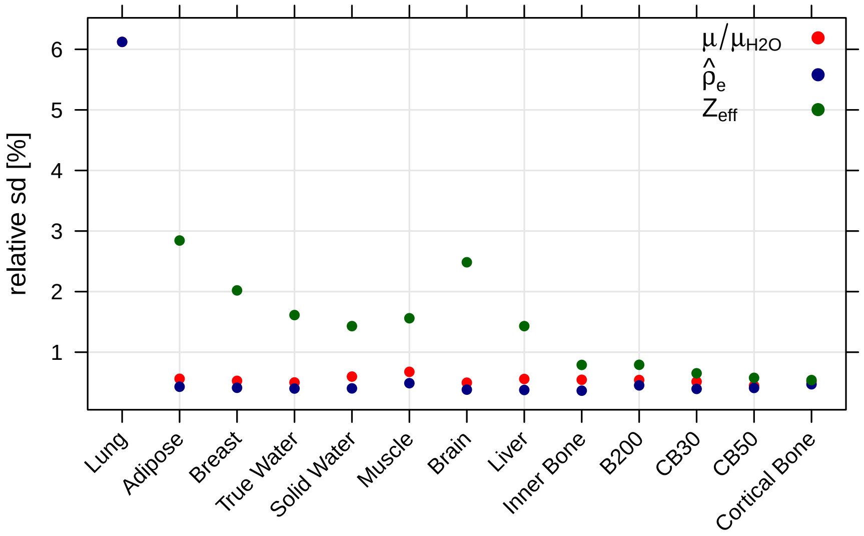

Figure 5.16: Measured uncertainties relative to mean values for the relative photon attenuation $\frac{\mu}{\mu_{\mathrm{H2O}}}$ at 100 kV, $\hat{\rho}_e$ and Z_{eff} for tissue surrogates. Z_{eff} could not be determined for lung material.

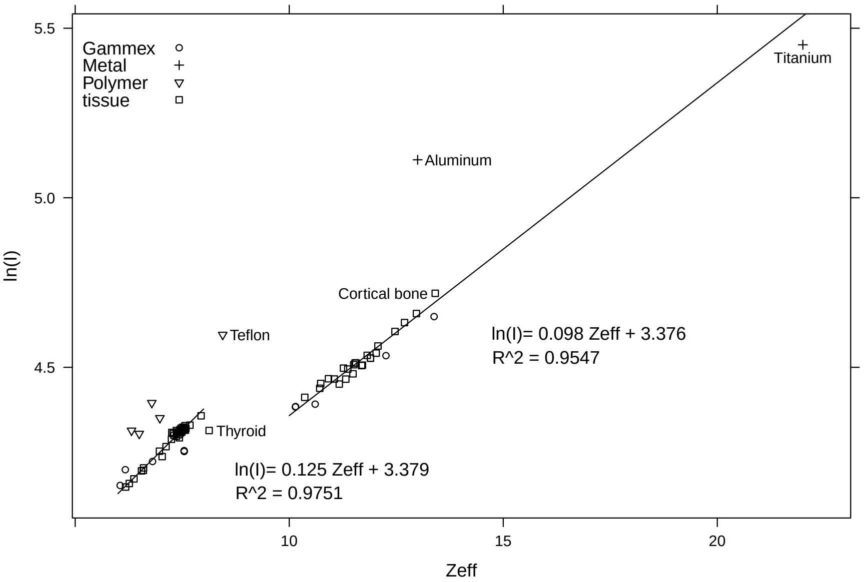

Figure 5.17: Linear parametrization of $\ln I$ as a function of Z_{eff} for soft and bone tissues taken from Schneider et al. [2000]. Thyroid was excluded for the soft tissue fit. Additional to tabulated tissues investigated in this thesis, reference data of tissue surrogates (Gammex), polymers (except printing materials), and both metals is shown. Figure reprinted from Hünemohr et al. [2014a].

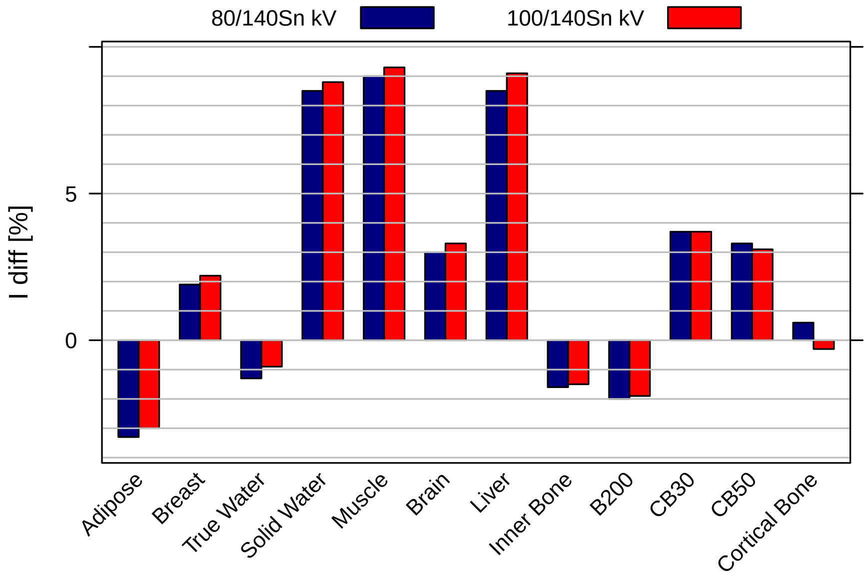

Figure 5.18: Measured residual differences of the I-value derived from Z_{eff} images for investigated homogeneous tissue surrogates compared to reference data. The reference I-value had to be calculated from non-batch specific, approximate material composition provided by the manufacturer (Tab. 3.1). Figure adapted from Hünemohr et al. [2014a].

assigned to the measured $\hat{\rho}_e$ of these pixels. The DECT-predicted SPR deviates from measured WEPL for the tissue surrogates by $(0.6 \pm 0.3)\%$ at the 80/140Sn kV acquisition. For polymers, the DECT-predicted SPR deviates by $(1.6 \pm 1.2)\%$ from the measured WEPL. For both metals, WEPL differences of around 2-10 % are observed for DECT-based prediction compared to measured values. SPR residuals for all measured materials are depicted in Fig. 5.19.

While the DECT-predicted $\hat{\rho}_e$ and SPR agrees for the tissue surrogates and polymers within 0.6 % and 1.6 % with reference values, larger residuals are observed for predicted Z_{eff} and I-values. Particularly DECT measured contrasts for metals are affected by larger residuals in the order of 3-8 % for $\hat{\rho}_e$ and up to 33 % for the I-value prediction compared to reference values (Tab. A.5, cf. metals in Fig. 5.17). A systematic superiority of one spectra combination was not observed and differences of both voltage pairs are marginal Solely the Z_{eff} was found to be more accurate (0.3 percentage points, pp) with the 80/140Sn kV acquisition compared to the 100/140Sn kV scan. Mean differences of DECT contrasts and derived quantities are summarized for the three investigated material groups in Tab. 5.2. Absolute and relative SPR residuals are summarized for all measured materials in Tab. A.5.

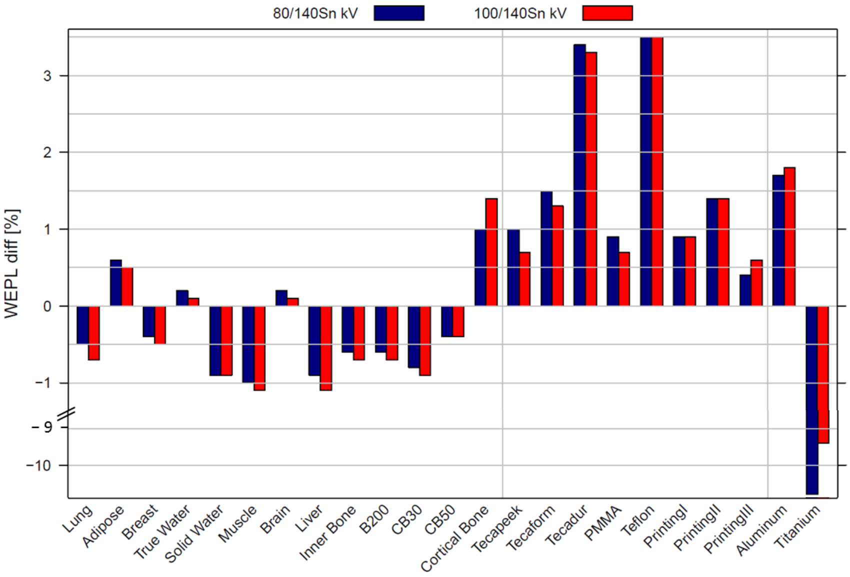

Figure 5.19: Residuals between SPR predicted from DECT data and WEPL measurements for all investigated materials. Figure adapted from Hünemohr et al. [2014a].

Table 5.2: Mean differences (± one standard deviation) between DECT based $\hat{\rho}_e$, Z_{eff}, I-value and SPR prediction and reference data for the three measured material groups (Tab. 3.1). Z_{eff} reference values for Gammex tissue surrogates are approximated from non batch specific manufacturer data. For polymers, all reference values were estimations that could provoke larger residuals. Both metals were supposed to be pure. Materials of which some quantities could not be estimated (such as elemental compositions of printing materials) or could not be measured with DECT (such as the Z_{eff} of lung rod Tab. A.4) were excluded for the evaluation.

Voltage pair [kV]	Class	$\hat{\rho}_e$ diff [%]	Z_{eff} diff [%]	I-value diff [%]	WEPL diff [%]
80/140Sn	Gammex	0.4±0.3	1.7±1.4	3.9±3.0	0.6±0.3
100/140Sn	Gammex	0.4±0.2	2.0±1.5	3.9±3.3	0.7±0.4
80/140Sn	Polymer	0.5±0.2	8.8±18.0	11.7±3.6	1.6±1.2
100/140Sn	Polymer	0.4±0.3	9.0±18.2	11.2±3.7	1.6±1.2
80/140Sn	Metal	5.6±4.1	4.4±0.2	26.7±9.5	6.3±6.4
100/140Sn	Metal	4.8±3.2	4.9±0.1	27.2±8.1	5.6±5.4

5.3 Comparison of DECT- and SECT-based SPR prediction in a patient

First, tissue regions in which the SPR prediction differs from SECT to DECT were identified and systematically evaluated in the patient images. Thereafter, hypothetical target volumes were positioned adjacent to the identified critical regions and a treatment planning study with carbon ions quantified the resulting range uncertainties.

5.3.1 SPR images

Ventricle region Fig. 5.20 shows a systematic difference between the SECT- and DECT-based SPR predictions in the ventricle region. Mean measured values of all CT contrasts and predicted SPR are listed in Tab. A.6 for contoured tissues regions (Sec. 4.3.3). Corresponding line plots in Fig. 5.21 show that DECT differentiates the ventricle region and predicts a 2.3 % smaller SPR as compared to the SECT (100 kV D30, Tab. A.6).

Difference between the D30 and D34 reconstruction are observable at the transition from brain tissue to cortical bone in Fig. 5.21(c). The D34 kernel is responsible for an edge enhancement and precise definition of large attenuation gradients. Slightly higher predicted SPR for cortical bone can be observed for the D34 reconstruction kernel compared to the D30 kernel (Fig. 5.21(c)). No SPR difference between both kernels is observed in soft tissue and ventricles at the center of the head. Fig. 5.21(b) suggests that a higher SECT tube voltage (140Sn kV) differentiates the ventricle better as compared to 100 kV (Tab. A.6). An exact differentiation comparable to the DECT method is, however, not achieved with SECT at 140Sn kV (SPR still differs by 1.7 % from the DECT predicted value).

Temporal bone region Dense bone tissue is the second tissue region that shows systematic differences between the SECT- and DECT-based SPR predictions. Difference for the cortical bone SPR prediction are observable in Fig. 5.20 but are particularly evident in the petrous part of the temporal bone and in the mastoid cavity depicted Fig. 5.22. For the petrous part of the temporal bone ("cortical bone" contour in Tab. A.6, Sec. 4.3.3), the DECT predicts a 5-8 % larger SPR compared to the SECT prediction (140Sn kV or 100 kV).

The systematic SPR difference in the dense bone is directly related to the DECT information and the $\hat{\rho}_\mathrm{e}$ measured with DECT (Fig. 5.22 last panel). Reconstruction kernel and tube voltage have only a small influence on SPR prediction in the dense bone (Fig. 5.23). The petrous part of the temporal bone exhibits one of the highest CT attenuation (around 1610 HU at 120 kV). Again, the SPR predicted with SECT at 140Sn kV is closer to the DECT SPR prediction as compared to the 100 kV SECT prediction. In general, the DECT and SECT at 140Sn kV predict higher SPR in dense tissue tissues and slightly lower SPR in some of the soft tissues as compared to the SECT at 100 kV.

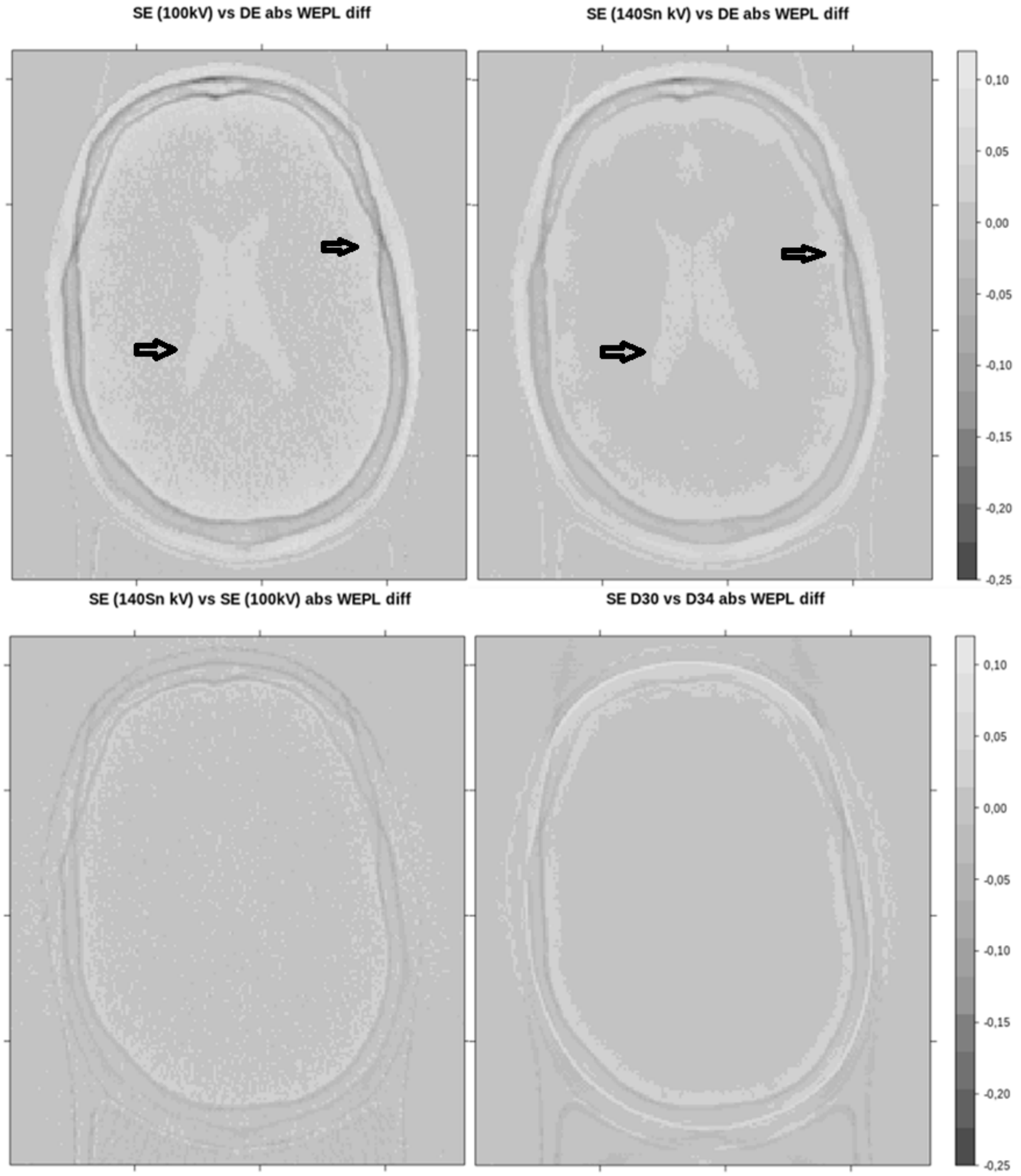

SE (100kV) vs DE abs WEPL diff

SE (140Sn kV) vs DE abs WEPL diff

SE (140Sn kV) vs SE (100kV) abs WEPL diff

SE D30 vs D34 abs WEPL diff

Figure 5.20: Absolute differences of WEPL predicted from SECT ("SE") and DECT ("DE"). The 100 kV images of the DECT acquisition served as a surrogate for the SECT. Influence of reconstruction kernels (SECT with D34 vs. D30) and tube voltage influence (SECT at 100kV vs. 140Sn kV) are considered separately to isolate the individual factors and ensure to extract the value of the DECT information. A systematic difference of SECT compared to DECT can be observed for the ventricle region. Differences at large attenuation gradients are observable in all difference images.

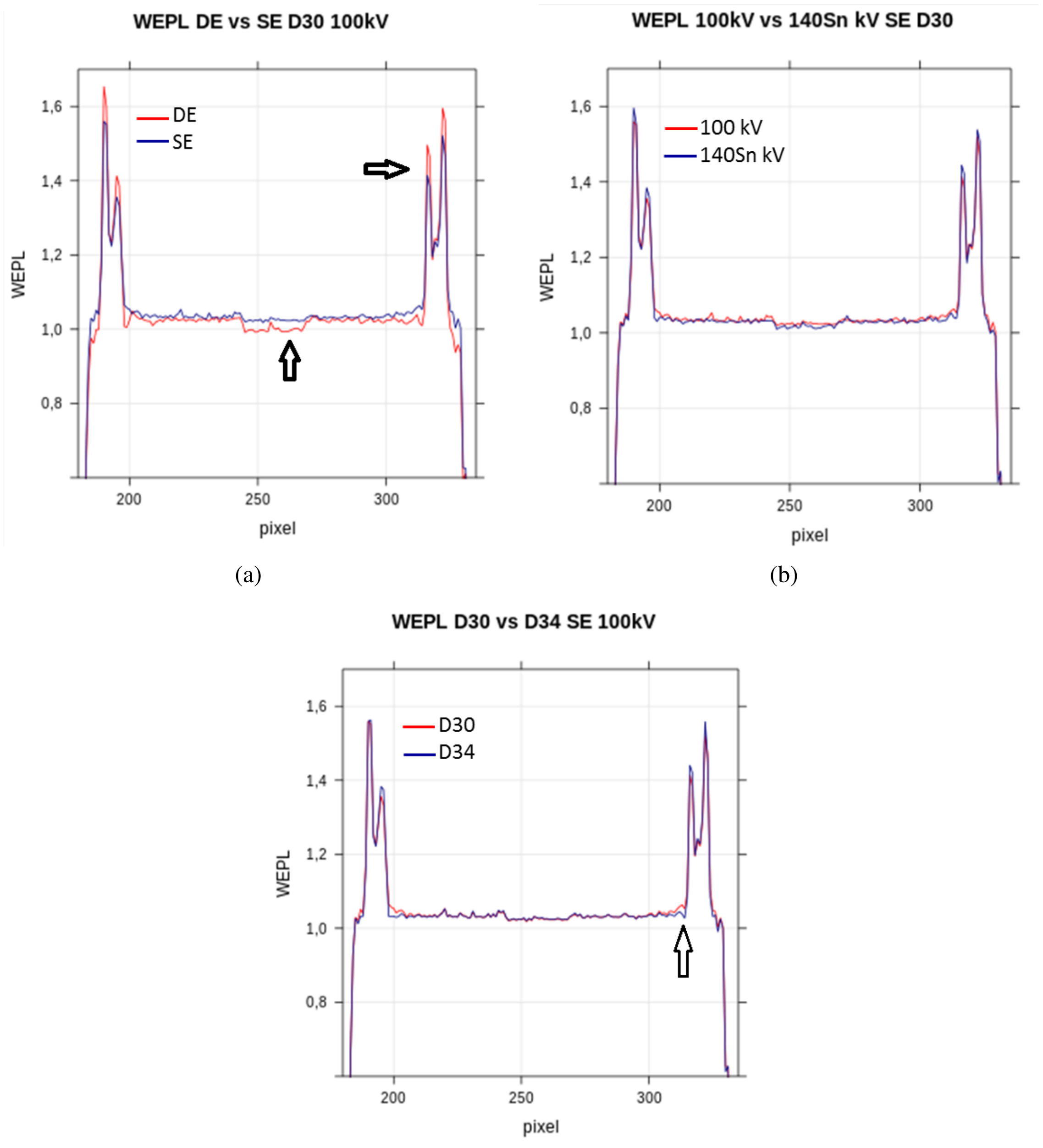

(a) (b)

(c)

Figure 5.21: Corresponding line plots of predicted SPR from Fig. 5.20 through the ventricular system (around pixel 250). SPR predictions are shown separately for (a) DECT in comparison to SECT, (b) SECT tube voltages and (c) reconstruction kernels. A systematic difference of SECT compared to DECT can be observed for the ventricle region and cortical bone (a). A higher tube voltage (140Sn kV) for SECT can resolve the ventricular system better (b). A better edge definition is observed for the D34 kernel in comparison to the D30 kernel.

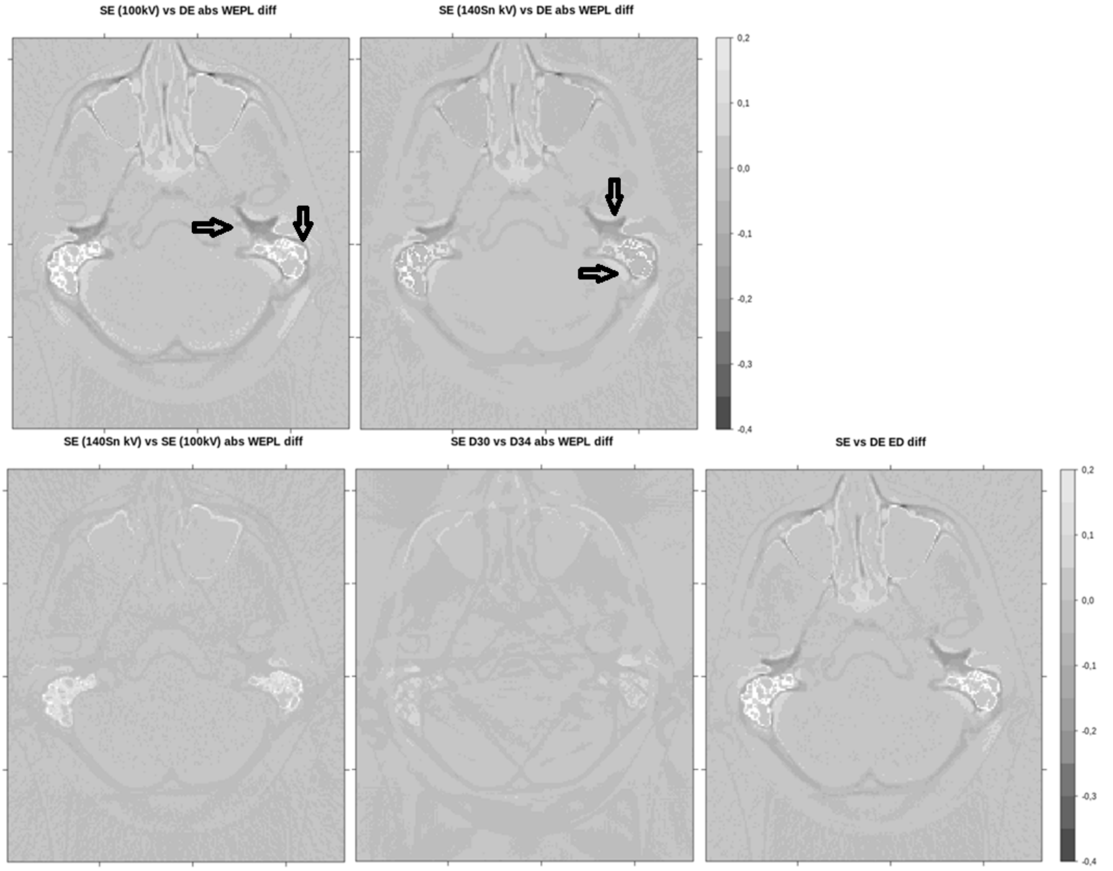

Figure 5.22: Absolute differences of WEPL predicted from SECT ("SE") and DECT ("DE") for different voltages and kernels. A systematic WEPL difference can be observed for the dense temporal bone and mastoid cavity. This difference in WEPL is directly related to the difference in $\hat{\rho}_e$ prediction from SECT and DECT (last panel). The SECT-based $\hat{\rho}_e$ prediction at 100 kV was derived with a stoichiometric calibration that converts CT numbers to $\hat{\rho}_e$ usually employed in photon therapy.

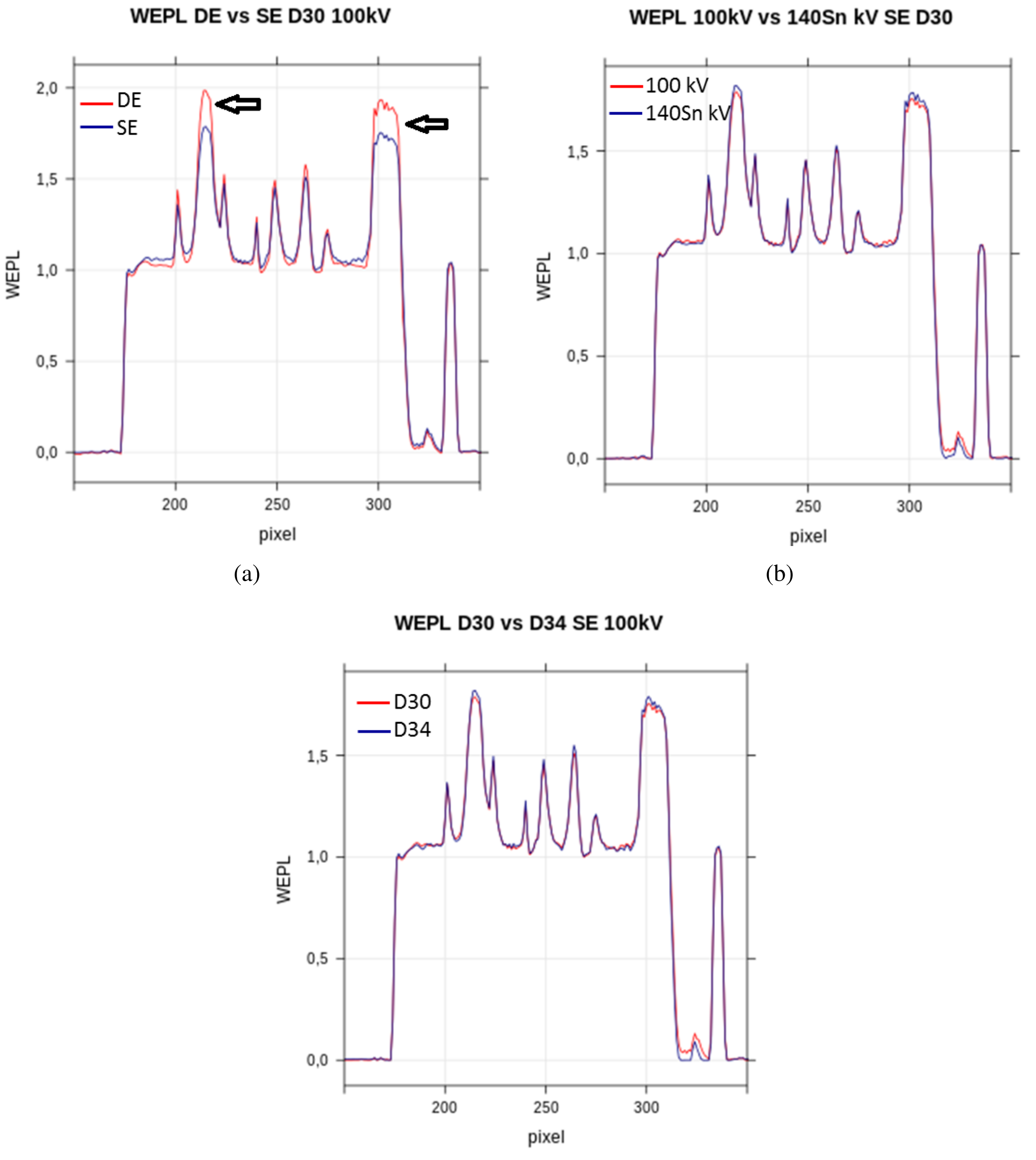

(a)

(b)

(c)

Figure 5.23: Corresponding line plots of predicted SPR from Fig. 5.22 through the petrous part of the temporal bone. SPR predictions are shown separately for (a) DECT in comparison to SECT, (b) SECT tube voltages and (c) reconstruction kernels.

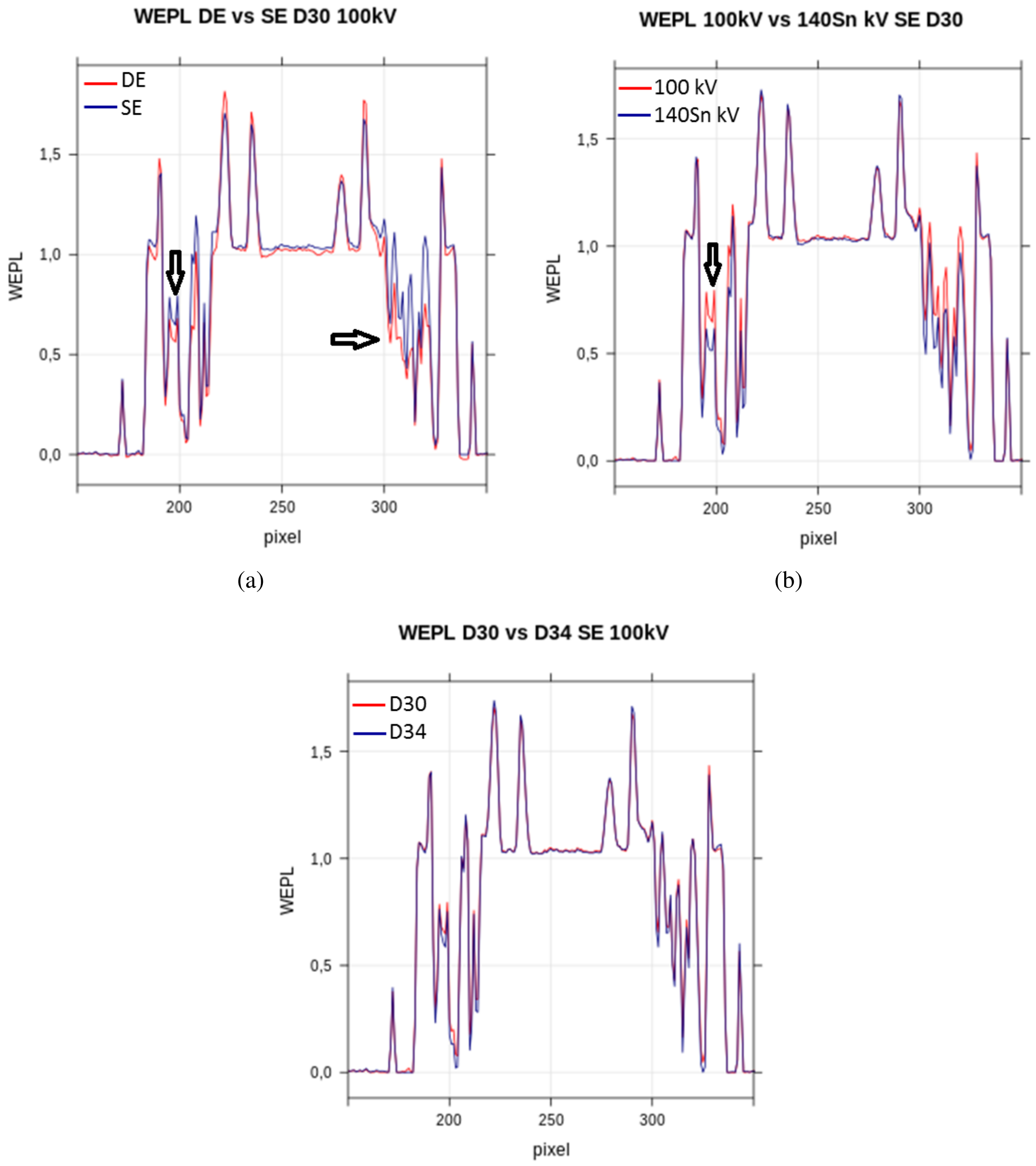

(a) (b)

(c)

Figure 5.24: Corresponding line plots of predicted SPR through the mastoid cavity (Fig. 5.22). SPR predictions are shown separately for DECT in comparison to SECT (a), (b) SECT tube voltages and (c) reconstruction kernels.

Mastoid region The mastoid region is the third anatomical structure that shows systematic SPR differences from DECT to SECT (Fig. 5.22). Large differences are observed for pixels that contain mixtures of high dense bone and air (SPR around 0.6). The DECT predicts a lower SPR than the SECT for these mixtures. Again, the 140Sn kV SECT SPR prediction is closer to the DECT prediction than the 100 kV SECT SPR image. Edges of large attenuation gradients are defined better with the D34 kernel as compared to the D30 kernel (Fig. 5.24).

5.3.2 SECT- and DECT-based treatment plan comparison

Ventricle region Fig. 5.25 shows resultant dose distributions of the hypothetical treatment plans in the ventricle region. At the distal target edge range differences in the order of 2 mm are observed between the DECT- and SECT-based (100 kV) plan. This range difference is slightly smaller for the 140Sn kV SECT-based plan irradiated on the 100 kV SPR map. The reconstruction kernel has almost no influence on the dose distribution except for small differences in the lateral dose fall off. The mean dose in the target volume differs by 1.1 pp between SECT- and DECT-based plans. The percentage of tissue that receives less than 90 % of the prescribed dose deviates by 2.6 pp (Fig. 5.26). These differences can be also observed in the corresponding DVHs (Fig. 5.25).

Temporal bone region Dose results for the second hypothetical treatment plan in the temporal bone region are shown in Fig. 5.27. Since the DECT predicts a much larger SPR for dense bones, the DECT machine file "overshoots" and maximal range differences of approximately 4 mm are observed for the DECT-based plan forward irradiated on the SECT SPR map (100 kV, D30). Range differences are particularly large for ray traces passing the petrous part of the temporal bone. Mean physical dose values deviate by 0.8 pp in the target volume (Fig. 5.28) which can be also observed in the DVH (Fig. 5.27). The amount of tissue that receives less than 90 % of the prescribed dose deviates also by 0.8 pp.

5.3.3 Tissue composition and photon HLUT verification

For the first time DECT data (CT number, $\hat{\rho}_e$, Z_{eff}, SPR) were evaluated for eight different tissue regions in a head and neck patient. Measured mean values and standard deviations are listed in Tab. A.6. A typical standard deviation in the CT number of 6-19 HU (soft tissue) translates to a standard deviation in $\hat{\rho}_e$ of 0.005-0.03 while the standard deviation in Z_{eff} is 0.1-0.4. For the inhomogeneous lung tissue and tissues largely affected by beam hardening (bone), standard deviations are much larger ($\hat{\rho}_e$: 0.05, Z_{eff}: 0.4). In the delineated mastoid region the mean negative CT number at around -330 HU for 140Sn kV exhibits a large standard deviation of 350 HU ($\hat{\rho}_e$ varies by 0.6±1.3 and Z_{eff} by 6.4±6.1 since air pixels in the VOI cannot be excluded in DIPP). These large standard deviations

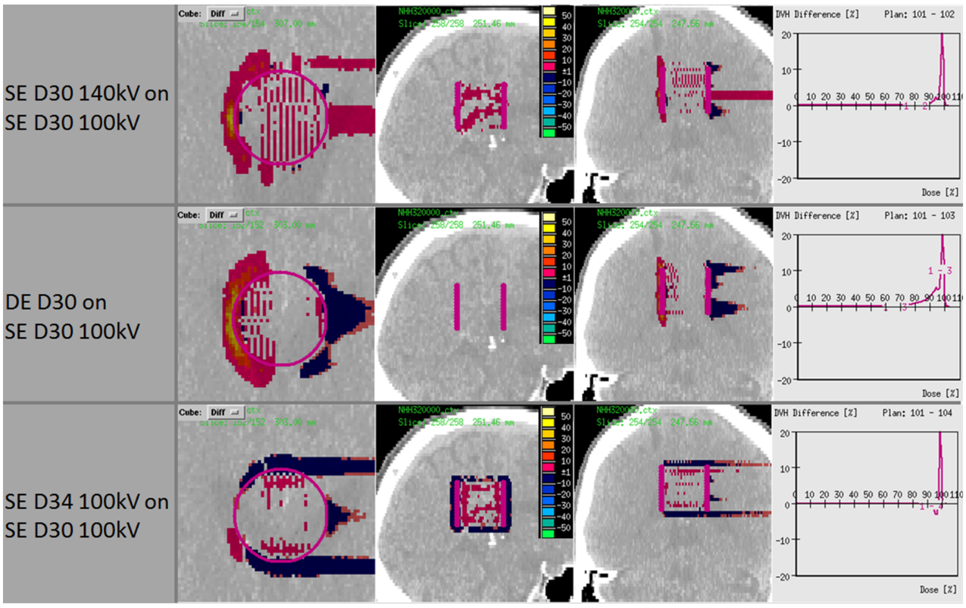

Figure 5.25: Dose results for the hypothetical treatment plan close to the ventricular system (Fig. 4.4(a)). Dose differences are shown in the traversal, sagittal and frontal image plane (left to right) as well as in the DVH. The SECT ("SE") 140Sn kV, the DECT ("DE") and the SECT 100 kV D34 machine files (top to bottom) were forward calculated on the ground truth SPR image (SECT 100 kV, D30).

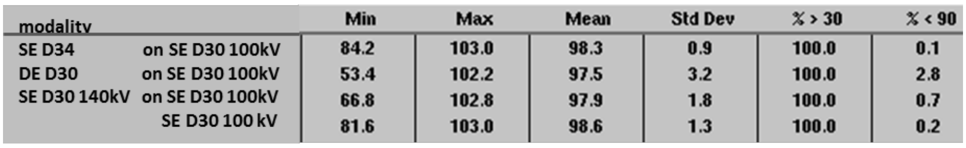

modality		Min	Max	Mean	Std Dev	% > 30	% < 90
SE D34	on SE D30 100kV	84.2	103.0	98.3	0.9	100.0	0.1
DE D30	on SE D30 100kV	53.4	102.2	97.5	3.2	100.0	2.8
SE D30 140kV	on SE D30 100kV	66.8	102.8	97.9	1.8	100.0	0.7
	SE D30 100 kV	81.6	103.0	98.6	1.3	100.0	0.2

Figure 5.26: Correspondent dose statistics for different treatment plans forward irradiated on the ground truth SPR image (SECT 100 kV, Fig. 5.25).

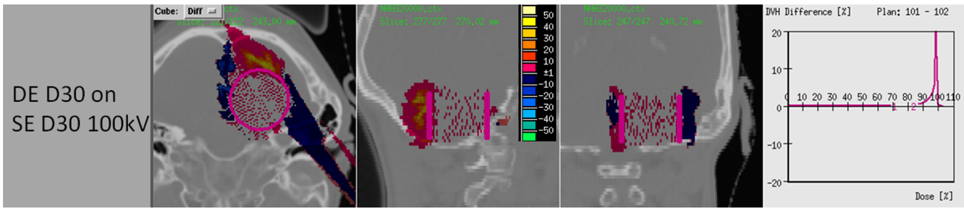

Figure 5.27: Dose results for the hypothetical plan in temporal bone region (Fig. 4.4(b)). Dose differences are sown in the transversal, sagittal and frontal image plane (left to right) as well as in the DVH. The DECT D30 was forward calculated on the ground truth SPR image (SECT 100 kV).

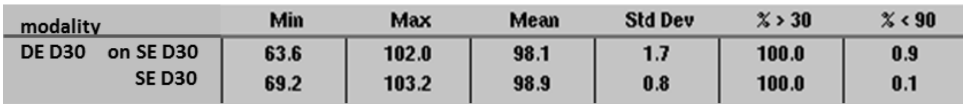

modality	Min	Max	Mean	Std Dev	% > 30	% < 90
DE D30 on SE D30	63.6	102.0	98.1	1.7	100.0	0.9
SE D30	69.2	103.2	98.9	0.8	100.0	0.1

Figure 5.28: Correspondent dose statistics for the DECT-based treatment plan forward irradiated on the ground truth SPR image (100 kV, Fig. 5.27).

reflect the inhomogeneous bony structures with air cavities in the temporal bone. Due to the bony structures, mean CT numbers of the mastoid region show a strong dependency on the tube voltage. In contrast, inhomogeneous lung tissue, denoting a mixture of water and air, shows no dependency on tube voltage (maximum spectral CT number difference 17 HU, 140Sn kV - 100 kV).

Fig. 5.29 shows measured $\hat{\rho}_e$ as a function of CT number at 100 kV (D30) for pixels of five exemplary CT slices of the head patient. The stoichiometric HLUT for photons and the measured mean values of the contoured tissues are superimposed. One can clearly observe a systematic difference between $\hat{\rho}_e$ predicted with the HLUT and measured with DECT. This applies particularly in the dense bone region. Being the densest bone in humans, the contoured petrous part of the temporal bone is not well represented by the HLUT.

Fig. 5.30 and Fig. 5.31 show the measured $\hat{\rho}_e$ vs. Z_{eff} and CT number vs. Z_{eff} of the patient superimposed with predictions for the tabulated tissue compositions. Fig. 5.30 shows a significant discrepancy between measured DECT $\hat{\rho}_e/Z_{\mathrm{eff}}$ and theoretical values of tabulated tissue composition in the dense bone region. Z_{eff} and CT numbers of tabulated tissue compositions predicted with a stoichiometric SECT HLUT agree well in soft tissue region with measured pixel values. In the bone region, residual differences are again significant.

5.3.4 Noise quantification of SPR prediction

Fig. 5.32 depicts the noise levels of SECT and DECT contrasts measured in two tissue surrogates at the same CTDI dose level. The dose of the 120 kV SECT scan was split to both tubes for the DECT scan. Consequently, noise levels of the relative photon attenuation coefficient are elevated for the DECT acquisitions (100 kV, 140Sn kV) by roughly 0.1 pp for cortical bone and 0.2 pp for muscle compared to the SECT 120 kV noise level. The Z_{eff} noise levels is particularly elevated (1 pp) as compared to the noise levels in $\hat{\rho}_e$ and photon attenuation. Noise levels in the cortical bone surrogate agree for all contrasts within 0.2 pp.

The noise level of the DECT-based SPR prediction is higher (0.2-0.4 pp) as compared to the SECT-based prediction (Fig. 5.33). SPR noise levels for the 120 kV SECT acquisition are the same for muscle and cortical bone. Again, relative noise levels are generally increased for the muscle surrogate compared with the levels for the cortical bone surrogate for both single DECT voltages (as the dose was split) and as well for the DECT-based

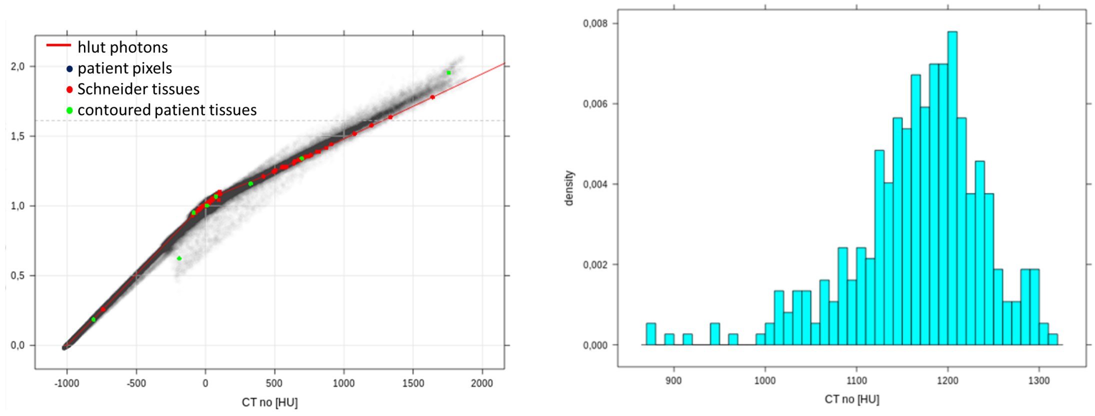

(a) (b)

Figure 5.29: (a) Comparison between DECT-based measurement of $\hat{\rho}_e$ and predictions with the photon therapy stoichiometric HLUT in a patient. The HLUT and corresponding predicted CT numbers for tabulated tissues (Sec. 3.2.3, Sec. 3.4.2) are superimposed on the CT number/$\hat{\rho}_e$ pairs measured with DECT (100 kV). Additionally mean values of contoured tissue regions in the patient are superimposed. (b) shows a histogram of the CT number distribution at $\hat{\rho}_e$ =1.6 in order to check the symmetry of the predicted CT number distribution.

SPR prediction. It has to be kept in mind, that the same image protocol was used as for the patient image acquisition. Tube currents were split equally to both tubes and the tube current was not increased for the lower kV spectrum.

5.4 Tissue decomposition for MC dose algorithms

5.4.1 Deriving ρ from $\hat{\rho}_e$

The linear fit of ρ as a function of $\hat{\rho}_e$ (Eq. 4.2) for tissues ranging from adipose to cortical bone resulted in fit parameters a =1.178 and b =-0.177 (R^2 =0.9999, Fig. 5.34). The maximum ρ residual of 0.008 g/cm^3 was observed for adipose tissue. For lung tissue, the linear fit in $\hat{\rho}_e$ (instead of using the CT number) reduces the ρ residual from 3.1 % (SECT) to 0.1 % with DECT compared to the reference data (Hünemohr et al. [2014c]). Mean ρ residuals for soft tissues could be improved from (0.5±0.6) % (SECT, Schneider et al. [2000]) to (0.2±0.2) % with the presented DECT fit (mean ± one standard deviation, Hünemohr et al. [2014c]). For bone tissues, ρ residuals could be reduced from (0.3±0.2) % (SECT) to (0.1±0.1) % (DECT) compared to reference data (Hünemohr et al. [2014c]).

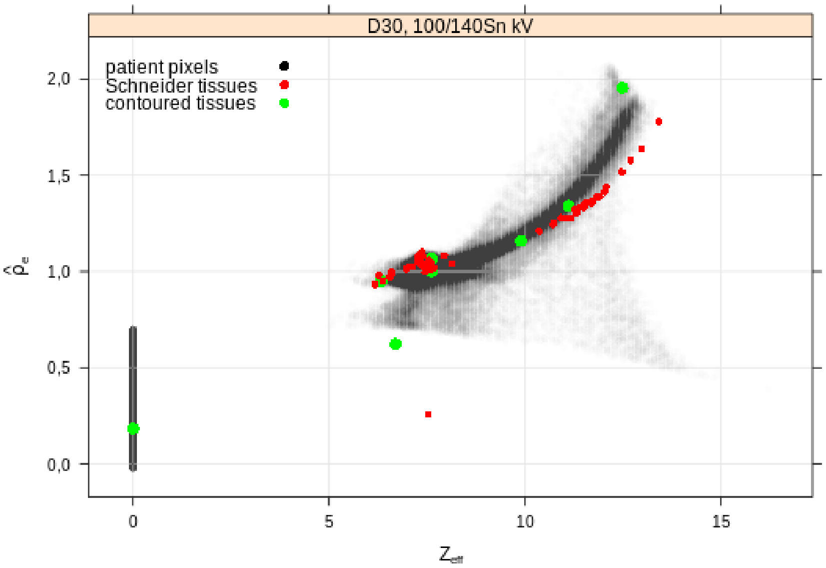

Figure 5.30: Measured pixel pairs ($\hat{\rho}_e$ and Z_{eff}) from five CT slices of the head patient. Superimposed are mean measured values for contoured tissue regions and quantities of the 71 tabulated tissue compositions (Schneider et al. [2000]). For low $\hat{\rho}_e$ ($\approx$0.0-0.7) the Z_{eff} could not be calculated and was set to zero.

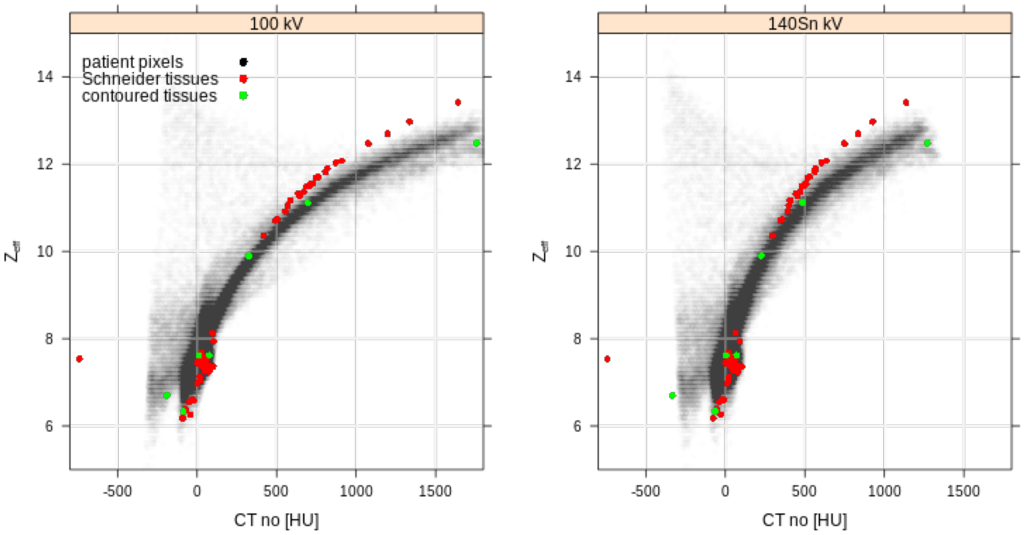

Figure 5.31: Measured pixel pairs (CT number and Z_{eff}) of the head patient superimposed on mean measured values for contoured VOIs and theoretical values calculated for the 71 tabulated tissue compositions and predicted with the specific stoichiometric calibration (Schneider et al. [2000]).

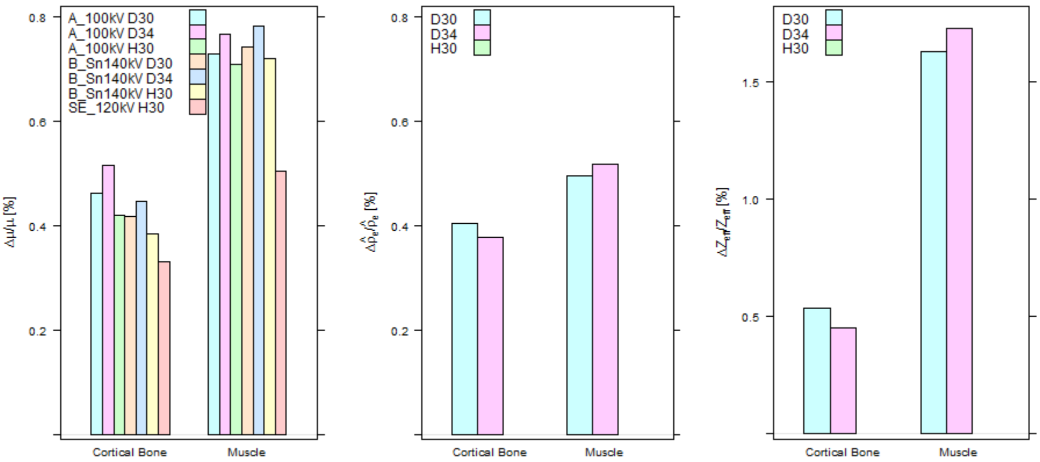

Figure 5.32: Noise levels of SECT and DECT data for two tissue surrogates measured at the same image dose level. The figure shows the relative noise level of the relative photon attenuation coefficient μ/μ_{H2O} measured for all three voltages (100/140Sn kV and the standard SECT voltage of 120 kV) as well as $\hat{\rho}_e$ and Z_{eff} calculated from DECT data.

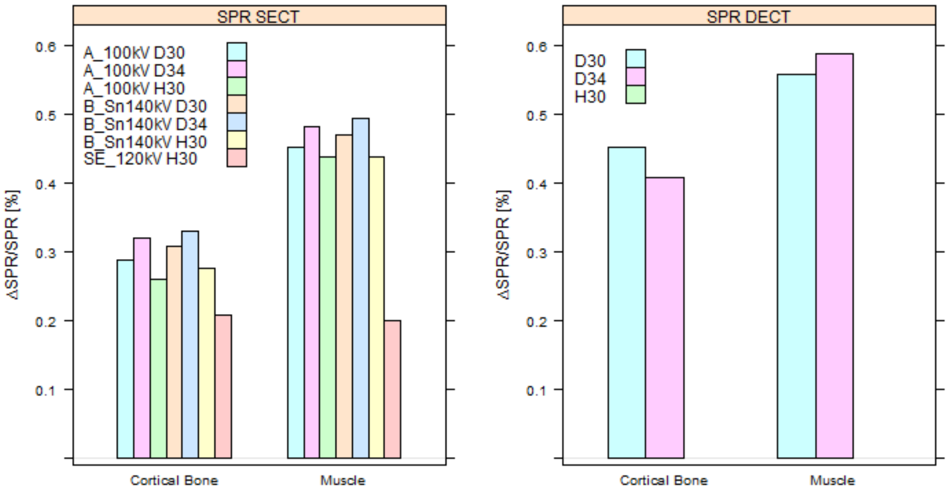

Figure 5.33: Noise levels of SECT- and DECT-based SPR predicted for two tissue surrogates measured at the same image dose level. SECT-based SPRs were predicted with dedicated stoichiometric HLUTs. DECT-based SPR prediction exploited $\hat{\rho}_e$ and Z_{eff} pair.

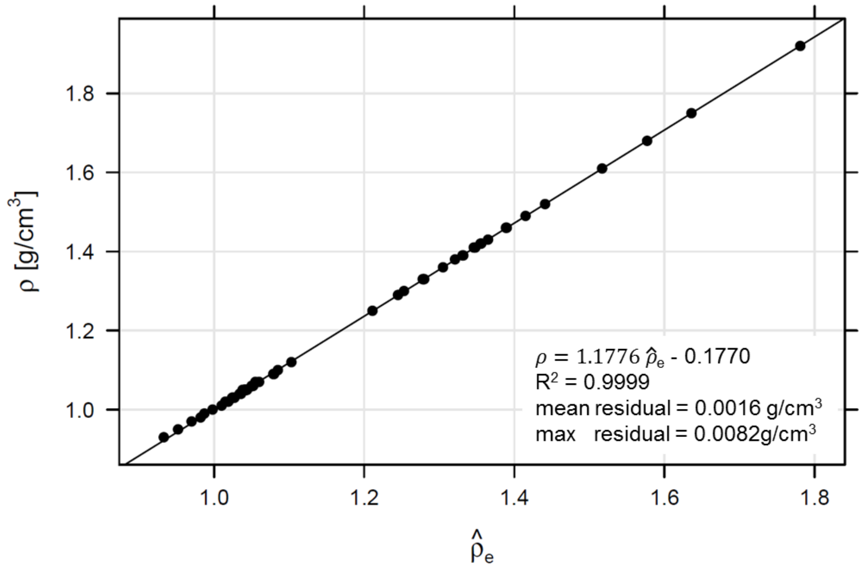

Figure 5.34: Linear correlation of ρ to $\hat{\rho}_\text{e}$ derived with 70 tabulated tissue compositions ranging from adipose to cortical bone (Schneider et al. [2000]). Figure adapted from Hünemohr et al. [2014c].

5.4.2 Tissue composition

Resulting parameters for the elemental linear fits in $\hat{\rho}_\text{e}$ and Z_eff are summarized in Tab. 5.3 with corresponding statistical evaluations. Mean residuals from predicted to reference elemental mass weights could be reduced by half with DECT compared to the standard SECT method for all elements in soft and bone tissue (except soft tissue hydrogen and nitrogen where the reduction was slightly smaller). Carbon and oxygen mass weights are most difficult to predict from a SECT CT number. For both elements, maximum residuals could be reduced with the novel DECT approach from 29 % (soft tissue carbon) and 31 % (soft tissue oxygen) to 10 % and 12 % respectively (Hünemohr et al. [2014c]). For bone tissues, maximum residuals in carbon and oxygen mass weights could be reduced from 4.3 % to 2.6 % with DECT. Predicted elemental mass weights are compared for SECT and DECT in Fig. 5.35 (soft tissues) and Fig. 5.36 (bone tissues).

The linear fits in $\hat{\rho}_\text{e}$ and Z_eff resulted in a negative mass weight prediction only for one tissue (adipose 3, nitrogen mass weight) which was set to 0 pp (Hünemohr et al. [2014c]). Normalization of predicted mass weights to 100 pp caused only minor changes (maximum deviation from 100 pp was 1 pp, Hünemohr et al. [2014c]).

With predicted elemental mass weights, the I-value, ρ and the SPR were accessible for every tissue. Residuals of the three tissue parameters predicted with DECT and SECT are depicted for the 71 tabulated tissues in Fig. 5.37. Using $\hat{\rho}_\text{e}$ directly instead of the detour via ρ and elemental compositions to calculate SPR is advantageous. Tab. 5.4 summarizes

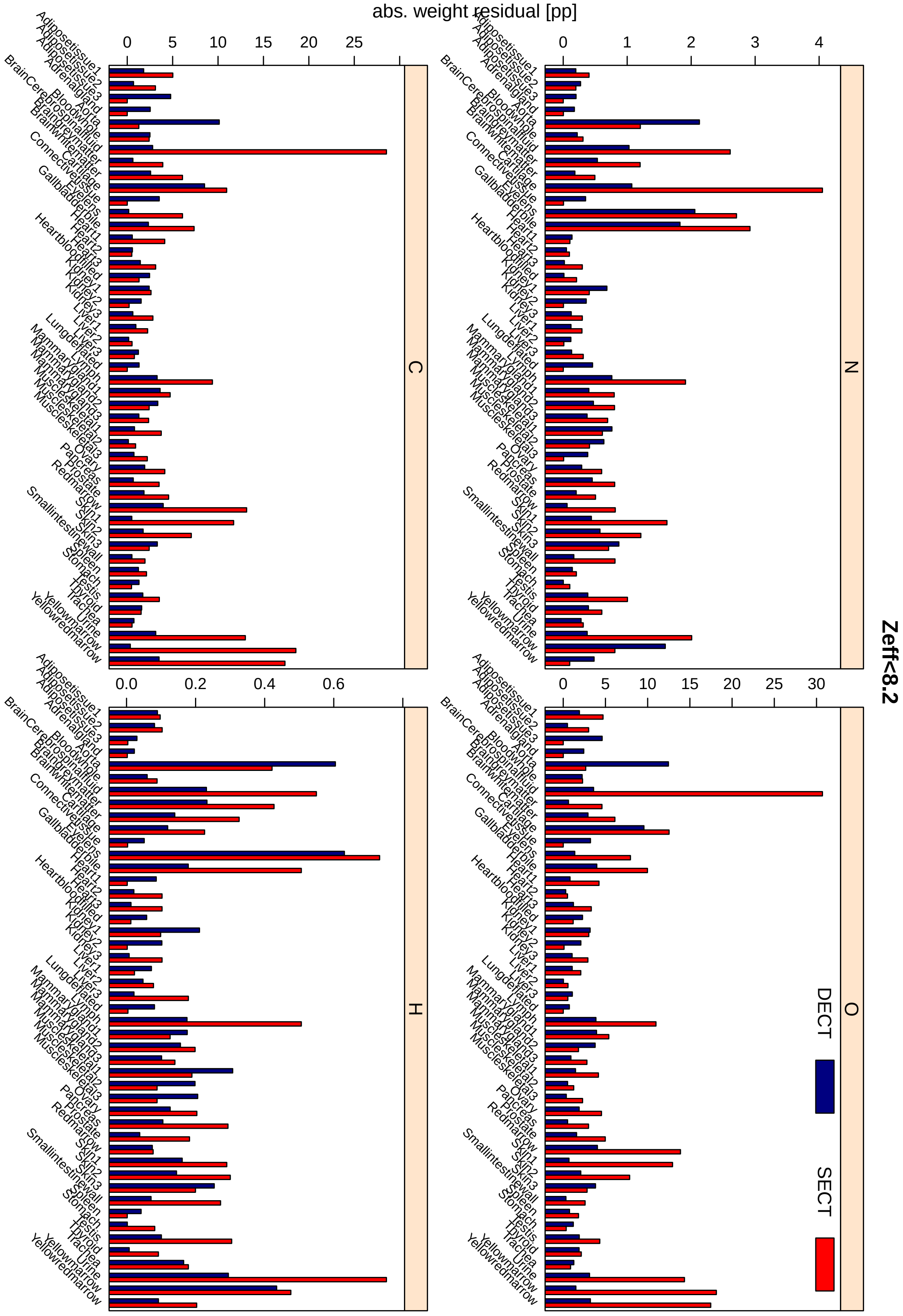

Figure 5.35: Absolute differences in percentage points for elemental mass weights predicted from SECT and DECT for soft tissues. Tissues having an unusual elemental composition benefit from the DECT information. Particularly the carbon and oxygen mass weight can be predicted more accurately with DECT.

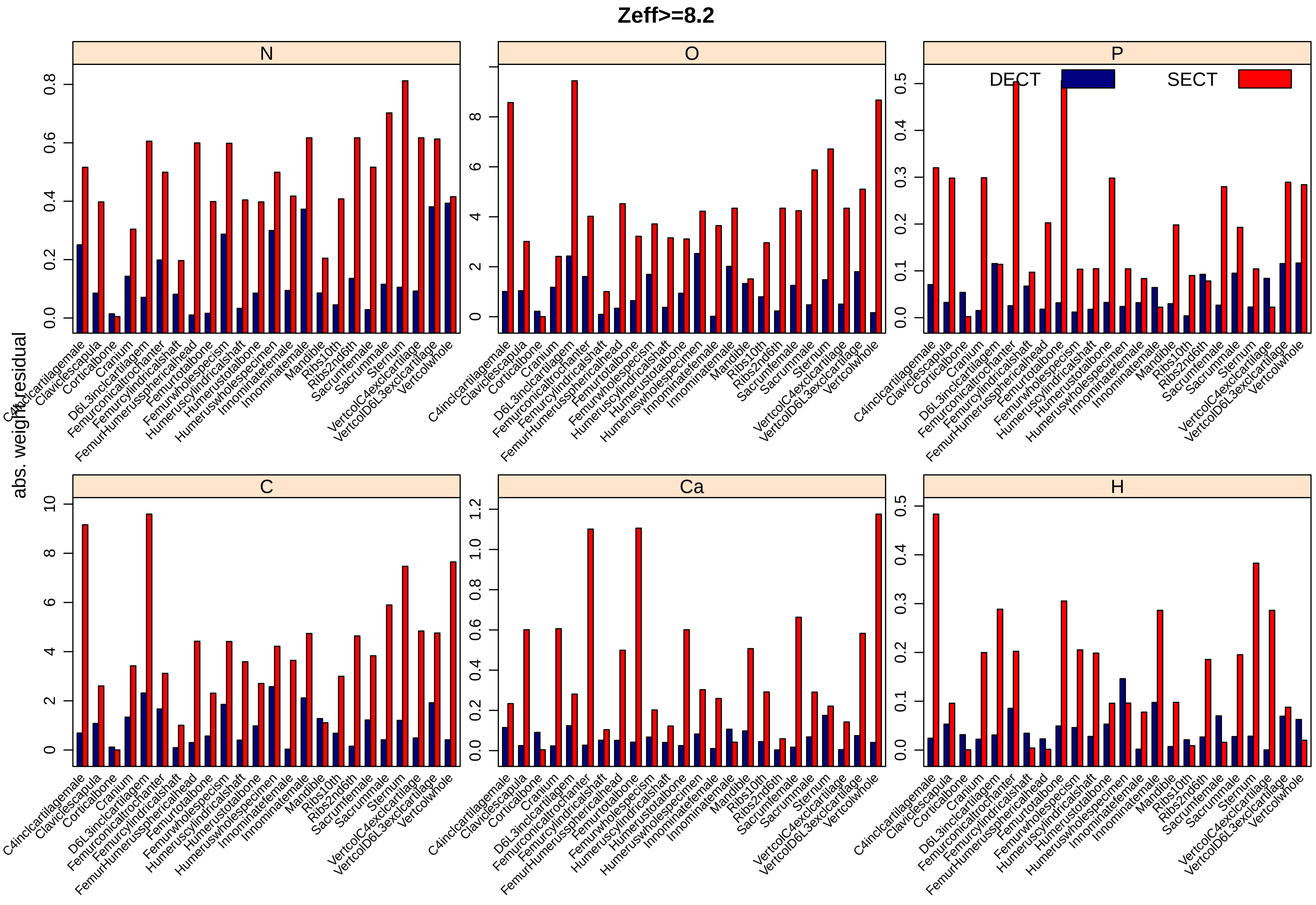

Figure 5.36: Absolute differences in percentage points for elemental mass weights predicted from SECT and DECT for bone tissues. Tissues having an unusual elemental composition benefit from the DECT information. Particularly the carbon and oxygen mass weight can be predicted more accurately with DECT.

]

Table 5.3: Statistical properties and fit parameter results of the DECT based elemental mass fraction fits (Eq. 4.3) for 47 soft tissues and 24 bone tissues (Schneider et al. [2000], only the six major elements were considered). Mean and maximum deviations to the ground truth are given for every element and are compared for SECT and DECT separately. Over-fitting is penalized by higher Bayesian information criterion values (BIC) while better fits (and sufficient model parameters) are represented by lower BIC values. Table reprinted from Hünemohr et al. [2014c].

		$Z_{\text{eff}} < 8.2$				$Z_{\text{eff}} \geq 8.2$					
		H	C	N	O	H	C	N	O	Ca	P
DECT	a_i	0.0838	-8.6159***	1.3823**	8.3296***	-0.2520***	-11.4336***	1.2322***	11.2376***	-0.6144***	-0.1698***
	b_i	0.0339	-1.7907***	0.1104	1.8154***	-0.0166***	-0.4299***	0.0459***	0.3902***	0.0049	0.0056**
	c_i	-0.0322	1.2969***	-0.1318	-1.3048***	0.0132***	0.6745***	-0.0734***	-0.6686***	0.0418***	0.0125***
	d_i	0.0153	12.3095***	-1.2167*	-11.2658***	0.3905***	10.1798***	-1.0138***	-8.8469***	0.2577***	0.0326
	R^2	0.8117	0.9706	0.6933	0.9621	0.9972	0.9478	0.8510	0.9114	0.9995	0.9982
	mean diff. (pp)	0.1	2.1	0.5	2.3	0.0	1.0	0.1	1.0	0.1	0.1
	max diff. (pp)	0.6	10.2	2.1	12.1	0.2	2.6	0.4	2.5	0.2	0.1
	BIC	-435	-183	-313	-172	-277	-127	-218	-127	-263	-271
SECT	mean diff. (pp)	0.1	4.8	0.8	5.2	0.2	4.3	0.5	4.3	0.4	0.2
	max diff. (pp)	0.8	28.5	4.1	30.7	0.5	9.6	0.8	9.4	1.2	0.5

$^{***}p < 0.01$, $^{**}p < 0.05$, $^{*}p < 0.1$

these tissue parameters predicted from the SECT- and DECT-based schemes for soft and bone tissue separately. The DECT-based tissue decomposition could improve the SPR, ρ and I-value prediction particularly for soft tissue (compared to predictions for bone tissue).

Table 5.4: Mean, maximum and standard deviations of SECT- and DECT-based predicted SPR, mass density and I-value compared to reference data (Schneider et al. [2000]). Caption and table reprinted from Hünemohr et al. [2014c].

(mean±sd), max differences to reference data [%]	CT modality	$Z_{\text{eff}} < 8.2$	$Z_{\text{eff}} \geq 8.2$
SPR	SECT	(0.53 ± 0.58), max: 3.08	(0.27 ± 0.22), max: 0.77
	DECT	(0.21 ± 0.13), max: 0.67	(0.06 ± 0.04), max: 0.14
	DECT with $\hat{\rho}_e$	(0.06 ± 0.04), max: 0.18	(0.05 ± 0.03), max: 0.11
ρ	SECT	(0.50 ± 0.57), max: 3.04	(0.30 ± 0.15), max: 0.66
	DECT	(0.20 ± 0.17), max: 0.88	(0.05 ± 0.04), max: 0.14
I	SECT	(1.08 ± 1.42), max: 5.82	(1.26 ± 0.99), max: 3.90
	DECT	(0.44 ± 0.29), max: 1.34	(0.33 ± 0.23), max: 0.96

5.4.3 Range study

No significant differences could be observed between proton and carbon ion ranges and the following paragraph summarizes the results observed for proton ranges (Hünemohr et al. [2014c]). No energy dependency of the range difference was observed. Some tissue

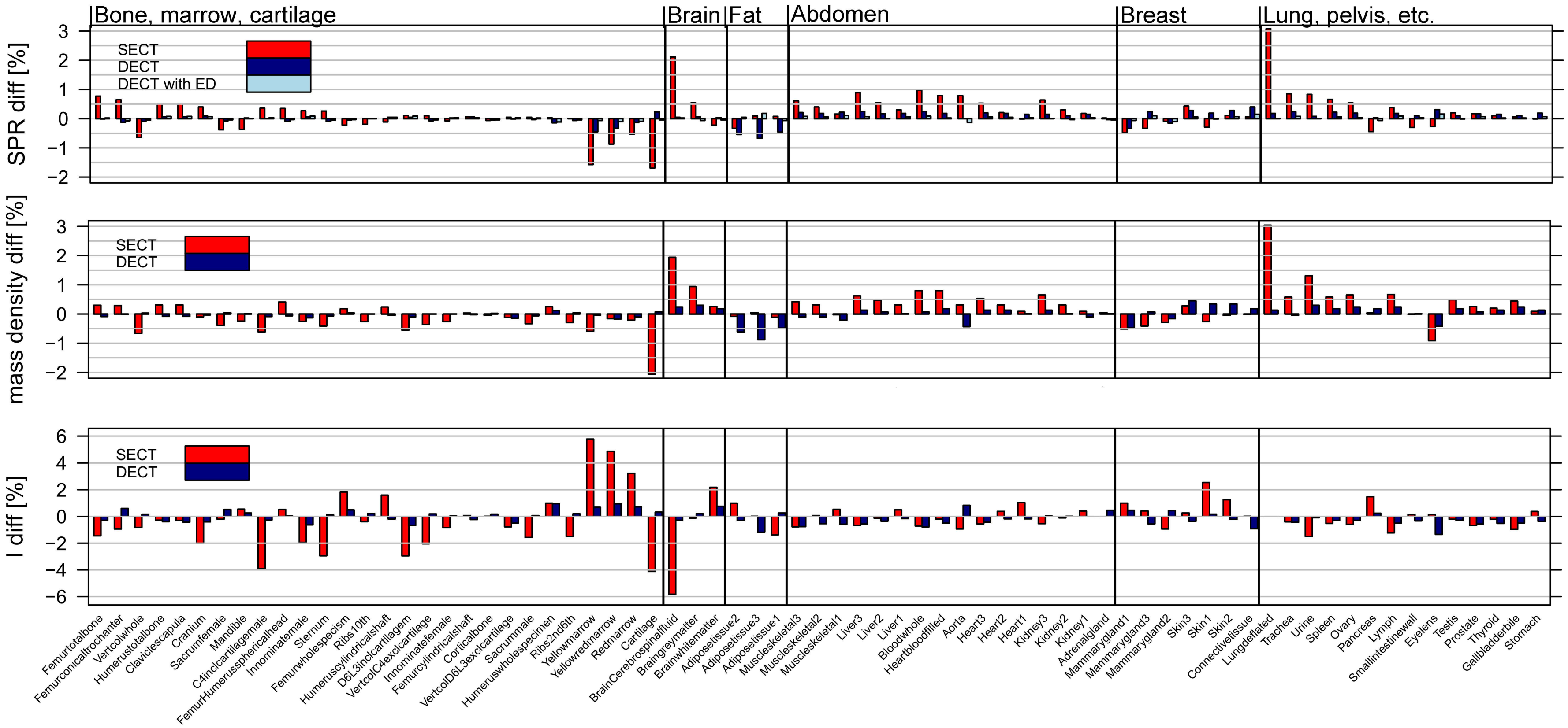

Figure 5.37: Residuals of predicted SPR, ρ, and I-values compared for SECT and DECT for 71 tissues to reference values. "DECT with ED" exploits the $\hat{\rho}_e$ directly for the SPR and the elemental mass fractions for the mean Z/A and I-value prediction. Figure reprinted from Hünemohr et al. [2014c].

benefit particularly from the DECT information: "For brain gray matter and humerus bone, the DECT improved range prediction by 0.5 pp; in yellow marrow the DECT predicted the range 1.2 pp better, and in cartilage an improvement in range difference from 1.8 % (SECT) to -0.2 % with DECT was observed. In liver 3 range differences to reference peak positions could be improved from -0.9 % (SECT) to -0.1 % (DECT). The most significant improvement was observed in brain cerebrospinal fluid from -2.2 % (SECT) to -0.1 % (DECT)", Hünemohr et al. [2014c]. Other tissues register only minor improvements of $\approx$0.2 pp (muscle, D6L3 bone male). For adipose 3 range prediction from DECT data was 0.7 pp worse compared to the SECT prediction (Hünemohr et al. [2014c]). For the artificial 'HCO' material range differences of 0.3 % were observed when changing the carbon and oxygen mass weight by ±10 %. Range differences are summarized in Tab. 5.5 and corresponding Bragg peak positions for the three different material compositions are depicted in Fig. 5.38.

Table 5.5: Residuals of Bragg peak positions simulated in SECT and DECT based predicted tissue compositions as compared to Bragg peak positions in reference compositions. Table reprinted from Hünemohr et al. [2014c].

Material	Modality	350 MeV/u 12C diff [%]	117 MeV p diff [%]	183 MeV p diff [%]	222 MeV p diff [%]
Adiposetissue3	DECT	0.7	0.7	0.7	0.7
Adiposetissue3	SECT	0.0	0.0	0.0	0.0
BrainCerebrospinalfluid	DECT	0.0	0.0	-0.1	0.0
BrainCerebrospinalfluid	SECT	-2.1	-2.2	-2.2	-2.2
Braingreymatter	DECT	-0.1	-0.1	-0.1	0.0
Braingreymatter	SECT	-0.6	-0.6	-0.6	-0.6
Cartilage	DECT	-0.2	-0.2	-0.2	-0.2
Cartilage	SECT	1.8	1.7	1.8	1.7
D6L3inclcartilagem	DECT	0.0	0.0	-0.1	-0.1
D6L3inclcartilagem	SECT	-0.1	-0.1	-0.1	-0.1
Femurtotalbone	DECT	0.0	0.0	0.0	0.0
Femurtotalbone	SECT	-0.8	-0.8	-0.7	-0.8
HCO	C10%O80%	0.1	0.3	0.3	0.3
HCO	C30%O60%	-0.1	-0.3	-0.2	-0.2
Humerustotalbone	DECT	0.0	0.0	0.0	0.0
Humerustotalbone	SECT	-0.5	-0.5	-0.5	-0.5
Liver3	DECT	-0.2	-0.1	-0.1	-0.2
Liver3	SECT	-0.9	-0.8	-0.9	-0.9
Muscleskeletal2	DECT	-0.1	-0.2	-0.2	-0.1
Muscleskeletal2	SECT	-0.4	-0.4	-0.4	-0.3
Urine	DECT	0.0	0.0	-0.1	-0.1
Urine	SECT	-0.7	-0.8	-0.8	-0.8
Yellowmarrow	DECT	0.6	0.6	0.6	0.5
Yellowmarrow	SECT	1.7	1.8	1.7	1.7

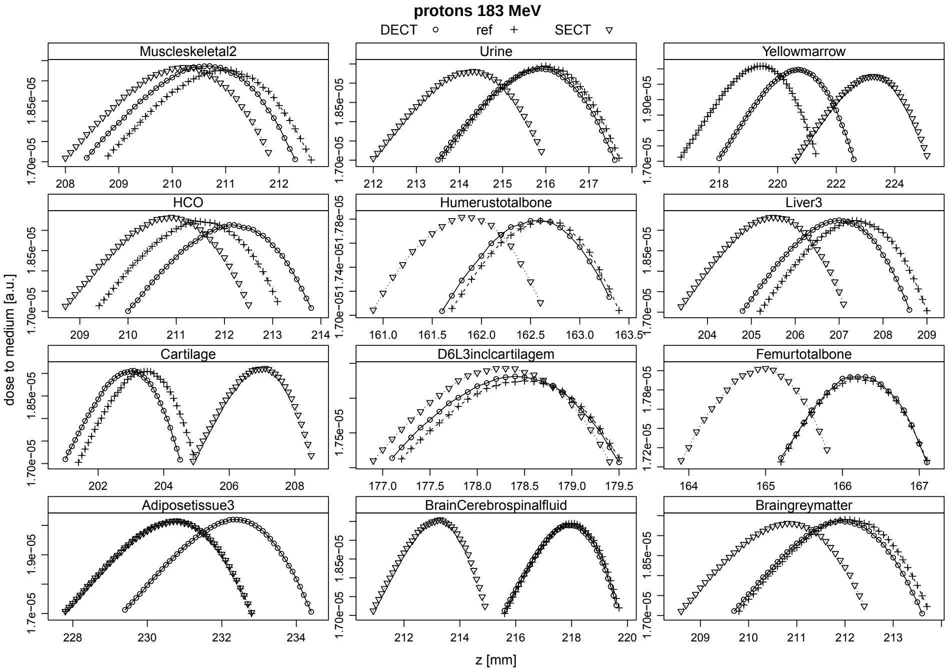

Figure 5.38: Bragg peak positions in three different material composition assigned with the standard SECT approach from a single CT number (Schneider et al. [2000]), the novel DECT method suggested in this thesis (exploiting $\hat{\rho}_e$ and Z_{eff}) and the reference composition taken from Schneider et al. [2000] (restricted to the six major elements). Figure reprinted from Hünemohr et al. [2014c].

6 Discussion and Outlook

6.1 Stoichiometric calibration robustness

Results presented in Sec. 5.1 show that variations in the generation of the basis CT number set for the subsequent optimization of k_1 and k_2 have a significant influence on the resultant stoichiometric calibration of up to 2.4 % (worst case scenario).

Robustness with applied X-ray tube voltage and reconstruction kernel

(Setting A) The most interesting finding is that the higher the X-ray tube voltage is chosen, the more robust appears the stoichiometric calibration method. A number of aspects described in Sec. 5.1 underline this thesis:

- At 140Sn kV, the optimization of k_1 and k_2 is less sensitive to changes in the measurement setup and assumed material compositions (Fig. 5.1).
- At 140Sn kV, the CT number prediction for the investigated tissue surrogates agrees significantly better with the actual measurements (Fig. 5.3, Fig. 5.4).
- At 140Sn kV, the resultant HLUT showed to be less dependent on the employed tissue surrogate selection, assumed material composition or phantom setting and fit residuals are smaller (Fig. 5.8)

Historically, 120 kV represents the standard voltage setting for diagnostic CT imaging. Trends lead towards low kV imaging with high contrast as the tube output is no longer a technical limitation today. For planning CTs in ion therapy, however, kV settings should be revised and the results of this thesis indicate that higher kV settings would be beneficial. Similar findings were discussed for ortho-voltage and MV CT in Yang et al. [2008] and Cheng et al. [2013]. The HLUT process could be improved by employing higher X-ray tube voltages, as the CT number gets more linear in the $\hat{\rho}_e$ with higher photon energies. A positive side effect represents the additional reduction of metal artifacts. The possibility of scanning the patient at higher tube voltages, e.g. at 140Sn kV or 150Sn kV (with the newest DECT scanner generation "Somatom Force", SIEMENS), should therefore be considered in the future. One has to keep in mind that the dose deposition increases with photon energy (Eq. 2.14), and it is therefore necessary to discuss acceptable noise levels of treatment planning CTs. X-ray detector efficiency and electronic noise reduction improved during the last decade and enable a dose efficient scanning at higher photon energies. Soft tissue contrast necessary for target and organ delineation could be superimposed from other image modalities (or contrast agent CT images) involved which is anyway a standard in today's treatment planning process. A major drawback might be the fact, that the information of the tin-filtered spectrum is only available in a smaller FOV due to the limited space for both detectors on the DECT gantry.

CT number residuals of lung tissue suggest the involvement of further post-processing specifically designed for an improved diagnostic quality of head scans (H30 kernel) where usually no lung tissue is involved. These changes of CT number may undercut the stoichiometric calibration process which relies explicitly on the accurate physical parametrization of the photon spectra. The D34 kernel and corresponding robust (positive) k_1 and k_2 parameters underline the application of advanced beam hardening corrections (cf. Fig. A.5). These results confirm, that the reconstruction kernel not only influences the image texture and sharpness but also the pixel value levels in general. Future investigations should therefore quantify the impact of additional image post-processing involved (see also Sec. 6.3.1 for the "PFO" optimization) and characterize the existing kernels to identify the reconstruction setting that is optimal for treatment planning CTs and the HLUT calibration.

Optimization of k_1 and k_2 and their influence on CT numbers

The heart of the stoichiometric calibration is the characterization of photon attenuation by two parameters. Fig. 6.1 shows that it is much easier to optimize k_2 (photoelectric absorption) due to high gradients in the parameter space as compared to the dependency on k_1 (scattering contribution) being flat over orders of magnitudes.

For realistic variations of k_1 and k_2 (cf. results generated in this thesis Tab. A.3), the photoelectric parameter k_2 has a larger influence on the predicted CT number than k_1 (Fig. 6.2). Fig. A.2 shows the dependency of μ/μ_{H2O} on relative changes in k_1 and k_2. Particularly for bone tissue, the accurate determination of k_2 determines how realistic the photon attenuation is characterized in these tissues. Fig. 5.1 shows that a higher X-ray tube voltage results in fewer variations of both parameters when measurement settings were varied.

Negative k_1 indicate further an unphysical parametrization of the photon attenuation and related employed constants in Eq. 3.1. Negative k_1 were particularly observed for the high 140Sn kV spectrum and the D30 reconstruction kernel. It was therefore decided to optimized Eq. 3.1 not only for attenuation parameter k_1 and k_2, but also for the exponents m_1 and m_2 to investigate the Z and energy dependency of the underlying parametrization more accurately. Results summarized in Tab. 6.1 reveal several aspects:

- with $m_1 = 2.86$ and $m_2 = 4.62$ (Schneider et al. [2000], Rutherford et al. [1976b]) exponents were chosen very adequately for the 140Sn kV spectrum, but not necessarily for the other two lower kV spectra.

- Again, k_2 remains relatively stable (particularly at 140Sn kV) while k_1 varies significantly dependent on the reconstruction kernel and start values of the parameters.

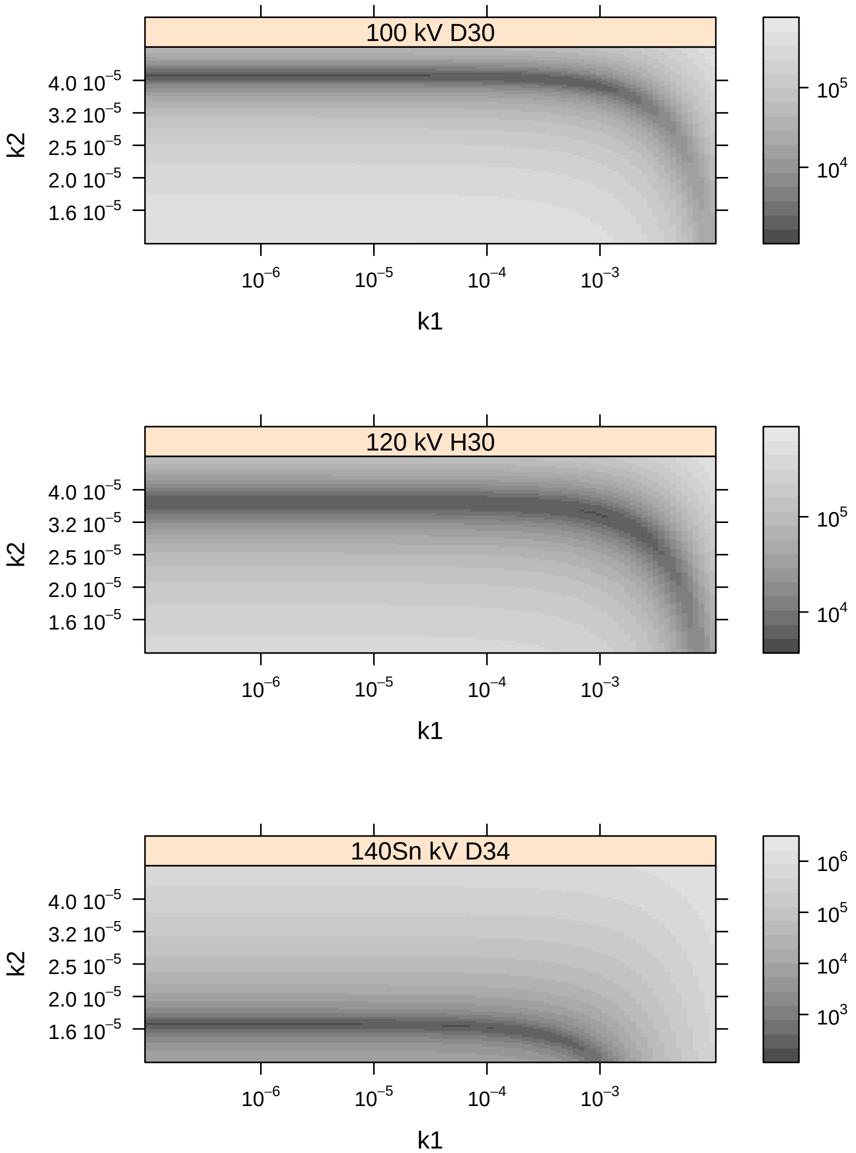

Figure 6.1: Results of Eq. 3.3 for different k_1 and k_2 combinations based on the measured CT numbers with the full Gammex tissue surrogate set (central axis PMMA tube phantom). 100×100 combinations of $k_1 \times k_2$ were sampled. The high gradient in k_2 facilitates finding the minimum, while finding the minimum in k_1 remains challenging.

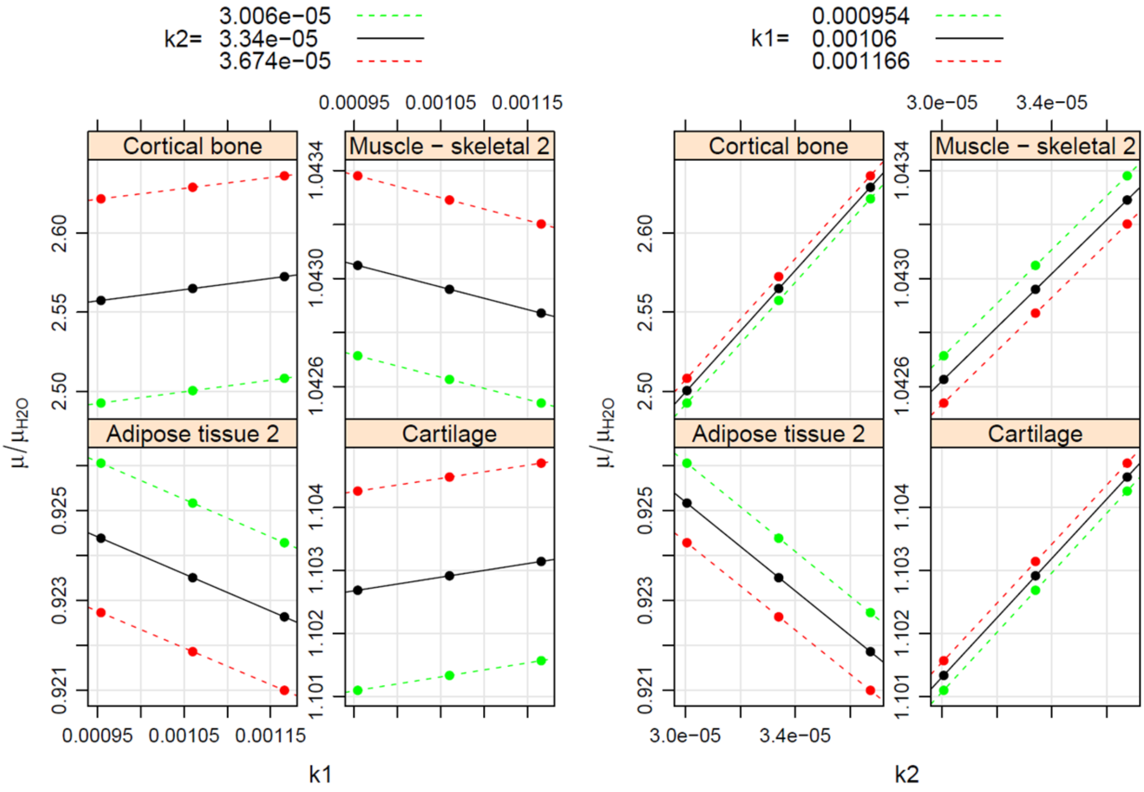

Figure 6.2: Sensitivity of relative photon attenuation coefficient as a function of k_1 (left, for three different k_2 values) and k_2 (right, for three different k_1 values). k_1 and k_2 values were varied according to optimized values in Tab. A.3 (120 kV). k_2 (photoelectric absorption) particularly influences CT numbers of high Z materials (cf. Eq. 3.1) and should be derived with high accuracy.

- The influence of start values on the optimization result underline how undefined the optimization parameter space is particularly at 120 kV and 100 kV (cf. Fig. 6.1).
- Reconstruction with the D30 kernel results again in negative k_1.
- Significant difference of m_1 and m_2 for the H30 optimization at 120 kV is observed which indicates again an additional involvement of image post-processing with H30

Vanderstraeten et al. [2007] observed in a multicenter study with the same tissue surrogate set variations in the optimized k_1 and k_2 for the same CT scanners as well as negative k_1 values. The authors argued that k_1 and k_2 are interrelated due to the common energy dependency and Eq. 3.1 would be over determined. It has to be clarified in the future, whether negative k_1 parameters, that represent the measurements and scanner well but describe an "unphysical" attenuation parametrization, should be adapted (i.e. forced to be positive in the optimization) or not.

Table 6.1: k_1, k_2 and m_1, m_2 optimized with Eq. 3.3. For this thesis, parameter start values were originally set to $k_1 = 8.20 \cdot 10^{-4}$, $k_2 = 3.39 \cdot 10^{-5}$, $m_1 = 2.86$, $m_1 = 4.62$ while keeping m_1 and m_2 fix (results listed in Tab. A.3). Here, m_1, m_2 were also optimized and different start values originating from Schneider et al. [2000] were employed ($k_1 = 1.24 \cdot 10^{-3}$, $k_2 = 3.06 \cdot 10^{-5}$, $m_1 = 2.86$, $k_2 = 4.62$).

k_1	k_2	m_1	m_2	result Eq. 3.3	iterations	voltage	kernel	k_1 start	k_2 start
-1.63E-03	8.39E-05	2.52	4.4	1638	755	100kV DE	D30	8.20E-04	3.39E-05
2.40E-05	3.82E-05	3.06	4.64	1644	161	100kV DE	D30	1.24E-03	3.06E-05
4.28E-03	1.26E-05	2.49	4.98	268	1051	100kV DE	D34	8.20E-04	3.39E-05
5.79E-03	1.45E-05	2.36	4.94	268	953	100kV DE	D34	1.24E-03	3.06E-05
3.07E-04	3.79E-05	3.18	4.63	552	157	100kV DE	H30	8.20E-04	3.39E-05
2.78E-04	3.12E-05	3.32	4.69	551	329	100kV DE	H30	1.24E-03	3.06E-05
1.80E-02	4.61E-09	2.19	7.55	4987	6839	120kV SE	H30	8.20E-04	3.39E-05
2.89E-03	1.70E-06	2.75	5.56	5061	2449	120kV SE	H30	1.24E-03	3.06E-05
-1.90E-04	1.91E-05	2.9	4.59	170	153	140Sn kV DE	D30	8.20E-04	3.39E-05
-1.64E-04	1.72E-05	2.89	4.62	170	153	140Sn kV DE	D30	1.24E-03	3.06E-05
3.17E-05	1.67E-05	2.88	4.61	216	147	140Sn kV DE	D34	8.20E-04	3.39E-05
2.88E-05	1.67E-05	2.89	4.61	216	145	140Sn kV DE	D34	1.24E-03	3.06E-05
8.99E-05	1.89E-05	2.89	4.62	240	155	140Sn kV DE	H30	8.20E-04	3.39E-05
9.71E-05	1.85E-05	2.89	4.63	240	151	140Sn kV DE	H30	1.24E-03	3.06E-05

Parametrization for dense bone

Trends of CT number residuals towards low and high $\hat{\rho}_e$ and different exponents m_1 and m_2 (dependent on X-ray energy) suggest, that the simplified parametrization of attenuation coefficient may not apply for the entire range of materials and diagnostic photon spectra. For the cortical bone surrogate, the CT number is overestimated by roughly 25 HU (120 kV) which implies a too low slope of the HLUT in the dense bone region (Fig. 5.3). When excluding the cortical bone rod, the same overestimation is recorded for the next lower surrogate. These observations indicates, that it is of major importance to include a high dense bone surrogate in the material set to derive the correct HLUT slope for bone tissue. de Kock and Schreuder [1996] published a comment on Schneider et al. [1996] in which errors "are expected to be quite significant for bone" since the dependency on Z with the fix exponents m_1 and m_2 (Eq. 3.1) is invalid for high Z elements such as calcium and phosphorus. Bourque et al. [2014] second the statement that the parametrization is "limited when it comes to modeling the photoelectric effect in human tissues containing high-Z media". Williamson et al. [2006] optimized fit parameters dependent on the Z and found similar variation as shown in Tab. 6.1. Statements in de Kock and Schreuder [1996] agree with the findings in this thesis: especially for bone tissue, the stoichiometric calibration has to be determined with caution and the awareness of possible systematic errors. This applies particularly for particle therapy, as bone tissues exhibits high SPRs and uncertainties in these would translate to considerable range uncertainties.

Future work on the stoichiometric calibration should therefore investigate the optimization of parameters and exponents for bone and soft tissue separately (and dependent on the X-ray tube potential, cf. Jackson and Hawkes [1981] and Williamson et al. [2006]). It should be considered to include more high dense and high Z materials in the calibration measurements in order to improve the spectral characterization represented by k_2. Improving the accuracy of k_2 (as the precision is very good, Fig. 5.1) and reducing the variability in k_1 would be beneficial particularly for bone tissue compositions. CT number residuals should be evaluated in the future in terms of relative μ as an apparent trend might be due to the definition of the CT number.

Dependency on the phantom used

The HLUTs at 120 kV vary by 0.9 % when different phantoms are employed for the base CT number measurement of the tissue surrogate. Cross scattering and variable beam hardening due to different rod positions in the "pizza" influence particularly the bone surrogate which showed to be crucial for an accurate HLUT generation. The "pizza" phantom should not be used as the CT numbers differ up to 2-8 % (Fig. A.1) and are supposed to be very sensitive to the specific filling.

Tabulated tissue compositions

Since the base data of tissue composition (Schneider et al. [2000]) used for the stoichiometric calibration were measured in the middle of last century (Sec. 3.2.3), data should be updated by the employment of modern analyze method such as mass spectroscopy. Particularly variations in tissue composition and pathologies would be of interest to test the robustness of the SECT stoichiometric calibration in unusual tissue compositions.

Presented results underline the specific need for tissue surrogates dedicated for particle therapy. Those should exhibit realistic radiological properties with photons *and* interaction properties for ion beams (Yohannes et al. [2012]). Up to now, only photon therapy specific tissue surrogates exist those allow a direct assessment of the calibration. For ion therapy, particularly high Z and high mass density compounds simulating e.g. cortical and temporal bone would be of interest as well as a larger variety of soft tissues would be highly appreciated (i.e. adipose/bone marrow, tumor/healthy tissue). These tissue surrogates, ambiguous in their CT number or SPR, could quantify residuals resulting from the SECT HLUT. The production of tissue surrogates that meet all requirements such as stability, reproducibility and realistic photon/ion interaction, however, face major challenges. The interchanged carbon and oxygen mass weight in artificial tissues as compared to their natural equivalences is just one of many other problems in this context (Hünemohr et al. [2013]).

6.1.1 Systematic influence HLUT polyline segments

Particularly for low kV settings where the linear fit segments change a few times over a small CT number range, systematic SPR influences of up to 0.27 % at the "bending" calibration points should be expected. Although denoting a relatively small effect, future work should establish a protocol for the generation of the linear line segments in the soft tissue region where various ambiguities in CT number and SPR are present (Sec. 6.3.1). The more linear the HLUT is (which applies for higher X-ray tube voltages) the smaller the systematic error in SPR prediction at the calibration points is.

6.2 DECT as an alternative image modality

6.2.1 DECT-based measurement of $\hat{\rho}_e$ and Z_{eff}

The accuracy of the DECT-based $\hat{\rho}_e$ $(0.4 \pm 0.3)\,\%$ and Z_{eff} $(1.7 \pm 1.4)\,\%$ measurement is found to be similar or better compared to other published data that employed similar image-based algorithms (Saito [2012], Tsukihara et al. [2013], Landry et al. [2013b], Landry et al. [2011]) or different algorithms that require the input of the photon spectra (Bourque et al. [2014], Bazalova et al. [2008], Torikoshi et al. [2003], Heismann et al. [2003]). The achieved mean absolute accuracies of 0.004 ($\hat{\rho}_e$) and 0.135 (Z_{eff}) provide the means to differentiate soft tissues and body fluids as demanded by Mahnken et al. [2009] and Heismann [2005] who asked for an accuracy of 0.1-0.2 in units of Z_{eff}.

The generally elevated noise in Z_{eff} results from the fact, that the Z_{eff} map is calculated with the ratio of the spectral CT number difference and sum which is then raised with the power of n that increases the relative noise level (Eq. 3.16). The $\hat{\rho}_e$ is calculated solely from the difference of both measured CT number images (Eq. 3.11). Spectral CT numbers in soft tissue do not differ much which provokes an elevated standard deviation in Z_{eff} for soft tissue as compared to bone tissue (Tab. A.4) that was also observed in Bourque et al. [2014] and Landry et al. [2013b]. Descriptively, this can be explained by the fact that the Compton effect dominates the photon interaction in low Z materials and it is difficult to separate $\hat{\rho}_e$ from Z_{eff} in these materials with DECT (cf. Alvarez and Macovski [1976], Semerci and Miller [2012]). To conclude, the DECT contrasts can be determined with a very high accuracy but seem to be more reliable in bone tissue than in soft tissue since the spectral information of $\mu(E)$ is more distinctive in high dense or high Z tissues. The negative correlation of Z_{eff} to $\hat{\rho}_e$ is depicted in Fig. A.4, dependencies of DECT contrasts on the distance to the central scanner axis (beam hardening) are shown for the cortical bone surrogate in Fig. A.5.

Future investigations should clarify, whether a lower tube voltage of e.g. 70 kV (i.e. available in the new SIEMENS "Somatom Force" scanner) could help to improve the Z_{eff} determination of soft tissues which is indicated by the slightly better Z_{eff} accuracy at 80/140Sn kV compared to the 100/140Sn kV acquisition (Tab. A.5). It should be quantified further, whether an increased tube current at the lower kV tube would decrease the noise level of Z_{eff}. Additionally, iterative reconstruction algorithm available in the recent scanner software should be employed. For this approach, Landry et al. [2013b] observed noise reduction in the CT numbers by a factor 2.

It has to be stressed again, that the Z_{eff} reference data for tissue surrogates is an approximation and elemental composition might vary from batch to batch due to different production processes. High Z_{eff} residuals in the order of 0.3 for brain and cortical bone surrogate might result from a different actual composition than assumed. A detailed elemental analysis would be of great help not only for the commercial Gammex surrogates but also for future customized phantom materials that will be exploited in multi-modality phantoms (Gallas et al. [2014]).

6.2.2 DECT-based SPR prediction

Correlation of the Z_{eff} to the I-value

For the SPR determination, the parametrization of the I-value through Z_{eff} represents a process similar to the stoichiometric SECT parametrization of the CT number. The advantages of the DECT parametrization should be clarified: Firstly, the corrective I-value term $\mathrm{f}(I_{\mathrm{m}}, I_{\mathrm{w}}, \beta)$ (Eq. 2.23) is comparatively small due to the logarithm and ranges from 1.02 for adipose tissue (I =63 eV) to 0.95 for cortical bone (I =112 eV, Tab. A.7). It is multiplied with $\hat{\rho}_{\mathrm{e}}$, the dominant target quantity for the SPR and which ranges from 0.26 (lung) to 1.78 (cortical bone, Tab. A.7). A high accuracy of the $\hat{\rho}_{\mathrm{e}}$ measurement is therefore essential for an accurate SPR prediction with DECT data. Secondly, the I-value parametrization through Z_{eff} is more robust as compared to the stoichiometric calibration since its setup is almost scanner independent, independent of tissue surrogate measurements and calculated only with tabulated tissue compositions. Still, one scanner specific parameter, the exponent n for the Z_{eff} calculation (Eq. 3.18), has to be determined with one calibration material, but the accuracy of this parameter can be assessed with any material of known elemental composition as the Z_{eff} concept is valid for all kinds of materials (except compounds containing high Z materials above iodine with Z =53, Hünemohr et al. [2014a]).

Measured accuracies of the I-value (3.9 ± 3.0) % and SPR (0.6 ± 0.3) % were found to be very similar to the data in Bourque et al. [2014]. With the I-value parametrization, an absolute Z_{eff} variation of ±0.2 translates roughly to an I-value variation of ±1.6 eV that, according to Paganetti [2012], translates to a SPR uncertainty of 0.2 %.

The SPR prediction utilizes the additional information on Z_{eff} particularly when tissues exhibiting the same $\hat{\rho}_{\mathrm{e}}$ but different Z_{eff}. In general, the Z_{eff} represents a better predictor for the I-value compared to the SECT CT number (Hounsfield Unit) which is a mixture of both, $\hat{\rho}_{\mathrm{e}}$ and Z_{eff}. It has to be stressed, however, that the I-value parametrization derived with tabulated tissue compositions cannot represent materials that differ much from these base data. A prominent example in Fig. 5.17 is aluminum exhibiting a Z_{eff} of 13 (which is similar to that of cortical bone) but has much higher I-value (+55 eV) as compared to cortical bone. This is caused by different electronic configurations between pure aluminum and the cortical bone compound which cannot be resolved with Z_{eff}. The same problem applies for teflon containing an unusual high amount of fluorine (76 %). To summarized, only materials with mass weights and elements similar to tissues (i.e. PMMA) are represented in the specified DECT ln$I$-Z_{eff} correlation. However, materials with different compositions as compared to standard tissues (such as teflon or aluminum) can be clearly identified in the $\hat{\rho}_e/Z_{\mathrm{eff}}$ space (Fig. 5.14). It is therefore suggested to apply different I-value parametrizations dependent on measured $\hat{\rho}_e/Z_{\mathrm{eff}}$ pairs.

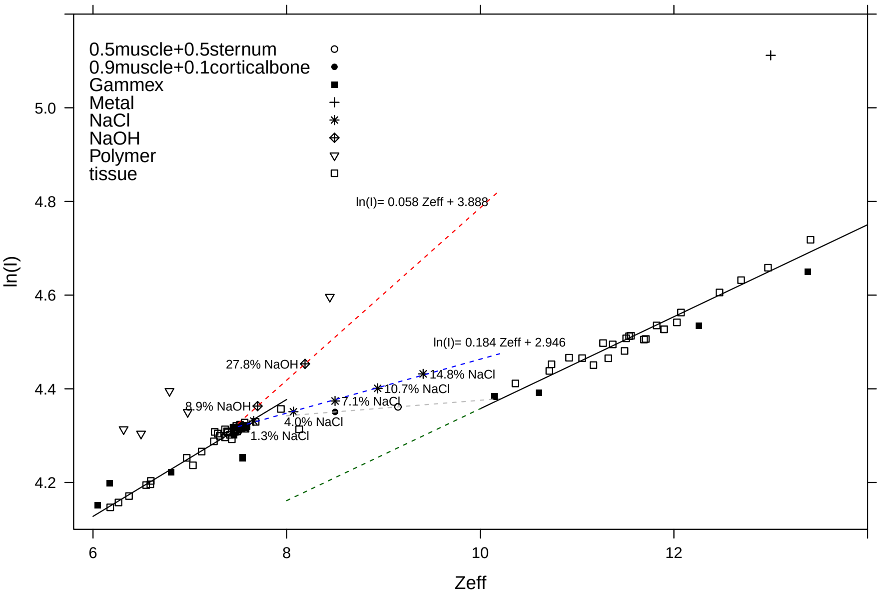

Figure 6.3: ln I dependence on Z_{eff} with additional data of aqueous solutions of NaOH and NaCl (diamonds and stars) and tissue mixtures (circles) covering the intermediate Z_{eff} range. Data of aqueous solution are summarized in Tab. A.9. Figure and caption reprinted from Hünemohr et al. [2014b].

The dependency of ln$I$ on Z_{eff} is far from trivial and Fig. 5.17 queries which I-value has to be assigned for intermediate Z_{eff} values ([8.5-10.0], Hünemohr et al. [2014b]). When a tissue is considered to be a *compound*, *ln*I is found to depend linearly on Z_{eff} which applies particularly for the tabulated soft and bone tissues (Schneider et al. [2000]) whose compositions are interpolated using base components like water, lipid, protein, carbohydrate, minerals and ash (Sec. 3.2.3, Hünemohr et al. [2014b]). Intermediate Z_{eff} values can be measured mainly for *mixtures* of tissues with very different compositions. These mixtures are naturally present due to finite voxel sizes and the related non-linear partial volume effect (Sec. 2.1.2, Hünemohr et al. [2014b]). For the patient head and neck case, the intermediate ln$I$ was set to 4.4 representing the linear connection of the soft and bone tissue fit (Fig. 5.17). The linear behavior was found to be true when studying aqueous solutions of sodium (Z=11) and chloride (Z=17) as well as tissue mixtures of soft and bone (Fig. 6.3). Reference calculation of Z_{eff} does not differentiate tissue mixtures and compounds (i.e. lung tissue has a very similar Z_{eff} as compared to muscle tissue, although the granularity differs significantly). The fact that Z_{eff} is independent from the mass densities (in contrast to the CT number and $\hat{\rho}_{\text{e}}$) could be exploited for further investigations of the partial volume effect with DECT.

DECT-based SPR prediction with Z_{eff} and $\hat{\rho}_{\text{e}}$

Tab. 5.2 shows that the SPR prediction with DECT achieves a very high accuracy of $(0.6 \pm 0.3)\,\%$ for tissue surrogates and $(1.6 \pm 0.2)\,\%$ for polymers. The accurate SPR prediction for non-tissue like materials has to be emphasized as the SECT HLUT does not represent these materials. PMMA is a prominent example: With a CT number of 127 HU (120 kV) the SECT HLUT predicts a SPR of 1.088 which underestimates the SPR by 7 %. Here, DECT can predict the SPR with an accuracy of 1 %. SPR for teflon and tecadur could be predicted with DECT with an accuracy of 3.5 %. This is due to the fact that particularly the I-value of teflon is not well represented by the linear correlation of Z_{eff} to $\ln I$.

The image noise in the $\hat{\rho}_{\text{e}}$ (0.004-0.009) and Z_{eff} (0.20-0.07) translates to a SPR noise of (0.007-0.01) and shows that the correction term in the Z_{eff} is of minor importance for the noise propagation. In general, residual differences in of $\hat{\rho}_{\text{e}}$ and Z_{eff} (and therewith the predicted I-value) can add up or compensate each other in the SPR calculation (Eq. 3.19). Since $\hat{\rho}_{\text{e}}$ is the most important target parameter, the high accuracy of the $\hat{\rho}_{\text{e}}$ determination directly translates into a good accuracy of the SPR estimation.

Tab. A.7 identifies tissue compositions where the Z_{eff} has an added value besides the information on $\hat{\rho}_{\text{e}}$ (i.e. red marrow vs. adrenal gland vs. small intestine wall, skin 3 vs. cartilage, mammary gland 2 vs. urine). In these specific tissues, the Z_{eff} information improves the SPR determination by maximal 1 % as compared to the simple approach of just exploiting $\hat{\rho}_{\text{e}}$ (approach published in Hünemohr et al. [2013]). However, future research should quantify, whether the additional information on Z_{eff} is also of use in patient images that are affected by noise and artifacts. This absolute comparison can only be accomplished with the knowledge on a reference SPR map.

Furthermore, the general uncertainty of the reference I-value determination with Bragg's additivity rule as well as in experimental data has to be emphasized again. The I-value of water influences directly the denominator in the DECT-based SPR prediction (Eq. 4.1) which applies also for the SECT calibration. The influence of the I-value of water on treatment planning and range accuracy is discussed in more detail in Andreo [2009] and Henkner [2009]. In general a 10 % uncertainty in the I-value roughly translates to 1 % uncertainty in the SPR (Sec. 2.3.4, Paganetti [2012]).

For completeness, calibration constants c_{e} and d_{e} (Sec. 3.5) calculated from measured CT numbers of the tissue surrogates are depicted in Fig. A.3.

6.3 Comparison of DECT- and SECT-based SPR prediction in a patient

It has to be stressed again, that an absolute comparison of DECT- and SECT-based SPR predictions for patient images is yet impossible as no reference SPR map exists. Differences between SECT- to DECT-based predicted SPR can be analyzed only relatively.

Future investigations should therefore pursue the absolute comparison of SPR prediction e.g. in animal tissue samples with a reference method like proton or heavy ion CT (Rinaldi [2011], Rinaldi et al. [2013]) that measures directly SPR maps with the therapeutic ion beam. A heavy ion CT could assess SPR predictions in inhomogeneous anthropomorphic geometries where CT images might be affected by artifacts such as beam hardening and partial volume effects. Accurate image registration and reproducible measurement setup (i.e. stable tissue behavior over time) have to be fulfilled in order to be able to point out relevant differences of both imaging modalities. Image quality of ion CTs remains to be improved for the comparison with standard CT data, not to speak about the high technical demands on the rotational beam application and detector system that prevents the method to enter the clinical routine so far (Rinaldi [2011], Telsemeyer et al. [2012]).

Alternatively, range probes through tissues (Schaffner and Pedroni [1998], Hünemohr et al. [2013]) provide only an integration of predicted SPRs in 1D, which implies that fluctuations or systematic differences can compensate with depth.

6.3.1 SPR images

The first relative comparison of DECT- and SECT-based calculated SPR images for a head and neck patient provided strong hints on the main differences between both techniques: the DECT seems to be able to differentiate tissues that appear ambiguous in the SECT HLUT (2 % SPR difference in the ventricles) and the SECT stoichiometric calibration might be problematical for dense bone tissues (5-8 % SPR difference in the petrous part of the temporal bone). The latter corresponds to the results in Sec. 5.1 and Sec. 6.1 showing that the stoichiometric calibration method is particularly sensitive to the employed measured bone surrogate and may not represent all variations of bones (cf. de Kock and Schreuder [1996], Jackson and Hawkes [1981], Williamson et al. [2006]).

Ventricle region SPR differences between SECT and DECT in the ventricles (Fig. 5.20, Fig. 5.21) can be explained when examine the linear segments of the HLUT in more detail in the soft tissue region and superimpose reference tissues as depicted in Fig. 6.4. Ventricles consist of cerebrospinal fluid which is basically water. Water is usually not part of the line segments, as the line fits have to represent neighboring adipose tissue and bone marrow (on the left) as well as soft tissue (on the right). The fact, that the SECT CT number is affected by both, $\hat{\rho}_e$ and Z_{eff}, is particularly obvious in the water region where CT number ambiguities dominate. The fit around 0 HU can hardly represent all present tissue types. Adipose tissue and bone marrow exhibit large $\hat{\rho}_e$ but small Z_{eff} due to the elevated hydrogen amount compared with water. The DECT can resolve these ambiguities in the CT number by separating $\hat{\rho}_e$ from Z_{eff}. This allows a more accurate and more composition specific prediction of the SPR. For completeness it has to be said, that the HLUT at HIT is forced through the water point to facilitate quality checks with water phantoms. Thus, this SECT HLUT would not show a mis-assignment of SPR in the ventricles. However, one has to wonder in turn that SPR predictions for neighboring tissues (bone marrow, soft tissue) might be inadequate.

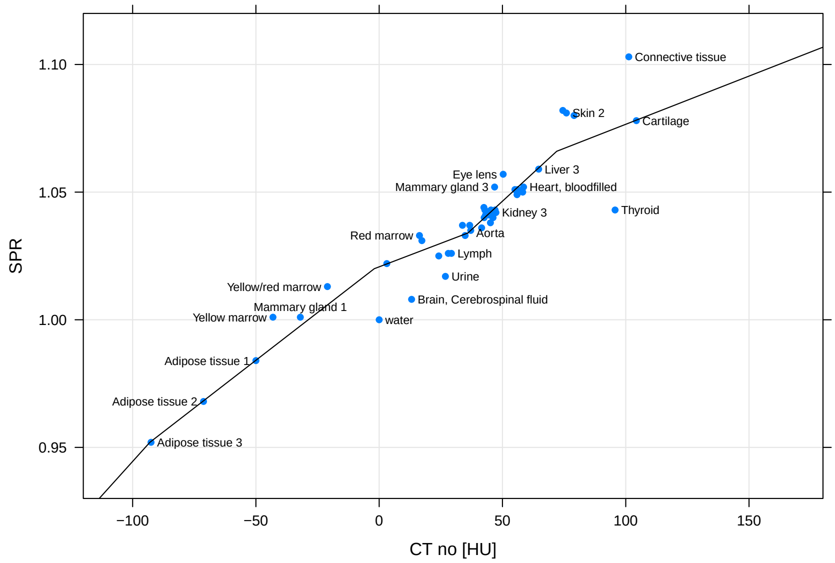

Figure 6.4: Stoichiometric HLUT for 100 kV. Linear fits are derived from the predicted CT numbers for the tabulated tissue (Schneider et al. [2000]). Water (SPR=1, CT no = 0 HU) is usually not part of the calibration. The SPR of water and brain cerebrospinal fluid are underestimated due to the linear line segments that have to cover neighboring tissues like adipose tissue (i.e. bone marrow) on the left and soft tissue on the right.

Temporal bone region Largest differences between SECT- and DECT-predicted SPR were found in the petrous part of the temporal bone (up to 5-8 %). Again, the 140Sn kV SECT-based predicted SPR is closer to the DECT-based predicted SPR than the 100 kV SECT SPR map. The temporal bone represents the densest bone in humans and forms several different bony structures in this anatomical region. The CT number measured in the petrous part is approximately 250 HU higher than the CT number of the Gammex cortical bone surrogate (both measured at 100 kV, Tab. A.4, Tab. A.6). For the contoured petrous part of the temporal bone a very high $\hat{\rho}_e$ of 1.948±0.051 at a standard Z_{eff} was measured with DECT (Z_{eff}=12.7±0.2, which is 0.3 units of Z_{eff} lower compared to the surrogate).

In order to exclude systematic errors resulting from the SECT HLUT at 100 kV and 140Sn kV, the contrast affected 120 kV images of the patient were cross checked with the clinical 120 kV head HLUT from HIT. For the contoured dense temporal bone (1610 HU-1760 HU, no contrast agent accumulation assumed) a SPR of 1.70-1.74 is predicted with the clinical HLUT. This SPR prediction agrees well with the prediction based on the SECT HLUT generated in this thesis. Additionally, an empirical calibration generated with the Gammex surrogates was cross-checked in order to confirmed that the stoichiometric HLUTs agrees within 1.3 % with the empirical HLUT (100 kV, D30) in the cortical bone region. Large SPR differences between DECT to SECT in the petrous part of the temporal bone can appear also due to additional image correction by the scanner software. A dedicated "Posterior Fossa Optimization" (PFO) that reduces beam hardening influences particularly for the soft tissue in the skull base might have been applied by default in the head scan. Unfortunately, it is not clear if CT numbers are changed only for the soft tissue or also for the temporal bone. It would therefore be of great interest to investigate the impact of the PFO correction on the CT values of the dense cortical bone with anthropomorphic phantoms or animal samples. Peterson and Dechow [2003] and Dechow et al. [2010] measured mass densities of the petrous part of the temporal bone structure and surrounding bones of around (1.9±0.1) g/cm^3. These measurements can serve as a hint, that DECT might represent dense bone structures better but have to be handled with care since different structures and volumes were evaluated.

Results and literature presented in Sec. 6.1 provide hints, that the SECT HLUT is affected with systematic errors in the bone region which would aggravate for very dense bones. Future phantom inventions should aim to cover the full range of tissues present in the human body and would therefore need to focus on high dense, respectively high Z_{eff} surrogates.

The considered head patient was scanned with a pitch of 0.6 and geometrical differences due to the tube offset or motion artifacts in the image space are supposed to be negligible. Future work should clarify, whether the tube offset of 95 ° results in small geometrically discrepancies in the image space that would explain SPR differences at the edges of large attenuation gradients.

Mastoid region and partial volume effects The mastoid forms a large inhomogeneous cavity of bone/air interfaces and large differences of predicted SPR between DECT and SECT were observed. Fig. 6.5 clearly identifies pixels in the mastoid cavity (turquoise) that are assumed to be affected by the partial volume effect (Sec. 2.1.2) and pixels present in the contoured petrous part of the temporal bone. Accounting the additional Z_{eff} information, Fig. 6.6 shows that the mastoid exhibits very large Z_{eff} (due to the mixture of cortical bone and air) and a low $\hat{\rho}_{\text{e}}$.

Since the photoelectric effect dominates in tissues of large Z_{eff}, the SECT predicts a significant larger SPR for pixels affected by the non-linear partial volume effect at 100 kV. In contrast, the DECT predicts a smaller SPR due to a small $\hat{\rho}_{\text{e}}$ and large Z_{eff}

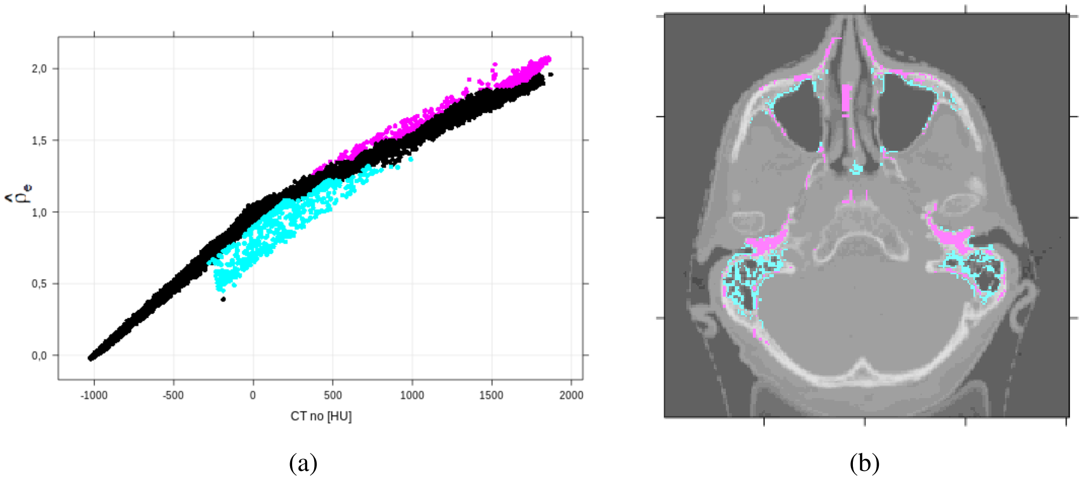

(a) (b)

Figure 6.5: (a) Measured $\hat{\rho}_e$/CT number (100 kV) pairs labeled to the mastoid cavity (turquoise), petrous part of the temporal bone (magenta) and surrounding tissue (grey/black). (b) shows the CT number image with the labeled pixels highlighted.

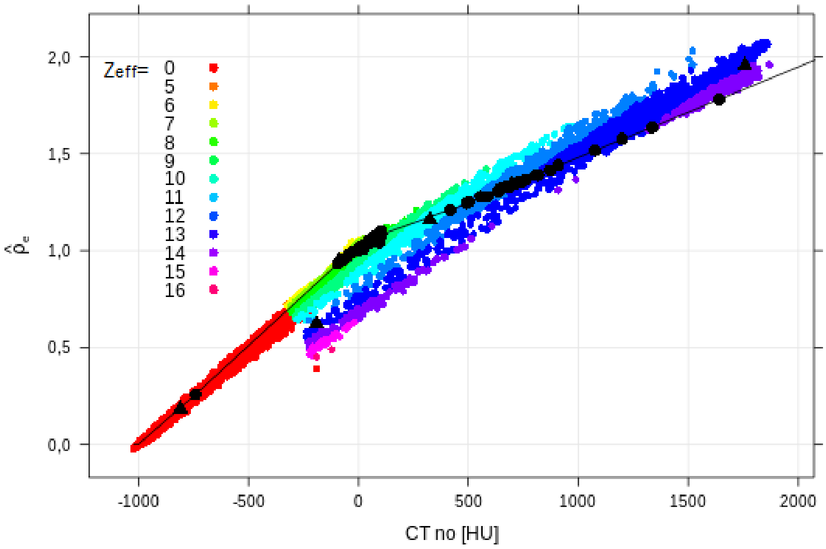

Figure 6.6: Pixel values ($\hat{\rho}_e$ and CT number at 100 kV) of the axial CT slice in the mastoid region dependent on measured Z_{eff} (color labeled). For pixels of low $\hat{\rho}_e$, Z_{eff} could not be calculated and was set to zero (red points). Black points depict predicted values of tabulated tissue compositions, black triangles show measured values of eight delineated tissue groups. A stoichiometric HLUT for photon therapy is superimposed. The additional value of Z_{eff} can be observed for tissues that have similar CT numbers (or $\hat{\rho}_e$), but different Z_{eff}.

(Fig. 6.6). Fig. 6.7 underlines, that tissue *mixtures* (i.e. present in the mastoid cavity) behave differently to tissue compounds and that DECT can differentiate both.

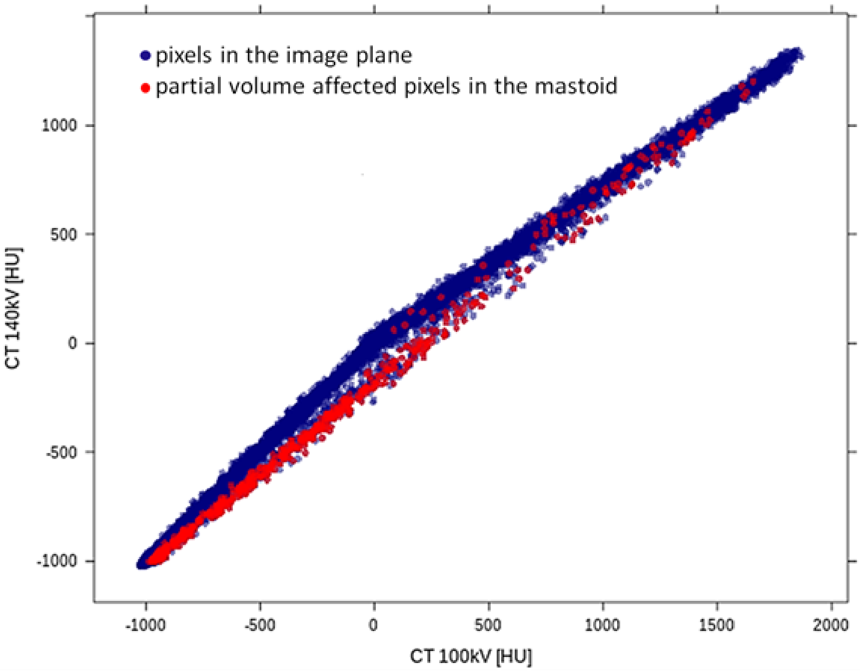

Figure 6.7: Labeled partial volume affected images in the mastoid cavity superimposed with the surrounding pixels.

Results presented in Fig. 5.24 suggest, that partial volume effects decrease with higher X-ray tube voltages as differences in attenuation coefficients decrease and the SECT 140Sn kV SPR prediction is closer to the DECT based prediction. Glover and Pelc [1980] showed that partial volume effects aggravate with the square root of attenuation gradients of tissue mixtures present in one pixel. In the mastoid region, gradients are particularly pronounced due to the bone/air interfaces (Fig. 6.8). It remains to be clarified, why the SECT predicts higher SPR in the mastoid cavity compared to DECT, although the non-linear partial volume effect usually provokes an underestimation of CT numbers. It is furthermore worthwhile to investigate the dependency of partial volume effects on the employed X-ray tube voltage. With higher X-ray tube voltages, partial volume effect will get smaller (cf. Fig. 6.8) due to the smaller influence of the photoelectric effect (Z_{eff} dependency), which again supports the choice of higher tube voltages. Future work is necessary to investigate in more detail, how DECT can improve SPR prediction for voxels affected by the partial volume effect particularly via the information on Z_{eff}.

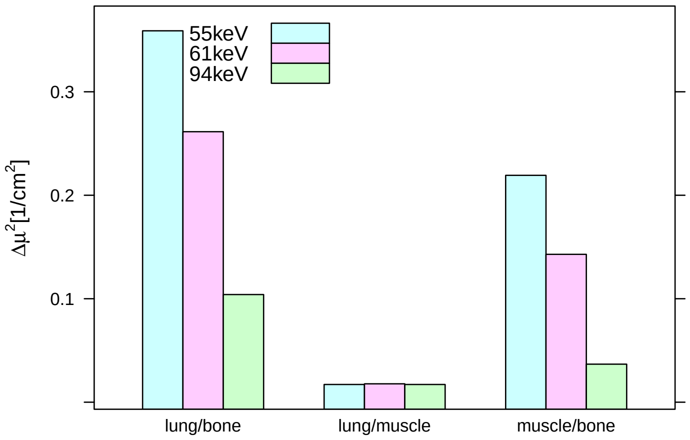

Figure 6.8: Quadratic differences of linear attenuation coefficients of bone/lung, bone/muscle and muscle/lung interfaces at different X-ray energies similar to the mean photon energies of the Siemens Somatom Definition (80/100/140Sn kV). Tissue composition taken from ICRU [1989], photon attenuation coefficient data taken from Berger et al. [1998].

6.3.2 SECT- and DECT-based treatment plan comparison

Both treatment plans showed, that range differences are related to the additional DECT information since the choice of reconstruction kernels or X-ray tube voltage for the SECT images has only a small influence on range determination (Fig. 5.25, Fig. 5.27). Range differences basically reflect SPR discrepancies observed in Sec. 5.3 which showed to be considerable high in dense bones (Fig. 5.20, Fig. 5.23). The overshoot of the DECT-based plan in the ventricle region can be explained with the large SPR difference in the dense cortical bone which has to be traversed by the particle beam. The lower SPR assignment for the ventricle by DECT has no significant influence on the range, as only small part of the ventricle is crossed by the treatment field (Fig. 4.4, Fig. 5.25).

Future studies of different treatment sides in clinical patient DECT images would be of great interest to identify further tissues where the SPR prediction differs systematically between SECT and DECT. For this, comprehensive patient image sets should be consistent in the SECT and DECT acquisition which implies to scan the patient with the same (reasonable high) image dose, without contrast agent and with the smallest time delay possible in between both acquisitions to reduce motion artifacts. Generating this SECT and DECT image set would mean to increase the dose level for the individual patient by a factor of two which may not be ethically justifiable. Alternatively, animals' tissue could be scanned with DECT and SECT and should be compared to a reference SPR map (i.e. derived with heavy ion CT). For such an absolute quantification of SPR residuals, careful attention on comparable image quality, geometric reproducibility and tissue stability over time is essential.

6.3.3 Tissue composition and photon HLUT verification

DECT measurements of the tissue surrogate proved how accurate the DECT can determine the $\hat{\rho}_\mathrm{e}$ and Z_eff. The $\hat{\rho}_\mathrm{e}$ determination for aluminum agreed within 2.5 % as compared to reference values (Tab. A.5). In contrast, Fig. 5.29, Fig. 5.30 and Fig. 5.31 clearly show significant discrepancies of $\hat{\rho}_\mathrm{e}$, Z_eff and CT numbers measured in real tissue compared to reference or predicted values of tabulated tissue compositions. The SECT translates high CT numbers either to too high Z_eff instead of higher $\hat{\rho}_\mathrm{e}$ (Fig. 5.30, Fig. 5.31), which results in a lower HLUT slope (Fig. 5.29), or the DECT measures too low Z_eff, respectively too high $\hat{\rho}_\mathrm{e}$.

Differences are observed particularly in the bone region. As mentioned above, this approach provides the means only for a relative comparison. The discrepancies shown in Sec. 5.3.3 ask therefore for an absolute validation, since the DECT contrasts could also be affected i.e. by the initial measurement of a single calibration material (Sec. 3.5). Further DECT measurements with dense and high Z bone phantom materials with compositions as close as possible to the natural equivalences are mandatory to validate the DECT-based $\hat{\rho}_\mathrm{e}$ and Z_eff determination in bone compositions.

The superimposed delineated tissues proved that specific tissue groups can differ from the majority of tissues. The delineated petrous part of the temporal bone exhibits for example an exceptional high $\hat{\rho}_\mathrm{e}$. These differences can be resolved only with DECT that is able to separate $\hat{\rho}_\mathrm{e}$ and Z_eff.

6.3.4 Noise quantification of SPR prediction

Fig. 5.32 shows, that an additional smoothing of the CT number maps was applied by the vendor since the relative noise levels of $\hat{\rho}_\mathrm{e}$ derived from DECT images (dose split to both tubes) are similar to the noise levels of the SECT CT number (120 kV with the full dose). Future investigations should determine, whether a high image dose for the low kV acquisition could improve the Z_eff precision.

Resulting noise levels of SPR prediction are elevated by 0.2-0.4 pp with DECT compared to SECT. The elevated Z_eff in the muscle surrogate was found to elevate the SPR noise by roughly 0.2 pp compared to the bone surrogate. Future investigations should characterize the consequences of noisy SPR maps for treatment plans in ion therapy. The applied image dose in planning CT protocols should be discussed. Diagnostic and therapy planning images should be better differentiated. Using MV CT takes the same line: the linearity of CT numbers in $\hat{\rho}_\mathrm{e}$ enables a very robust HLUT as discussed in the previous sections and metal artifacts are significantly reduced due to the higher photon energy. Major drawbacks for body contour, target and organ delineation are expected due to the poor image quality and due to the decreased detector efficiency for MeV photons. As already mentioned in the previous sections, the 140Sn kV image acquisition is a promising alternative and should be further investigated as a possible standard for the SECT acquisition. Additionally, it should be investigated how much dose is necessary for a treatment planning CT. For range determination, SPR noise will cancel out with tumor proximity in depth and would only be critical for superficial tumors. With the standardized consult of other image modalities in the treatment planning process of modern radiotherapy, acceptable noise levels in the planning CT need to be revised in the future.

6.4 Tissue decomposition for MC dose algorithms

6.4.1 Deriving ρ from $\hat{\rho}_e$

Compared with a single CT number, the $\hat{\rho}_e$ is a more accurate predictor for ρ. The DECT fit of ρ to $\hat{\rho}_e$ is more robust as compare to the five SECT fits in the CT number that showed an additional discontinuity of 0.004 g/cm^3 (Hünemohr et al. [2014c]). Particularly in the soft tissue region, ambiguities in the CT number or SPR can appear since both are influenced by the elemental composition (represented by Z_{eff}) *and* the $\hat{\rho}_e$. Future work could additionally improve the ρ to $\hat{\rho}_e$ fit for adipose tissue: due to the large amount of hydrogen in adipose tissue, the $\langle Z/A \rangle$ is elevated and one could introduce an additional fit segment dedicated to hydrogen rich materials starting from adipose tissue up to bone marrow (cf. Fig. A.6, Hünemohr et al. [2014c]). The SECT HU-to-ρ fit for the lung tissue region could be improved by interpolating between lung and muscle tissue instead of air and adipose tissue that significantly differ in their $\langle Z/A \rangle$ ratios (Hünemohr et al. [2014c]) and do not represent lung tissue compositions.

6.4.2 Tissue composition

Particularly tissues that are not well represented by the mean composition of the corresponding CT number bin benefit from the additional DECT information (Fig. 5.35, Fig. 5.36): Similarly to the tissues identified in the patient case (Sec. 5.3) these tissues have an unusual hydrogen mass weight (cf. ventricles) or different carbon or oxygen mass weights as compare to neighboring tissues in the CT number bin.

However, for SPR prediction the ρ has to be predicted as accurately as possible and correct elemental composition is only of minor importance for MC-based dose planning in ion therapy. The continuous assignment of I-values instead of fix I-values for each of the SECT CT number bins improves the I-value determination by 0.6-0.9 pp which hardly influences the SPR prediction for ions (only $\approx 0.1\,\%$, Paganetti [2012]). In contrast, for 250 kV, 18 MV photon and 18 MeV electron beams Bazalova et al. [2008] showed significant improvements of absorbed dose predictions in soft tissue with a DECT-based tissue segmentation scheme in the $\hat{\rho}_e/Z_{\text{eff}}$ space. Malusek et al. [2013] presented a three material decomposition for brachytherapy and Landry et al. [2013a] assigned elemental

Table 6.2: Statistical properties and fit parameter results of the DECT-based elemental mass fraction fits for 47 soft tissues and 24 bone tissues according to $w_\mathrm{i} = a_\mathrm{i} + b_\mathrm{i} \cdot Z_\mathrm{eff}$. Mean and maximum deviations to the ground truth are given for every element and are compared for SECT and DECT separately.

		$Z_\mathrm{eff} < 8.2$				$Z_\mathrm{eff} \geq 8.2$					
		H	C	N	O	H	C	N	O	Ca	P
DECT	a_i	0.1614***	3.5415***	-0.0468	2.6309***	0.2247***	0.7992***	0.0156	0.5108***	–0.3820***	-0.1682***
	b_i	-0.0078***	-0.4679***	0.01037*	0.4615***	-0.0140***	-0.0447***	0.0017	-0.0081	0.0450***	0.0200***
	R^2	0.3694	0.9604	0.0780	0.9456	0.9727	0.3563	0.0672	0.0200	0.9951	0.9937
	mean diff. (pp)	0.3	1.9	0.9	2.4	0.1	3.9	0.4	3.6	0.2	0.1
	max diff. (pp)	1.0	15.3	3.6	15.7	0.3	8.0	0.9	7.7	0.6	0.4
	BIC	-386	-177	-269	-163	-229	-73	-180	-75	-214	-246

$^{***}p < 0.01$, $^{**}p < 0.05$, $^{*}p < 0.1$

composition according to the minimal Mahalanobis distance to a reference composition in the $\hat{\rho}_\mathrm{e}/Z_\mathrm{eff}$ space (Hünemohr et al. [2014c]). Complementarily, the presented approach in this thesis *continuously* assigns tissue compositions and is therewith "able to reflect variations of compositions between reference tissues" (Hünemohr et al. [2014c]) which could apply for example for tumor tissues.

Likewise in ion therapy, the accuracy of PET- and prompt-gamma-based range verification would benefit from the improved carbon and oxygen mass weight prediction that represent both important interaction channels (Parodi et al. [2007], Smeets et al. [2012], Min et al. [2010]). For other elements (soft tissue hydrogen and nitrogen, bone calcium, Tab. 5.3), the full DECT information is not necessarily of additional value (Hünemohr et al. [2014c]). Tab. 6.2 summarizes therefore parameters with corresponding statistical evaluations for elemental fits that take only the information on Z_eff into account ($w_i = a \cdot Z_\mathrm{eff} + b$). When $\hat{\rho}_\mathrm{e}$ is not exploited, prediction of elemental mass weights exhibit larger residuals (Tab. 5.3 vs. Tab. 6.2). In addition, lower BIC values (Krueger et al. [2002]) of the complex model (Eq. 4.3, Tab. 5.3) indicate better quality of the fitting model as compared to the simple fit in Z_eff (Tab. 6.2). It is therefore recommended to exploit both DECT contrasts, if available, for the composition prediction for MC-based dose planning.

Influence of noise associated $\hat{\rho}_\mathrm{e}$ and Z_eff on elemental mass weight predictions

Presented elemental fits (Tab. 5.3) were tested with noise associated base data ($\hat{\rho}_\mathrm{e}$ and Z_eff) in order to quantify the uncertainties of mass weight predictions for realistic image data. This noise setting [2] represents a worst case scenario since Fig. A.4 shows that both DECT contrasts are usually correlated. Predicted elemental mass weights with the uncertainty resulting from noise associated DECT base data are depicted in Fig. 6.9. Mean uncertainties observed for the predicted mass weights from noise associated base data are

---

[2] "A uniform Gaussian distributed noise with one standard deviation of 0.01 units of $\hat{\rho}_\mathrm{e}$ and 0.2 units of Z_eff [..] was applied in the simulation of 1000 measurements of every material" (Hünemohr et al. [2014c]).

as followed: 0.1 % H, 9.9 % C, 0.9 % N, 10.3 % O, 1.1 % P, and 0.2 % Ca (Hünemohr et al. [2014c]). In comparison, Landry et al. [2013a] observed noise levels of 5 % for the carbon and oxygen mass weight at a dose of 40 mGy and with iteratively reconstructed images. It was also stated in Landry et al. [2013a] that DECT would benefit more from reduced noise levels as compare with SECT. Future investigations on DECT-based tissue decomposition for MC dose calculation should therefore exploit iterative reconstruction algorithm and test, whether the presented approach is suitable in clinical patient images that are affected by artifacts.

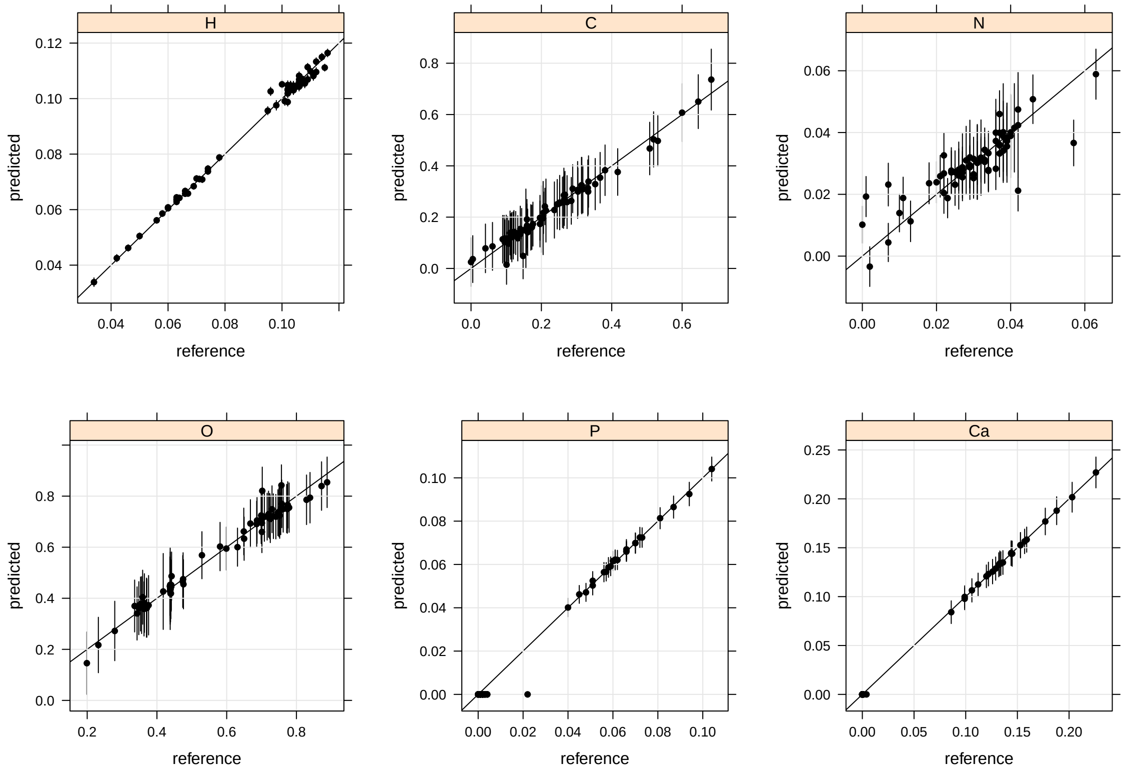

Figure 6.9: Results (mean±sd) for elemental mass weight predictions from noise associated DECT base data ($\hat{\rho}_e$ and Z_{eff}).

6.4.3 Range study

Differences observed for the electronic SPR (DECT to SECT predictions, Fig. 5.37) directly translated into range differences as nuclear interactions hardly influence range. Variations of 10 % in the carbon and oxygen mass weight ("HCO") have not significant influence on the range. It is therefore concluded, that particularly the $\hat{\rho}_e$ image is of high value for MC simulations. Accurate elemental mass weight prediction (influencing also the I-value) and the Z_{eff} image is only of minor importance for range prediction. These findings correspond to the results discussed for the analytical planning dose calculation (Sec. 6.2 and Sec. 6.3). A single energy CT number is affected by ρ and Z making the exploration of the spectral attenuation information with DECT valuable for ion therapy. Particularly the separation to the $\hat{\rho}_e$ image, that is not affected by the Z_{eff}, allows a better tissue characterization for ion therapy.

Analog to the analytical TPS, MC systems cannot handle two sets of CT data images and future work should focus on the full integration of DECT image data. It would be particularly beneficial to exploit $\hat{\rho}_e$ directly for the electronic SPR estimation instead of the standard detour via ρ (and a subsequent SPR/$\hat{\rho}_e$ determination with the predicted elemental mass weights).

Similarly to the studies on the analytical stoichiometric HLUT, the presented characterizations for MC-based dose algorithm were also based on the tissue set summarized in Schneider et al. [2000]. Novel measurement data of tissue compositions would be of great interest and should also provide more detail on tissue variations in ρ and $\hat{\rho}_e$ as well as tissue pathologies such as tumor tissue.

6.5 Metal artifact reduction with DECT

Artifacts in CT imaging due to high Z metals consists of two types: photon starvation provoking streak artifacts and beam hardening artifacts provoking lower CT number e.g. in between two hip prosthesis or cupping artifacts. The first (streak artifacts) can hardly be corrected with the DECT technique as the information is also missing in both raw data sets. The only way to overcome the lack of information is to employ higher photon energies or to try a different projection angle and avoid shooting through the thickest part of the metal.

On the contrary, metal artifact reduction in DECT imaging is based on the principle of "monochromatic image" calculation. A monochromatic image can be reconstructed via material decomposition into two base materials of mass attenuation coefficients (Eq. 2.17 repeated):

$$\mu(E_i) = w_1 \frac{\mu_1(E_i)}{\rho_1} + w_2 \frac{\mu_2(E_i)}{\rho_2}. \tag{6.1}$$

Measuring $\mu(E_i)$ at two distinct photon spectra enables to determine both mass weights w_1 and w_2 of the base materials that exhibits the known mass attenuation coefficients $\mu_1(E_i)/\rho_1$ and $\mu_2(E_i)/\rho_2$. As Eq. 2.11 is a non-linear equation, a calibration material composed of base materials with known mass weights is mandatory. In practice, various mixtures of the two base materials are measured at different spectra energies to determine the prior knowledge on $\mu_1(E_i)$ and $\mu_2(E_i)$ (Yu et al. [2011], Yu et al. [2012]). The corresponding monochromatic CT number at an energy E of choice is derived according to Eq. 2.2 (Goodsitt et al. [2011]):

$$\text{CT no}\,(E) = \left(\frac{w_1 \cdot \mu_1(E)/\rho_1 + w_2 \cdot \mu_2(E)/\rho_2 - \mu_{\rm w}(E)}{\mu_{\rm w}(E)}\right) \cdot 1000\,\text{HU}. \tag{6.2}$$

DECT techniques in which projections of both spectra are geometrically consistent (i.e. in the rapid kV switching GE scanner, Sec. 2.2) allow a "virtual monochromatic" image reconstruction that is in theory free of beam hardening artifacts. In practice, mono-energetic reconstructions for low energies showed beam hardening effects as well (Goodsitt et al. [2011]). On the contrary, dual source CT scanners allow only a "pseudo monochromatic" image calculation in the artifact affected image space (Bamberg et al. [2011]). Reconstructing "pseudo monochromatic" images at low keV provide an enhanced image contrast and allow therewith to reduce either the amount of contrast agent or to reduce the image dose at the same diagnostic image quality. Reconstructing pseudo monochromatic images at high keV (i.e. 105 keV, Bamberg et al. [2011]) reduce artifacts that emerge from high Z materials, sufficient photon statistics assumed. In the literature promising results were achieved for small metal implants through which the high energy photon spectra is not perturbed (Bamberg et al. [2011]). For massive solid metal implants like hip prosthesis, DECT does not necessarily improve image quality. It was rather seen that image space algorithms aggravate streaking artifact present in both images (Yu et al. [2012]).

Fig. 6.10 shows the $\hat{\rho}_{\rm e}$ image of the patient head and neck case (Sec. 5.3) affected by severe metal artifacts caused by dental implants. Original CT number images were reconstructed with an in-house metal artifact reduction (MAR) workstation provided by Siemens (filtered back projection with an additional 2D iMAR, default settings, version 9.7, "Korrekturprofil dental"). The algorithm is based on Meyer et al. [2010] and Meyer et al. [2012] which is usually exploited for SECT data and not specifically optimized for DECT raw data. In the sinogram space, a "metal sinogram" is extracted from which adjacent sinusoidals are interpolated and normalized. Depicted $\hat{\rho}_{\rm e}$ maps show that iMAR can achieve good results in slices with small metal geometries present, while in other slices image information is missing and streaking artifacts can aggravate.

For dual source dual energy scanners, the focus should rather be to exploit further the available energy information. Available SECT MAR corrections should be applied to both raw data sets in combination with iterative reconstruction algorithms to improve the base image data further (Verburg and Seco [2012]). For reliable radiotherapy treatment planning it necessary to characterize and quantify the CT number assignment in between and adjacent to the metal geometries. Tremmel [2012] showed that the presented $\hat{\rho}_{\rm e}$ and $Z_{\rm eff}$ algorithm (Sec. 3.5) reaches the limit for metals having a Z>22.

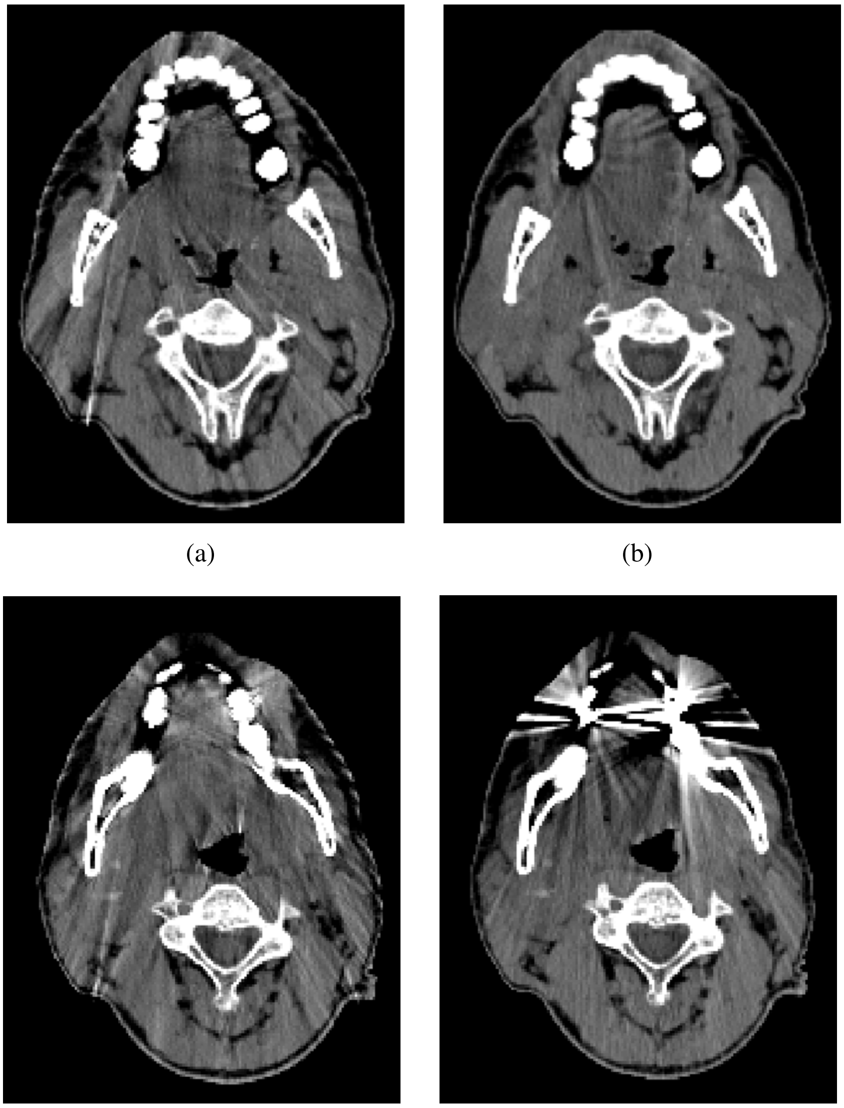

(a) (b)

(c) (d)

Figure 6.10: $\hat{\rho}_\mathrm{e}$ images of two axial slices of the head and neck patient (Sec. 5.3). On the left hand side images ((a),(c)) no iMAR correction was applied while (b) and (c) show $\hat{\rho}_\mathrm{e}$ images reconstructed with an "iMAR" correction. The sinogram-based correction was calculated at the DKFZ in-house workstation provided by Siemens. The upper image slice shows the reduction of streaking artifacts (in particular for the soft tissue at the chin) while the lower slice depicts that iMAR can also aggravate streaking artifacts. The implemented algorithm is not specifically foreseen for DECT raw data and does not exploit the spectral information. The iMAR workstation is rather used for SECT data.

7 Conclusions

"What you see is all there is"
Daniel Kahneman

Treatment planning in proton and ion radiotherapy is based on CT images that have to be translated to stopping power ratio maps for ions. The reliability of the CT image information and the corresponding calibration is crucial for the accurate dose delivery. This thesis aimed to quantify uncertainties related to the generation of the stoichiometric calibration and investigated the dual energy CT technique as an alternative for analytical and Monte-Carlo-based dose planning systems.

The stoichiometric calibration (Schneider et al. [2000]), today's gold standard, was found to vary up to 2.4 % (additive scenario) in the bone region dependent on different settings for the CT number measurement of tissue surrogates. Optimization of the photoelectric parameter k_2 was found to be more straightforward than the optimization of the coherent scattering parameter k_1. The accurate determination of k_2 is crucial for the HLUT slope in the bone region, while the considerable sensitivity of k_1 to the measurement setting was found to be negligible for correct prediction of CT numbers (cf. negative k_1 values). These results therefore suggest to include more high Z and high mass density materials in the initial CT number measurement to achieve a robust determination of k_2. Future investigations should determine whether the parametrization of the photon attenuation needs to be optimized for soft and bone tissue separately. It was demonstrated also, that the calibration process gets more robust with higher photon energy. It is therefore strongly suggested to employ higher X-ray tube voltages for treatment planning CTs (i.e. 140 kV with additional filters) in combination with advanced beam hardening correction kernels. These results reveal that a better differentiation between the requirements of diagnostic and treatment planning CTs is necessary for ion therapy. The integration and consultation of various imaging modalities in the modern treatment planning process provide sufficient soft tissue contrast for structure delineation. As a consequence, CT protocol parameters should be reviewed not in terms of diagnostic quality but for treatment planning purposes i.e. with special regard on the employed X-ray tube voltage and current.

With a clinical dual source scanner, an excellent accuracy of measured $\hat{\rho}_e$ ($(0.4 \pm 0.3)\%$) and Z_{eff} ($(1.7 \pm 1.4)\%$) could be achieved for tissue surrogates. Both image-based calculated contrasts allowed to predict the SPR (approach suggested by Yang et al. [2010]) within $(0.6 \pm 0.3)\%$ compared to measured WEPL (Hünemohr et al. [2014a]). The logarithm of the mean excitation energy was correlated to Z_{eff}. The calculation of Z_{eff} was found to agree slightly better with reference data when the 80/140Sn kV voltage pair was employed compared with 100/140Sn kV. Future investigations should clarify, whether an even lower X-ray tube voltage (available in the third dual source scanner generation) at higher tube currents can improve the Z_{eff} determination for soft tissue. The correlation of $\ln I$ to Z_{eff} was characterized for intermediate Z_{eff} (Hünemohr et al. [2014b]) and identified the potential of Z_{eff} to improve SPR prediction for pixels affected by partial volume artifacts. Additionally, it was suggested to exploit the information on measured $\hat{\rho}_e/Z_{\text{eff}}$ pairs for $\ln I$ to Z_{eff} correlations specified for materials of unusual compositions compared to tissues (i.e. low Z metals or polymers). The presented investigations underlined that $\hat{\rho}_e$ is the crucial tissue parameter for an accurate and precise SPR prediction. Although the information on Z_{eff} theoretically improves SPR prediction for some tissue compositions, it remains to be determined in the future whether the information on $\hat{\rho}_e$ is not sufficient for the SPR prediction in clinical patient images. Therefore, the technical prerequisites in the planning systems that enable dose calculation on the two DECT image stacks need to be established.

In a first patient study, SPR predictions based on SECT and DECT images could be compared relatively. SPR differences of 2 % in the ventricles and 5-8 % in the petrous part of the temporal bone were found. Results suggested that, due to the separation of $\hat{\rho}_e$ and Z_{eff}, the DECT can resolve tissues of unusual composition compared to tissues neighboring in the HLUT. The presented discrepancies, however, strongly ask for a comparison of SECT- and DECT-based SPR prediction with a reference method like heavy ion CT e.g. in animal tissue. It would be of great importance to include high density and high Z bone and quantify the uncertainties emerging from imaging artifacts like beam hardening and partial volume effects. Hypothetical carbon ion treatment plans for the head patient showed, that SPR differences in the petrous part of the temporal bone can result in relative range differences of up to 4 mm when crossing the structure. Noise levels of DECT-based SPR predictions for two tissue surrogates were found to be elevated by only 0.2-0.4 pp compared to SECT measured at the same image dose. Future investigations should therefore review tube currents, related CT image doses and noise levels for CT planning protocols and should characterize the consequences of noisy SPR maps for treatment plans in ion therapy.

Exploiting both DECT contrasts for tissue decomposition in Monte-Carlo-based dose calculation improves particularly the carbon and oxygen mass weight prediction as compared with the standard SECT conversion scheme (Hünemohr et al. [2014c]). For accurate ion range prediction, however, a correct mass density assignment was rather found to be the crucial factor. For that purpose, $\hat{\rho}_e$ was found to be a better and more robust predictor compared with a SECT CT number that is affected by both, $\hat{\rho}_e$ and Z_{eff}. Particularly tissues with unusual compositions (different hydrogen, oxygen or carbon mass weight) benefit from the improved mass density assignment.

From the presented results it is concluded, that the DECT separation of $\hat{\rho}_e$ from Z_{eff} is of high value for the proton and ion therapy planning. SPR uncertainties resulting from ambiguities in SECT CT numbers can be significantly reduced. The spectral information available with DECT is particularly of help for tissues, which have an uncommon composition or mass density. It is therefore also of great interest for ion therapy to have better knowledge on variation in the tissue composition and mass density with age, sex, health status and in tumor pathologies. Reference tabulated compositions which represent the basis for many investigations in radiotherapy and were measured in the middle of last century, have to be updated using modern analyze methods. Presented results indicated also the necessity of novel phantoms for ion therapy that exhibit realistic photon attenuation *and* interaction with ions to assess the conversion schemes.

A validation of DECT-predicted SPR in absolute terms with a reference method, such as heavy ion CT, would help to translate the presented potential benefits of DECT to its future clinical application in ion radiotherapy.

Bibliography

AAPM (2008). The Measurement, Reporting, and Management of Radiation Dose in CT: Report of AAPM Task Group 23 of the Diagnostic Imaging Council CT Committee. *American Association of Physicists in Medicine*. (cited on page 10)

Alvarez, R. E. and Macovski, A. (1976). Energy-selective Reconstructions in X-ray Computerized Tomography. *Physics in Medicine and Biology*, 21(5):733–744. (cited on pages 10, 12, 29, and 95)

Andreo, P. (2009). On the clinical spatial resolution achievable with protons and heavier charged particle radiotherapy beams. *Physics in Medicine and Biology*, 54(11):N205–N215. (cited on pages 17 and 98)

Bamberg, F., Dierks, A., Nikolaou, K., Reiser, M. F., Becker, C. R., and Johnson, T. R. (2011). Metal artifact reduction by dual energy computed tomography using monoenergetic extrapolation. *European Radiology*, 21(7):1424–1429. (cited on page 110)

Bazalova, M., Carrier, J.-F., Beaulieu, L., and Verhaegen, F. (2008). Dual-energy CT-based material extraction for tissue segmentation in Monte Carlo dose calculations. *Physics in Medicine and Biology*, 53(9):2439–2456. (cited on pages 13, 95, and 106)

Bendl, R. (2011). *Benutzerhandbuch VIRTUOS Version VOX-4.7.9*. DKFZ. (cited on page 34)

Bendl, R., Pross, J., Keller, M., Bürkelbach, J., and Schlegel, W. (1993). VIRTUOS—A program for VIRTUal radiotherapy Simulation. In *Computer Assisted Radiology/Computergestützte Radiologie*, pages 676–682. Springer. (cited on page 33)

Berger, M. J., Hubbell, J., Seltzer, S., Chang, J., Coursey, J., Sukumar, R., Zucker, D., and Olsen, K. (1998). XCOM: photon cross sections database. *NIST Standard Reference Database*, 8(1):3587–3597. (cited on pages 5, 7, and 104)

Bethe, H. (1930). Zur Theorie des Durchgangs schneller Korpuskularstrahlen durch Materie. *Annalen der Physik*, 397(3):325–400. (cited on page 14)

Bichsel, H. and Hiraoka, T. (1992). Energy loss of 70 MeV protons in elements. *Nuclear Instruments and Methods in Physics Research Section B: Beam Interactions with Materials and Atoms*, 66(3):345–351. (cited on page 17)

Bloch, F. (1933). Bremsvermögen von Atomen mit mehreren Elektronen. *Zeitschrift für Physik A Hadrons and Nuclei*, 81(5):363–376. (cited on pages 14 and 16)

Bourque, A. E., Carrier, J.-F., and Bouchard, H. (2014). A stoichiometric calibration method for dual energy computed tomography. *Physics in Medicine and Biology*, 59(8):2059. (cited on pages 93, 95, and 96)

Bragg, W. H. and Kleeman, R. (1905). XXXIX. On the α particles of radium, and their loss of range in passing through various atoms and molecules. *The London, Edinburgh, and Dublin Philosophical Magazine and Journal of Science*, 10(57):318–340. (cited on page 16)

Brooks, R. A. (1977). A quantitative theory of the Hounsfield Unit and Its Application to Dual Energy Scanning. *Journal of Computer Assisted Tomography*, 1(4):487–493. (cited on page 13)

Bushberg, J. T. and Boone, J. M. (2011). *The essential physics of medical imaging*. Lippincott Williams & Wilkins. (cited on pages 4, 5, 6, 7, and 8)

Chen, G. T., Singh, R. P., Castro, J. R., Lyman, J. T., and Quivey, J. M. (1979). Treatment planning for heavy ion radiotherapy. *International Journal of Radiation Oncology*Biology*Physics*, 5(10):1809 – 1819. (cited on pages 13, 18, 19, 25, and 26)

Cheng, C.-W., Zhao, L., Wolanski, M., Zhao, Q., James, J., Dikeman, K., Mills, M., Li, M., Srivastava, S. P., Lu, X. Q., et al. (2013). Comparison of tissue characterization curves for different CT scanners: implication in proton therapy treatment planning. *Translational Cancer Research*, 1(4):236–246. (cited on page 89)

de Kock, E. A. and Schreuder, A. N. (1996). Comments "The calibration of CT Hounsfield units for radiotherapy treatment planning". *Physics in Medicine and Biology*, 41:1524–1526. (cited on pages 39, 93, and 99)

De Marzi, L., Lesven, C., Ferrand, R., Sage, J., Boulé, T., and Mazal, A. (2013). Calibration of CT Hounsfield units for proton therapy treatment planning: use of kilovoltage and megavoltage images and comparison of parameterized methods. *Physics in Medicine and Biology*, 58(12):4255. (cited on page 38)

Dechow, P. C., Wang, Q., and Peterson, J. (2010). Edentulation alters material properties of cortical bone in the human craniofacial skeleton: functional implications for craniofacial structure in primate evolution. *The Anatomical Record*, 293(4):618–629. (cited on page 101)

Evans, R. D. and Noyau, A. (1955). *The atomic nucleus*. McGraw-Hill New York. (cited on page 6)

Fano, U. (1964). Penetrations of protons, alpha particles, and mesons. *Studies in Penetration of Charged Particles in Matter*, 1133:287. (cited on pages 15, 16, and 17)

Floca, R. (2010). MatchPoint: on bridging the innovation gap between algorithmic research and clinical use in image registration. In *World Congress on Medical Physics and Biomedical Engineering, September 7-12, 2009, Munich, Germany*, pages 1105–1108. Springer. (cited on page 34)

Flohr, T., McCollough, C., Bruder, H., Petersilka, M., Gruber, K., Süss, C., Grasruck, M., Stierstorfer, K., Krauss, B., Raupach, R., Primak, A., Küttner, A., Achenbach, S., Becker, C., Kopp, A., and Ohnesorge, B. (2006). First performance evaluation of a dual-source CT (DSCT) system. *European Radiology*, 16:1405–1405. (cited on page 11)

Forbes, R., Cooper, A., and Mitchell, H. (1953). The composition of the adult human body as determined by chemical analysis. *Journal of Biological Chemistry*, 203(1):359–366. (cited on page 24)

Forbes, R., Mitchell, H., and Cooper, A. (1956). Further studies on the gross composition and mineral elements of the adult human body. *Journal of Biological Chemistry*, 223(2):969–975. (cited on page 24)

Gallas, R. R., Hünemohr, N., Runz, A., Niebuhr, N. I., Jäkel, O., and Greilich, S. (2014). An anthropomorphic multimodality (CT/MRI) phantom prototype for end-to-end tests in radiation therapy. *arXiv e-prints*, 1402.3793. (cited on pages 23 and 96)

Gammex (2011). Tissue Characterization Phantom 467. *Middleton USA*. (cited on page 23)

Glover, G. and Pelc, N. (1980). Nonlinear partial volume artifacts in x-ray computed tomography. *Medical Physics*, 7(3):238–248. (cited on page 103)

Goodsitt, M. M., Christodoulou, E. G., and Larson, S. C. (2011). Accuracies of the synthesized monochromatic CT numbers and effective atomic numbers obtained with a rapid kVp switching dual energy CT scanner. *Medical Physics*, 38(4):2222–2232. (cited on pages 11, 12, 13, and 110)

Haberer, T., Debus, J., Eickhoff, H., Jäkel, O., Schulz-Ertner, D., and Weber, U. (2004). The Heidelberg ion therapy center. *Radiotherapy and Oncology*, 73:S186–S190. (cited on page 33)

Heismann, B. (2005). Atomic number measurement precision of spectral decomposition methods for ct. In *Nuclear Science Symposium Conference Record, 2005 IEEE*, volume 5, pages 2741–2742. IEEE. (cited on page 95)

Heismann, B., Leppert, J., and Stierstorfer, K. (2003). Density and atomic number measurements with spectral x-ray attenuation method. *Journal of Applied Physics*, 94(3):2073–2079. (cited on page 95)

Henkner, K. (2009). *Monte Carlo Simulations for Dosimetry and Treatment Planning in Hadron Therapy*. Dissertation, Martin-Luther-Universität Halle-Wittenberg. (cited on pages 17 and 98)

Hünemohr, N. (2011). Improvement of ion therapy planning by the use of dual energy computed tomography. Diplomarbeit, University of Heidelberg. (cited on page 39)

Hünemohr, N., Krauss, B., Dinkel, J., Gillmann, C., Ackermann, B., Jäkel, O., and Greilich, S. (2013). Ion range estimation by using dual energy computed tomography. *Zeitschrift für Medizinische Physik* , 23(4):300 – 313. (cited on pages 22, 33, 94, 98, and 99)

Hünemohr, N., Krauss, B., Tremmel, C., Ackermann, B., Jäkel, O., and Greilich, S. (2014a). Experimental verification of ion stopping power prediction from dual energy CT data in tissue surrogates. *Physics in Medicine and Biology*, 59(1):83–96. (cited on pages 22, 29, 30, 31, 32, 41, 42, 65, 66, 67, 68, 96, 113, and IV)

Hünemohr, N., Niebuhr, N., and Greilich, S. (2014b). Reply on "Comment on 'Experimental verification of ion stopping power prediction from dual energy CT data in tissue surrogates'". *Physics in Medicine and Biology*, to be published. (cited on pages 41, 97, 114, and VIII)

Hünemohr, N., Paganetti, H., Greilich, S., Jäkel, O., and Seco, J. (2014c). Tissue decomposition from dual energy CT data for MC based dose calculation in particle therapy. *Medical Physics*, 41(6):061714. (cited on pages 35, 47, 48, 49, 50, 78, 81, 84, 85, 86, 87, 106, 107, 108, 114, and XII)

Hounsfield, G. N. (1973). Computerized transverse axial scanning (tomography): Part 1. Description of system. *The British Journal of Radiology*, 46(552):1016–1022. (cited on pages 3 and 10)

Hsu, R.-F. (1979). Mean excitation energy of the elements proton penetration in matter. *Journal of Normal University*, 24:318–352. (cited on page 16)

IAEA (2000). Absorbed Dose Determination in External Beam Radiotherapy: An International Code of Practice for Dosimetry based on Standards of Absorbed Dose to Water (TRS-398). (cited on page 18)

ICRP (1975). Reference Man (Report 23). *Journal of the ICRP*. (cited on page 24)

ICRU (1984). Stopping powers for electrons and positrons (Report 37). *Journal of the ICRU*. (cited on page 16)

ICRU (1989). Tissue substitutes in radiation dosimetry and measurement (Report 44) . *Journal of the ICRU*. (cited on pages 5 and 104)

ICRU (1993). Stopping Powers and Ranges for Protons and Alpha Particles (Report 49). *Journal of the ICRU*. (cited on pages 14, 16, 17, 32, and VIII)

ICRU (2005). Stopping of ions heavier than helium (Report 73). *Journal of the ICRU*. (cited on pages 15, 16, and 17)

Jackson, D. F. and Hawkes, D. (1981). X-ray attenuation coefficients of elements and mixtures. *Physics Reports*, 70(3):169–233. (cited on pages 4, 26, 94, and 99)

Jackson, J. D. (2006). *Klassische Elektrodynamik*. Walter de Gruyter. (cited on page 16)

Jäkel, O. (2001). Relation between carbon ion ranges and X-ray CT numbers. *Medical Physics*, 28(4):701–703. (cited on pages 18, 22, and 26)

Johns, H. E. (1983). *The Physics of Radiology*. Charles River Media. (cited on pages 4, 5, 6, and 31)

Johnson, T. R., Fink, C., Schönberg, S. O., and Reiser, M. F. (2011). *Dual energy CT in clinical practice*. Springer. (cited on pages 12, 13, and 21)

Kalender, W. A. (2006). *Computertomographie: Grundlagen, Gerätetechnologie, Bildqualität, Anwendungen*. Publicis Corporate Publ. (cited on page 3)

Kanematsu, N., Matsufuji, N., Kohno, R., Minohara, S., and Kanai, T. (2003). A CT calibration method based on the polybinary tissue model for radiotherapy treatment planning. *Physics in Medicine and Biology*, 48(8):1053. (cited on pages 19 and 25)

Kemerink, G. J., Lamers, R. J. S., Thelissen, G. R. P., and van Engelshoven, J. M. A. (1995). The nonlinear partial volume effect and computed tomography densitometry of foam and lung. *Medical Physics*, 22(9):1445–1450. (cited on page 9)

Krieger, H. (2009). Grundlagen der Strahlungsphysik und des Strahlenschutzes, 3. überarb. u. erw. *Vieweg+ Teubner/GWV Fachverlage, Wiesbaden*. (cited on page 7)

Krämer, M., Jäkel, O., Haberer, T., Kraft, G., Schardt, D., and Weber, U. (2000). Treatment planning for heavy-ion radiotherapy: physical beam model and dose optimization. *Physics in Medicine and Biology*, 45(11):3299. (cited on pages 18 and 33)

Krueger, R. F., Hicks, B. M., Patrick, C. J., Carlson, S. R., Iacono, W. G., and McGue, M. (2002). Etiologic connections among substance dependence, antisocial behavior and personality: Modeling the externalizing spectrum. *Journal of Abnormal Psychology*, 111(3):411. (cited on page 107)

Landry, G., Parodi, K., Wildberger, J. E., and Verhaegen, F. (2013a). Deriving concentrations of oxygen and carbon in human tissues using single- and dual-energy CT for ion therapy applications. *Physics in Medicine and Biology*, 58(15):5029. (cited on pages 106 and 108)

Landry, G., Reniers, B., Granton, P. V., van Rooijen, B., Beaulieu, L., Wildberger, J. E., and Verhaegen, F. (2011). Extracting atomic numbers and electron densities from a dual source dual energy CT scanner: Experiments and a simulation model. *Radiotherapy and Oncology*, 100(3):375 – 379. (cited on pages 39 and 95)

Landry, G., Seco, J., Gaudreault, M., and Verhaegen, F. (2013b). Deriving effective atomic numbers from DECT based on a parameterization of the ratio of high and low linear attenuation coefficients. *Physics in Medicine and Biology*, 58(19):6851–6856. (cited on pages 39, 95, and 96)

Mahnken, A. H., Stanzel, S., and Heismann, B. (2009). Spectral ρZ-Projection Method for Characterization of Body Fluids in Computed Tomography: Ex Vivo Experiments1. *Academic Radiology*, 16(6):763–769. (cited on page 95)

Malusek, A., Karlsson, M., Magnusson, M., and Carlsson, G. A. (2013). The potential of dual-energy computed tomography for quantitative decomposition of soft tissues to water, protein and lipid in brachytherapy. *Physics in Medicine and Biology*, 58(4):771. (cited on page 106)

McCollough, C. H., Leng, S., Yu, L., Cody, D. D., Boone, J. M., and McNitt-Gray, M. F. (2011). CT dose index and patient dose: they are not the same thing. *Radiology*, 259(2):311–316. (cited on page 10)

McCullough, E. C. (1975). Photon attenuation in computed tomography. *Medical Physics*, 2(6):307–320. (cited on pages 4, 15, and 31)

McNitt-Gray, M. F. (2002). AAPM/RSNA Physics Tutorial for Residents: Topics in CT: Radiation Dose in CT 1. *Radiographics*, 22(6):1541–1553. (cited on page 10)

Meyer, E., Raupach, R., Lell, M., Schmidt, B., and Kachelrieß, M. (2010). Normalized metal artifact reduction (NMAR) in computed tomography. *Medical Physics*, 37(10):5482–5493. (cited on pages 9 and 110)

Meyer, E., Raupach, R., Lell, M., Schmidt, B., and Kachelrieß, M. (2012). Frequency split metal artifact reduction (FSMAR) in computed tomography. *Medical Physics*, 39(4):1904–1916. (cited on page 110)

Min, C. H., Lee, H. R., Yeom, Y. S., Cho, S. K., and Kim, C. H. (2010). Determination of the distal dose edge in a human phantom by measuring the prompt gamma distribution: a Monte Carlo study. *Journal of the Korean Physical Society*, 56:2059–2062. (cited on page 107)

Mozumder, A. (2002). Ionization and excitation yields in liquid water due to the primary irradiation: Relationship of radiolysis with far UV-photolysis. *Physical Chemistry Chemical Physics*, 4(8):1451–1456. (cited on page 16)

Nelder, J. A. and Mead, R. (1965). A simplex method for function minimization. *Computer Journal*, 7(4):308–313. (cited on page 38)

Newhauser, W. D., Giebeler, A., Langen, K. M., Mirkovic, D., and Mohan, R. (2008). Can megavoltage computed tomography reduce proton range uncertainties in treatment plans for patients with large metal implants? *Physics in Medicine and Biology*, 53(9):2327. (cited on page 41)

Niebuhr, N. (2012). Gel-based Multimodality (CT/MR) Phantoms for Ion Radiotherapy. Bachelor thesis, Heidelberg University. (cited on page VIII)

Nolden, M., Zelzer, S., Seitel, A., Wald, D., Müller, M., Franz, A. M., Maleike, D., Fangerau, M., Baumhauer, M., Maier-Hein, L., et al. (2013). The Medical Imaging Interaction Toolkit: challenges and advances. *International Journal of Computer Assisted Radiology and Surgery*, 8(4):607–620. (cited on page 34)

Paganetti, H. (2009). Dose to water versus dose to medium in proton beam therapy. *Physics in Medicine and Biology*, 54(14):4399–4421. (cited on page 18)

Paganetti, H. (2012). Range uncertainties in proton therapy and the role of Monte Carlo simulations. *Physics in Medicine and Biology*, 57(11):R99–R117. (cited on pages 1, 96, 98, and 106)

Parodi, K., Paganetti, H., Shih, H. A., Michaud, S., Loeffler, J. S., DeLaney, T. F., Liebsch, N. J., Munzenrider, J. E., Fischman, A. J., Knopf, A., et al. (2007). Patient Study of In Vivo Verification of Beam Delivery and Range, Using Positron Emission Tomography and Computed Tomography Imaging After Proton Therapy. *International Journal of Radiation Oncology* Biology* Physics*, 68(3):920–934. (cited on pages 28 and 107)

Paul, H., Geithner, O., and Jäkel, O. (2007). The influence of stopping powers upon dosimetry for radiation therapy with energetic ions. *Advances in Quantum Chemistry*, 52:289–306. (cited on page 17)

Paul, H., Grande, P. L., and Smith, D. (2009). Optical oscillator strengths, mean excitation energy, shell corrections and experimental values for stopping power. *Nuclear Instruments and Methods in Physics Research Section B: Beam Interactions with Materials and Atoms*, 267(15):2471–2474. (cited on page 16)

Perl, J., Shin, J., Schümann, J., Faddegon, B., and Paganetti, H. (2012). TOPAS: An innovative proton Monte Carlo platform for research and clinical applications. *Medical Physics*, 39(11):6818–6837. (cited on pages 34 and 35)

Peterson, J. and Dechow, P. C. (2003). Material properties of the human cranial vault and zygoma. *The Anatomical Record Part A: Discoveries in Molecular, Cellular, and Evolutionary Biology*, 274(1):785–797. (cited on page 101)

Podgorsak, E. B. (2010). *Radiation Physics for Medical Physicists*. Biological and Medical Physics, Biomedical Engineering. Springer-Verlag Berlin Heidelberg. (cited on pages 4 and 6)

Primak, A. N., Giraldo, J. C. R., Eusemann, C. D., Schmidt, B., Kantor, B., Fletcher, J. G., and McCollough, C. H. (2010). Dual-source dual-energy CT with additional tin filtration: Dose and image quality evaluation in phantoms and in-vivo. *American Journal of Roentgenology*, 195(5):1164–1174. (cited on page 21)

Pshenichnov, I., Mishustin, I., and Greiner, W. (2008). Comparative study of depth–dose distributions for beams of light and heavy nuclei in tissue-like media. *Nuclear Instruments and Methods in Physics Research Section B: Beam Interactions with Materials and Atoms*, 266(7):1094–1098. (cited on page 35)

R Development Core Team (2008). *R: A Language and Environment for Statistical Computing*. R Foundation for Statistical Computing, Vienna, Austria. ISBN 3-900051-07-0. (cited on page 33)

Rinaldi, I. (2011). Investigation of novel imaging methods using therapeutic ion beams. *University of Heidelberg*, Physics Faculty. (cited on page 99)

Rinaldi, I., Brons, S., Gordon, J., Panse, R., Voss, B., Jäkel, O., and Parodi, K. (2013). Experimental characterization of a prototype detector system for carbon ion radiography and tomography. *Physics in Medicine and Biology*, 58(3):413. (cited on page 99)

Rutherford, R., Pullan, B., and Isherwood, I. (1976a). X-ray energies for effective atomic number determination. *Neuroradiology*, 11(1):23–28. (cited on page 13)

Rutherford, R. A., Pullan, B. R., and Isherwood, I. (1976b). Measurement of effective atomic number and electron density using an EMI scanner. *Neuroradiology*, 11:15–21. (cited on pages 10, 13, and 90)

Saito, M. (2012). Potential of dual-energy subtraction for converting CT numbers to electron density based on a single linear relationship. *Medical Physics*, 39(4):2021–30. (cited on page 95)

Sakurai, J. J. and Tuan, S. F. (1993). *Modern quantum mechanics*, volume 2. Addison-Wesley Reading, Massachusetts. (cited on pages 15 and 16)

Sawakuchi, G. O., Titt, U., Mirkovic, D., and Mohan, R. (2008). Density heterogeneities and the influence of multiple Coulomb and nuclear scatterings on the Bragg peak distal edge of proton therapy beams. *Physics in Medicine and Biology*, 53(17):4605. (cited on page 18)

Schaffner, B. and Pedroni, E. (1998). The precision of proton range calculations in proton radiotherapy treatment planning: experimental verification of the relation between CT-HU and proton stopping power. *Physics in Medicine and Biology*, 43(6):1579. (cited on page 99)

Schaffner, B., Pedroni, E., and Lomax, A. (1999). Dose calculation models for proton treatment planning using a dynamic beam delivery system: an attempt to include density heterogeneity effects in the analytical dose calculation. *Physics in Medicine and Biology*, 44(1):27. (cited on page 18)

Schenzle, J., Sommer, W., Neumaier, K., Michalski, G., Lechel, U., Nikolaou, K., Becker, C. R., Reiser, M. F., and Johnson, T. R. C. (2010). Dual Energy CT of the Chest: How About the Dose? *Investigative Radiology*, 45:347–353. (cited on page 46)

Schlegel, W. and Bille, J., editors (2002). *Medizinische Physik 2: Medizinische Strahlenphysik*. Springer. (cited on page 9)

Schneider, U., Pedroni, E., and Lomax, A. (1996). The calibration of CT Hounsfield units for radiotherapy treatment planning. *Physics in Medicine and Biology*, 41(1):111. (cited on pages 19, 25, 26, and 93)

Schneider, U., Schaffner, B., Lomax, T., Pedroni, E., and Tourovsky, A. (1998). A technique for calculating range spectra of charged particle beams distal to thick inhomogeneities. *Medical Physics*, 25(4):457–463. (cited on page 18)

Schneider, W., Bortfeld, T., and Schlegel, W. (2000). Correlation between CT numbers and tissue parameters needed for Monte Carlo simulations of clinical dose distributions. *Physics in Medicine and Biology*, 45(2):459. (cited on pages 2, 19, 22, 23, 24, 26, 27, 28, 39, 42, 47, 48, 49, 66, 78, 79, 81, 84, 87, 90, 93, 94, 97, 100, 109, 113, and VII)

Seidensticker, P. R. and Hofmann, L. K. (2008). *Dual source CT imaging*. Springer. (cited on page 13)

Seltzer, S. M. and Berger, M. J. (1982). Evaluation of the collision stopping power of elements and compounds for electrons and positrons. *The International Journal of Applied Radiation and Isotopes*, 33(11):1189–1218. (cited on pages 15 and 16)

Semerci, O. and Miller, E. L. (2012). A parametric level-set approach to simultaneous object identification and background reconstruction for dual-energy computed tomography. *IEEE Transactions on Image Processing*, 21(5):2719–2734. (cited on page 95)

Sheldon, J. H. and Ramage, H. (1931). A spectrographic analysis of human tissues. *Biochemical Journal*, 25(5):1608. (cited on page 24)

Sigmund, P. (2004). *Stopping of Heavy Ions: A Theoretical Approach*. Springer. (cited on pages 15 and 16)

Sigmund, P. (2006). *Particle Penetration and Radiation Effects: General Aspects and Stopping of Swift Point Charges*, volume 151. Springer. (cited on pages 15 and 16)

Sigmund, P., Schinner, A., and Paul, H. (2009). Errata and Addenda for ICRU Report 73, Stopping of ions heavier than helium. *Journal of the ICRU*, 5(1). (cited on page 17)

Smeets, J., Roellinghoff, F., Prieels, D., Stichelbaut, F., Benilov, A., Fiorini, C., Peloso, R., Basilavecchia, M., Frizzi, T., Dehaes, J., et al. (2012). Prompt gamma imaging with a slit camera for real-time range control in proton therapy. *Physics in Medicine and Biology*, 57(11):3371. (cited on page 107)

Szymanowski, H. and Oelfke, U. (2003). CT calibration for two-dimensional scaling of proton pencil beams. *Physics in Medicine and Biology*, 48(7):861. (cited on page 19)

Telsemeyer, J., Jäkel, O., and Martišíková, M. (2012). Quantitative carbon ion beam radiography and tomography with a flat-panel detector. *Physics in Medicine and Biology*, 57(23):7957. (cited on page 99)

Thomas, S. (1999). Relative electron density calibration of CT scanners for radiotherapy treatment planning. *The British Journal of Radiology*, 72(860):781–786. (cited on page 3)

Torikoshi, M., Tsunoo, T., Sasaki, M., Endo, M., Noda, Y., Ohno, Y., Kohno, T., Hyodo, K., Uesugi, K., and Yagi, N. (2003). Electron density measurement with dual-energy x-ray CT using synchrotron radiation. *Physics in Medicine and Biology*, 48(5):673. (cited on pages 8, 13, and 95)

Tremmel, C. (2012). Improving ion beam therapy treatment planning for metal implants by using dual-energy CT scanning. Master's thesis, University of Heidelberg. (cited on pages 22, 42, and 110)

Tsukihara, M., Noto, Y., Hayakawa, T., and Saito, M. (2013). Conversion of the energy-subtracted CT number to electron density based on a single linear relationship: an experimental verification using a clinical dual-source CT scanner. *Physics in Medicine and Biology*, 58(9):N135. (cited on page 95)

Urie, M., Goitein, M., Holley, W., and Chen, G. T. (1986). Degradation of the Bragg peak due to inhomogeneities. *Physics in Medicine and Biology*, 31(1):1. (cited on page 18)

Vanderstraeten, B., Chin, P. W., Fix, M., Leal, A., Mora, G., Reynaert, N., Seco, J., Soukup, M., Spezi, E., De Neve, W., et al. (2007). Conversion of CT numbers into tissue parameters for Monte Carlo dose calculations: a multi-centre study. *Physics in Medicine and Biology*, 52(3):539. (cited on pages 39 and 92)

Verburg, J. M. and Seco, J. (2012). CT metal artifact reduction method correcting for beam hardening and missing projections. *Physics in Medicine and Biology*, 57(9):2803. (cited on page 110)

Wertz, H. and Jäkel, O. (2004). Influence of iodine contrast agent on the range of ion beams for radiotherapy. *Medical Physics*, 31(4):767–773. (cited on pages 14 and 43)

Whitcher, B., Schmid, V. J., and Thornton, A. (2011). Working with the DICOM and NIfTI Data Standards in R. *Journal of Statistical Software*, 44(6):1–28. (cited on page 33)

White, D. R., Woodard, H. Q., and Hammond, S. M. (1987). Average soft-tissue and bone models for use in radiation dosimetry. *The British Journal of Radiology*, 60(717):907–913. (cited on page 24)

Widdowson, E. M. and Dickerson, J. (1960). The effect of growth and function on the chemical composition of soft tissues. *Biochemical Journal*, 77(1):30. (cited on page 24)

Williamson, J. F., Li, S., Devic, S., Whiting, B. R., and Lerma, F. A. (2006). On two-parameter models of photon cross sections: application to dual-energy CT imaging. *Medical Physics*, 33(11):4115–4129. (cited on pages 5, 93, 94, and 99)

Wolf, I., Vetter, M., Wegner, I., Böttger, T., Nolden, M., Schöbinger, M., Hastenteufel, M., Kunert, T., and Meinzer, H.-P. (2005). The medical imaging interaction toolkit. *Medical Image Analysis*, 9(6):594 – 604. (cited on page 34)

Wolf, I., Vetter, M., Wegner, I., Nolden, M., Böttger, T., Hastenteufel, M., Schöbinger, M., Kunert, T., and Meinzer, H.-P. (2004). The medical imaging interaction toolkit (MITK): a toolkit facilitating the creation of interactive software by extending VTK and ITK. In *Medical Imaging 2004*, pages 16–27. International Society for Optics and Photonics. (cited on page 34)

Woodard, H. Q. and White, D. R. (1986). The composition of body tissues. *The British Journal of Radiology*, 59(708):1209–1218. (cited on page 24)

Yamada, S., Ueguchi, T., Ogata, T., Mizuno, H., Ogihara, R., Koizumi, M., Shimazu, T., Murase, K., and Ogawa, K. (2014). Radiotherapy treatment planning with contrast-enhanced computed tomography: feasibility of dual-energy virtual unenhanced imaging for improved dose calculations. *Radiation Oncology*, 9(1):1–10. (cited on page 14)

Yang, M., Virshup, G., Clayton, J., Zhu, X. R., Mohan, R., and Dong, L. (2010). Theoretical variance analysis of single- and dual-energy computed tomography methods for calculating proton stopping power ratios of biological tissues. *Physics in Medicine and Biology*, 55(5):1343. (cited on pages 2, 32, 42, and 113)

Yang, M., Virshup, G., Mohan, R., Shaw, C. C., Zhu, X. R., and Dong, L. (2008). Improving accuracy of electron density measurement in the presence of metallic implants using orthovoltage computed tomography. *Medical Physics*, 35(5):1932–1941. (cited on pages 38, 39, and 89)

Yohannes, I., Kolditz, D., Langner, O., and Kalender, W. A. (2012). A formulation of tissue- and water-equivalent materials using the stoichiometric analysis method for CT-number calibration in radiotherapy treatment planning. *Physics in Medicine and Biology*, 57(5):1173. (cited on page 94)

Yu, L., Christner, J. A., Leng, S., Wang, J., Fletcher, J. G., and McCollough, C. H. (2011). Virtual monochromatic imaging in dual-source dual-energy CT: radiation dose and image quality. *Medical Physics*, 38(12):6371–6379. (cited on pages 46 and 109)

Yu, L., Leng, S., and McCollough, C. H. (2012). Dual-energy CT–based monochromatic imaging. *American Journal of Roentgenology*, 199(5_supplement):S9–S15. (cited on pages 109 and 110)

Zatz, L. M. (1976). The Effect of the kVp Level on EMI Values: Selective Imaging of Various Materials with Different kVp Settings 1. *Radiology*, 119(3):683–688. (cited on page 13)

Zhang, D., Li, X., and Liu, B. (2011). Objective characterization of GE discovery CT750 HD scanner: gemstone spectral imaging mode. *Medical Physics*, 38(3):1178–1188. (cited on page 11)

Ziegler, J., Biersack, J., and Ziegler, M. (2008). *SRIM, the stopping and range of ions in matter*. SRIM Company. (cited on page 14)

Ziegler, J. F. (1999). Stopping of energetic light ions in elemental matter. *Journal of Applied Physics*, 85(3):1249–1272. (cited on page 14)

Appendix

Table A.1: CT protocol parameters employed for the measurements in this thesis.

measured materials	mode	protocol	80/140Sn kV	CTDI 80/140Sn kV [mGy]	tube current [mAs] 100/140Sn kV	CTDI 100/140Sn kV [mGy]	collimation width (single/total)	rotation [s]	pitch	
Gammex	DECT	LiverVNC	300/116	20.6	300/232	42.5 (32cm)	0.6/12	1	0.6	a)
polymers	DECT	LiverVNC	180/70	12.4	180/140	25.5 (32cm)	0.6/12	1	0.6	b)
printing materials	DECT	LiverVNC	240/93	15	300/232	38.9 (32cm)	0.6/19.2	1	0.6	c)
Gammex/patient	DECT	RT 13 BPL KopfHalsDE			215/215	73.7 (16cm)	0.6/12	1	0.6	d)
Gammex (120 kV)	SECT	RT 13 BPL KopfHalsDE			264 (120kV)	73.4 (16cm)	0.6/38.4	1	0.55	e)

Protocol to convert $\hat{\rho}_\mathrm{e}$ and Z_eff images to SPR

The $\hat{\rho}_\mathrm{e}$ and Z_eff had to be directly converted to SPR with the following customized protocol for data conversion, as the treatment planning software could not handle the two DICOM DECT image stacks available:

1. DECT acquisition (e.g. at 100kV/140Sn kV)
2. Image based conversion of both CT number images to $\hat{\rho}_\mathrm{e}$ and Z_eff images (Sec. 3.5)
3. Read in the $\hat{\rho}_\mathrm{e}$ and Z_eff image with R (Sec. 3.7.1) and the oro.dicom package
4. Process the $\hat{\rho}_\mathrm{e}$ and Z_eff image to SPR image according to Eq. 4.1
5. Write out a .ctx file containing the SPR·1000 and an associated header (".hed") file that can be read by VIRTUOS and contains all necessary image information (slice thickness, pixel size and number) for TRIP
6. VIRTUOS and TRIP are now able to calculate dose on the SPR image grid when providing the simple HLUT of 1000:1 that transforms the SPR·1000 back to the unscaled SPR
7. To export a SPR DICOM image, read in the .ctx and .hed file in VIRTUOS and export the .ctx image to DICOM via the "DICOM export plugin"

Table A.2: CT numbers of tissue surrogates measured for different phantom settings (central axis PMMA phantom, "Pizza", "Pizza" with CB and fat extra (Sec. 4.1.1). Employed protocols are listed in Tab. A.1(d),(e) and were the same as for the patient scans.

Material	voltage [kV]	kernel	CT no central axis [HU]	sd CT no central axis [HU]	mean CT no Pizza [HU]	sd CT no Pizza [HU]	mean Pizza CT no (CB, Fat extra) [HU]	sd Pizza CT no (CB, Fat extra) [HU]
Adipose	100	D30	-110	6				
Adipose	100	D34	-111	7				
Adipose	100	H30	-112	5				
Adipose	120	H30	-117	4	-105	4	-107	4
Adipose	140Sn	D30	-85	7				
Adipose	140Sn	D34	-86	7				
Adipose	140Sn	H30	-87	6				
B200	100	D30	293	8				
B200	100	D34	271	8				
B200	100	H30	285	7				
B200	120	H30	269	5	269	6		
B200	140Sn	D30	183	7				
B200	140Sn	D34	178	6				
B200	140Sn	H30	188	7				
Brain	100	D30	5	6				
Brain	100	D34	5	7				
Brain	100	H30	3	5				
Brain	120	H30	6	4	22	3		
Brain	140Sn	D30	30	7				
Brain	140Sn	D34	30	7				
Brain	140Sn	H30	30	6				
Breast	100	D30	-52	6				
Breast	100	D34	-52	7				
Breast	100	H30	-53	5				
Breast	120	H30	-59	4	-46	4		
Breast	140Sn	D30	-39	7				
Breast	140Sn	D34	-39	7				
Breast	140Sn	H30	-40	6				
CB30	100	D30	551	8				
CB30	100	D34	524	9				
CB30	100	H30	546	8				
CB30	120	H30	525	6	494	8		
CB30	140Sn	D30	384	7				
CB30	140Sn	D34	377	8				
CB30	140Sn	H30	401	7				
CB50	100	D30	1009	10				
CB50	100	D34	994	11				
CB50	100	H30	1017	9				
CB50	120	H30	955	11	945	6		
CB50	140Sn	D30	690	8				
CB50	140Sn	D34	684	8				
CB50	140Sn	H30	725	7				
Cortical Bone	100	D30	1509	13				
Cortical Bone	100	D34	1532	13				
Cortical Bone	100	H30	1546	11				
Cortical Bone	120	H30	1417	17	1397	9	1428	7
Cortical Bone	140Sn	D30	1040	9				
Cortical Bone	140Sn	D34	1042	9				
Cortical Bone	140Sn	H30	1102	8				
Inner Bone	100	D30	285	8				
Inner Bone	100	D34	264	8				
Inner Bone	100	H30	278	7				
Inner Bone	120	H30	260	6	258	5		
Inner Bone	140Sn	D30	176	8				
Inner Bone	140Sn	D34	175	6				
Inner Bone	140Sn	H30	179	8				
Liver	100	D30	75	7				
Liver	100	D34	75	7				
Liver	100	H30	76	6				
Liver	120	H30	71	4	80	5		
Liver	140Sn	D30	68	7				
Liver	140Sn	D34	68	7				
Liver	140Sn	H30	69	6				
Lung	100	D30	-559	29				
Lung	100	D34	-560	30				
Lung	100	H30	-563	28				
Lung	120	H30	-607	31	-573	35		
Lung	140Sn	D30	-559	29				
Lung	140Sn	D34	-561	30				
Lung	140Sn	H30	-564	28				
Muscle	100	D30	36	8				
Muscle	100	D34	36	8				
Muscle	100	H30	36	7				
Muscle	120	H30	28	5	41	6		
Muscle	140Sn	D30	30	8				
Muscle	140Sn	D34	29	8				
Muscle	140Sn	H30	29	7				
Solid Water	100	D30	5	7				
Solid Water	100	D34	5	7				
Solid Water	100	H30	3	6				
Solid Water	120	H30	-5	4	-1	5		
Solid Water	140Sn	D30	-1	7				
Solid Water	140Sn	D34	-1	7				
Solid Water	140Sn	H30	-3	6				
True Water	100	D30	0	6				
True Water	100	D34	0	7				
True Water	100	H30	-1	5				
True Water	120	H30	-5	4	5	4		
True Water	140Sn	D30	1	7				
True Water	140Sn	D34	1	7				
True Water	140Sn	H30	-1	6				

Table A.3: Optimized k_1 and k_2 values for different CT acquisition and material sets (Eq. 3.3). m_1 and m_2 in Eq. 3.1 were kept fixed, start values were set to $k_1 = 8.20 \cdot 10^{-4}$ and $k_2 = 3.39 \cdot 10^{-5}$. CT numbers were acquired in the dual source mode for the 100/140Sn kV and in the standard single energy, single source mode for the 120 kV aquisition. Employed CT protocol are listed in Tab. A.1(d) and (e), measured CT numbers are summarized in Tab. A.2

voltage [kV]	kernel	phantom	mode	k_1	k_2	result Eq. 3.3
100	D30	central axis	Ca up H down 1%	7.69E-04	3.77E-05	1155
100	D30	central axis	normal	-2.62E-05	4.12E-05	1643
100	D30	central axis	wo B200 IB	1.89E-04	4.04E-05	1370
100	D30	central axis	wo Brain	-3.89E-04	4.23E-05	1456
100	D30	central axis	wo CB	4.87E-04	4.18E-05	326
100	D30	central axis	wo Lung	-6.05E-05	4.13E-05	1561
100	D34	central axis	Ca up H down 1%	1.80E-03	3.44E-05	369
100	D34	central axis	normal	9.58E-04	3.82E-05	307
100	D34	central axis	wo B200 IB	8.30E-04	3.87E-05	220
100	D34	central axis	wo Brain	8.46E-04	3.86E-05	291
100	D34	central axis	wo CB	9.30E-04	3.82E-05	303
100	D34	central axis	wo Lung	9.22E-04	3.83E-05	220
100	H30	central axis	Ca up H down 1%	1.46E-03	3.68E-05	345
100	H30	central axis	normal	5.87E-04	4.07E-05	551
100	H30	central axis	wo B200 IB	6.03E-04	4.06E-05	549
100	H30	central axis	wo Brain	3.61E-04	4.13E-05	485
100	H30	central axis	wo CB	8.26E-04	4.10E-05	284
100	H30	central axis	wo Lung	5.36E-04	4.09E-05	379
120	H30	central axis	Ca up H down 1%	1.63E-03	3.04E-05	4644
120	H30	central axis	normal	8.98E-04	3.37E-05	5189
120	H30	Pizza	normal	-2.86E-04	3.61E-05	1804
120	H30	Pizza (CB, Fat extra)	normal	-2.30E-06	3.62E-05	1077
120	H30	central axis	wo B200 IB	1.09E-03	3.29E-05	4991
120	H30	central axis	wo Brain	7.07E-04	3.42E-05	5143
120	H30	central axis	wo CB	1.52E-03	3.42E-05	3453
120	H30	central axis	wo Lung	6.82E-04	3.43E-05	2053
140Sn	D30	central axis	Ca up H down 1%	-2.50E-04	1.76E-05	205
140Sn	D30	central axis	normal	-1.73E-04	1.72E-05	170
140Sn	D30	central axis	wo B200 IB	-1.01E-04	1.68E-05	136
140Sn	D30	central axis	wo Brain	-3.59E-04	1.79E-05	116
140Sn	D30	central axis	wo CB	-1.08E-04	1.72E-05	147
140Sn	D30	central axis	wo Lung	-2.02E-04	1.73E-05	96
140Sn	D34	central axis	Ca up H down 1%	-3.68E-05	1.67E-05	239
140Sn	D34	central axis	normal	4.13E-05	1.62E-05	216
140Sn	D34	central axis	wo B200 IB	8.57E-05	1.60E-05	202
140Sn	D34	central axis	wo Brain	-1.00E-04	1.68E-05	186
140Sn	D34	central axis	wo CB	-2.28E-06	1.62E-05	205
140Sn	D34	central axis	wo Lung	8.39E-06	1.64E-05	117
140Sn	H30	central axis	Ca up H down 1%	1.03E-04	1.90E-05	240
140Sn	H30	central axis	normal	9.31E-05	1.90E-05	240
140Sn	H30	central axis	wo B200 IB	2.49E-05	1.93E-05	208
140Sn	H30	central axis	wo Brain	3.12E-05	1.93E-05	234
140Sn	H30	central axis	wo CB	7.17E-05	1.90E-05	237
140Sn	H30	central axis	wo Lung	4.55E-05	1.92E-05	61

Table A.4: Measured mean values of CT numbers, ρ_e and Z_{eff} dependent on two different dual energy tube voltage pairs (D30). CT protocol listed in Tab. A.1(a),(b),(c). SPRs and I-values were calculated pixel wise from the ρ_e and Z_{eff} according to Eq. 4.1 except for both metals where only the mean values were evaluated and further processed (likewise in Hünemohr et al. [2014a]). Pixels for which the Z_{eff} algorithm failed (Z_{eff} assigned to zero) were excluded in the mean Z_{eff} evaluation.

Voltage pair [kV]	Material	Class	pixels	CT no$_{\mathrm{low\,kV}}$	CT no$_{\mathrm{high\,kV}}$	$\hat{\rho_e}$	Z_{eff}	SPR$_{\mathrm{DECT}}$	I [eV]
80/140Sn	Lung	Gammex	31331	-556±27	-559±28	0.442±0.027	NA	0.442±0.027	NA±NA
100/140Sn	Lung	Gammex	31331	-559±27	-560±27	0.441±0.027	NA	0.441±0.027	NA±NA
80/140Sn	Adipose	Gammex	39576	-124±8	-85±8	0.932±0.005	6.30±0.20	0.949±0.007	64.4±1.6
100/140Sn	Adipose	Gammex	39576	-109±5	-85±6	0.931±0.004	6.33±0.18	0.948±0.006	64.6±1.4
80/140Sn	Breast	Gammex	37927	-59±8	-39±9	0.970±0.005	6.91±0.16	0.979±0.007	69.5±1.4
100/140Sn	Breast	Gammex	37927	-51±5	-39±6	0.970±0.004	6.93±0.14	0.978±0.005	69.7±1.2
80/140Sn	True Water	Gammex	18139	-2±8	-1±9	1.000±0.005	7.40±0.14	1.002±0.007	74.0±1.3
100/140Sn	True Water	Gammex	18139	0±5	0±6	1.000±0.004	7.44±0.12	1.001±0.005	74.3±1.1
80/140Sn	Solid Water	Gammex	28033	8±8	-1±9	0.994±0.006	7.67±0.13	0.992±0.007	76.4±1.3
100/140Sn	Solid Water	Gammex	28033	5±6	-1±6	0.994±0.004	7.69±0.11	0.992±0.005	76.6±1.1
80/140Sn	Muscle	Gammex	39576	39±9	29±10	1.025±0.006	7.67±0.13	1.023±0.007	76.5±1.3
100/140Sn	Muscle	Gammex	39576	36±7	29±7	1.024±0.005	7.69±0.12	1.022±0.006	76.7±1.1
80/140Sn	Brain	Gammex	39576	-8±8	32±9	1.049±0.005	6.41±0.17	1.066±0.007	65.4±1.4
100/140Sn	Brain	Gammex	39576	7±5	32±6	1.048±0.004	6.44±0.16	1.065±0.006	65.6±1.3
80/140Sn	Liver	Gammex	39576	78±8	69±9	1.065±0.006	7.65±0.12	1.063±0.007	76.3±1.2
100/140Sn	Liver	Gammex	39576	76±6	68±7	1.063±0.004	7.69±0.11	1.061±0.005	76.7±1.0
80/140Sn	Inner Bone	Gammex	39576	351±10	176±9	1.098±0.006	10.11±0.09	1.092±0.007	78.8±0.7
100/140Sn	Inner Bone	Gammex	39576	286±7	176±7	1.097±0.004	10.13±0.08	1.091±0.004	78.9±0.6
80/140Sn	B200	Gammex	37927	360±10	185±10	1.107±0.006	10.08±0.09	1.101±0.007	78.6±0.7
100/140Sn	B200	Gammex	37927	295±7	185±7	1.106±0.005	10.10±0.08	1.100±0.005	78.7±0.6
80/140Sn	CB30	Gammex	39576	657±11	389±10	1.269±0.007	10.73±0.08	1.253±0.007	83.8±0.7
100/140Sn	CB30	Gammex	39576	557±8	389±7	1.269±0.005	10.74±0.07	1.252±0.005	83.8±0.6
80/140Sn	CB50	Gammex	37927	1212±14	695±11	1.463±0.008	12.16±0.08	1.420±0.009	96.3±0.7
100/140Sn	CB50	Gammex	39576	1014±9	694±8	1.463±0.006	12.14±0.07	1.421±0.007	96.1±0.6
80/140Sn	Cortical Bone	Gammex	39576	1823±21	1045±12	1.696±0.009	13.05±0.08	1.628±0.010	105.1±0.8
100/140Sn	Cortical Bone	Gammex	41225	1515±13	1044±9	1.700±0.008	12.97±0.07	1.635±0.009	104.2±0.8
80/140Sn	Tecapeek	Polymer	28033	160±10	210±12	1.232±0.008	6.32±0.21	1.254±0.010	64.6±1.7
100/140Sn	Tecapeek	Polymer	29682	180±7	209±9	1.230±0.006	6.41±0.18	1.250±0.007	65.4±1.5
80/140Sn	Tecaform	Polymer	28033	324±12	350±13	1.362±0.008	6.94±0.19	1.374±0.010	69.8±1.6
100/140Sn	Tecaform	Polymer	29682	336±8	350±9	1.361±0.007	6.99±0.21	1.372±0.009	70.3±1.8
80/140Sn	Tecadur	Polymer	29682	595±20	432±17	1.359±0.012	9.59±0.11	1.360±0.013	74.9±0.8
100/140Sn	Tecadur	Polymer	28033	536±16	432±15	1.358±0.012	9.63±0.09	1.358±0.012	75.2±0.7
80/140Sn	PMMA	Polymer	28033	100±11	139±12	1.157±0.007	6.52±0.21	1.175±0.010	66.2±1.7
100/140Sn	PMMA	Polymer	28033	116±7	140±8	1.157±0.005	6.56±0.18	1.173±0.007	66.6±1.5
80/140Sn	Teflon	Polymer	29682	972±15	899±15	1.865±0.011	8.29±0.13	1.845±0.013	82.3±2.3
100/140Sn	Teflon	Polymer	26384	949±10	900±10	1.865±0.008	8.35±0.13	1.845±0.012	82.3±3.5
80/140Sn	PrintingI	Polymer	2490	131±7	164±8	1.178±0.003	6.71±0.10	1.193±0.004	67.9±0.9
100/140Sn	PrintingI	Polymer	2490	143±5	164±5	1.178±0.005	6.71±0.13	1.193±0.006	67.8±1.1
80/140Sn	PrintingII	Polymer	2241	105±7	143±8	1.159±0.003	6.59±0.11	1.176±0.004	66.7±1.2
100/140Sn	PrintingII	Polymer	2241	120±5	144±5	1.160±0.005	6.57±0.14	1.176±0.006	66.8±1.0
80/140Sn	PrintingIII	Polymer	249	350±10	228±7	1.179±0.005	9.29±0.07	1.184±0.005	72.7±0.5
100/140Sn	PrintingIII	Polymer	249	304±7	229±6	1.181±0.006	9.28±0.08	1.186±0.005	72.7±0.5
80/140Sn	Aluminum	Metal	193	2751±20	1761±13	2.280±0.016	13.55±0.05	2.176	110.5
100/140Sn	Aluminum	Metal	193	2365±15	1764±11	2.285±0.013	13.62±0.04	2.179	111.4
80/140Sn	Titanium	Metal	193	12338±166	6011±20	3.438±0.069	22.99±0.33	2.904	279.4
100/140Sn	Titanium	Metal	193	9530±100	6029±22	3.496±0.017	23.11±0.16	2.947	282.8

Table A.5: Absolute and relative residuals from DECT measured $\hat{\rho}_e$, Z_{eff}, predicted I-value and SPR (Tab. A.4) compared to reference values (Tab. 3.1). Only for the Gammex tissue surrogates, reference values were given by the manufacturer (for the Z_{eff} only approximations). For the polymers and metals, compositions and related material parameters were estimated and might deviated from actual composition. For the printing materials composition could not be estimated.

Voltage pair [kV]	Material	Class	$\hat{\rho}_e$ diff abs	$\hat{\rho}_e$ diff %	Z_{eff} diff abs	Z_{eff} diff %	I diff abs [eV]	I diff %	WEPL diff abs	WEPL diff %
80/140Sn	Lung	Gammex	-0.002	-0.5	NA	NA	NA	NA	-0.002	-0.5
100/140Sn	Lung	Gammex	-0.003	-0.7	NA	NA	NA	NA	-0.003	-0.7
80/140Sn	Adipose	Gammex	0.007	0.8	0.10	1.6	-2.2	-3.3	0.006	0.6
100/140Sn	Adipose	Gammex	0.006	0.6	0.13	2.1	-2.0	-3.0	0.005	0.5
80/140Sn	Breast	Gammex	0.005	0.5	0.11	1.6	1.3	1.9	-0.004	-0.4
100/140Sn	Breast	Gammex	0.005	0.5	0.13	1.9	1.5	2.2	-0.005	-0.5
80/140Sn	True Water	Gammex	0.000	0.0	0.00	0.0	-1.0	-1.3	0.002	0.2
100/140Sn	True Water	Gammex	0.000	0.0	0.04	0.5	-0.7	-0.9	0.001	0.1
80/140Sn	Solid Water	Gammex	0.005	0.5	0.17	2.3	6.0	8.5	-0.009	-0.9
100/140Sn	Solid Water	Gammex	0.005	0.5	0.19	2.5	6.2	8.8	-0.009	-0.9
80/140Sn	Muscle	Gammex	0.006	0.6	0.17	2.3	6.3	9.0	-0.010	-1.0
100/140Sn	Muscle	Gammex	0.005	0.5	0.19	2.5	6.5	9.3	-0.011	-1.1
80/140Sn	Brain	Gammex	0.001	0.1	0.31	5.1	1.9	3.0	0.002	0.2
100/140Sn	Brain	Gammex	0.000	0.0	0.34	5.6	2.1	3.3	0.001	0.1
80/140Sn	Liver	Gammex	0.007	0.7	0.15	2.0	6.0	8.5	-0.010	-0.9
100/140Sn	Liver	Gammex	0.005	0.5	0.19	2.5	6.4	9.1	-0.012	-1.1
80/140Sn	Inner Bone	Gammex	-0.001	-0.1	0.01	0.1	-1.3	-1.6	-0.007	-0.6
100/140Sn	Inner Bone	Gammex	-0.002	-0.2	0.03	0.3	-1.2	-1.5	-0.008	-0.7
80/140Sn	B200	Gammex	0.002	0.2	-0.02	-0.2	-1.6	-2.0	-0.007	-0.6
100/140Sn	B200	Gammex	0.001	0.1	0.00	0.0	-1.5	-1.9	-0.008	-0.7
80/140Sn	CB30	Gammex	-0.009	-0.7	0.13	1.2	3.0	3.7	-0.010	-0.8
100/140Sn	CB30	Gammex	-0.009	-0.7	0.14	1.3	3.0	3.7	-0.011	-0.9
80/140Sn	CB50	Gammex	-0.007	-0.5	-0.14	-1.1	3.1	3.3	-0.006	-0.4
100/140Sn	CB50	Gammex	-0.007	-0.5	-0.16	-1.3	2.9	3.1	-0.005	-0.4
80/140Sn	Cortical Bone	Gammex	0.001	0.1	-0.35	-2.6	0.6	0.6	0.016	1.0
100/140Sn	Cortical Bone	Gammex	0.005	0.3	-0.43	-3.2	-0.3	-0.3	0.023	1.4
80/140Sn	Tecapeek	Polymer	0.002	0.2	0.02	0.3	-10.1	-13.5	0.013	1.0
100/140Sn	Tecapeek	Polymer	0.000	0.0	0.11	1.7	-9.3	-12.4	0.009	0.7
80/140Sn	Tecaform	Polymer	0.009	0.7	-0.06	-0.9	-7.7	-9.9	0.020	1.5
100/140Sn	Tecaform	Polymer	0.008	0.6	-0.01	-0.1	-7.2	-9.3	0.018	1.3
80/140Sn	Tecadur	Polymer	-0.005	-0.4	2.79	41.0	-6.2	-7.6	0.045	3.4
100/140Sn	Tecadur	Polymer	-0.006	-0.4	2.83	41.6	-5.9	-7.3	0.043	3.3
80/140Sn	PMMA	Polymer	0.008	0.7	0.02	0.3	-7.8	-10.5	0.010	0.9
100/140Sn	PMMA	Polymer	0.008	0.7	0.06	0.9	-7.4	-10.0	0.008	0.7
80/140Sn	Teflon	Polymer	0.005	0.3	-0.11	-1.3	-16.8	-17.0	0.063	3.5
100/140Sn	Teflon	Polymer	0.005	0.3	-0.05	-0.6	-16.8	-17.0	0.063	3.5
80/140Sn	PrintingI	Polymer	NA	NA	NA	NA	NA	NA	0.011	0.9
100/140Sn	PrintingI	Polymer	NA	NA	NA	NA	NA	NA	0.011	0.9
80/140Sn	PrintingII	Polymer	NA	NA	NA	NA	NA	NA	0.016	1.4
100/140Sn	PrintingII	Polymer	NA	NA	NA	NA	NA	NA	0.016	1.4
80/140Sn	PrintingIII	Polymer	NA	NA	NA	NA	NA	NA	0.005	0.4
100/140Sn	PrintingIII	Polymer	NA	NA	NA	NA	NA	NA	0.007	0.6
80/140Sn	Aluminum	Metal	-0.063	-2.7	0.55	4.2	-55.5	-33.4	0.036	1.7
100/140Sn	Aluminum	Metal	-0.058	-2.5	0.62	4.8	-54.6	-32.9	0.039	1.8
80/140Sn	Titanium	Metal	-0.321	-8.5	0.99	4.5	46.4	19.9	-0.350	-10.8
100/140Sn	Titanium	Metal	-0.263	-7.0	1.11	5.0	49.8	21.4	-0.307	-9.4

Table A.6: Mean measured pixel values for contoured tissue volumes (Sec. 4.3.3) in the head and neck patient images. SPR were calculated from mean CT numbers (SECT, with protocol specific HLUTs) and mean $\hat{\rho}_e$ and Z_{eff} values of the defined VOIs (DECT). The 120 kV H30 SECT was registered to the DECT acquisition with the rigid image registration in DIPP (Sec. 3.7.4). For inhomogeneous tissue (lung and mastoid) the comparison of SPR is inaccurate due to the contouring based on region growing in the DECT image. Here, solid structures in the lung were excluded but could be included in the registered 120 kV image and provokes large unrealistic WEPL differences. Z_{eff} cannot be calculated for pixels of low mass density appearing in the lung and mastoid VOI.

Material	Kernel	Voltage [kV]	CT no [HU]	sd CT no [HU]	$\hat{\rho}_e$	sd $\hat{\rho}_e$	Z_{eff}	sd Z_{eff}	WEPL DECT	WEPL SECT	SPR difference DECT to SECT [%]
Adipose	D30	100	-86	16	0.950	0.011	6.3	0.4	0.967	0.957	1.1
Adipose	D34	100	-77	16	0.946	0.012	6.9	0.3	0.956	0.969	-1.3
Adipose	H30	100	-81	14						0.965	0.2
Adipose	H30	120	-78	19						0.967	0.0
Adipose	D30	140	-64	14						0.962	0.6
Adipose	D34	140	-62	15						0.965	-1.0
Adipose	H30	140	-62	13						0.967	0.0
Ventricle	D30	100	10	7	1.002	0.005	7.6	0.1	1.001	1.024	-2.3
Ventricle	D34	100	11	8	1.002	0.005	7.6	0.1	1.001	1.025	-2.4
Ventricle	H30	100	8	7						1.025	-2.3
Ventricle	H30	120	7	6						1.024	-2.3
Ventricle	D30	140	4	7						1.018	-1.7
Ventricle	D34	140	5	8						1.019	-1.8
Ventricle	H30	140	3	6						1.018	-1.7
Eye Lens	D30	100	75	8	1.067	0.010	7.6	0.1	1.065	1.067	-0.2
Eye Lens	D34	100	68	9	1.073	0.010	7.3	0.1	1.076	1.064	1.2
Eye Lens	H30	100	74	6						1.066	-0.1
Eye Lens	H30	120	128	17						1.088	-2.1
Eye Lens	D30	140	71	13						1.067	-0.1
Eye Lens	D34	140	72	14						1.066	0.9
Eye Lens	H30	140	73	11						1.067	-0.1
Inner Bone	D30	100	325	57	1.159	0.025	9.9	0.3	1.148	1.162	-1.2
Inner Bone	D34	100	306	56	1.166	0.027	9.4	0.3	1.155	1.155	0.0
Inner Bone	H30	100	322	53						1.159	-0.9
Inner Bone	H30	120	346	45						1.177	-2.5
Inner Bone	D30	140	226	40						1.157	-0.7
Inner Bone	D34	140	221	39						1.153	0.2
Inner Bone	H30	140	234	39						1.155	-0.6
Inner C. Bone	D30	100	696	83	1.340	0.043	11.1	0.2	1.317	1.309	0.6
Inner C. Bone	D34	100	675	86	1.337	0.043	11.0	0.2	1.316	1.300	1.2
Inner C. Bone	H30	100	716	86						1.314	0.3
Inner C. Bone	H30	120	772	107						1.359	-3.1
Inner C. Bone	D30	140	484	60						1.309	0.7
Inner C. Bone	D34	140	473	62						1.302	1.1
Inner C. Bone	H30	140	517	64						1.312	0.4
Cortical Bone	D30	100	1758	83	1.955	0.054	12.5	0.4	1.890	1.743	8.4
Cortical Bone	D34	100	1844	94	1.948	0.051	12.7	0.2	1.878	1.774	5.9
Cortical Bone	H30	100	1824	83						1.757	7.6
Cortical Bone	H30	120	1610	155						1.716	10.1
Cortical Bone	D30	140	1270	60						1.776	6.4
Cortical Bone	D34	140	1292	66						1.789	5.0
Cortical Bone	H30	140	1352	68						1.782	6.1
Mastoid	D30	100	-190	408	0.623	1.288	(6.7)	(6.2)	0.631	NA	NA
Mastoid	D34	100	-218	431	0.609	1.305	(6.3)	(6.0)	0.620	NA	NA
Mastoid	H30	100	-196	392						NA	NA
Mastoid	H30	120	-263	368						NA	NA
Mastoid	D30	140	-333	349						NA	NA
Mastoid	D34	140	-347	362						NA	NA
Mastoid	H30	140	-336	334						NA	NA
Lung	D30	100	-809	34	0.185	0.032	NA	NA	0.185	NA	NA
Lung	D34	100	-814	35	0.181	0.033	NA	NA	0.181	NA	NA
Lung	H30	100	-813	32						NA	NA
Lung	H30	120	-753	226						NA	NA
Lung	D30	140	-822	35						NA	NA
Lung	D34	140	-825	36						NA	NA
Lung	H30	140	-826	34						NA	NA

Table A.7: Tabulated compositions, mass density, CT numbers and bins of reference tissues presented in Schneider et al. [2000]. SPR, Z_{eff}, I-value and $\hat{\rho}_e$ values were calculated according to Eq. 2.23, Eq. 3.18 ($n = 3.1$), Eq. 2.21, Eq. 2.24 and Tab. A.8.

Material	$\hat{\rho}_e$	ρ [g/cm^3]	SPR	Z_{eff}	I-value [eV]	CT no [HU]	CT no bin	H	C	N	O	Na	Mg	P	S	Cl	K	Ca	Fe	I
Lung - deflated	0.260	0.26	1.041	7.54	75.17	-741	[-951,-120]	10.3	10.5	3.1	74.9	0.2	0	0.2	0.3	0.3	0.2	0	0	0
Adipose tissue 3	0.933	0.93	0.952	6.18	63.24	-98	[-119,-83]	11.6	68.1	0.2	19.8	0.1	0	0	0.1	0.1	0	0	0	0
Adipose tissue 2	0.951	0.95	0.968	6.37	64.78	-77	[-82,-53]	11.4	59.8	0.7	27.8	0.1	0	0	0.1	0.1	0	0	0	0
Adipose tissue 1	0.970	0.97	0.984	6.55	66.32	-55	[-82,-53]	11.2	51.7	1.3	35.5	0.1	0	0	0.1	0.1	0	0	0	0
Yellow marrow	0.982	0.98	1.001	6.26	63.90	-49	[-52,-23]	11.5	64.4	0.7	23.1	0.1	0	0	0.1	0.1	0	0	0	0
Mammary gland 1	0.987	0.99	1.001	6.60	66.91	-37	[-52,-23]	10.9	50.6	2.3	35.8	0.1	0	0.1	0.1	0.1	0	0	0	0
Yellow/red marrow	0.998	1.00	1.013	6.59	66.43	-22	[-22,7]	11	52.9	2.1	33.5	0.1	0	0.1	0.1	0.1	0.1	0	0	0
Brain, Cerebrospinal fluid	1.009	1.01	1.008	7.57	75.79	13	[8,18]	11.1	0	0	88.0	0.5	0	0	0	0.4	0	0	0	0
Mammary gland 2	1.014	1.02	1.022	6.97	70.29	-1	[-22,7]	10.6	33.2	3.0	52.7	0.1	0	0.1	0.2	0.1	0	0	0	0
Urine	1.018	1.02	1.017	7.68	75.90	26	[19,80]	11.0	0.5	1.0	86.2	0.4	0	0.1	0	0.6	0.2	0	0	0
Red marrow	1.023	1.03	1.033	7.03	69.18	11	[8,18]	10.5	41.4	3.4	43.9	0	0	0.1	0.2	0.2	0.2	0	0.1	0
Adrenal gland	1.024	1.03	1.031	7.12	71.24	14	[8,18]	10.6	28.4	2.6	57.8	0	0	0.1	0.2	0.2	0.1	0	0	0
Small intestine wall	1.024	1.03	1.025	7.39	74.29	23	[19,80]	10.6	11.5	2.2	75.1	0.1	0	0.1	0.1	0.2	0.1	0	0	0
Gallbladder bile	1.026	1.03	1.026	7.48	75.25	27	[19,80]	10.8	6.1	0.1	82.2	0.4	0	0	0	0.4	0	0	0	0
Lymph	1.026	1.03	1.026	7.52	75.45	29	[19,80]	10.8	4.1	1.1	83.2	0.3	0	0	0.1	0.4	0	0	0	0
Prostate	1.033	1.04	1.033	7.45	74.96	34	[19,80]	10.5	8.9	2.5	77.4	0.2	0	0.1	0.2	0	0.2	0	0	0
Pancreas	1.034	1.04	1.037	7.36	73.43	32	[19,80]	10.6	16.9	2.2	69.4	0.2	0	0.2	0.1	0.2	0.2	0	0	0
Brain, white matter	1.034	1.04	1.037	7.43	73.13	34	[19,80]	10.6	19.4	2.5	66.1	0.2	0	0.4	0.2	0.3	0.3	0	0	0
Testis	1.034	1.04	1.035	7.48	74.73	36	[19,80]	10.6	9.9	2.0	76.6	0.2	0	0.1	0.2	0.2	0.2	0	0	0
Brain, grey matter	1.035	1.04	1.036	7.58	74.79	40	[19,80]	10.7	9.5	1.8	76.7	0.2	0	0.3	0.2	0.3	0.3	0	0	0
Aorta	1.038	1.05	1.038	7.58	75.16	43	[19,80]	9.9	14.7	4.2	69.8	0.2	0	0.4	0.3	0	0.1	0.4	0	0
Muscle - skeletal 1	1.039	1.05	1.040	7.46	74.28	40	[19,80]	10.1	17.1	3.6	68.1	0.1	0	0.2	0.3	0.1	0.4	0	0	0
Kidney 1	1.040	1.05	1.041	7.45	74.29	41	[19,80]	10.2	16.0	3.4	69.3	0.2	0	0.2	0.2	0.2	0.2	0.1	0	0
Muscle - skeletal 2	1.040	1.05	1.041	7.50	74.62	43	[19,80]	10.2	14.3	3.4	71.0	0.1	0	0.2	0.3	0.1	0.4	0	0	0
Muscle - skeletal 3	1.040	1.05	1.040	7.55	75.26	44	[19,80]	10.2	11.2	3.0	74.5	0.1	0	0.2	0.3	0.1	0.4	0	0	0
Heart 1	1.041	1.05	1.043	7.41	73.83	41	[19,80]	10.3	17.5	3.1	68.1	0.1	0	0.2	0.2	0.2	0.3	0	0	0
Kidney 2	1.041	1.05	1.042	7.50	74.66	43	[19,80]	10.3	13.2	3.0	72.4	0.2	0	0.2	0.2	0.2	0.2	0.1	0	0
Liver 1	1.041	1.05	1.042	7.49	74.36	43	[19,80]	10.3	15.6	2.7	70.1	0.2	0	0.3	0.3	0.2	0.3	0	0	0
Stomach	1.042	1.05	1.044	7.39	74.20	41	[19,80]	10.4	13.9	2.9	72.1	0.1	0	0.1	0.2	0.1	0.2	0	0	0
Thyroid	1.042	1.05	1.043	8.13	74.71	42	[19,80]	10.4	11.9	2.4	74.5	0.2	0	0.1	0.1	0.2	0.1	0	0	0.1
Heart 2	1.042	1.05	1.043	7.47	74.31	43	[19,80]	10.4	13.9	2.9	71.8	0.1	0	0.2	0.2	0.2	0.3	0	0	0
Heart 3	1.042	1.05	1.042	7.53	75.00	45	[19,80]	10.4	10.3	2.7	75.6	0.1	0	0.2	0.2	0.2	0.3	0	0	0
Kidney 3	1.042	1.05	1.042	7.53	74.98	45	[19,80]	10.4	10.6	2.7	75.2	0.2	0	0.2	0.2	0.2	0.2	0.1	0	0
Ovary	1.043	1.05	1.043	7.51	75.02	46	[19,80]	10.5	9.3	2.4	76.8	0.2	0	0.2	0.2	0.2	0.2	0	0	0
Trachea	1.049	1.06	1.049	7.56	75.04	54	[19,80]	10.1	13.9	3.3	71.3	0.1	0	0.4	0.4	0.1	0.4	0	0	0
Mammary gland 3	1.050	1.06	1.052	7.29	74.03	45	[19,80]	10.2	15.8	3.7	69.8	0.1	0	0.1	0.2	0.1	0	0	0	0
Liver 2	1.050	1.06	1.051	7.52	74.82	53	[19,80]	10.2	13.9	3.0	71.6	0.2	0	0.3	0.3	0.2	0.3	0	0	0
Blood whole	1.050	1.06	1.050	7.59	75.20	56	[19,80]	10.2	11.0	3.3	74.5	0.1	0	0.1	0.2	0.3	0.2	0	0.1	0
Spleen	1.051	1.06	1.051	7.53	74.98	54	[19,80]	10.3	11.3	3.2	74.1	0.1	0	0.3	0.2	0.2	0.3	0	0	0
Heart, bloodfilled	1.051	1.06	1.052	7.57	74.81	56	[19,80]	10.3	12.1	3.2	73.4	0.1	0	0.1	0.2	0.3	0.2	0	0.1	0
Eye lens	1.055	1.07	1.057	7.26	74.29	49	[19,80]	9.6	19.5	5.7	64.6	0.1	0	0.1	0.3	0.1	0	0	0	0
Liver 3	1.059	1.07	1.059	7.54	75.21	63	[19,80]	10.1	12.6	3.3	72.7	0.2	0	0.3	0.3	0.2	0.3	0	0	0
Skin 1	1.078	1.09	1.082	7.25	72.81	72	[19,80]	10.0	25.0	4.6	59.4	0.2	0	0.1	0.3	0.3	0.1	0	0	0
Skin 2	1.078	1.09	1.081	7.31	73.66	74	[19,80]	10.0	20.4	4.2	64.5	0.2	0	0.1	0.2	0.3	0.1	0	0	0
Skin 3	1.079	1.09	1.080	7.39	74.38	77	[19,80]	10.1	15.8	3.7	69.5	0.2	0	0.1	0.2	0.3	0.1	0	0	0
Cartilage	1.083	1.10	1.078	7.94	78.02	102	[81,120]	9.6	9.9	2.2	74.4	0.5	0	2.2	0.9	0.3	0	0	0	0
Connective tissue	1.102	1.12	1.103	7.36	74.70	100	[81,120]	9.4	20.7	6.2	62.2	0.6	0	0	0.6	0.3	0	0	0	0
Sternum	1.210	1.25	1.197	10.36	82.39	385	[301,400]	7.8	31.6	3.7	43.8	0	0.1	4.0	0.2	0.1	0.1	8.5	0.1	0
Sacrum male	1.244	1.29	1.227	10.71	84.62	454	[401,500]	7.4	30.2	3.7	43.8	0	0.1	4.5	0.2	0.1	0.1	9.8	0.1	0
D6, L3 incl. cartilage m	1.253	1.30	1.233	10.74	85.83	466	[401,500]	7.3	26.5	3.6	47.3	0.1	0.1	4.8	0.3	0.1	0.1	9.8	0	0
Vert. col.(D6. L3), excl cartilage	1.278	1.33	1.256	11.05	86.96	526	[501,600]	7.0	28.7	3.8	43.7	0	0.1	5.1	0.2	0.1	0.1	11.1	0.1	0
Vert. col. - whole	1.279	1.33	1.257	10.92	87.04	514	[501,600]	7.1	25.8	3.6	47.2	0.1	0.1	5.1	0.3	0.1	0.1	10.5	0	0
Femur/Humerus, spherical head	1.279	1.33	1.259	11.17	85.68	538	[501,600]	7.1	37.9	2.6	34.2	0.1	0.1	5.6	0.2	0	0	12.2	0	0
Femur, conical trochanter	1.305	1.36	1.283	11.32	86.94	586	[501,600]	6.9	36.6	2.7	34.7	0.1	0.1	5.9	0.2	0	0	12.8	0	0
C4 incl. cartilage (male)	1.321	1.38	1.293	11.27	89.80	599	[501,600]	6.6	24.3	3.7	47.1	0.1	0.1	5.7	0.3	0.1	0.1	11.9	0	0
Sacrum female	1.330	1.39	1.302	11.37	89.55	621	[601,700]	6.6	27.1	3.8	43.5	0.1	0.1	5.8	0.3	0.1	0.1	12.5	0	0
Humerus whole specimen	1.331	1.39	1.306	11.49	88.31	636	[601,700]	6.7	35.2	2.8	35.2	0.1	0.1	6.2	0.2	0	0	13.5	0	0
Innominate male	1.346	1.41	1.315	11.54	91.13	658	[601,700]	6.3	26.2	3.9	43.6	0.1	0.1	6.1	0.3	0.1	0.1	13.2	0	0
Ribs (2nd. 6th)	1.347	1.41	1.317	11.51	90.72	657	[601,700]	6.4	26.3	3.9	43.6	0.1	0.1	6.0	0.3	0.1	0.1	13.1	0	0
Vert. col.(C4), excl. cartilage	1.355	1.42	1.324	11.56	91.22	672	[601,700]	6.3	26.1	3.9	43.6	0.1	0.1	6.1	0.3	0.1	0.1	13.3	0	0
Femur - total bone	1.355	1.42	1.325	11.69	90.48	688	[601,700]	6.3	33.3	2.9	36.2	0.1	0.1	6.6	0.2	0	0	14.3	0	0
Femur (whole specism)	1.364	1.43	1.334	11.71	90.59	702	[701,800]	6.3	33.1	2.9	36.3	0.1	0.1	6.6	0.2	0	0	14.4	0	0
Innominate female	1.389	1.46	1.354	11.82	93.25	742	[701,800]	6.0	25.0	3.9	43.5	0.1	0	6.6	0.3	0.1	0.1	14.3	0.1	0
Humerus - total bone	1.389	1.46	1.355	11.90	92.48	756	[701,800]	6.0	31.4	3.1	36.9	0.1	0.1	7.0	0.2	0	0	15.2	0	0
Clavicle, scapula	1.389	1.46	1.355	11.90	92.50	756	[701,800]	6.0	31.3	3.1	37.0	0.1	0.1	7.0	0.2	0	0	15.2	0	0
Humerus, cylindrical shaft	1.415	1.49	1.378	12.03	93.86	805	[801,900]	5.8	30.1	3.2	37.4	0.1	0.2	7.2	0.2	0	0	15.8	0	0
Ribs (10th)	1.441	1.52	1.400	12.07	95.86	843	[801,900]	5.6	23.5	4.0	43.4	0.1	0.1	7.2	0.3	0.1	0.1	15.6	0	0
Cranium	1.517	1.61	1.466	12.47	100.05	999	[901,1000]	5.0	21.2	4.0	43.5	0.1	0.2	8.1	0.3	0	0	17.6	0	0
Mandible	1.577	1.68	1.519	12.69	102.71	1113	[1101,1200]	4.6	19.9	4.1	43.5	0.1	0.2	8.6	0.3	0	0	18.7	0	0
Femur, cylindrical shaft	1.636	1.75	1.570	12.97	105.48	1239	[1201,1300]	4.2	20.4	3.8	41.5	0.1	0.2	9.3	0.3	0	0	20.2	0	0
Cortical bone	1.780	1.92	1.696	13.41	111.97	1524	[1501,1600]	3.4	15.5	4.2	43.5	0.1	0.2	10.3	0.3	0	0	22.5	0	0

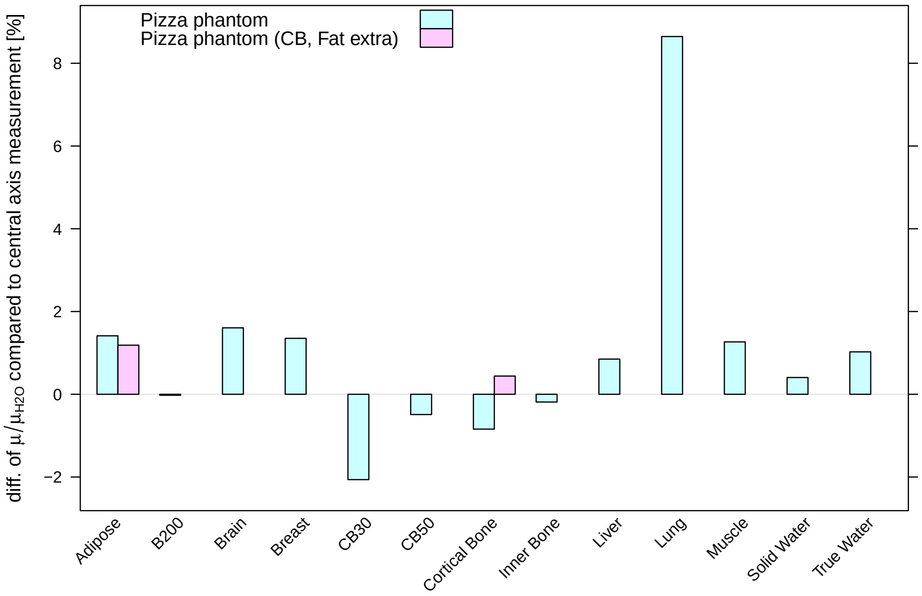

Figure A.1: Differences of relative photon attenuation coefficients for the employed tissue surrogate rods measured in three different phantom configurations (Sec. 4.1.1)

Table A.8: Physical properties for atomic constituents of compounds important for the calculation of SPR, $\hat{\rho}_e$ and I-value for tabulated tissue compositions. I-values were taken from ICRU [1993] or by multiplying elemental I-value with 1.13 according to ICRU [1993].

element	H	C	N	O	Na	Mg	P	S	Cl	K	Ca	Fe	I
Z	1	6	7	8	11	12	15	16	17	19	20	26	53
A	1.00794	12.0107	14.0067	15.9994	22.9898	24.305	30.9736	32.065	35.453	39.0983	40.078	55.845	126.9045
Z/A	0.9921	0.4996	0.4998	0.5	0.4785	0.4937	0.4843	0.499	0.4795	0.486	0.499	0.4656	0.4176
compound I [eV]	19.2	81	82	106	168.4	176.3	195.5	203.4	180	214.7	215.8	323.2	554.8

Table A.9: Elemental composition, I-value and Z_{eff} of seven aqueous solutions of sodium chloride and sodium hydroxide (data partly taken from Niebuhr [2012]). Table reprinted from Hünemohr et al. [2014b].

element solution	H	O	Na	Cl	reference I-value [eV]	reference Z_{eff}	measured Z_{eff} 80/140Sn kV	measured Z_{eff} 100/140Sn kV
1.3% NaCl	11.05	87.65	0.51	0.79	76.04	7.66	7.65	7.62
4% NaCl	10.74	85.26	1.57	2.43	77.56	8.07	8.08	8.06
7.1% NaCl	10.4	82.5	2.79	4.31	79.36	8.5	8.53	8.48
10.7% NaCl	9.99	79.31	4.21	6.49	81.53	8.94	8.98	8.97
14.8% NaCl	9.53	75.67	5.82	8.98	84.09	9.41	9.45	9.44
8.9% NaOH	10.42	84.47	5.12	0	78.5	7.7	7.7	7.65
27.8% NaOH	8.78	75.24	15.98	0	85.91	8.19	8.22	8.17

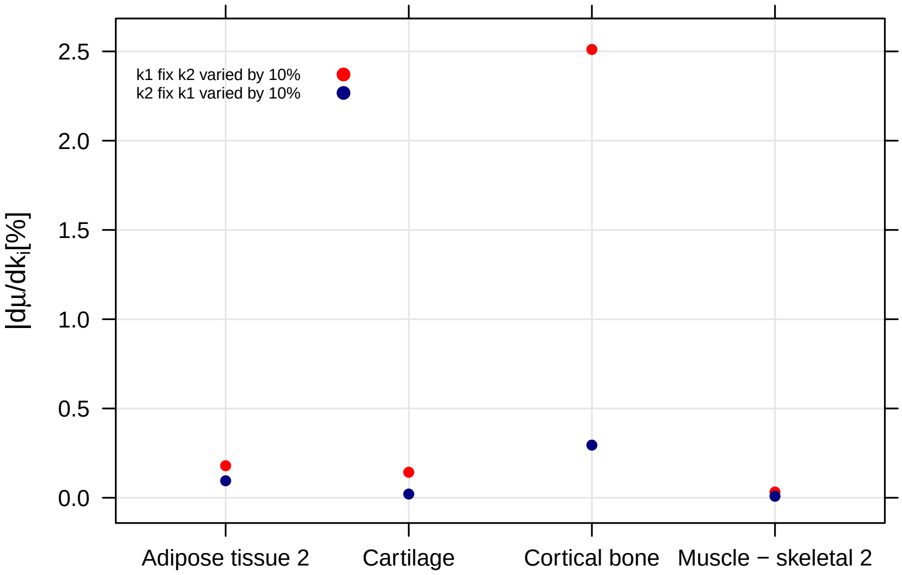

Figure A.2: Dependency of μ/μ_{H2O} on relative changes (±10 %) in k_1 and k_2. Particularly for bone tissue, accurate optimization of k_2 (photoelectric part, Eq. 3.1) is mandatory for a realistic characterization of photon attenuation.

Table A.10: Correlation of $\hat{\rho}_e$ to Z_{eff} for tissue surrogates (Fig. A.4). Correlation for lung is not calculated as Z_{eff} cannot be determined.

Material	80/140Sn kV	100/140Sn kV
True Water	-0.45	-0.47
Adipose	-0.36	-0.39
Breast	-0.41	-0.44
Brain	-0.41	-0.44
Muscle	-0.34	-0.26
Liver	-0.36	-0.34
Inner Bone	-0.45	-0.03
B200	-0.46	-0.08
CB30	-0.49	-0.20
CB50	-0.62	-0.49
Cortical Bone	-0.39	-0.54

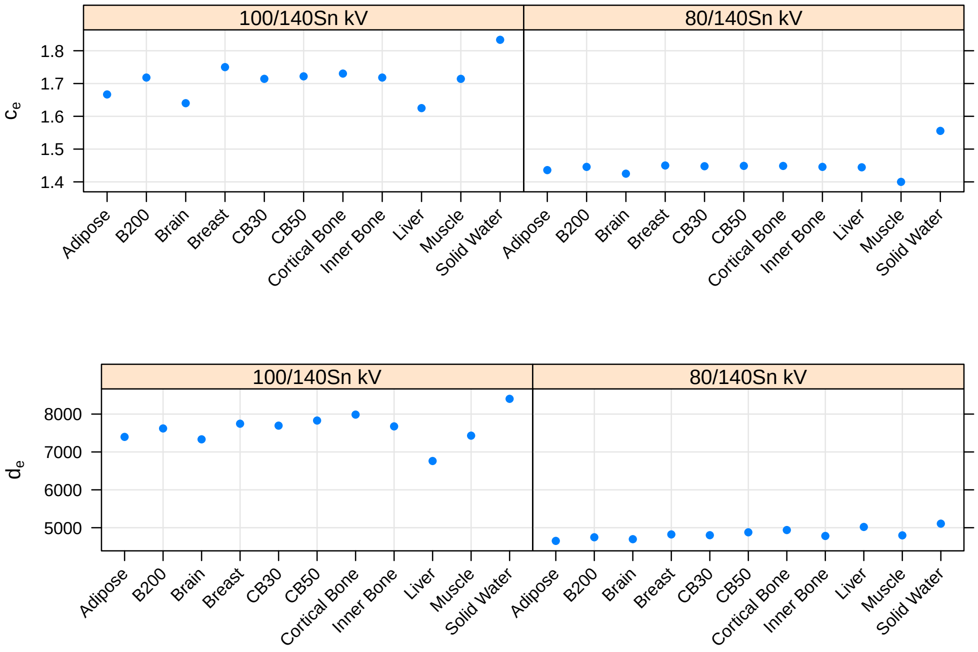

Figure A.3: Calibration constants (Sec. 3.5) calculated with measured CT numbers listed in Tab. A.4. Siemens applied additional image processing and beam hardening correction and consequently there is no single calibration constant when c_e and d_e are back calculated.

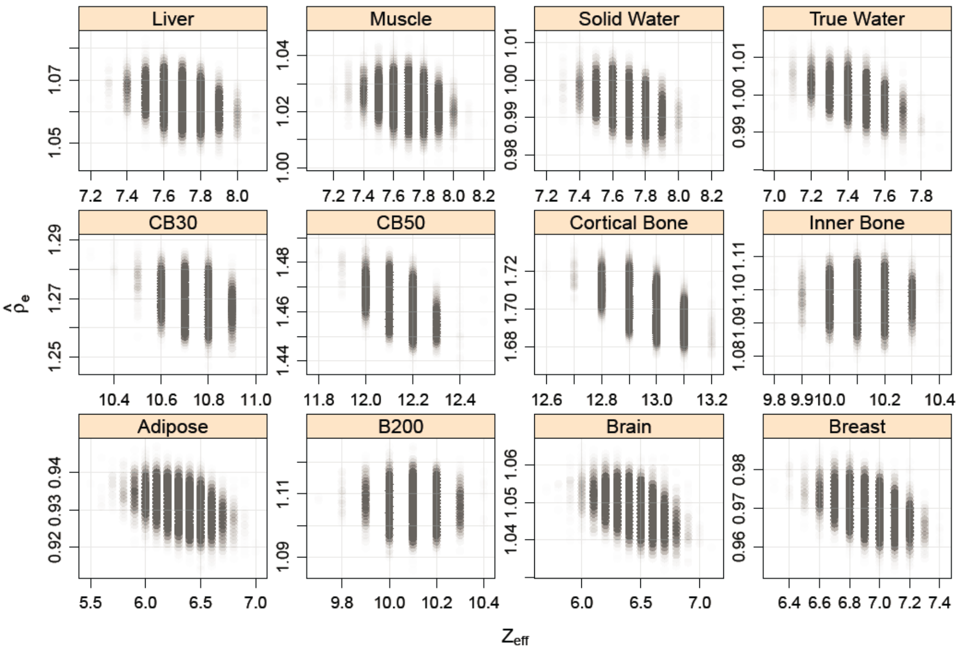

Figure A.4: Correlation between $\hat{\rho}_e$ and Z_{eff} for all pixels of a defined VOI measured for different tissue surrogates at 100 kV/140Sn kV. The lower $\hat{\rho}_e$ the higher Z_{eff} (cf. Eq. 3.16, Eq. 3.11). Corresponding correlation coefficients are summarized in Tab. A.10.

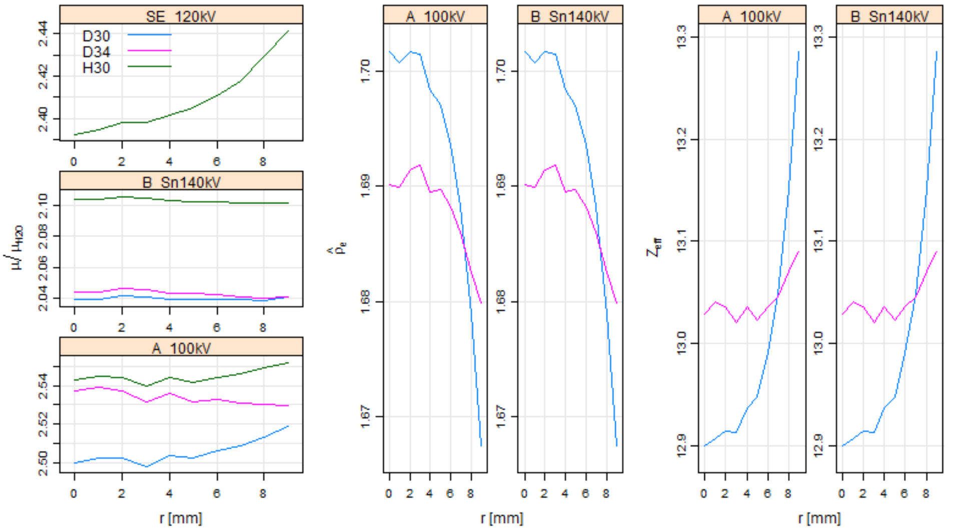

Figure A.5: DECT contrasts measured in the cortical bone surrogate as a function of the inserts' radius. Reconstruction with the D34 kernel is found to be less affected by beam hardening compared to H30 and D30.

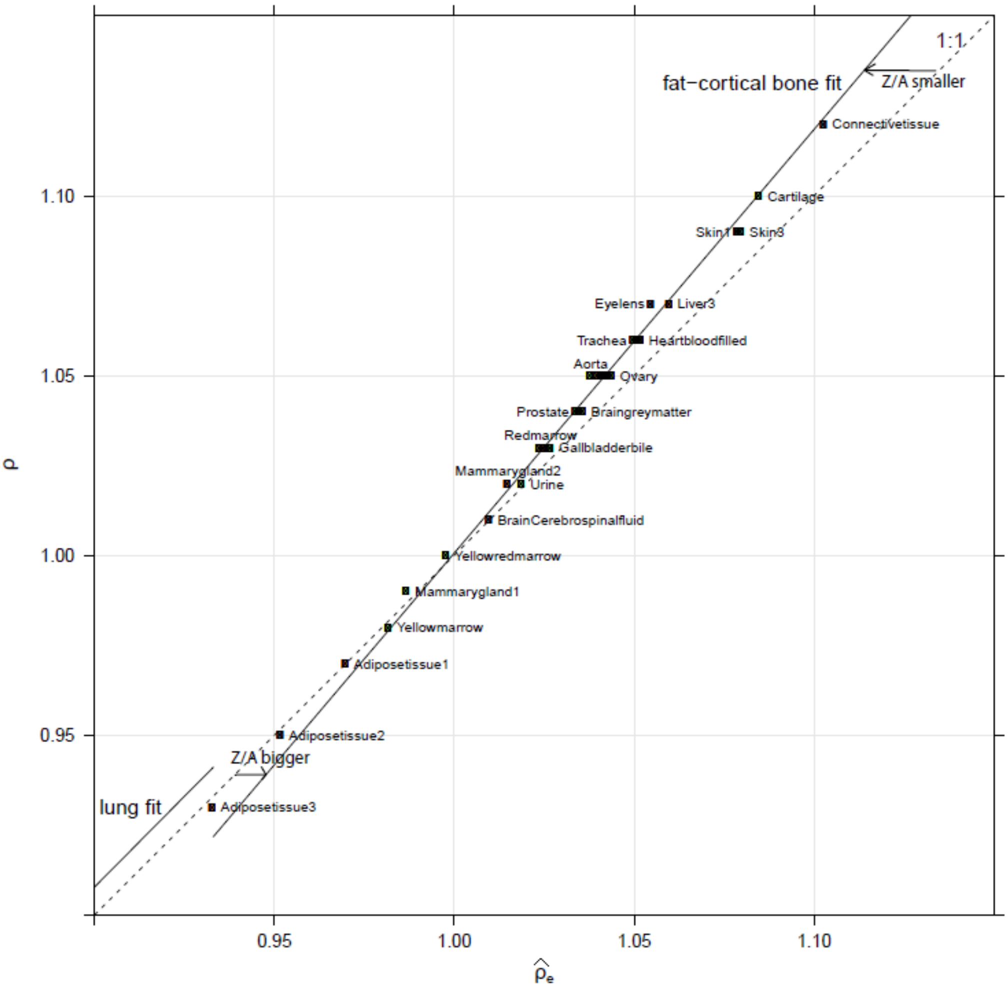

Figure A.6: "ρ to $\hat{\rho}_e$ fits in the soft tissue region. Shown are the lung and adipose-bone fits (applied in this paper in Sec. 2.B), and the identity (1:1). Three different regions appear, mainly determined by different Z/A ratios: lung (Z/A similar to muscle), adipose region (Z/A bigger than water due to increased hydrogen amount), and one region with decreasing Z/A ratio toward cortical bone. An additional fit for the adipose region might improve ρ prediction for hydrogen rich tissues", figure and caption reprinted from Hünemohr et al. [2014c].

Acknowledgments

I would like to thank Prof. Dr. Oliver Jäkel for the possibility to pursue this project in his research group. I highly appreciate his continuous and always encouraging support throughout the last years. I wish to thank Prof. Dr. Wolfgang Schlegel for agreeing to be the second referee of this thesis. I am particularly grateful to Dr. Steffen Greilich for being an excellent supervisor, for his guidance and sound advice that enhanced my scientific work. It was a great pleasure to spend half a year in Boston and I am grateful to Prof. Dr. Harald Paganetti and Prof. Dr. Joao Seco for giving me the chance to work in the physics division at MGH. I would like to thank both of them for their scientific advise and I am grateful for the positive experiences and the knowledge I gained. I wish to thank Dr. Bernhard Krauss (Siemens Forchheim) for providing the DECT algorithm and the support concerning my research. Prof. Dr. Heinz-Peter Schlemmer is acknowledged for the continuous support of this project. I am grateful to the Helmholtz Association for granting the PhD stipend at the DKFZ graduate school.

The presented measurements were only possible through the help of several people: Martina Jochim is acknowledged for help with the CT scans; Dr. Stephan Brons, Raya Gallas, Dr. Clarissa Gillmann, Julia-Maria Osinga and Dr. Marcus Winter for their help with the WEPL measurements. I am thankful to Benjamin Ackermann, Sebastian Faby, Stefan Kuchenbecker, Andrea Schwahofer for the scientific discussions. Throughout the last years I really enjoyed the pleasant atmosphere in the e0409 research group and I would like to express my sincere gratitude to all current and former colleagues for the good times.